THE MINISTRY OF SCIENCE AND HIGHER EDUCATION OF THE RUSSIAN FEDERATION

ST. PETERSBURG STATE POLYTECHNICAL UNIVERSITY

JOURNAL

Physics and Mathematics

VOLUME 17, No. 1, 2024

Peter the Great St. Petersburg
Polytechnic University
2024

ST. PETERSBURG STATE POLYTECHNICAL UNIVERSITY JOURNAL.
PHYSICS AND MATHEMATICS

The journal is included in the List of leading peer-reviewed scientific journals and other editions to publish major findings of theses for the research degrees of Doctor of Sciences and Candidate of Sciences.

The publications are presented in the VINITI RAS Abstract Journal and Ulrich's Periodical Directory International Database.

The journal is published since 2008 as part of the periodical edition 'Nauchno-tekhnicheskie vedomosti SPb-GPU'.

The journal is registered with the Federal Service for Supervision in the Sphere of Telecom, Information Technologies and Mass Communications (ROSKOMNADZOR). Certificate ПИ № ФС77-52144 issued December 11, 2012.

The journal is distributed through the CIS countries catalogue, the «Press of Russia» joint catalogue and the «Press by subscription» Internet catalogue. The subscription index is **71823.**

The journal is in the **Web of Science** (Emerging Sources Citation Index), **Scopus**, the **Russian Science Citation Index** (RSCI) and the **Directory of Open Access Journals** (DOAJ) databases.

© Scientific Electronic Library (http://www.elibrary.ru).

Address: 195251 Politekhnicheskaya St. 29, St. Petersburg, Russia.

Phone: (812) 294-22-85.
http://ntv.spbstu.ru/physics

МИНИСТЕРСТВО НАУКИ И ВЫСШЕГО ОБРАЗОВАНИЯ РОССИЙСКОЙ ФЕДЕРАЦИИ

НАУЧНО-ТЕХНИЧЕСКИЕ ВЕДОМОСТИ

САНКТ-ПЕТЕРБУРГСКОГО ГОСУДАРСТВЕННОГО ПОЛИТЕХНИЧЕСКОГО УНИВЕРСИТЕТА

Физико-математические науки

ТОМ 17, № 1

2024

Санкт-Петербургский политехнический
университет Петра Великого
2024

НАУЧНО-ТЕХНИЧЕСКИЕ ВЕДОМОСТИ САНКТ-ПЕТЕРБУРГСКОГО ГОСУДАРСТВЕННОГО ПОЛИТЕХНИЧЕСКОГО УНИВЕРСИТЕТА. ФИЗИКО-МАТЕМАТИЧЕСКИЕ НАУКИ

Журнал с 2002 г. входит в Перечень ведущих рецензируемых научных журналов и изданий, в которых должны быть опубликованы основные результаты диссертаций на соискание ученых степеней доктора и кандидата наук.

Сведения о публикациях представлены в Реферативном журнале ВИНИТИ РАН, в международной справочной системе «Ulrich's Periodical Directory».

С 2008 года выпускается в составе сериального периодического издания «Научно-технические ведомости СПбГПУ».

Журнал зарегистрирован Федеральной службой по надзору в сфере информационных технологий и массовых коммуникаций (Роскомнадзор). Свидетельство о регистрации ПИ № ФС77-52144 от 11 декабря 2012 г.

Распространяется по Каталогу стран СНГ, Объединенному каталогу «Пресса России» и по Интернет-каталогу «Пресса по подписке». Подписной индекс **71823**.

Журнал индексируется в базе данных **Web of Science** (Emerging Sources Citation Index), **Scopus**, а также включен в базы данных **«Российский индекс научного цитирования»** (РИНЦ), размещенную на платформе Научной электронной библиотеки на сайте http://www.elibrary.ru, и **«Directory of Open Access Journals»** (DOAJ)

Адрес редакции и издательства:
Россия, 195251, Санкт-Петербург, ул. Политехническая, д. 29.
Тел. редакции (812) 294-22-85.
http://ntv.spbstu.ru/physics

Contents

Condensed matter physics

Simulation of physical processes

Experimental technique and devices

Physical electronics

Physical materials technology

Biophysics and medical physics

Nuclear physics

Radiophysics

Mechanics

Содержание

Физика конденсированного состояния

Математическое моделирование физических процессов

Приборы и техника физического эксперимента

Физическая электроника

Физическое материаловедение

Биофизика и медицинская физика

Ядерная физика

Радиофизика

Механика

CONDENSED MATTER PHYSICS

Original article
UDC 621.38:539.1
DOI: https://doi.org/10.18721/JPM.17101

THE ELECTRON AND PROTON IRRADIATION EFFECTS ON THE PROPERTIES OF HIGH-VOLTAGE 4H-SiC SCHOTTKY DIODES WITHIN THE OPERATING TEMPERATURE RANGE

V. V. Kozlovski [1] ✉, *A. A. Lebedev* [2], *R. A. Kuzmin* [2],
D. A. Malevsky [2], *M. E. Levinshtein* [2], *G. A. Oganesyan* [2]

[1] Peter the Great St. Petersburg Polytechnic University, St. Petersburg, Russia;

[2] Ioffe Institute, St. Petersburg, Russia

✉ kozlovski@physics.spbstu.ru

Abstract. In the paper, the effects of type, dose and temperature of irradiation with stable elementary particles (0.9 MeV electrons and 15 MeV protons) on the properties of the high-voltage 4H-SiC Junction Barrier Schottky diodes at room temperature (23°C) and the limiting operating one (175°C) have been compared. The electron irradiation of the objects with equal doses at 23°C и 175°C was found to cause a significant increase in its base differential resistance in the former case and the absence of this effect in the latter. However, in the latter, DLTS spectra exhibited a noticeable increase in the concentration of deep levels in the upper half of the band gap. The proton irradiation resulted in a noticeable rise in the mentioned resistance even at 175°C. The results obtained make it possible to evaluate the radiation resistance of the studied devices to proton and electron irradiation within the framework of any given requirements.

Keywords: silicon carbide, Schottky diode, irradiation, DLTS spectrum, current–voltage characteristic, annealing

Funding: This work was partly supported by Russian Science Foundation through project No. 22-12-00003.

For citation: Kozlovski V. V., Lebedev A. A., Kuzmin R. A., Malevsky D. A., Levinshtein M. E., Oganesyan G. A., The electron and proton irradiation effects on the properties of high-voltage 4H-SiC Schottky diodes within the operating temperature range, St. Petersburg State Polytechnical University Journal. Physics and Mathematics. 17 (1) (2024) 9–20. DOI: https://doi.org/10.18721/JPM.17101

Научная статья
УДК 621.38:539.1
DOI: https://doi.org/10.18721/JPM.17101

ВЛИЯНИЕ ЭЛЕКТРОННОГО И ПРОТОННОГО ОБЛУЧЕНИЯ НА СВОЙСТВА ВЫСОКОВОЛЬТНЫХ 4H-SiC ДИОДОВ ШОТТКИ В РАБОЧЕМ ТЕМПЕРАТУРНОМ ДИАПАЗОНЕ

В. В. Козловский [1] ✉, *А. А. Лебедев* [2], *Р. А. Кузьмин* [2],
Д. А. Малевский [2], *М. Е. Левинштейн* [2], *Г. А. Оганесян* [2]

[1] Санкт-Петербургский политехнический университет Петра Великого,
Санкт-Петербург, Россия;

[2] Физико-технический институт им. А. Ф. Иоффе РАН, Санкт-Петербург, Россия

✉ kozlovski@physics.spbstu.ru

Аннотация. В работе сопоставлено влияние вида, дозы и температуры облучения стабильными элементарными частицами (электронами и протонами с энергиями 15 и 0.9 МэВ соответственно) на свойства высоковольтных 4H-SiC интегрированных диодов Шоттки (JBS) при комнатной (23°C) и предельно допустимой рабочей (175°C) температурах. Установлено, что электронное облучение объекта одинаковыми дозами при температурах 23°C и 175°C приводит к существенному росту дифференциального сопротивления базовых слоев в первом случае и отсутствию этого эффекта во втором. Однако во втором случае DLTS-спектры демонстрируют заметный рост концентрации глубоких уровней в верхней половине запрещенной зоны. Протонное же облучение даже при 175°C приводит к существенному росту указанного сопротивления. Исследовано влияние отжига на облученные протонами структуры. Полученные результаты позволяют оценивать устойчивость исследованных приборов к протонному и электронному облучению в рамках любых заданных требований.

Ключевые слова: карбид кремния, диод Шоттки, облучение, спектр DLTS, вольт-амперная характеристика, отжиг

Финансирование: Исследование выполнено при частичной финансовой поддержке Российского научного фонда (соглашение № 22-12-00003).

Для цитирования: Козловский В. В., Лебедев А. А., Кузьмин Р. А., Малевский Д. А., Левинштейн М. Е., Оганесян Г. А., Влияние электронного и протонного облучения на свойства высоковольтных 4H-SiC диодов Шоттки в рабочем температурном диапазоне // Научно-технические ведомости СПбГПУ. Физико-математические науки. 2024. Т. 17. № 1. С 9–20. DOI: https://doi.org/10.18721/JPM.17101

Introduction

High-voltage 4H-SiC Schottky diodes are important components of automotive and space-based electronics, nuclear power plant equipment, reactive power compensators, photovoltaic cells, etc. The radiation resistance of such components to electron and proton irradiation is an essential criterion for the possibility of using them in nuclear reactor equipment and aerospace electronics [1 – 4].

The effect of electron irradiation on the properties of SiC-based devices has been studied in a number of papers (see, for example, Refs. [5 – 7] and references therein). In these papers, irradiation was carried out only at room temperature. In Ref. [8], for 1700 V 4H-SiC integrated junction barrier Schottky diodes (JBS), the influence of the electron irradiation temperature at very high temperatures T_i (300°C and 500°C) was studied. These temperatures are much higher than the limit operating temperature of high voltage SiC industrial JBS diodes (175°C).

The effect of 100 keV–60 MeV proton irradiation on the properties of the 4H-SiC devices has also been studied in a number of papers. In the vast majority of papers, irradiation was carried out at room temperature (see, for example, references in Ref. [9]). In Ref. [10], the T_i irradiation temperature was within 100–400 K. In Ref. [11], the maximum irradiation temperature T_i was 500°C.

Studies of the irradiation effect at high (up to 500°C) temperatures have shown that the radiation resistance of SiC devices increases monotonically with the irradiation temperature growth. It has been demonstrated that high-temperature ("hot") irradiation produces defects that are absent during irradiation at room temperature. As shown earlier, when studying the defect creation in the silicon and gallium arsenide, it is very important to pay attention to high-temperature investigations specifically, due to the possibility of formation of secondary defects [12, 13].

However, as a practical matter, of prime importance is analyzing the effect of electron and proton irradiation and subsequent annealing on the properties of high-voltage Schottky diodes in the range from the room temperature to the limiting operation temperature of 175°C (CPW3-1700S010 Datasheet | Silicon Carbide Schottky Diode Chip. (n.d.), Accessed November 20, 2023), because 4H-SiC diodes are elements of power industrial electronics including automotive electronics, power converters, solar cells drives, and numerous other applications [14 – 17].

The goal of this study was to compare the effects of electron and proton irradiation carried out at room temperature and the maximum operating temperature, as well as post-irradiation annealing, on the parameters of high-power 4H-SiC JBS.

This study allows us to suggest some practical recommendations for improving their radiation resistance.

In this paper, we have compared the effect of irradiation with 0.9 MeV electrons and 15 MeV protons at T_i = 23°C and 175°C on the parameters of 4H-SiC high-voltage 4H-SiC JBS diodes with 600 and 1700 V blocking voltage U_b.

Materials and methods

4H-SiC Schottky diodes (JBS structures) with blocking voltage U_b = 600 V (CPW3-0600S002.0)[1] and U_b = 1700 V (CPW3-1700SO10)[2] were investigated [14]. The concentration of uncompensated impurity ($N_d - N_a$) in the base of structures with U_b = 600 V was $1 \cdot 10^{16}$ cm^{-3}; this value for the diodes with U_b = 1700 V was $3.4 \cdot 10^{15}$ cm^{-3}. At small forward bias, in the region of the exponential part of forward current–voltage characteristic, the I–V characteristics of both types of diodes were very well described by the dependence [11, 18]:

$$I = I_0 \exp(qU/\beta kT),$$

where I_0 is the saturation current, $I_0 = 10^{-12} - 10^{-11}$ A; β is the ideality factor, β = 1.02 – 1.05; q is the elementary charge; k is the Boltzmann constant.

Irradiation by electrons with an energy of 0.9 MeV was carried out in a pulsed mode (the pulse repetition rate was 490 Hz; its duration was 330 μs). The irradiation was carried out in a target chamber in air, where the temperature was maintained with an accuracy of ±5°C.

Irradiation by protons with an energy of 15 MeV was carried out at the MGTs-20 cyclotron in a pulsed mode (the pulse repetition rate was 100 Hz; its duration was 2.5 ms). The current density of the proton beam did not exceed 100 nA/cm^2.

The path lengths of electrons with an energy of 0.9 MeV and protons with an energy of 15 MeV in SiC were about 1.0 mm [19]. Thus, at base thicknesses $L \approx 10$ μm for 600 V diodes and $L \approx 20$ μm for diodes with U_b = 1700 V, defects were introduced uniformly over the sample volume.

The structures were subjected to post-irradiation annealing in the atmosphere of dry nitrogen at 300°C for 120 min. The I–V characteristics of the diodes were measured at 23°C in a pulsed mode, which ensured the isothermal nature of the measurements. The parameters of the formed radiation defects were determined by the method of non-stationary capacitance spectroscopy (DLTS). The measurements were carried out both in the initial samples and after each irradiation and/or annealing.

Results and discussion

The forward I–V characteristics of a diode with U_b = 600 V for an unirradiated structure (curve *1*) and those irradiated with electrons at temperatures T_i = 23°C and 175°C are compared in Fig. 1.

At small forward biases U_f, less than the cutoff voltage $U_c \approx 0.8$ V, i.e., in the region of the exponential part of the I–V curve, the electron irradiation has only a slight effect on the parameters of the current – voltage characteristics [8]. At $U_f \geq U_c$, the I–V curves are characterized by a linear forward current dependence on the forward voltage.

In an unirradiated diode, the differential resistance R_d of the base is 0.075 Ω. Irradiation with a fluence $\Phi_e = 1 \cdot 10^{16}$ cm^{-2} at room temperature leads to an increase in R_d by 1.9 times, to the value of $R_d \approx 0.142$ Ω. Irradiation with a fluence $\Phi_e = 2 \cdot 10^{16}$ cm^{-2} leads to an increase in R_d by approximately 4.6 times, to the value of $R_d \approx 0.345$ Ω. The concentration in the base of the

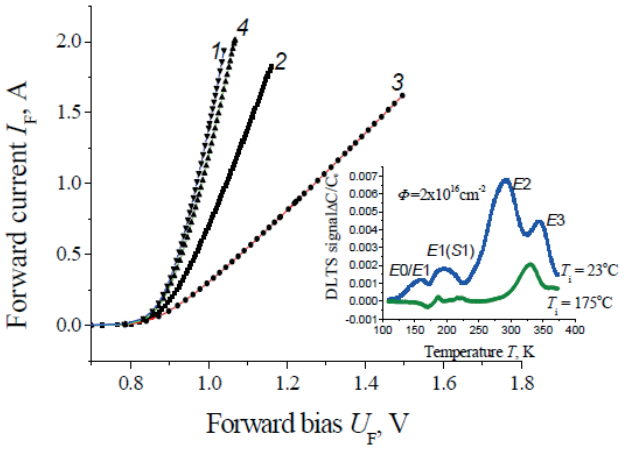

Fig. 1. A comparison of forward current – voltage characteristics of a diode (the blocking voltage is 600 V) obtained before (*1*) and after (*2* – *4*) its electron irradiation with fluences $\Phi_e = 1 \cdot 10^{16}$ cm^{-2} (*2*) и $2 \cdot 10^{16}$ cm^{-2} (*3*, *4*) at $T_i = 23$°C (*2*, *3*) and 175°C (*4*).
The data was obtained in the region of biases exceeding the cut-off voltage; $T_i = 23$°C (*1*).
In the inset: the DLTS spectra of the sample irradiated with electrons with fluence $\Phi_e = 2 \cdot 10^{16}$ cm^{-2} at two temperatures. The rate window was 51 s^{-1}

non-irradiated structure n_0 approximately equals to 10^{16} cm^{-3} [20]. Assuming that the change in the mobility under the influence of irradiation can be neglected [21] and that the change in the base resistance is due to a decrease in the electron concentration only, it is easy to calculate that, for the both fluence values, the removal rate η_e of electrons under the influence of irradiation is

$$\eta_e = (n_0 - n)/\Phi_e \approx 0.40 \text{ cm}^{-1}, \quad (1)$$

where n is the electron concentration after irradiation.

The η_e value obtained is less than that of 1.67 cm^{-1} specified in Ref. [6], and slightly more than that of 0.25 cm^{-1} reported in Ref. [22].

After electron irradiation with fluence $\Phi_e = 2 \cdot 10^{16}$ cm^{-2} at $T_i = 175$°C, the differential resistance of the base R_d is 0.085 Ω (see curve *4* in Fig. 1), i. e. the value of R_d increases as a result of irradiation by only approximately 13 %. It is quite obvious that an increase in the irradiation temperature T_i, even within the permissible operating temperature, radically increases the radiation resistance of the devices.

Inset in Fig. 1 shows the DTLS spectra describing the levels in the upper half of the band gap after electron irradiation of diodes with fluence $\Phi_e = 2 \cdot 10^{16}$ cm^{-2} at $T_i = 23$°C and 175°C. The temperature position of the DLTS peaks at $T_i = 23$°C agrees satisfactory with the data of Ref. [7], in which the DLTS spectra were studied after irradiation of JBS structures with $U_b = 1700$ V by electrons with an energy of 1.05 MeV. The concentrations of acceptor levels N_t determined from the position of the peaks in the inset (see Fig. 1) are $N_t^{E0/E1} = 2.35 \cdot 10^{13}$ cm^{-3}, $N_t^{E1/S1} = 3.70 \cdot 10^{13}$ cm^{-3}, $N_t^{E2} = 1.40 \cdot 10^{14}$ cm^{-3}, and $N_t^{E3} = 1.02 \cdot 10^{14}$ cm^{-3} for the E_0/E_1, E_1/S_1, E_2, and E_3 peaks, respectively.

It is well known that electron irradiation creates also EH6/7 acceptor level, which corresponds to a maximum in DTLS spectra at a temperature of ~ 570 K [6]. When measuring the samples (see the data in Fig. 1), the maximum temperature did not exceed 400 K in order to avoid spontaneous annealing [5]. The DLTS spectra measured up to temperature of ~ 630 K on control samples showed that the EH6/7 level with concentration of about 10^{14} cm^{-3} corresponds to fluence $\Phi_e = 2 \cdot 10^{16}$ cm^{-2} at $T_i = 23$°C.

Thus, the total concentration of acceptor centers in the upper half of the forbidden zone after electron irradiation with fluence $\Phi_e = 2 \cdot 10^{16}$ cm^{-2} at a temperature of $T_i = 23$°C is approximately $4 \cdot 10^{14}$ cm–3. At the initial electron concentration $n_0 = 10^{16}$ cm^{-3}, one would expect an increase in the resistance of the diode base by ≈ 10 %. Meanwhile, the experiment shows that the resistance

increases by ~ 4.6 times. It should be assumed that electron irradiation creates acceptor levels in the lower half of the band gap as well. However, to the best of our knowledge, data on the concentration and parameters of the acceptor centers created by electron irradiation in 4H-SiC in the lower half of the band gap are not available in the literature.

Under irradiation at T_i = 175°C (see inset in Fig. 1), the peak with the maximum amplitude at $T \approx 330$ K (peak E_2) corresponds to the $Z1/Z2$ level. Its concentration $N_t^{Z1/Z2}$ is $5.0 \cdot 10^{13}$ cm^{-3}. The peaks observed at $T = 171$ K, 185 K, and 220 K correspond to the concentration of $N_{t171} \approx 9.0 \cdot 10^{12}$ cm^{-3}, $N_{t185} \approx 4.2 \cdot 10^{12}$ cm^{-3}, and $N_{t220} \approx 5.0 \cdot 10^{12}$ cm^{-3}, respectively. Assuming that the concentrations of the EH6/7 and $Z1/Z2$ levels are equal [23], the total concentration of acceptor levels generated by fluence $\Phi_e = 2 \cdot 10^{16}$ cm^{-2} in the upper half of the band gap at $T_i = 175$°C can be considered equal to $1.2 \cdot 10^{14}$ cm^{-3}. An increase in resistance due to irradiation expected from such data should be ~1.2 %. Meanwhile, as can be seen from a comparison between curves *1* and *4* in Fig. 1, the resistance R_d increases in this case by about ~13%, i.e., about an order of magnitude stronger.

The forward I–V characteristics of a diode with U_b = 600 V for an unirradiated structure (curve *1*) and those irradiated with protons at temperatures T_i = 23°C and 175°C, as well as the structures after subsequent annealing (see inset in Fig. 2), are compared in Fig. 2.

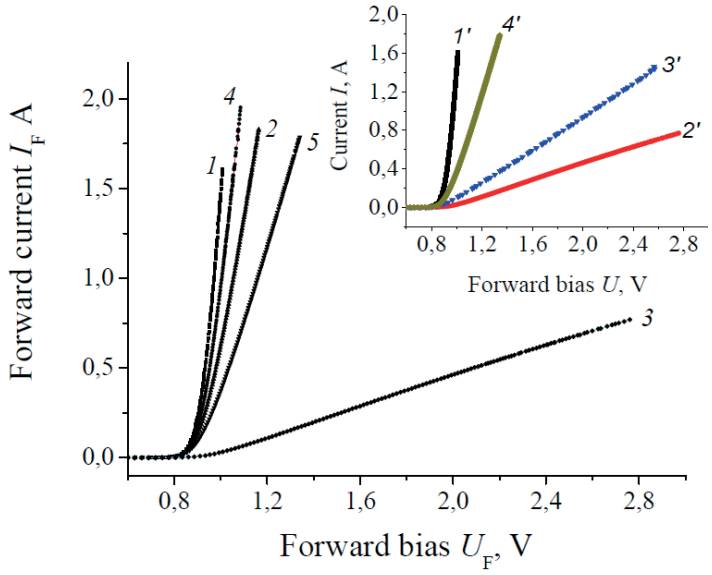

Fig. 2. A comparison of forward current – voltage characteristics of a diode (the blocking voltage is 600 V) obtained before (*1*, *1′* in the inset) and after (*2*, *2′* in the inset, *3* – *5*) its proton irradiation with fluences $\Phi_p = 5 \cdot 10^{13}$ cm^{-2} (*2*, *2′*, *4*) and $1 \cdot 10^{14}$ cm^{-2} (*3*, *5*) at T_i = 23°C (*2*, *2′*, *3*) and 175°C (*4*, *5*).
In the inset: the I–V curves of the diode irradiated ($5 \cdot 10^{13}$ cm^{-2}, 23°C) without subsequent annealing (*2′*); irradiated ($1 \cdot 10^{14}$ cm^{-2} , 23°C) and then annealed at 300°C for 2 hrs (*3′*), irradiated ($5 \cdot 10^{13}$ cm^{-2}, 175°C) and then annealed twice at 300°C for 2 hrs in the both cases (*4′*). All the data was obtained in the region of biases exceeding the cut-off voltage

After irradiation with protons at room temperature with fluence $\Phi_p = 5 \cdot 10^{13}$ cm^{-2} (see curve *2* in Fig. 2), the differential base resistance R_d was 0.15 Ω.

In a similar manner (see Eq. (1)), the electron removal rate

$$\eta_p = (n_0 - n)/\Phi_p \approx 100 \text{ cm}^{-1}, \quad (2)$$

where n is the electron concentration after irradiation.

Note that approximately the same increase in R_d results from electron irradiation with fluence $\Phi_e = 1 \cdot 10^{16}$ cm^{-2} (see curve *2* in Fig. 1).

After proton irradiation with fluence $\Phi_p = 1 \cdot 10^{14}$ cm^{-2}, the R_d value was about 2.3 Ω, i. e., it increased by a factor of 30 compared to the R_d value in the nonirradiated diode. However,

at $n_0 = 1.0 \cdot 10^{16}$ cm^{-3}, $\eta_e \approx 100$ cm^{-1}, and $\Phi_p = 1 \cdot 10^{14}$ cm^{-2}, the electron concentration in the base n would have to be equal to zero. Such a discrepancy between the estimate established from the value of η_e determined at $\Phi_p = 5 \cdot 10^{13}$ cm^{-2} and the experimental result presented by curve *3* in Fig. 2 can be explained by the "flattening" of the dependence $n(\Phi)$ when approaching the situation of full compensation ($n = 0$).

At $T_i = 175$°C and irradiation with fluence $\Phi_p = 5 \cdot 10^{13}$ cm^{-2} (see curve *4* in Fig. 2), the R_d value becomes equal to ≈ 0.09 Ω, i. e., it increases by only 1.2 times compared to the differential resistance of the nonirradiated diode. After irradiation with fluence $\Phi_p = 1 \cdot 10^{14}$ cm^{-2}, the R_d value is 0.24 Ω (see curve *5*), i.e., an order of magnitude less than that after irradiation with the same fluence at room temperature.

The inset in Fig. 2 shows the results of post-irradiation annealing (proton irradiation of the diodes had fluence $\Phi_p = 1 \cdot 10^{14}$ cm^{-2} at $T_i = 23$°C and 175°C). Annealing at 300°C for 120 min led to a noticeable decrease in the base differential resistance for the diode irradiated at $T_i = 23$°C (compare curves *2′* and *3′*). However, even after annealing, the value of R_d (see curve *3′*) significantly exceeds the value of R_d in an unirradiated diode (see curve *1′*). After irradiation at $T_i = 175$°C, the diode was twice subjected to subsequent annealing at 300°C. The duration of each annealing was 120 min. However, annealing did not have any noticeable effect on the current–voltage characteristic of the diode irradiated at $T_i = 175$°C (see curve *4′*).

It should be noted that an increase in the annealing temperature to a value significantly exceeding 300°C can lead to degradation of devices even in the absence of a voltage applied to the device. As noted in Ref. [24], heating to temperatures $T > 370$°C leads to partial melting of nickel into the silicon carbide surface.

The results of the study of electron and proton irradiation effects on the parameters of JBS devices with blocking voltage $U_b = 1700$ V qualitatively correlate well with the above results for diodes with $U_b = 600$ V.

Fig. 3 shows the forward current–voltage characteristics of a diode with a blocking voltage of 1700 V in the region of biases exceeding the cut-off voltage.

In the unirradiated diode, the differential resistance of the base R_d is 0.082 Ω. Electron irradiation at room temperature with fluence $\Phi_e = 5.0 \cdot 10^{15}$ cm^{-2} leads to an increase in R_d by a factor of 1.8, up to $R_d \approx 0.15$ Ω. After irradiation with fluence $\Phi_e = 1.5 \cdot 10^{16}$ cm^{-2}, the

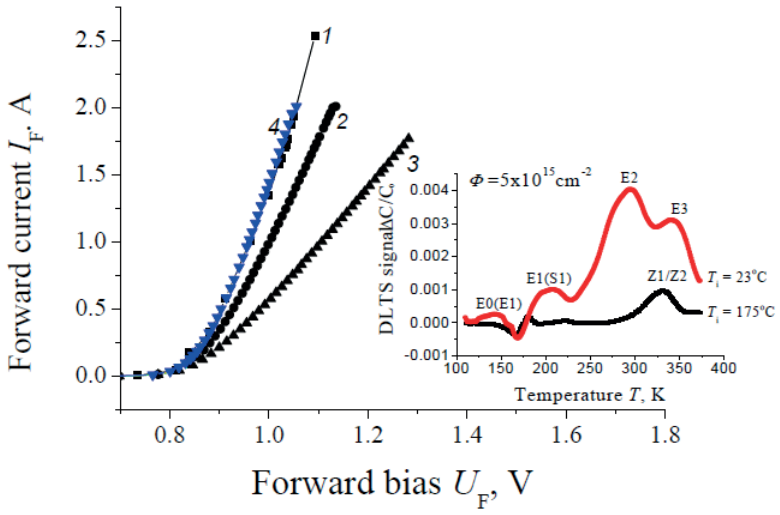

Fig. 3. A comparison of forward current–voltage characteristics of a diode (the blocking voltage is 1700 V) obtained before (*1*) and after (*2* – *4*) its electron irradiation with fluences $\Phi_e = 5.0 \cdot 10^{15}$ cm^{-2} (*2*, *4*) and $\Phi_e = 1.5 \cdot 10^{16}$ cm^{-2} (*3*) at $T_i = 23$°C (*2*, *3*) and 175°C (*4*).
The data was obtained in the region of biases exceeding the cut-off voltage.
In the inset: the DLTS spectra of the sample irradiated with electrons with fluence $\Phi_e = 5.0 \cdot 10^{15}$ cm^{-2} at two temperatures. The rate window was 51 s^{-1}

value of R_d was ≈ 0.23 Ω, i.e. increased approximately 2.8 times. At the initial concentration $n_0 = 3.4 \cdot 10^{15}$ cm^{-3}, this result corresponds to the electron removal rate $\eta_e \approx 0.15$ cm^{-1}. This value agrees well with that one found for similar diodes in Ref. [7] upon irradiation with electrons with an energy of 1.05 MeV.

After electron irradiation of the sample with a fluence $\Phi_e = 5.0 \cdot 10^{15}$ cm^{-2} at $T_i = 175$°C (see curve *4* in Fig. 3), the $I-V$ curve precisely coincides with the corresponding one of the unirradiated sample. However, as can be seen from the inset in Fig. 3, the DLTS spectra corresponding to the levels in the upper half of the band gap demonstrate changes in the amplitudes of the peaks not only after irradiation at room temperature, but also after irradiation at $T_i = 175$°C. One can see in Fig 3 that at $\Phi_e = 0$, the amplitudes of the maxima of the DLTS spectra are negligible compared to the amplitudes of the DLTS spectra of irradiated ones.

Comparing the results shown in the inset in Fig. 3 with those shown in the inset in Fig. 1, it is easy to see that in both cases DLTS registers almost identical maxima. A small difference in the positions and widths of the maxima is explained by the inevitable change in these parameters with a significant change in fluence.

For the DLTS spectrum at $T_i = 175$°C, the maximum at $T = 317$ K was identified as $Z1/Z2$ level with a concentration of $N_{Z1/Z2} \approx 1.2 \cdot 10^{13}$ cm^{-3}. The total concentration of all levels observed in the upper half of the band gap corresponding to the irradiation temperature $T_i = 175$°C, taking into account the concentration of the EH6/7 level, taken equal to the concentration of the $Z1/Z2$ level, is $N_t^{\Sigma} \approx 2.6 \cdot 10^{13}$ cm^{-3}, i. e. less than one percent on the electron concentration $n_0 = 3.4 \cdot 10^{15}$ cm^{-3} in the nonirradiated sample. Thus, as in the discussion of the data shown in Fig. 1, it should be assumed that acceptor levels with a considerable concentration are created by electron irradiation also in the lower half of the band gap.

Fig. 4 shows the effect of proton irradiation at temperatures $T_i = 23$°C and 175°C as well as subsequent annealing on forward $I-V$ characteristics of a diode with $U_b = 1700$ V.

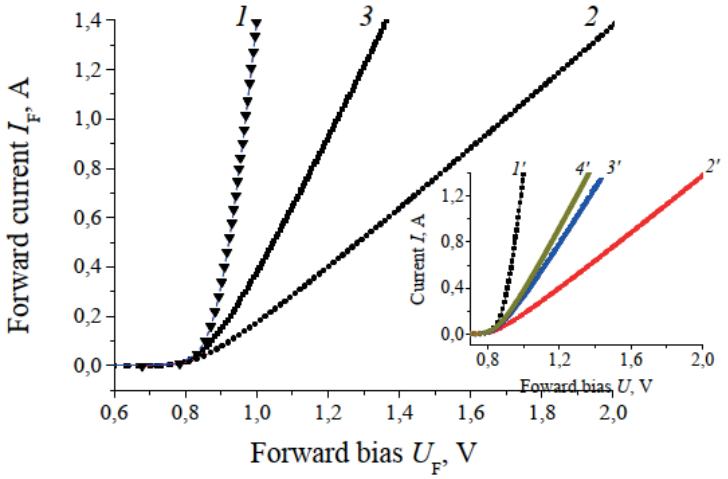

Fig. 4. A comparison of forward current – voltage characteristics of a diode (the blocking voltage is1700 V) obtained before (*1*, *1′* in the inset) and after (*2*, *2′* in the inset, *3*) its proton irradiation with fluence $\Phi_p = 3 \cdot 10^{13}$ cm^{-2} (*2*, *2′*, *3*) at $T_i = 23$°C (*2*, *2′*) and 175°C (*3*, *3′*).

In the inset: the $I-V$ curves of the diode irradiated ($3 \cdot 10^{13}$ cm^{-2}, 23°C) without subsequent annealing (*2′*); irradiated ($3 \cdot 10^{13}$ cm^{-2}, 23°C) and then annealed at 300°C for 2 hrs (*3′*), irradiated ($3 \cdot 10^{13}$ cm^{-2}, 175°C) and then annealed twice at 300°C for 2 hrs in the both cases (*4′*). All the data was obtained in the region of biases exceeding the cut-off voltage

After proton irradiation with fluence $\Phi_p = 3 \cdot 10^{13}$ cm^{-2} at $T_i = 23$°C, the base differential resistance R_d increased from 0.082 to 0.812 Ω, which corresponds to an order of magnitude decrease in the electron concentration in the base. Thus, the removal rate of electrons due to the generation of acceptor centers by protons is in this case

$$\eta_p = (n_0 - n)/\Phi_p \approx 100 \text{ cm}^{-1}, \quad (3)$$

which agrees with the data obtained above for diodes with U_b = 600 V very well (see Eq. (2)).

At the same fluence $\Phi_p = 3 \cdot 10^{13}$ cm^{-2}, but at the irradiation temperature T_i = 175°C, the value of the base differential resistance after irradiation was R_d = 0.38 Ω, i. e., about 2.1 times less than that after irradiation with the same fluence at room temperature (23°C). Annealing for two hours at 300°C reduces the differential resistance R_d of the diode irradiated at 23°C from 0.812 to 0.420 Ω, i. e., almost two times (compare curves *2′* and *3′* in the inset in Fig. 4). However, this value is still greater than the R_d value after irradiation with the same fluence at T_i = 175°C (R_d = 0.38 Ω, curve *4′*). On the other hand, annealing in the same mode (120 min at 300°C) has practically no effect on the R_d value of the diodes irradiated at T_i = 175°C. This result turns out to be partly expected, since some of the defects introduced during irradiation were annealed at 200 − 350°C [25].

Conclusions

The effects of 0.9-MeV-electron and 15-MeV-proton irradiation on the parameters of the high-voltage 4H-SiC Schottky diodes with blocking voltages U_b = 600 V and 1700 V were studied at irradiation temperatures T_i = 23°C (room temperature) and 175°C (limiting operating temperature). Removal rate η_e under electron irradiation for diodes with U_b = 600 V was found to be 0.40 cm^{-1} for T_i = 23°C. For diodes with U_b = 1700 V, the value of η_e was found to be $\eta_e \approx$ 0.15 cm^{-1}. Electron irradiation at T_i = 175°C practically does not affect the resistance of the base. Thus, heating during irradiation even to a relatively low temperature significantly increases the radiation resistance of devices with respect to electron irradiation. Both for T_i = 23°C and 175°C, a comparison of the DLTS spectra describing the levels in the upper half of the band gap with the data on the changes in the base resistance leads to the assumption that acceptor levels with a noticeable concentration are created during electron irradiation also in the lower half of the band gap. Under proton irradiation, both for the diodes with U_b = 600 V and 1700 V, the removal rate η_p for T_i = 23°C was found to be about 100 cm^{-1}. Annealing for 120 min at 300°C after irradiation with fluence $\Phi_p = 1 \cdot 10^{14}$ cm^{-2} at T_i = 23°C leads to a noticeable decrease in the differential resistance of the base. Double annealing for 120 min at 300°C after irradiation with the same fluence at T_i = 175°C practically does not change the current−voltage characteristic of the diodes.

In summary, it may be said that the radiation hardness of high-voltage SiC Schottky diodes subjected to electron irradiation, can be significantly improved if they are heated to a relatively low temperature during irradiation. As for the proton irradiation, the radiation resistance of these devices also increases noticeably with increasing the irradiation temperature. At relatively low irradiation doses, even a relatively short-term post-irradiation annealing at a temperature of 300°C can significantly reduce the differential resistance of the diode base.

REFERENCES

1. **Claeys C., Simoen E.,** Radiation effects in advanced semiconductor materials and devices (Springer Series in Materials Science. Vol. 57). Springer, Berlin, Heidelberg, 2002.

2. **Lee K. K., Ohshima T., Saint A., et al.,** A comparative study of the radiation hardness of silicon carbide using light ions, Nucl. Instrum. Methods Phys. Res. B. 210 (Sept) (2003) 489−494.

3. **Ohshima T., Onoda Sh., Iwamoto N., et al.,** Radiation response of silicon carbide diodes and transistors, In book: Physics and Technology of Silicon Carbide Devices. Ch. 16. Ed. by Y. Hijikata, InTechOpen, Rijeka (Republic of Croatia), 2012.

4. **Lioliou G., Chan H. K., Gohil T., et al.,** 4H-SiC Schottky diode arrays for X-ray detection, Nucl. Instrum. Methods Phys. Res. A. 840 (21 Dec) (2016) 145−152.

5. **Castaldini A., Cavallini A., Rigutti L., Nava F.,** Low temperature annealing of electron irradiation induced defects in 4H-SiC, Appl. Phys. Lett. 85 (17) (2004) 3780−3782.

6. **Omotoso E., Meyer W. E., Auret F. D., et al.,** The influence of high energy electron irradiation on the Schottky barrier height and the Richardson constant of Ni/4H-SiC Schottky diodes, Mater. Sci. Semicond. Proc. 39 (Nov) (2015) 112−118.

7. **Hazdra P., Vobecký J.,** Radiation defects created in *n*-type 4H-SiC by electron irradiation in the energy range of 1–10 MeV, Phys. Status Solidi. A. 216 (17) (2019) 1900312.

8. **Lebedev A. A., Kozlovski V. V., Davydovskaya K. S., Levinshtein M. E.**, Radiation hardness of silicon carbide upon high-temperature electron and proton irradiation, Mater. 14 (17) (2021) 4976.

9. **Siddiqui A., Hallén A., Hussain A., Usman M.,** Carrier removal rates in 4H–SiC power diodes – A predictive analytical model, Mater. Sci. Semicond. Proc. 167 (15 Nov) (2023) 107771.

10. **Zhao L., Tang Y., Bai Y., et al.,** Analysis of defects and electrical characteristics of variable-temperature proton-irradiated 4H-SiC JBS diodes, Electronics. 11 (9) (2022) 1341.

11. **Lebedev A. A., Kozlovski V. V., Levinshtein M. E., et al.,** Effect of high temperature irradiation with 15 MeV protons on characteristics of power SiC Schottky diodes, Solid-State Electron. 181–182 (Aug) (2021) 108009.

12. **Zakharenkov L. F., Kozlovskii V. V., Shustrov B. A.,** Transmutation doping of indium phosphide and gallium arsenide due to protons and α-particles, Phys. Status Solidi A. 17 (1) (1990) 85–90.

13. **Lindström J. L., Murin L. I., Hallberg T., et al.,** Defect engineering in Czochralski silicon by electron irradiation at different temperatures, Nucl. Instrum. Methods Phys. Res. B. 186 (1–4) (2002) 121–125.

14. **Kimoto T.,** High-voltage SiC power devices for improved energy efficiency, Proc. Jpn. Acad. Ser. B., Phys. Biol. Sci. 98 (4) (2022) 161–189.

15. **Mauromicale G., Raciti A., Rizzo S. A., et al.,** SiC power modules for traction inverters in automotive applications, Proc. 45th Annu. Conf. IEEE Industr. Electron. Soc. (IECON 2019). 14–17 Oct., 2019. Lisbon, (Portugal); IEEE (2019) 1973–1978.

16. **Ni Z., Lyu X., Yadav O. P., et al.,** Overview of real-time lifetime prediction and extension for SiC power converters, IEEE Trans. Power Electron. 35 (8) (2020) 7765–7794.

17. **Chen Z., Chen C., Huang A. Q.,** Driver integrated online *RDS*-on monitoring method for SiC power converters, Proc. 2022 IEEE Energy Conversion Congress and Exposition (ECCE), Oct. 9–13, Detroit, MI, USA. IEEE (2022) 01–07.

18. **Vobecky J., Hazdra P., Popelka S., Sharma R. K.,** Impact of electron irradiation on the ON-State characteristics of a 4H–SiC JBS diode, IEEE Trans. Electron Devices. 62 (6) (2015) 1964–1969.

19. **Ziegler J. F., Biersack J. P.,** The stopping and range of ions in matter, In book: Treatise on heavy-ion science, Ed. by Bromley D. A., Springer, Boston, MA, USA (1985) 93–129.

20. **Ivanov P. A., Levinshtein M. E.,** The impact of parasitic inductance on the *dV/dt* ruggedness of 4H-SiC Schottky diodes, Microelectron. Reliab. 122 (July) (2021) 114159.

21. **Levinshtein M., Shur M.,** Handbook series on semiconductor parameters: Ternary and quaternary III-V compounds. Vol. 2. Ed. by Rumyantsev S. L., World Scientific, Singapore, 1999.

22. **Kozlovski V. V., Lebedev A. A., Bogdanova E. V.,** Model for conductivity compensation of moderately doped *n*- and *p*-4H-SiC by high-energy electron bombardment, J. Appl. Phys. 117 (15) (2015) 155702.

23. **Kaneko H., Kimoto T.,** Formation of a semi-insulating layer in *n*-type 4H-SiC by electron irradiation, Appl. Phys. Lett. 98 (26) (2011) 262106.

24. **Karsthof R., Bathen M. E., Galeckas A., Vines L.,** Conversion pathways of primary defects by annealing in proton-irradiated *n*-type 4H-SiC, Phys. Rev. B. 102 (18) (2020) 184111.

25. **Lebedev A. A., Veinger A. I., Davydov D. V., et al.,** Doping of *n*-type 6H–SiC and 4H–SiC with defects created with a proton beam, J. Appl. Phys. 88 (11) (2000) 6265–6271.

СПИСОК ЛИТЕРАТУРЫ

1. **Claeys C., Simoen E.** Radiation effects in advanced semiconductor materials and devices (Springer Series in Materials Science. Vol. 57). Berlin, Heidelberg: Springer, 2002. 404 p.

2. **Lee K. K., Ohshima T., Saint A., Kamiya T., Jamieson D. N., Iton H.** A comparative study of the radiation hardness of silicon carbide using light ions // Nuclear Instruments and Methods in Physics Research B // 2003. Vol. 210. September. Pp. 489–494.

3. **Ohshima T., Onoda Sh., Iwamoto N., Makino T., Arai M., Tanaka Y.** Radiation response of silicon carbide diodes and transistors // Physics and Technology of Silicon Carbide Devices. Chapter 16. Edited by Y. Hijikata. Rijeka (Republic of Croatia): InTechOpen, 2012. 414 p.

4. **Lioliou G., Chan H. K., Gohil T., Vassilevski K. V., Wright N. G., Horsfall A. B., Barnett A. M.** 4H-SiC Schottky diode arrays for X-ray detection // Nuclear Instruments and Methods in Physics Research A. 2016. Vol. 840. 21 December. Pp. 145–152.

5. **Castaldini A., Cavallini A., Rigutti L., Nava F.** Low temperature annealing of electron irradiation induced defects in 4H-SiC // Applied Physics Letters. 2004. Vol. 85. No. 17. Pp. 3780–3782.

6. **Omotoso E., Meyer W. E., Auret F. D., Paradzan A. T., Diale M., Coelho S. M. M., van Rensburg P. J. J.** The influence of high energy electron irradiation on the Schottky barrier height and the Richardson constant of Ni/4H-SiC Schottky diodes // Materials Science in Semiconductor Processing. 2015. Vol. 39. November. Pp. 112–118.

7. **Hazdra P., Vobecký J.** Radiation defects created in *n*-type 4H-SiC by electron irradiation in the energy range of 1–10 MeV // Physica Status Solidi A. 2019. Vol. 216. No. 17. P. 1900312.

8. **Lebedev A. A., Kozlovski V. V., Davydovskaya K. S., Levinshtein M. E.** Radiation hardness of silicon carbide upon high-temperature electron and proton irradiation // Materials. 2021. Vol. 14. No. 17. P. 4976.

9. **Siddiqui A., Hallén A., Hussain A., Usman M.** Carrier removal rates in 4H–SiC power diodes – A predictive analytical model // Materials Science in Semiconductor Processing. 2023. Vol. 167. 15 November. P. 107771.

10. **Zhao L., Tang Y., Bai Y., Qiu M., Wu Zh., Yang Y., Yang Ch., Tian X., Liu X.** Analysis of defects and electrical characteristics of variable-temperature proton-irradiated 4H-SiC JBS diodes // Electronics. 2022. Vol. 11. No. 9. P. 1341.

11. **Lebedev A. A., Kozlovski V. V., Levinshtein M. E., Ivanov A. E., Davydovskaya K. S.** Effect of high temperature irradiation with 15 MeV protons on characteristics of power SiC Schottky diodes // Solid-State Electronics. 2021. Vol. 181–182. August. P. 108009.

12. **Zakharenkov L. F., Kozlovskii V. V., Shustrov B. A.** Transmutation doping of indium phosphide and gallium arsenide due to protons and α-particles // Physica Status Solidi A. 1990. Vol. 17. No. 1. Pp. 85–90.

13. **Lindström J. L., Murin L. I., Hallberg T., Markevich V. P., Svensson B. G., Kleverman M., Hermansson J.** Defect engineering in Czochralski silicon by electron irradiation at different temperatures // Nuclear Instruments and Methods in Physics Research B. 2002. Vol. 186. No. 1–4. Pp. 121–125.

14. **Kimoto T.** High-voltage SiC power devices for improved energy efficiency // Proceedings of the Japan Academy. Series B: Physical and Biological Sciences. 2022. Vol. 98. No. 4. Pp. 161–189.

15. **Mauromicale G., Raciti A., Rizzo S. A., Susinni G., Abbatelli L., Buonomo S., Cavallaro D., Giuffrida V.** SiC power modules for traction inverters in automotive applications // Proceedings of the 45th Annual Conference of the IEEE Industrial Electronics Society (IECON 2019). 14–17 October, 2019. Lisbon, (Portugal); IEEE, 2019. Pp. 1973–1978.

16. **Ni Z., Lyu X., Yadav O. P., Singh B. N., Zheng H., Cao D.** Overview of real-time lifetime prediction and extension for SiC power converters // IEEE Transactions on Power Electronics. 2020. Vol. 35. No. 8. Pp. 7765–7794.

17. **Chen Z., Chen C., Huang A. Q.** Driver integrated online *RDS*-on monitoring method for SiC power converters // Proceedings of 2022 IEEE Energy Conversion Congress and Exposition (ECCE), October 9–13, Detroit, MI, USA. IEEE, 2022. Pp. 01–07.

18. **Vobecky J., Hazdra P., Popelka S., Sharma R. K.** Impact of electron irradiation on the ON-State characteristics of a 4H–SiC JBS diode // IEEE Transactions on Electron Devices. 2015. Vol. 62. No. 6. Pp. 1964–1969.

19. **Ziegler J. F., Biersack J. P.** The stopping and range of ions in matter // Treatise on heavy-ion science. Edited by Bromley D. A. Boston, MA: Springer, 1985. Pp. 93–129.

20. **Ivanov P. A., Levinshtein M. E.** The impact of parasitic inductance on the *dV/dt* ruggedness of 4H-SiC Schottky diodes // Microelectronics Reliability. 2021. Vol. 122. July. P. 114159.

21. **Levinshtein M., Shur M.** Handbook series on semiconductor parameters: Ternary and quaternary III-V compounds. Vol. 2. Edited by Rumyantsev S. L. Singapore: World Scientific, 1999. 205 p.

22. **Kozlovski V. V., Lebedev A. A., Bogdanova E. V.** Model for conductivity compensation of moderately doped *n*- and *p*-4H-SiC by high-energy electron bombardment // Journal of Applied Physics. 2015. Vol. 117. No. 15. P. 155702.

23. **Kaneko H., Kimoto T.** Formation of a semi-insulating layer in *n*-type 4H-SiC by electron irradiation // Applied Physics Letters. 2011. Vol. 98. No. 26. P. 262106.

24. **Karsthof R., Bathen M. E., Galeckas A., Vines L.** Conversion pathways of primary defects by annealing in proton-irradiated *n*-type 4H-SiC // Physical Review B. 2020. Vol. 102. No. 18. P. 184111.

25. **Lebedev A. A., Veinger A. I., Davydov D. V., Kozlovski V. V., Savkina N. S., Strel'chuk A. M.** Doping of *n*-type 6H−SiC and 4H−SiC with defects created with a proton beam // Journal of Applied Physics. 2000. Vol. 88. No. 11. Pp. 6265−6271.

THE AUTHORS

KOZLOVSKI Vitali V.
Peter the Great St. Petersburg Polytechnic University
29 Politechnicheskaya St., St. Petersburg, 195251, Russia
kozlovski@physics.spbstu.ru
ORCID: 0000-0002-1752-6

LEBEDEV Alexander A.
Ioffe Institute of RAS
26 Polytekhnicheskaya St., St. Petersburg, 194021, Russia
shura.lebe@mail.ioffe.ru
ORCID: 0000-0003-0829-5053

KUZMIN Roman A.
Ioffe Institute of RAS
26 Polytekhnicheskaya St., St. Petersburg, 194021, Russia
kuzminra@mail.ioffe.ru
ORCID: 0000-0001-6681-7046

MALEVSKY Dmitry A.
Ioffe Institute of RAS
26 Polytekhnicheskaya St., St. Petersburg, 194021, Russia
dmalevsky@scell.ioffe.ru
ORCID: 0000-0002-9337-4137

LEVINSHTEIN Mikhail E.
Ioffe Institute of RAS
26 Polytekhnicheskaya St., St. Petersburg, 194021, Russia
melev@nimis.ioffe.ru
ORCID: 0000-0002-9712-7387

OGANESYAN Gagik A.
Ioffe Institute of RAS
26 Polytekhnicheskaya St., St. Petersburg, 194021, Russia
Gagik.Oganesyan@mail.ioffe.ru
ORCID: 0000-0001-7111-6316

СВЕДЕНИЯ ОБ АВТОРАХ

КОЗЛОВСКИЙ Виталий Васильевич – *доктор физико-математических наук, профессор кафедры физики Санкт-Петербургского политехнического университета Петра Великого, Санкт-Петербург, Россия.*
195251, Россия, г. Санкт-Петербург, Политехническая ул., 29
kozlovski@physics.spbstu.ru
ORCID: 0000-0002-1752-6

ЛЕБЕДЕВ Александр Александрович – *доктор физико-математических наук, профессор, заведующий лабораторией и Отделением твердотельной электроники Физико-технического института им. А. Ф. Иоффе Российской академии наук, Санкт-Петербург, Россия.*
194021, Россия, г. Санкт-Петербург, Политехническая ул., 26
shura.lebe@mail.ioffe.ru
ORCID: 0000-0003-0829-5053

КУЗЬМИН Роман Алексеевич – *инженер лаборатории твердотельной электроники Физико-технического института им. А. Ф. Иоффе Российской академии наук, Санкт-Петербург, Россия.*
194021, Россия, г. Санкт-Петербург, Политехническая ул., 26
kuzminra@mail.ioffe.ru
ORCID: 0000-0001-6681-7046

МАЛЕВСКИЙ Дмитрий Андреевич – *научный сотрудник ООО «Научно-технический центр тонкопленочных технологий в энергетике при Физико-техническом институте им. А. Ф. Иоффе» Российской академии наук, Санкт-Петербург, Россия.*
194021, Россия, г. Санкт-Петербург, Политехническая ул., 26
dmalevsky@scell.ioffe.ru
ORCID: 0000-0002-9337-4137

ЛЕВИНШТЕЙН Михаил Ефимович – *доктор физико-математических наук, главный научный сотрудник Отделения твердотельной электроники Физико-технического института им. А. Ф. Иоффе Российской академии наук, Санкт-Петербург, Россия.*
194021, Россия, г. Санкт-Петербург, Политехническая ул., 26
melev@nimis.ioffe.ru
ORCID: 0000-0002-9712-7387

ОГАНЕСЯН Гагик Араратович – *кандидат физико-математических наук, старший научный сотрудник Отделения твердотельной электроники Физико-технического института им. А. Ф. Иоффе Российской академии наук, Санкт-Петербург, Россия.*
194021, Россия, г. Санкт-Петербург, Политехническая ул., 26
Gagik.Oganesyan@mail.ioffe.ru
ORCID: 0000-0001-7111-6316

Received 23.11.2023. Approved after reviewing 12.12.2023. Accepted 12.12.2023.
Статья поступила в редакцию 23.11.2023. Одобрена после рецензирования 12.12.2023. Принята 12.12.2023.

Original article
DOI: https://doi.org/10.18721/JPM.17102

A CHAOTIC POTENTIAL OF CHARGED DISLOCATIONS IN GROUP III-NITRIDE HETEROJUNCTIONS DURING LOCALIZATION OF A TWO-DIMENSIONAL ELECTRON GAS

A. V. Filimonov ✉, *V. B. Bondarenko*

Peter the Great St. Petersburg Polytechnic University, St. Petersburg, Russia

✉ filimonov@rphf.spbstu.ru

Abstract. This work studies a chaotic potential (CP) in the heterojunctions of III-nitrides, the CP caused by the electrostatic field of charged dislocations, under localization conditions of a two-dimensional electron gas in the near-contact region. Within the framework of the statistical analysis of a Poisson ensemble of linear defects, the amplitude and scale of the CP in the contact plane have been determined. The CP parameter dependence on the density of surface states and the concentration of dislocations at the mobility threshold of the two-dimensional electron gas was shown. The CP amplitude was established to exceed 100 meV in a wide range of changes in the system parameters, in the presence of electronic charge localization effects in the heterojunctions.

Keywords: chaotic potential, III-nitride heterojunction, two-dimensional electron gas, natural size effect

Funding: The reported study was carried out within the framework of the State Assignment for Fundamental Research (Subject Code FSEG-2023-0016).

Citation: Filimonov A. V., Bondarenko V. B., A chaotic potential of charged dislocations in group III-nitride heterojunctions during localization of a two-dimensional electron gas, St. Petersburg State Polytechnical University Journal. Physics and Mathematics. 17 (1) (2024) 21–28. DOI: https://doi.org/10.18721/JPM.17102

УДК 538.91
DOI: https://doi.org/10.18721/JPM.17102

ХАОТИЧЕСКИЙ ПОТЕНЦИАЛ ЗАРЯЖЕННЫХ ДИСЛОКАЦИЙ В ГЕТЕРОКОНТАКТАХ III-НИТРИДОВ ПРИ ЛОКАЛИЗАЦИИ ДВУМЕРНОГО ЭЛЕКТРОННОГО ГАЗА

А. В. Филимонов ✉, *В. Б. Бондаренко*

Санкт-Петербургский политехнический университет Петра Великого,

Санкт-Петербург, Россия

✉ flimonov@rphf.spbstu.ru

Аннотация. В работе исследуется хаотический потенциал (ХП) в гетероконтактах III-нитридов, обусловленный электростатическим полем заряженных дислокаций, в условиях локализации двумерного электронного газа в приконтактной области. В рамках статистического анализа пуассоновского ансамбля линейных дефектов определены амплитуда и масштаб ХП в плоскости контакта. Показана зависимость параметров ХП от плотности поверхностных состояний и концентрации дислокаций на пороге подвижности двумерного электронного газа. Установлено, что при наличии эффектов

локализации электронного заряда в гетероконтактах амплитуда ХП превышает 100 мэВ в широком диапазоне изменения параметров системы.

Ключевые слова: хаотический потенциал, гетероконтакт III-нитридов, двумерный электронный газ, естественный размерный эффект

Финансирование: Работа выполнена в рамках Государственного задания на проведение фундаментальных исследований (код темы FSEG-2023-0016).

Ссылка для цитирования: Филимонов А. В., Бондаренко В. Б. Хаотический потенциал заряженных дислокаций в гетероконтактах III-нитридов при локализации двумерного электронного газа // Научно-технические ведомости СПбГПУ. Физико-математические науки. 2024. Т. 17. № 1. С. 21–28. DOI: https://doi.org/10.18721/JPM.17102

Introduction

Two-dimensional electron gas (2DEG) generally has high mobility in heterojunctions based on III-nitrides. However, this property of the system considerably depends on the defect concentration in semiconductor structures. The defect concentration of the contacting semiconductors and the interface limits the mobility of free charge carriers [1]. In some cases, the mean free path of charge carriers can also be decreased as a result of their scattering by charged dislocations [1–3]. Evidently, studies into this type of processes should take into account both the possible concentrations of these extended defects in heterojunctions and the population of dislocation states [4]. The redistribution of electron density between the surface states and the linear defect states leads to changes in the electric field and potential in the junction plane. At certain threshold values of random fields, a state of strong localization of 2DEG may occur [5].

Estimates indicate that fluctuations in electric fields on the surface of semiconductors and the formation of chaotic potential (CP) can be associated not only with the defect concentration of the surface itself, but also with localized charges in the near-surface depletion layers. A classical size effect occurs in heterojunctions of semiconductor structures with a wide range of parameters, associated with the naturally commensurable characteristic scales in the space-charge region of a semiconductor [6]. It was found that an increase in the amplitude and characteristic scale of CP occurs under the conditions of this size effect and the inhomogeneity of the local fields of charged defects in heterojunctions with a decrease in the density of delocalized surface states [7]. Furthermore, the actual distribution of the electron charge in the junction region self-consistently depends on the CP formed at the interface, since the spectrum of surface states and possibly their localization change. In view of the weakened screening effect of localized 2DEG, it seems important to investigate the CP structures of charged dislocations in heterojunctions of nitride semiconductors.

The goal of this study is to determine the given CP in heterojunctions of III-nitrides and the nature of its dependence on system parameters.

Distribution of charged dislocation potential in a heterojunction

For example, let us analyze the heterostructure based on the AlGaN/GaN heterojunctions [8]. Consider a model where threading of misfit dislocations with a surface concentration N_{disl} in the given heterostructure is represented as charged defects oriented normal to the junction plane. If we neglect the interaction between dislocations, their number distribution can be assumed to be Poissonian. The probability that N of the given linear defects are located in the junction region of radius R in this representation is equal to

$$p(N) = \frac{< N >^N \exp(- < N >)}{N!}, \quad (1)$$

where $<N>$ is the average number of these defects in a given region, and $N_{disl} = \pi R^2$.

Due to the polarity of the chemical bond in aluminum and gallium nitride crystals, a piezoelectric effect and spontaneous polarization occur in mechanically stressed heterojunctions [8]. As a result of injection of electrons into the junction region, a surface field and corresponding band bending are formed in gallium nitride, while the magnitude of the latter exceeds half the band gap (about 1.8 eV). Since the formed channel layer of the considered heterostructure almost always contains undoped or compensated gallium nitride (GaN), the space charge in the region of band bending is mainly produced by charged dislocations. In the presence of large band bending, such extended defects within the space-charge regions are assumed to be uniformly charged with a certain linear density λ. If there is only a localized surface charge in the heterojunction, then it is possible to use the superposition principle to determine the parameters of the CP. It can be proved that in this case, the dominant contribution to large-scale fluctuations of the field in the junction is made by a system of charged dislocations [7].

The potential of the field of an arbitrarily selected dislocation in the junction plane is determined in the polar coordinate system, where ρ is the radial coordinate determining the distance from this linear defect to the observation point. Integration along a charged dislocation within the space-charge region of width L_0 gives the potential energy of the surface electron in the junction plane:

$$U_i(\rho) = \frac{2e\lambda}{\varepsilon_1 + \varepsilon_2} \ln \frac{\sqrt{\rho^2 + L_0^2} + L_0}{\rho}, \tag{2}$$

where ε_1, ε_2 are the values of the dielectric constant of the semiconductors brought into contact.

The volume charge in the band bending region of GaN has a density equal to λN_{disl} within the model representations given above. In this case, the characteristic width of the space-charge region can be represented as

$$L_0 = \sqrt{\frac{\varepsilon_2 U_0}{2\pi e \lambda N_{disl}}}, \tag{3}$$

where U_0 is the band bending.

Simple calculations similar to those in [7] are necessary for further analysis of the system. First, the average contribution to the potential energy of the surface electron in the electric field of a single dislocation can be determined within the framework of the given method. Similar averaging of expression (2) over an area with radius yields the following result:

$$< U_i > (R) = \frac{2e\lambda}{(\varepsilon_1 + \varepsilon_2) R^2} \left(L_0 \sqrt{R^2 + L_0^2} - L_0^2 + R^2 \ln \frac{\sqrt{R^2 + L_0^2} + L_0}{R} \right). \tag{4}$$

Taking into account the distribution of charged dislocations (1), we can also represent the standard deviation of their number on the given surface region as

$$\delta N(R) = R\sqrt{\pi N_{disl}}. \tag{5}$$

Multiplying expressions (4) and (5), followed by a search for the maximum of the resulting product, we can estimate the characteristic magnitude of the inhomogeneities in the potential energy of the surface electron in the field of charged dislocations. The corresponding passage to the limit $R \to \infty$ gives the required value:

$$\delta U = \frac{4e\lambda L_0 \sqrt{\pi N_{disl}}}{\varepsilon_1 + \varepsilon_2}. \tag{6}$$

Substituting dependence (3) of the width of the space-charge region on the system parameters into expression (6), we obtain the following result:

$$\delta U = \frac{2}{\varepsilon_1 + \varepsilon_2} \sqrt{2e\lambda\varepsilon_2 U_0}. \tag{7}$$

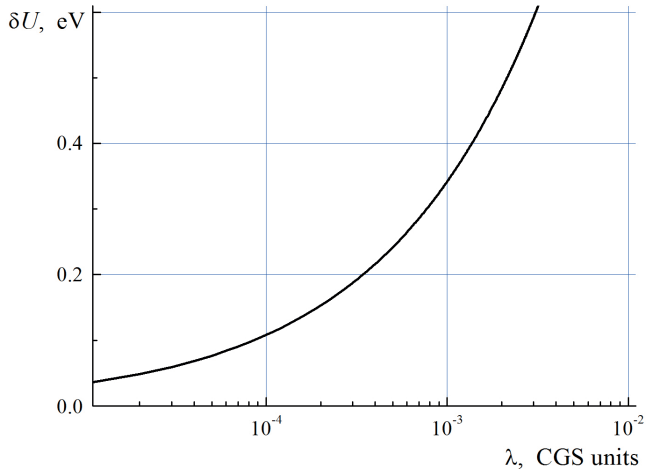

Fig. 1. Dependence of the average fluctuations in the chaotic potential of charged dislocations in the AlGaN/GaN heterojunction on the linear charge density. The band bending U_0 = 1.8 eV

The dielectric permittivities of aluminum nitride and gallium nitride in the considered heterostructure are 9.2 and 10.4, respectively [8]. The characteristic form of the obtained dependence $\delta U(\lambda)$ (see Eq. (7)) is shown in Fig. 1 for the value of band bending parameter U_0 = 1.8 eV. Since expression (6) for δU was obtained with a formal passage to the limit $R \to \infty$, the CP found in this manner is large-scale.

Density of surface states in the heterojunction

The presence of large-scale CP of charged dislocations in the near-contact region of the heterostructure under consideration modifies the quasi-classical spectrum of surface states and leads to the appearance of 'tails' in their density. In this case, with the known form of the law for the distribution of the potential energy of the electron, we can obtain the corresponding energy dependence of the density of states $D(E)$ [9]. In view of the quasi-continuity of the spectrum of electron states, the initial expression for their density takes the form

$$D(E) = \int_{-\infty}^{E} D_0(E-U) \cdot f(U)\, dU, \tag{8}$$

where $D_0(E)$ is the unperturbed density of states, $f(U)$ is the probability density function for the potential energy of the electron U on the surface.

The quasi-classical density of surface states for parabolic dispersion is constant within the allowed band in the absence of CP and valley degeneracy [10], depending only on the effective electron mass. Therefore, expression (8) can be simplified:

$$D(E) = D_0 \int_{-\infty}^{E} f(U)\, dU. \tag{9}$$

Thus, the type of functional dependence $D = D(E)$ is completely determined by the nature of the potential energy distribution of the surface electron. The Gaussian model of CP distribution is adequate for taking into account the superposition of fields of randomly located charged dislocations [11]:

$$f(U) = \frac{1}{\delta U \sqrt{2\pi}} \cdot \exp\left(-\frac{U^2}{2 \cdot \delta U^2}\right). \tag{10}$$

After substituting probability density function (10) into expression (9) and calculating the integral, we obtain the density of surface states in terms of the error function:

$$D(E) = \frac{D_0}{2} \cdot \left[1 + erf\left(\frac{E}{\delta U \sqrt{2}} \right) \right]. \quad (11)$$

This formula allows to obtain the expression for the concentration of 2DEG

$$n_S = \int_{-\infty}^{E_F} D(E)\, dE, \quad (12)$$

at low temperatures T (formally at $T \to 0$ K), which has the following form [12]:

$$n_S = \frac{D_0}{2} \cdot \left\{ E_F \left[1 + erf\left(\frac{E_F}{\delta U \sqrt{2}} \right) \right] + \delta U \sqrt{\frac{2}{\pi}} \exp\left(-\frac{E_F^2}{2 \cdot \delta U^2} \right) \right\}. \quad (13)$$

Here E_F is the Fermi energy in the surface zone.

Chaotic potential in the heterojunction at the mobility threshold of two-dimensional electron gas

The specific values of the quantities δU and n_S can be estimated under known conditions characteristic of the contacting structures formed. First of all, it can be assumed that the electroneutrality condition is satisfied in the equilibrium state:

$$N_S = n_S + \frac{\lambda}{e} N_{disl} L_0, \quad (14)$$

where N_S is the surface charge density in the junction.

If quantity (14) depends only on the nature of the contacting semiconductors, then $N_S = const$ for the given heterostructure. In this case, only the redistribution of localized charge between the surface and dislocation states is possible, depending on the specific scenario. For example, almost all localized surface states are filled at the classical mobility threshold (i.e., provided that $E_F = 0$ [9]), which corresponds to the condition that the maximum electron charge appear on the dielectric surface. In this case, an explicit dependence of the characteristic values of CP on the number of charged dislocations per unit surface area of the junction can be obtained from expression (14) in view of (3), (7) and (13)

$$\delta U = \frac{4\sqrt{2\pi} \cdot e^2 N_S}{4e^2 D_0 + (\varepsilon_1 + \varepsilon_2)\sqrt{2N_{disl}}}. \quad (15)$$

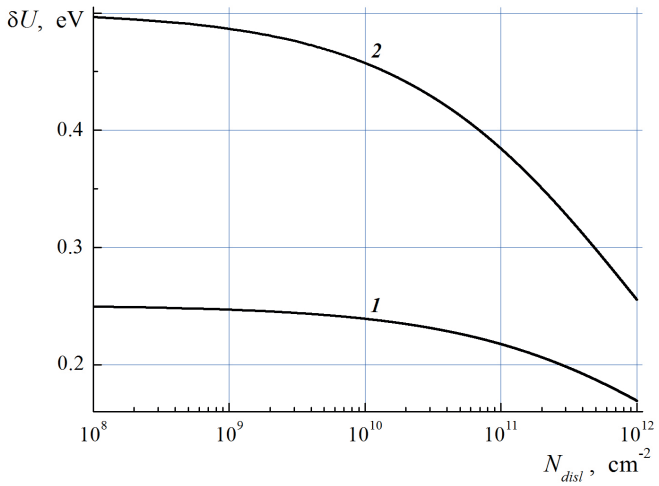

Fig. 2. Dependences of the average fluctuations in the chaotic potential of charged dislocations in the heterojunction on their concentration at the mobility threshold of two-dimensional electron gas, at two surface state densities D_0, $cm^{-2} \cdot eV^{-1}$: $1 \cdot 10^{14}$ (*1*) and $5 \cdot 10^{13}$ (*2*); $N_S = const$

The dependence of the average potential energy fluctuations (15) on the concentration of charged dislocations for the surface charge density $N_S = 10^{13}$ cm^{-2} and two densities of surface states D_0 is shown in Fig. 2.

Results and discussion

Analysis shows that the amplitude of CP in the heterojunction for localized 2DEG can reach several hundred millielectronvolts (see Fig. 1) even at fairly moderate values of the linear charge density in dislocations (compared with the maximum possible values of the order of 0.01 CGE units [7]). The dependence $\delta U = \delta U(\lambda)$ obtained for this case is rather weak: according to expression (7), the quantity δU is proportional to the square root of the linear charge density λ. In other words, the indicated values of the characteristic inhomogeneities of the potential in the junction are preserved in a fairly wide variation range of the system parameters. Moreover, due to the presence of unscreened Coulomb fields of form (2), slowly varying in space, the resulting CP in the junction turns out to be large-scale.

The natural consequences of the existence of large-scale CP in the heterojunction are the appearance of 'tails' in the density of surface states and the possibility of redistribution of localized charge. If the total surface charge remains unchanged in the heterojunction, then the average value of fluctuations in the potential energy of the surface electron decreases with an increase in the charged dislocation concentration within the framework of the model approximation adopted (see Fig. 2). This behavior of the quantity δU is associated with a weakening of the intrinsic size effect, since in this case the charge is distributed over a larger number of extended defects and better statistical averaging of inhomogeneous fields is achieved. A decrease in the density of surface states (which corresponds to lower effective electron masses in the surface zone) leads to a noticeable increase in δU.

Conclusion

The paper reports on the behavior of the chaotic potential (CP) in III-nitride heterojunctions, induced by the electrostatic field of dislocations for localized two-dimensional electron gas in the near-contact region. The amplitude of the CP in the junction plane and the nature of the spatial distribution of the corresponding field are determined. The dependence of the characteristic values of CP on the system parameters is considered. It is established that the magnitude of CP amplitude can exceed 100 MeV in the presence of electron charge localization effects in III-nitride heterojunctions. This result is important both from the standpoint of improving the technology for synthesis of semiconductor devices based the corresponding heterostructuctures, and from the standpoint of theoretical studies into the properties of two-dimensional electron gas.

REFERENCES

1. **Weimann N. G., Eastman L. F., Doppalapudi D., et al.,** Scattering of electrons at threading dislocations in GaN, J. Appl. Phys. 83 (7) (1998) 3656–3659.

2. **Debdeep J., Gossard A. C., Mishra U. K.,** Dislocation scattering in a two-dimensional electron gas, Appl. Phys. Lett. 76 (13) (2000) 1707–1709.

3. **Protasov D. Yu., Malin T. V., Tikhonov A. V., et al.,** Electron scattering in AlGaN/GaN heterostructures with a two-dimentional electron gas, Semiconductions. 47 (1) (2013) 33–44.

4. **Shikin V. B., Shikina Yu. V.,** Charged dislocations in semiconductor crystals, Physics – Uspekhi. 38 (8) (1995) 845–876.

5. **Bondarenko V. B., Filimonov A. V.,** Criterion for strong localization in the Tomas – Fermi approximation, Semiconductors. 51 (10) (2017) 1321– 1325.

6. **Bondarenko V. B., Davydov S. N., Filimonov A. V.,** Inherent potential inhomogeneity on the semiconductor surface for equilibrium impurity distribution, Semiconductors. 44 (1) (2010) 41–44.

7. **Jena D., Wood C.,** Polarization effects in semiconductors: From *ab initio* theory to device applications, Springer, New York. 2008.

8. **Bondarenko V. B., Filimonov A. V., Kumar R.,** A chaotic potential of charged dislocations in group III-nitride heterojunctions, Tech. Phys. Lett. 47 (1) (2021) 8–10.

9. **Shklovskii B. I., Efros A. L.,** Electronic properties of doped semiconductors (Springer Series in Solid-State Sciences, Vol. 45) Springer-Verlag, Berlin, Heidelberg GmbH, 2012.

10. **Bonch-Bruyevich V. L., Zvyagin I. P., R. Kayper R., et al.,** Elect ronic theory of disordered semiconductors, Nauka, Moscow, 1981 (in Russian).

11. **Gradshteyn I. S., Ryzhik I. M.,** Table of integrals, series, and products, Edited by D. Zwillinger and V. Moll, Academic Press, Elsevier Inc., 2014.

СПИСОК ЛИТЕРАТУРЫ

1. **Weimann N. G., Eastman L. F., Doppalapudi D., Ng H. M., Maustakus T. D.** Scattering of electrons at threading dislocations in GaN // Journal of Applied Physics. 1998. Vol. 83. No. 7. Pp. 3656–3659.

2. **Debdeep J., Gossard A. C., Mishra U. K.** Dislocation scattering in a two-dimensional electron gas // Applied Physics Letters. 2000. Vol. 76. No. 13. Pp. 1707–1709.

3. **Протасов Д. Ю., Малин Т. В., Тихонов А. В., Цацульников А. Ф., Журавлев К. С.** Рассеяние электронов в гетероструктурах AlGaN/GaN с двумерным электронным газом // Физика и техника полупроводников. 2013. Т. 47. No 1. С. 36–47.

4. **Шикин В. Б., Шикина Ю. В.** Заряженные дислокации в полупроводниковых кристаллах // Успехи физических наук. 1995. Т. 165. № 8. С. 887–917.

5. **Бондаренко В. Б., Филимонов А. В.** Критерий сильной локализации на поверхности полупроводника в приближении Томаса – Ферми // Физика и техника полупроводников. 2017. Т. 51. № 10. С. 1372–1375.

6. **Бондаренко В. Б., Давыдов С. Н., Филимонов А. В.** Естественные неоднородности потенциала на поверхности полупроводника при равновесном распределении примеси // Физика и техника полупроводников. 2010. Т. 44. № 1. С. 44–47.

7. **Jena D., Wood C.** Polarization effects in semiconductors: From *ab initio* theory to device applications. New York: Springer, 2008. 515 p.

8. **Бондаренко В. Б., Филимонов А. В., Kumar R.** Хаотический потенциал заряженных дислокаций в гетероконтактах III-нитридов // Письма в Журнал технической физики. 2021. Т. 47. № 1. С. 12–14.

9. **Шкловский Б. И., Эфрос А. Л.** Электронные свойства легированных полупроводников. М.: Наука, 1979. 416 с.

10. **Бонч-Бруевич В. Л., Звягин И. П., Кайпер Р., Миронов А. Г., Эндерлайн Р., Эссер Б.** Электронная теория неупорядоченных полупроводников. М.: Наука, 1981, 384 с.

11. **Градштейн И. С., Рыжик И. М.** Таблицы интегралов, сумм, рядов и произведений. М.: Наука, 1971. 1108 с.

THE AUTHORS

FILIMONOV Alexey V.
Peter the Great St. Petersburg Polytechnic University
29 Politechnicheskaya St., St. Petersburg, 195251, Russia
filimonov@rphf.spbstu.ru
ORCID: 0000-0002-2793-5717

BONDARENKO Vyacheslav B.
Peter the Great St. Petersburg Polytechnic University
29 Politechnicheskaya St., St. Petersburg, 195251, Russia
vyacheslav.b.bondarenko@mail.ru
ORCID: 0000-0002-2669-0471

СВЕДЕНИЯ ОБ АВТОРАХ

ФИЛИМОНОВ Алексей Владимирович – *доктор физико-математических наук, профессор Высшей инженерно-физической школы, соруководитель научно-образовательного центра «Физика нанокомпозитных материалов электронной техники» Санкт-Петербургского политехнического университета Петра Великого.*

195251, Россия, г. Санкт-Петербург, Политехническая ул., 29
filimonov@rphf.spbstu.ru
ORCID: 0000-0002-2793-5717

БОНДАРЕНКО Вячеслав Борисович – *кандидат физико-математических наук, доцент Высшей инженерно-физической школы Санкт-Петербургского политехнического университета Петра Великого.*

195251, Россия, г. Санкт-Петербург, Политехническая ул., 29
vyacheslav.b.bondarenko@mail.ru
ORCID: 0000-0002-2669-0471

Received 14.09.2023. Approved after reviewing 20.10.2023. Accepted 20.10.2023.
Статья поступила в редакцию 14.09.2023. Одобрена после рецензирования 20.10.2023. Принята 20.10.2023.

Original article
UDC 538.9
DOI: https://doi.org/10.18721/JPM.17103

THE EFFECT OF THE MONTMORILLONITE-BASED FILLER ON THE ELECTRET PROPERTIES OF POLYPROPYLENE

E. A. Karulina [1] ✉, *E. A. Volgina* [1], *S. M. Kulemina* [1],
M. F. Galikhanov [2,3], *A. M. Minzagirova* [3]

[1] Herzen State Pedagogical University of Russia, St. Petersburg, Russia;
[2] Institute of Applied Research, Tatarstan Academy of Sciences, Kazan, Republic of Tatarstan, Russia;
[3] Kazan National Research Technological University, Kazan, Republic of Tatarstan, Russia

✉ karulina@mail.ru

Abstract. In the paper, the studies of electret properties of polypropylene with different percentages of montmorillonite have been carried out by methods of thermally stimulated potential relaxation and thermally stimulated currents. A significant effect of filler concentration on the electret state stability was revealed. The parameters of electrically active defects and the storage time of the electret state were determined. It was established that polypropylene with a 4% mass content of montmorillonite exhibited the best electret properties.

Keywords: electret, composite polymer film, electret state, polypropylene, montmorillonite

Funding: This study was supported by the Ministry of Education of the Russian Federation as a part of the Government Assignment (project No. VRFY-2023-0005).

For citation: Karulina E. A., Volgina E. A., Kulemina S. M., Galikhanov M. F., Minzagirova A. M., The effect of the montmorillonite-based filler on the electret properties of polypropylene, St. Petersburg State Polytechnical University Journal. Physics and Mathematics. 17 (1) (2024) 29–37. DOI: https://doi.org/10.18721/JPM.17103

Научная статья
УДК 538.9
DOI: https://doi.org/10.18721/JPM.17103

ВЛИЯНИЕ НАПОЛНИТЕЛЯ НА ОСНОВЕ МОНТМОРИЛЛОНИТА НА ЭЛЕКТРЕТНЫЕ СВОЙСТВА ПОЛИПРОПИЛЕНА

Е. А. Карулина [1] ✉, *Е. А. Волгина* [1], *С. М. Кулемина* [1],
М. Ф. Галиханов [2,3], *А. М. Минзагирова* [3]

[1] Российский государственный педагогический университет им. А. И. Герцена, Санкт-Петербург, Россия;
[2] Институт прикладных исследований Академии наук Республики Татарстан, г. Казань, Республика Татарстан, Россия;
[3] Казанский национальный исследовательский технологический университет, г. Казань, Республика Татарстан, Россия

✉ karulina@mail.ru

Аннотация. Проведены исследования электретных свойств полипропилена с различным процентным содержанием монтмориллонита методами термостимулированной релаксации потенциала и термостимулированных токов короткого замыкания. Выявлено заметное влияние концентрации наполнителя на стабильность электретного состояния. Определены параметры электрически активных дефектов и время хранения электретного состояния для разного содержания наполнителя в образцах. Установлено, что наилучшими электретными свойствами обладает полипропилен с 4 %-м массовым содержанием монтмориллонита.

Ключевые слова: электрет, полимерный композитный материал, электретное состояние, полипропилен, монтмориллонит

Финансирование: Исследование выполнено при финансовой поддержке Министерства образования Российской Федерации как часть Государственного задания (проект № VRFY-2023-0005).

Для цитирования: Карулина Е. А., Волгина Е. А., Кулемина С. М., Галиханов М. Ф., Минзагирова А. М. Влияние наполнителя на основе монтмориллонита на электретные свойства полипропилена // Научно-технические ведомости СПбГПУ. Физико-математические науки. 2024. Т. 17. № 1. С 29–37. DOI: https://doi.org/10.18721/JPM.17103

Introduction

The field of application of polymer electrets is quite wide: electroacoustics, medicine, filtering devices, radioactive radiation sensors, etc. [1].

An important parameter for the practical use of a polymer as an electret material is the stability of the electret state formed in it [2]. The influence of the electret electric field on microorganisms and bacteria is described in Refs. [3, 4]. It has been found that the effect of the field on microorganisms leads to a slowdown in the processes of their vital activity and can significantly increase the shelf life of food products.

Currently, an effective and technologically advanced way to form a stable electret charge in polymer films is the method of charging films in a corona discharge.

Promising objects of research are polymer films based on polypropylene (PP). Low density, high mechanical strength and resistance to chemical influences, as well as low cost make polypropylene a popular and easily accessible material.

It is known that the addition of dispersed fillers to the polymer matrix has a positive effect on the stability of the electret state in the polymer under study. This leads to the creation of new materials with improved electret properties and opens up new possibilities for their application [5, 6].

The results of studies [7, 8] have shown that the introduction of fillers such as diatomite and aerosil into the polyethylene matrix significantly increases the stability of the electret state, while pure polypropylene does not exhibit its high stability. Another possible filler in the polypropylene matrix is montmorillonite (MM). Montmorillonite is a cheap material with sorption properties.

Previous studies [9 – 12] have shown that the introduction of montmorillonite has a significant effect on the complex properties of polymers. For example, when chrysotile or montmorillonite is added to the polymer matrix, it leads to a significant change in the electrophysical properties of the starting material. The hydrophilicity of the fillers used may be one of the reasons for this. In Ref. [13], it was shown that the addition of montmorillonite particles to chitosan increased the activation energy of the electrical conductivity of this material from 0.20 eV to 0.31 eV, and as a result, the specific electrical conductivity of this polymer decreased by reducing the concentration of free ions.

In this regard, the goal of this study was to introduce montmorillonite into polypropylene films and investigate the filler effect on the electret properties of the modified material.

Materials and methods

In this work, the initial polypropylene films of the PP4215M brand (EP1X35F) and composite films based on it have been studied.

Composites based on PP with 2 and 4 wt.% of montmorillonite were prepared in the melt at the laboratory station "Plastograph EC" of the company "Brabender" (Germany) with adjustable electric heating at a temperature of 190°C and rotor speeds of 50 – 150 rpm for 300 s. The samples were produced by pressing on a GotechGT-7014-H10C hydraulic press at 190 ± 5°C with a heating time of 5 min, a pressure exposure of 3 min, and subsequent cooling of 3 min. The sample thickness of the initial films and composites varied from 0.12 ± 0.05 to 0.14 ± 0.05 mm.

Montmorillonite (mark 15A) is a clay mineral belonging to a subclass of layered silicates. The three-layer structure of this mineral, consisting of two silicon-oxygen and one aluminum hydroxide layers, is provided due to sufficiently weak molecular bonds. As a result, water molecules can easily penetrate into the interlayer space, and the mineral itself has good sorption properties.

The electret properties of the samples were investigated by the following methods:

thermally stimulated relaxation of the surface potential (TSRSP),

thermally stimulated currents (TSC).

When studying the films by the TSRSP technique, the samples were pre-polarized in a corona discharge at a temperature of 80°C. Further, the temperature dependence of the surface potential in the linear heating mode was removed.

In the TSC procedure, polarization was carried out at room temperature also in a corona discharge. The result of the study was a graph of the depolarization current dependence on temperature. The maximal temperature positions of the thermally stimulated depolarization currents and the nature of the TSD curves made it possible to determine the activation energy and the effective frequency factor of electrically active defects, as well as to obtain information about the relaxation mechanisms of the objects under study.

Results and discussion

Fig. 1,*a* presents the dependences of the surface potential decay on temperature at a heating rate of 5°C/min for PP samples without filler charged in the field of positive and negative corona discharges.

From this graphs we notice that the decreasing curves of the surface potential at different polarities of the polarizing field turn out to be identical. This result indicates that the relaxation process of the charge state is associated either with the reorientation of the dipoles in the samples or with the neutralization of the trapped charge due to the intrinsic conductivity of the polymer [14].

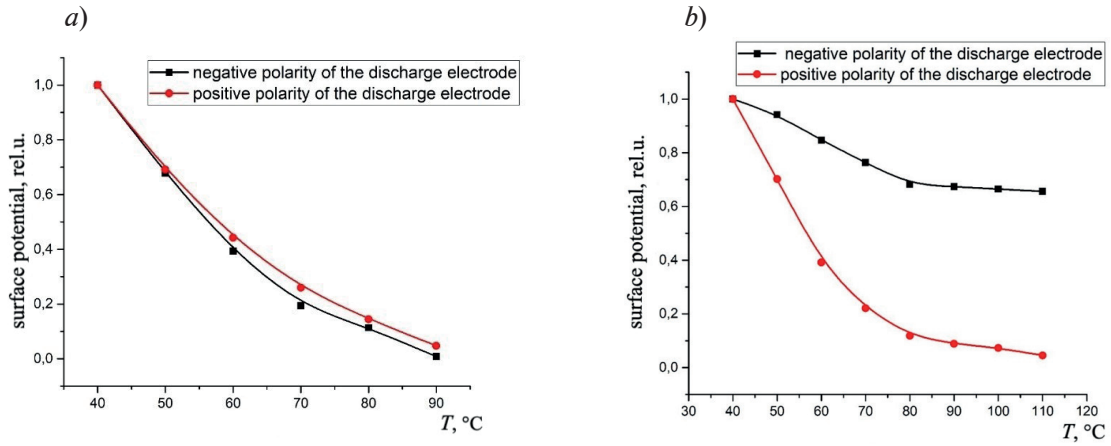

Fig. 1. Temperature dependences of the surface potential (relative units) for polypropylene (PP) charged samples without filler (*a*) and PP + 4 % montmorillonite (MM) charged composite films (*b*); they were treated in the field of positive and negative corona discharges in both cases (a heating rate was 5°C/min)

Fig. 1,*b* shows the similar dependences of the surface potential decay but for samples PP + 4 % MM charged in the same fields. In this case, the decline of the surface potential becomes strongly dependent on the polarity of the corona discharge. The process of surface potential decay for samples charged in the positive corona discharge field is more intense than that for samples charged in the negative one. It can be assumed that in this case, sufficiently deep electronegative traps are formed at the polymer–filler interface. A similar effect was observed in polyethylene films filled with talc [15], simultaneously with a decrease in the conductivity of the polymer due to the sorption properties of the filler [16].

An additional confirmation of the above-mentioned double effect of the hydrophilic filler on the charge relaxation in the polypropylene is the temperature dependences of the current for PP films with different percentages of MM, pre-polarized in the negative corona discharge field at room temperature (Fig. 2).

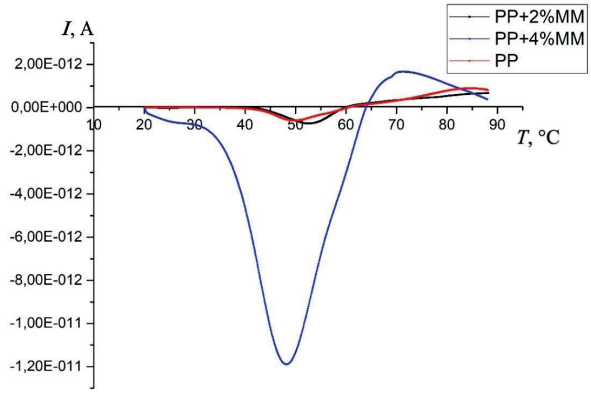

Fig. 2. Thermostimulated currents for the initial films, composite films PP + *n* MM (*n* = 2 and 4 % by weight), polarized in the field of the negative corona discharge field (a heating rate was 9°C/min)

Here the intensity of the TST peaks grows significantly with an increase in the percentage of filler from 2 to 4 % (not proportional to the percentage), which can be explained not only by an increase in the quantity of traps at the polymer – montmorillonite boundary, but also by a decrease in the conductivity of the polymer.

The activation energy and frequency factor of the electrically active defects responsible for relaxation processes in both the initial and filled polymer samples were calculated using the method of varying the heating rate. As an example, Fig. 3,*a*,*b* shows the TSC curves for two heating rates for the initial PP films and PP ones with 4% of the filler mass.

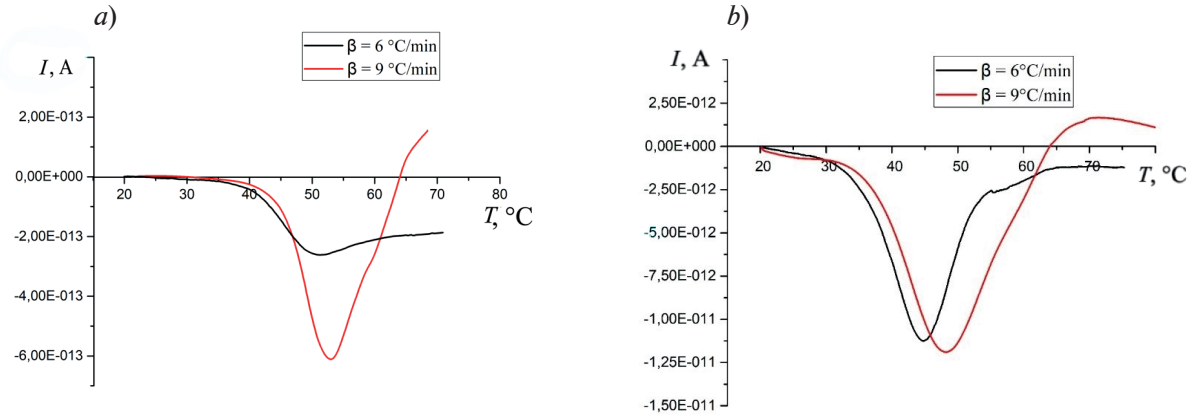

Fig. 3. Thermostimulated currents for PP + 4 % MM composite films (4 % by weight) (*a*) and the initial polypropylene films (*b*) polarized in the negative corona discharge field at different linear heating rates (6 and 9°C /min)

The formula for finding the activation energy W of relaxers by the temperature positions of the peaks at two heating rates has the form:

$$W = \frac{kT_{m_1}T_{m_2}}{T_{m_1} - T_{m_2}} \ln \frac{\beta_1 T_{m_2}^{\ 2}}{\beta_2 T_{m_1}^{\ 2}}, \quad (1)$$

where T_{m1}, T_{m2} are the temperature values of the maximal currents; β_1, β_2 are the heating rates; k is the Boltzmann constant.

The value of the frequency factor ω was determined by the following formula:

$$\omega = \frac{W\beta}{kT_m^{\ 2}} \exp\left(\frac{W}{kT_m}\right), \quad (2)$$

where T_m is the temperature of the maximal current at the heating rate β.

The calculation results show an increase in the activation energy W for the composite polymer compared to the initial one from 0.75 ± 0.05 to 1.01 ± 0.05 eV at a frequency factor ω of the order of 10^{11} s^{-1}. Obviously, such results should increase the relaxation time τ_p of the electret state in the MM-filled polymer compared to the initial one.

Indeed, calculated the relaxation time of the electret state by the formula

$$\tau_p = \frac{1}{\omega} \exp\left(\frac{W}{kT_k}\right) \quad (3)$$

at room temperature, increases from 4 min (for PP without filler) to 256 hrs (for PP + 4% MM).

The temporary stability rise of the electret state when filling polypropylene with montmorillonite is accompanied by an increase in temperature stability. The temperature dependences of the surface potential in relative units for samples with different percentages of montmorillonite charged in the negative corona discharge field are shown in Fig. 4.

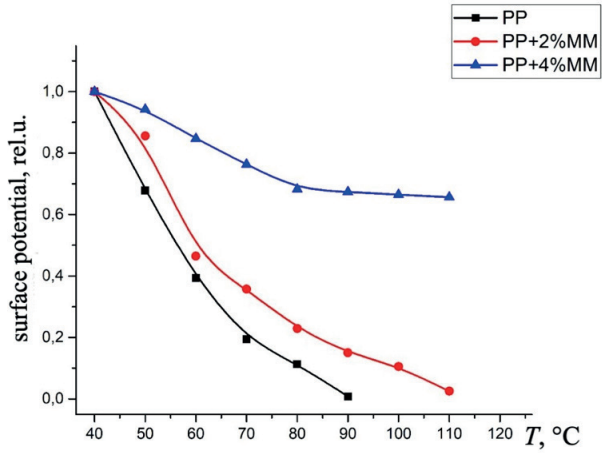

Fig. 4. Temperature dependences of the surface potential for PP films and PP + n MM (n = 2 and 4 % by weight) composite films charged in the negative corona discharge field

Similarly, according to the current spectroscopy data presented in Fig. 2, a significant change in the decline of the surface potential with an increase in temperature occurs when 4 wt. % MM is added., as well as the curve at 2 wt.% of the thermally stimulated relaxation of the potential almost coincides with a similar dependence for the initial polypropylene.

Conclusion

The electret properties of the initial polypropylene films and composite polypropylene ones with montmorillonite filler were studied by the TSRP and TSC methods.

It was revealed that the stability of the electret state increases compared to the initial PP with an increase in the percentage of montmorillonite to 4 wt.% in polypropylene films. This results from two reasons: the formation of sufficiently deep charge traps at the polymer–filler interface and a decrease in the conductivity of the polymer due to the sorption properties of the MMT filler.

The relaxation time of the electret state in the PP films with 4 wt.% of montmorillonite is about 256 hrs at room temperature; this result makes it possible to use these composite polymer films as an active packaging material for food products.

Further studies of the electret properties of polypropylene with a high percentage of montmorillonite will allow us to determine the optimal percentage of the filler.

REFERENCES

1. **Boitsov V., Rychkov D.,** Polymeric electrets in innovative technologies, Izvestia: Herzen University Journal of Humanities & Sciences. (2 (4)) (2002) 118–132 (in Russian).

2. **Rychkov A., Rychkov D., Trifonov S.,** Electret state stability in polymers with modified surface, Izvestia: Herzen University Journal of Humanities & Sciences. (4 (8)) (2004) 122–134 (in Russian).

3. **Krynitskaya A. Y., Borisova A. N., Galikhanov M. F., et al.,** Influence of "active" packing material on development of microorganisms in foodstuff, Food Processing Industry. (1) (2011) 27–29 (in Russian).

4. **Galikhanov M., Guzhova A., Borisova A.,** Effect of active packaging material on milk quality, Bulgar. Chem. Commun. 46 (Jan) (2014) 142–145.

5. **Gorokhovatsky Yu., Aniskina L., Burda V., et al.,** On the nature of the electret state in composite low-density films of polyethylene with nano-dispersed SiO_2 fillers, Izvestia: Herzen University Journal of Humanities & Sciences. (95) (2009) 63–67 (in Russian).

6. **Temnov D., Fomicheva E.,** The dependence of the electret state stability of the polypropylene films on the share of the disperse filler (aerosil), Izvestia: Herzen University Journal of Humanities & Sciences. (135) (2010) 92–100 (in Russian).

7. **Gorokhovatsky Yu. A., Demidova N. S., Temnov D. E.,** Electric charge relaxation in the polyethylene with mineral inclusions of diatomite, St. Petersburg Polytechnic University Journal. Physics and Mathematics. 13 (2) (2020) 9–16.

8. **Ignatyeva D., Karulina E., Chistyakova O.,** The mechanism of electret state relaxation in polyactide films containing dispersed filler, Izvestia: Herzen University Journal of Humanities & Sciences. (173) (2015) 39–45 (in Russian).

9. **Bobritskaia E., Temnov D.,** Chitosan as a material for tissue engineering, The Scientific Opinion. (3) (2013) 206–211 (in Russian).

10. **Galikhanov M. F., Minzagirova A. M., Spiridonova R. R.,** Modifying the properties of polyethylene electrets through the incorporation of montmorillonite, Surf. Eng. Appl. Electrochem. 55 (6) (2019) 679–683.

11. **Minzagirova A. M., Galikhanov M. F., Spiridonova R. R., et al.,** Effect of montmorillonite on the properties of polyethylene electret, AIP Conf. Proc. 2174 (Dec. 06) (2019) 020041.

12. **Bobritskaya E., Kubrakova E., Temnov D., Fomicheva E.,** Electric relaxation in chitosan films with mineral nanodimentional inclusions, Izvestia: Herzen University Journal of Humanities & Sciences. (154) (2013) 69–76 (in Russian).

13. **Bobritskaya E. I., Kastro R. A., Temnov D. E.,** Thermoactivation and dielectric spectroscopy of chitosan films, Physics of the Solid State. 55 (1) (2013) 225–228 (in Russian).

14. **Gorokhovatski Yu., Temnov D.,** Thermally stimulated relaxation of surface potential and thermally stimulated short circuit currents in the charged dilectric, Izvestia: Herzen University Journal of Humanities & Sciences. (8(38)) (2007) 24–34 (in Russian).

15. **Temnov D. E., Fomicheva E. E., Stozharov V. M.,** Vliyaniye talka na elektretnyye svoystva i strukturu polietilena vysokogo davleniya [The effect of talc on electret properties and the structure of high-pressure polyethylene], Herald of Kazan Technological University. (14) (2014) 321–323 (in Russian).

16. **Galikhanov M., Gorokhovatskiy Yu., Gulyakova A., et al.,** The investigation of electret state stability in composite polymer films with dispersed filler, Izvestia: Herzen University Journal of Humanities & Sciences. (138) (2011) 25–34 (in Russian).

СПИСОК ЛИТЕРАТУРЫ

1. **Бойцов В. Г., Рычков Д. А.** Полимерные электреты в инновационных технологиях // Известия Российского государственного педагогического университета им. А. И. Герцена. 2002. № 2 (4). С. 118–132.

2. **Рычков А. А., Рычков Д. А., Трифонов С. А.** Стабильность электретного состояния в полимерах с модифицированной поверхностью // Известия Российского государственного педагогического университета им. А. И. Герцена. 2004. № 4 (8). С. 122–134.

3. **Крыницкая А. Ю., Борисова А. Н., Галиханов М. Ф., Сысоева М. А., Гамаюрова В. С.** Влияние «активного» упаковочного материала на развитие микроорганизмов в пищевых продуктах // Пищевая промышленность. 2011. № 1. С. 27–29.

4. **Galikhanov M., Guzhova A., Borisova A.** Effect of active packaging material on milk quality // Bulgarian Chemical Communications. 2014. Vol. 46. January. Pp. 142–145.

5. **Гороховатский Ю. А., Анискина Л. Б., Бурда В. В., Галиханов М. Ф., Гороховатский И. Ю., Тазенков Б. А., Чистякова О. В.** О природе электретного состояния в композитных пленках полиэтилена высокого давления с нанодисперсными наполнителями SiO_2 // Известия Российского государственного педагогического университета им. А. И. Герцена. 2009. № 95. С. 63–77.

6. **Темнов Д., Фомичева Е.** Стабильность электретного состояния пленок полипропилена в зависимости от содержания дисперсного наполнителя (аэросил) // Известия Российского государственного педагогического университета им. А. И. Герцена. 2010. № 135. С. 92–100.

7. **Gorokhovatsky Yu. A., Demidova N. S., Temnov D. E.,** Electric charge relaxation in the polyethylene with mineral inclusions of diatomite // St. Petersburg Polytechnic University Journal. Physics and Mathematics. 2020. Vol. 13. No. 2. Pp. 9–16.

8. **Игнатьева, Д. А., Карулина, Е. А., Чистякова О. В.** Механизм релаксации электретного состояния в пленках полилактида с дисперсным наполнителем // Известия Российского государственного педагогического университета им. А. И. Герцена. 2015. № 173. С. 39–45.

9. **Бобрицкая Е., Темнов Д.** Хитозан – материал для тканевой инженерии // Научное мнение. 2013. № 3. С. 206–211.

10. **Galikhanov M. F., Minzagirova A. M., Spiridonova R. R.** Modifying the properties of polyethylene electrets through the incorporation of montmorillonite // Surface Engineering and Applied Electrochemistry. 2019. Vol. 55. No. 6. Pp. 679–683.

11. **Minzagirova A. M., Galikhanov M. F., Spiridonova R. R., Khairyllin R. Z., Spiridonova A. O.** Effect of montmorillonite on the properties of polyethylene electret // AIP Conference Proceedings. 2019. Vol. 2174. December 06. P. 020041.

12. **Бобрицкая Е. И., Кубракова Е. С., Темнов Д. Э., Фомичева Е. Е.** Процессы электрической релаксации в пленках хитозана с минеральными наноразмерными включениями // Известия Российского государственного педагогического университета им. А. И. Герцена. 2013. № 154. С. 69–76.

13. **Бобрицкая Е. И., Кастро Р. А., Темнов Д. Э.** Термоактивационная и диэлектрическая спектроскопия пленок хитозана. // Физика твердого тела. 2013. Т. 55. № 1. С. 193–196.

14. **Гороховатский Ю. А., Темнов Д. Э.** Термостимулированная релаксация поверхностного потенциала и термостимулированные токи короткого замыкания в предварительно заряженном диэлектрике // Известия Российского государственного педагогического университета им. А. И. Герцена. 2007. № 8 (38). С. 24–34.

15. **Темнов Д. Э., Фомичева Е. Е., Стожаров В. М.** Влияние талька на электретные свойства и структуру полиэтилена высокого давления // Вестник Казанского технологического университета. 2014. № 14. С. 321–323.

16. **Галиханов М. Ф., Гороховатский Ю. А., Гулякова А. А., Темнов Д. Э., Фомичева Е. Е.** Исследование стабильности электретного состояния в композитных полимерных пленках с дисперсным наполнителем // Известия Российского государственного педагогического университета им. А. И. Герцена. 2011. № 138. С. 25–34.

THE AUTHORS

KARULINA Elena A.
Herzen State Pedagogical University of Russia
48 Moyka Emb., St. Petersburg, 191186, Russia
karulina@mail.ru
ORCID: 0000-0001-9604-4769

VOLGINA Elena A.
Herzen State Pedagogical University of Russia
48 Moyka Emb., St. Petersburg, 191186, Russia
volgina.elena.1999@mail.ru
ORCID: 0000-0002-1536-5841

KULEMINA Sofya M.
Herzen State Pedagogical University of Russia
48 Moyka Emb., St. Petersburg, 191186, Russia
sonia.kulemina@yandex.ru
ORCID: 0009-0002-3569-4981

GALIKHANOV Mansur F.
Institute of Applied Research of Tatarstan Academy of Sciences,
Kazan National Research Technological University
20 Bauman St., Kazan, 420111, Russia
mgalikhanov@yandex.ru
ORCID: 0000-0001-5647-1854

MINZAGIROVA Alsu M.
Kazan National Research Technological University
68 Karl Marx St., Kazan, Republic of Tatarstan, 420015, Russia
alsu.minzagirova@mail.ru
ORCID: 0000-0002-8859-5621

СВЕДЕНИЯ ОБ АВТОРАХ

КАРУЛИНА Елена Анатольевна – *кандидат физико-математических наук, доцент кафедры общей и экспериментальной физики Российского государственного педагогического университета им. А. И. Герцена, Санкт-Петербург, Россия.*
191186, Россия, г. Санкт-Петербург, наб. р. Мойки, 48
karulina@mail.ru
ORCID: 0000-0001-9604-4769

ВОЛГИНА Елена Алексеевна – *ассистентка кафедры общей и экспериментальной физики Российского государственного педагогического университета им. А. И. Герцена, Санкт-Петербург, Россия.*
191186, Россия, г. Санкт-Петербург, наб. р. Мойки, 48
volgina.elena.1999@mail.ru
ORCID: 0000-0002-1536-5841

КУЛЕМИНА Софья Михайловна – *аспирантка кафедры общей и экспериментальной физики Российского государственного педагогического университета им. А. И. Герцена, Санкт-Петербург, Россия.*
191186, Россия, г. Санкт-Петербург, наб. р. Мойки, 48
sonia.kulemina@yandex.ru
ORCID: 0009-0002-3569-4981

ГАЛИХАНОВ Мансур Флоридович – *доктор технических наук, ведущий научный сотрудник Центра новых материалов и перспективных технологий Института прикладных исследований Академии наук Республики Татарстан; профессор кафедры технологии переработки полимеров и композиционных материалов Казанского национального исследовательского технологического университета г. Казань, Республика Татарстан, Россия.*

420111, Россия, г. Казань, ул. Баумана, 20

mgalikhanov@yandex.ru

ORCID: 0000-0001-5647-1854

МИНЗАГИРОВА Алсу Мударрисовна – *аспирантка кафедры технологии переработки полимеров и композиционных материалов Казанского национального исследовательского технологического университета, г. Казань, Республика Татарстан, Россия.*

420015, Россия, Республика Татарстан, г. Казань, ул. К. Маркса, 68

alsu.minzagirova@mail.ru

ORCID: 0000-0002-8859-5621

Received 29.11.2023. Approved after reviewing 14.12.2023. Accepted 14.12.2023.

Статья поступила в редакцию 29.11.2023. Одобрена после рецензирования 14.12.2023. Принята 14.12.2023.

SIMULATION OF PHYSICAL PROCESSES

Original article
DOI: https://doi.org/10.18721/JPM.17104

NUMERICAL SIMULATION OF OPERATING MODES OF HETEROSTRUCTURAL PHOTODIODES BASED ON INDIUM ARSENIDE NANOWIRES ON THE SILICON SUBSTRATES

L. N. Dvoretckaia[1,2], *A. M. Mozharov*[1,2], *A. S. Goltaev*[1]✉,
V. V. Fedorov[1,2], *I. S. Mukhin*[1,2]

[1] Alferov University, St. Petersburg, Russia;
[2] Peter the Great St. Petersburg Polytechnic University, St. Petersburg, Russia
✉ goltaev@goltaev.ru

Abstract. The paper presents the results of numerical simulation of the heterostructural diodes operation based on the array of indium arsenide nanowires on the silicon substrates with different polarities, namely *n*- or *p*-types. It has been found that it is possible to achieve theoretical values of the ideality factor equal to 1.1 and 2.1 respectively. The high quantum efficiency values are typical for the investigated heterostructures during separation of photogenerated charge carriers in the temperature range of 150–300 K.

Keywords: indium arsenide, nanowire, heterostructure, silicon substrate, numerical calculation

Funding: The research has been funded by the Ministry of Science and Higher Education of the Russian Federation, within the framework of the State Assignment FSEG-2023-0016 (Grant awarded to the authors L. N. Dvoretckaia, I. S. Mukhin, V. V. Fedorov).

Citation: Dvoretckaia L. N., Mozharov A. M., Goltaev A. S., Fedorov V. V., Mukhin I. S., Numerical simulation of operating modes of heterostructural photodiodes based on indium arsenide nanowires on the silicon substrates, St. Petersburg State Polytechnical University Journal. Physics and Mathematics. 17 (1) (2024) 38–46. DOI: https://doi.org/10.18721/JPM.17104

Научная статья
УДК 621.383.522
DOI: https://doi.org/10.18721/JPM.17104

ЧИСЛЕННОЕ МОДЕЛИРОВАНИЕ РЕЖИМОВ РАБОТЫ ГЕТЕРОСТРУКТУРНЫХ ФОТОДИОДОВ НА ОСНОВЕ НИТЕВИДНЫХ НАНОКРИСТАЛЛОВ АРСЕНИДА ИНДИЯ НА КРЕМНИЕВЫХ ПОДЛОЖКАХ

Л. Н. Дворецкая[1,2], *А. М. Можаров*[1,2], *А. С. Голтаев*[1]✉,
В. В. Фёдоров[1,2], *И. С. Мухин*[1,2]

[1] Академический университет им. Ж. И. Алфёрова РАН, Санкт-Петербург, Россия;
[2] Санкт-Петербургский политехнический университет Петра Великого, Санкт-Петербург, Россия
✉ goltaev@goltaev.ru

Аннотация. В работе представлены результаты численного моделирования работы гетероструктурных диодов на основе массива нитевидных нанокристаллов арсенида индия (InAs) на кремниевых подложках, обладающих разными полярностями, а именно – *n*- и *p*-типов. Установлено, что в этих случаях удается достичь теоретических значений коэффициента идеальности, равных 1,1 и 2,1, соответственно. Для исследованных гетероструктур в температурном диапазоне 150 – 300 K характерны высокие значения квантовой эффективности при разделении фотогенерированных носителей заряда.

Ключевые слова: арсенид индия, нитевидный нанокристалл, гетероструктура, кремниевая подложка, численное моделирование

Финансирование: Исследование выполнено при финансовой поддержке Министерства науки и высшего образования Российской Федерации (грант Государственного задания FSEG-2023-0016 выделен авторам Л. Н. Дворецкой, И. С. Мухину и В. В. Федорову).

Ссылка для цитирования: Дворецкая Л. Н., Можаров А. М., Голтаев А. С., Фёдоров В. В., Мухин И. С. Численное моделирование режимов работы гетероструктурных фотодиодов на основе нитевидных нанокристаллов арсенида индия на кремниевых подложках // Научно-технические ведомости СПбГПУ. Физико-математические науки. 2024. Т. 17. № 1. С. 38–46. DOI: https://doi.org/10.18721/JPM.17104

Introduction

A promising direction in seminconductor physics is the development of photodetector devices based on crystalline nanowires (NW). This is of particular importance due to the obvious advantages of NW over thin-film structures of the same composition.

Firstly, relaxation of elastic stresses occurs on the lateral surface of NW during synthesis due to the difference in the lattice constants of the semiconductor crystals comprising the substrate and the NW. This circumstance makes it possible to carry out epitaxial synthesis of a number of semiconductor materials, such as InGaN, GaPAs, InAsP [1, 2], for which lattice-matched substrates are either difficult to procure or completely unavailable. In particular, semiconductor devices can be constructed for axial NW with diameters below the critical value (24–110 nm) [3] and lattice-mismatched thick layers. The thicknesses of the layers exceed the critical value (several nanometers) for similar planar structures [4].

Secondly, an equally important advantage of NW is their applications in devices with electronic size effects or subwavelength-scale localization of the electromagnetic field. Such devices can be used to create effective photodiodes, single-photon sources, etc. [5].

A third advantage of NWs is that the structure of the devices can be formed not only in the axial direction (normal to the substrate), but also on the lateral face of the NW (radial geometry, or core–shell geometry). This circumstance makes it possible to distinguish between physical processes, such as, for example, light absorption and separation of charge carriers, which is fundamentally impossible in the case of planar geometry.

This work analyzes the effect of doping type of silicon substrates in the system of indium arsenide nanowires (referred to as InAs/Si) on the characteristics of the photodetector diode structure. The study was conducted within the framework of numerical simulation.

Experimental samples and computational procedure

The paper considers two simplified configurations of axial diode heterostructures based on indium arsenide nanowires on silicon substrates:

n-InAs/*i*-InAs/*p*-Si (configuration *n*–*i*–*p*);

p-InAs/*i*-InAs/*n*-Si (configuration *p*–*i*–*n*).

The choice of NW sizes was dictated by the optimal waveguide geometry for constructing a photodiode structure in the communication wavelength range for such NW [6]: length of 2.5 μm, diameter of 300 nm. Notably, with these characteristic sizes of NW, there are no size effects of energy level quantization in them.

The thickness of the upper emitter was chosen to be 50 nm at a doping level of 10^{18} cm^{-3}, which provided a sufficient number of charge carriers for the formation of a space-charge region mainly inside the NW.

Numerical simulation of the diodes was carried out in the Comsol Multiphysics package. The calculations were performed within the framework of the drift-diffusion model, taking into account the Fermi–Dirac statistics for both types of charge carriers. The Shockley–Read–Hall model was used to account for the effects of charge carrier recombination, with carrier lifetimes in indium arsenide equal to 30 ns for electrons and 3 μs for holes [7, 8]. The parameters of semiconductor materials were taken from [8, 9].

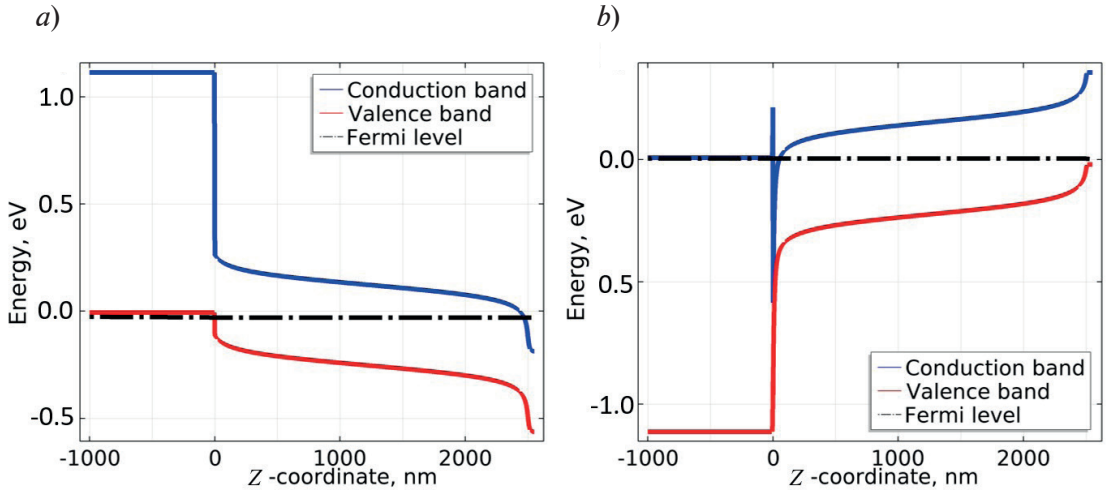

Fig. 1. Band structures of the diode at 200 K for cases of *p*- (*a*) or *n*-type (*b*) substrate chosen

To account for the imperfections in the NW structure, for example, the presence of point defects or the occurrence of various polytypes in the NW, the carrier diffusion length was varied during the simulation process. The considered values of carrier diffusion length ranged from 500 nm to 20 μm.

Importantly, the influence of surface conditions on the operation of the diode was not taken into account in this study.

Results and discussion

According to the literature data, the InAs/Si heterointerface is a type-II heterojunction, where the top of the valence band in both materials is located approximately at the same energy level, so it is natural to choose a silicon substrate with p-type conductivity for constructing diode structures (Fig. 1,*a*). In turn, a distinct characteristic of this configuration is the propagation of the space-charge region into the heterointerface region, which in the case of the considered geometry of the photodetector structure can lead to leakage currents under experimental conditions [10, 11]. Despite the large energy gap between the positions of the conduction band bottom in the two materials, a reverse-polarity diode can be formed due to the low effective mass for electrons in indium arsenide. Indeed, if an n-type substrate is chosen, electrons from the substrate must move to the NW, which can lead to the formation of an electron-depleted region in silicon and an electron-rich region in indium arsenide.

The position of the Fermi level E_F relative to the bottom of the conduction band for degenerate semiconductors can be expressed by the following formula [12]:

$$E_F = \frac{\check{z}^2}{2m^*} \cdot (3\pi^2 n)^{\frac{2}{3}}, \quad (1)$$

where m^* is the effective electron mass, n is the carrier concentration, $\hbar$ is the reduced Planck constant.

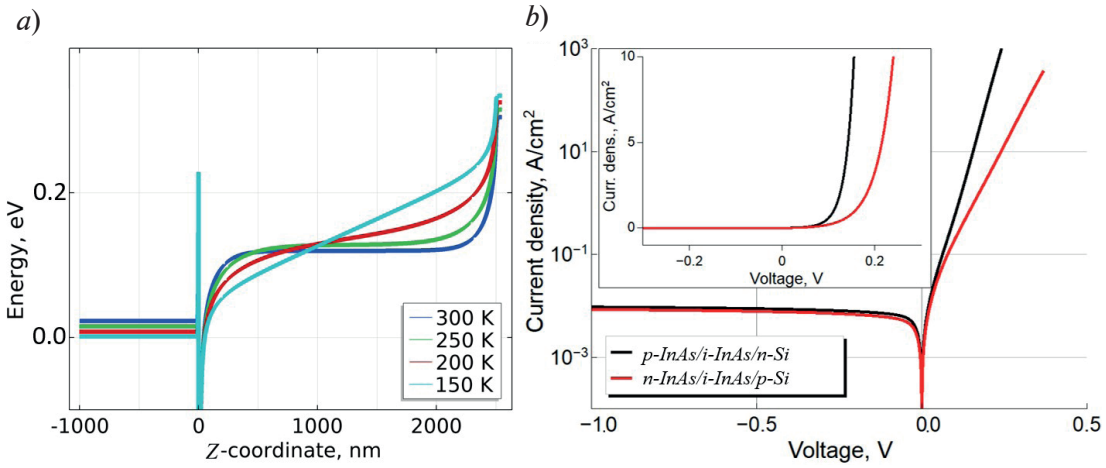

Fig. 2. Simulation of photodiode operation: positions of conduction band bottom forp-InAs/i-InAs/n-Si heterostructure at different temperatures (*a*); current–voltage characteristics for two types of diodes at 200 K on logarithmic (modulus) and linear scales (*b*)

Substituting the effective mass of InAs equal to 0.023 m_0 (m_0 is the electron mass) into this formula, we obtain that the doping level of the substrate about 10^{19} cm^{-3} is sufficient to compensate for the band discontinuity between *n*-Si and InAs.

Notably, such substrates are commercially available. The required value may be actually even lower, due to the appearance of size quantization in InAs along the NW axis with sharp band bending and a consequent decrease in electron filling density (Fig. 1,*b*).

Fig. 1 shows the band diagrams for diodes of both polarity types at a temperature of 200 K, above which (as we discuss below) thermogenerated charge carriers begin to effectively shield the potential difference between the emitters of the structure.

Apparently, in the case of choosing an *n*-type substrate, the doping level of 10^{19} cm^{-3} is sufficient to ensure the required band bending. The height of the potential barrier for electrons in silicon turns out to be relatively small and provides high conductivity of the heterointerface.

To determine the optimal operating conditions of the considered photodetector structures, simulation was carried out for various temperatures of the system. It was found for both configurations at room temperature that shielding of the electric field occurs in the NW volume due to intrinsic carrier concentration (Fig. 2,*a*). The intrinsic concentration decreases with a

decrease in temperature, ensuring an increase in the space-charge region in NW, which is most noticeable at temperatures below 200 K. Thus, it can be expected that additional cooling of the structure may be required for efficient operation of the NW array as a photodiode.

The next stage of the simulation was the analysis of the current–voltage (I–V) characteristics of the considered diode heterostructures (Fig. 2,*b*) for a characteristic temperature of 200 K determined earlier. We established that the reverse currents practically coincide for both configurations and correspond to the value of the current formed by the separation of charge carriers arising in the NW volume due to the thermogeneration process. The forward-bias region of the current–voltage characteristic exhibits a significant difference between the two configurations, namely, that the diode formed on n-type silicon substrate opens earlier.

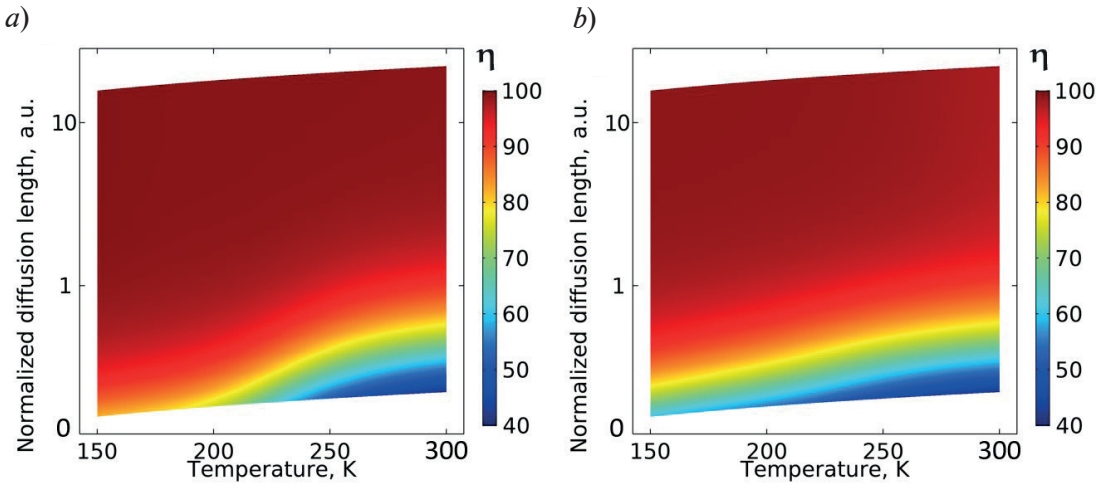

Fig. 3. Maps for dependence of quantum efficiency of separation of photogenerated charge carriers on temperature and carrier diffusion length normalized by the length of active region of the NW for configurations n–i–p (*a*) and p–i–n (*b*)

Approximation of the forward-bias region of the current–voltage characteristic using the Shockley equation [13] for a loaded diode shows that this circumstance is due to the difference in the ideality factor for two configurations: the p–i–n system has an ideality factor equal to 1.1, while this value for the n–i–p system is 2.1, which leads to an increase in the open-circuit voltage of the diode. Analysis of this result allows to conclude that the p–i–n system is more suitable in cases when low open-circuit voltages are important, for example, as detector diodes in high-frequency mixers.

At the next stage, we studied the operation of heterostructures as photodiodes. For this purpose, we carried out numerical simulation of the dependence of separation processes of photogenerated charge carriers in NW on temperature and diffusion length for two configurations at zero bias voltage. The electron–hole pairs were produced under optical irradiation of a photoactive structure by setting a fixed uniform generation rate equal to $1.4 \cdot 10^{19}$ cm^{-3}/s, which corresponds to the absorption of optical radiation with a wavelength of 1.55 μm and an intensity of 1 W/m^2 by a semiconductor material.

The quantum efficiency η was used as a comparative characteristic, calculated as the ratio of the carrier flux formed in the structure to the total generation rate over the NW volume. Fig. 3 shows maps for the dependence of quantum efficiency η on the temperature of the structure and the carrier diffusion length normalized by the length of the active region of the NW.

Evidently, almost complete separation of photogenerated charge carriers is achieved for both configurations at high diffusion lengths. A further decrease in the carrier diffusion length reveals the difference between the configurations. A decrease in the diffusion length down to values below the NW length leads to the appearance of a temperature dependence of quantum efficiency. In particular, there is an increase in quantum efficiency from 0.4 to 0.8 with a decrease in temperature from 300 to 150 K for the n–i–p system. In turn, the p–i–n system turns out to be more sensitive

to a decrease in the diffusion length: the quantum efficiency at 300 K also corresponds to a value of 0.4, but it increases only to a value of 0.6 with a decrease in temperature. In addition, the *p*—*i*—*n* system demonstrates a lower quantum efficiency even for high values of the diffusion length. This phenomenon is likely related to the difference between the configurations, that is, the presence of an electron-rich region near the heterointerface, which leads to an increased recombination rate of holes near the interface and, as a result, their exclusion from the total photocurrent.

Conclusion

In this paper, we carried out numerical simulation to study the operational modes of two configurations of a heterostructure photodetector diode based on indium arsenide nanowires on silicon substrates. As a result of the simulation, we found that the diode structure on the *n*-type silicon substrate demonstrates a lower value of the ideality factor and it is more suitable for problems where low open-circuit voltages are required. The structures had almost identical parameter values for both systems in photodiode mode, however, the system using the *p*-type substrate gives higher values of quantum efficiency. Despite this, both configurations can be used to build photodiodes based on them, and the choice of specific configuration should be determined by the technological requirements for synthesis of the structure or the requirements for the polarity of the system.

REFERENCES

1. **Dubrovskii V. G., Consonni V., Trampert A., et al.,** Scaling thermodynamic model for the self-induced nucleation of GaN nanowires, Phys. Rev. B. 85 (16) (2012) 165317.

2. **Dubrovskii V. G.,** Understanding the vapor—liquid—solid growth and composition of ternary III—V nanowires and nanowire heterostructures, J. Phys. D: Appl. Phys. 50 (45) (2017) 453001.

3. **Cirlin G. E., Dubrovskii V. G., Samsonenko Y. B., et al.,** Self-catalyzed, pure zincblende GaAs nanowires grown on Si(111) by molecular beam epitaxy, Phys. Rev. B. 82 (3) (2010) 035302.

4. **De La Mata M., Magйn C., Caroff P., Arbiol J.,** Atomic scale strain relaxation in axial semiconductor III-V nanowire heterostructures, Nano Lett. 14 (11) (2014) 6614—6620.

5. **Leandro L., Gunnarsson C. P., Reznik R., et al.,** Nanowire quantum dots tuned to atomic resonances, Nano Lett. 18 (11) (2018) 7217—7221.

6. **Dvoretckaia L., Mozharov A., Pavlov A., et al.,** Numerical study of detectivity for near-IR photodetectors based on InAsP NWs, Scr. Mater. 226 (15 March) (2023) 115246.

7. **Dalal V. L., Hicinbothem W. A., Kressel H.,** Carrier lifetimes in epitaxial InAs, Appl. Phys. Lett. 24 (4) (1974) 184—185.

8. **Adachi S.,** Physical properties of III-V semiconductor compounds: InP, InAs, GaAs, GaP, InGaAs, and InGaAsP, John Wiley & Sons, New York, Chichester, 1992.

9. **Adachi S.,** Properties of semiconductor alloys: group-IV, III-V and II-VI semiconductors, John Wiley and Sons Ltd., New York, Chichester, 2009.

10. **Shugurov K. Y., Mozharov A. M., Bolshakov A. D., et al.,** Hydrogen passivation of the *n*-GaN nanowire/*p*-Si heterointerface, Nanotechnol. 31 (24) (2020) 244003.

11. **Mozharov A. M., Fedorov V. V., Shugurov K. Y., et al.,** Study of the electrical properties of InAs nanowires/Si substrate for IR photodetector. Proc. 20th Int.Conf. Laser Optics (ICLO-2022). 20.06.2022—24.06.2022. Saint Petersburg,Russia. Institute of Electrical and Electronics Engineers Inc. (2022) 18.

12. **Bonch-Bruyevich V. L., Kalashnikov S. G.,** Physics of semiconductors, VEB Verlag Technic, Berlin, 1982.

13. **Shockley W.,** The theory of *p*—*n* junctions in semiconductors and *p*—*n* junction transistors, Bell Syst. Tech. J. 28 (3) (1949) 435—489.

СПИСОК ЛИТЕРАТУРЫ

1. **Dubrovskii V. G., Consonni V., Trampert A., Geelhaar L., Riechert H.** Scaling thermodynamic model for the self-induced nucleation of GaN nanowires // Physical Review B. 2012. Vol. 85. No.16. P. 165317.

2. **Dubrovskii V. G.** Understanding the vapor–liquid–solid growth and composition of ternary III–V nanowires and nanowire heterostructures// Journal of Physics D: Applied Physics. 2017. Vol. 50. No. 45. P. 453001.

3. **Cirlin G. E., Dubrovskii V. G., Samsonenko Y. B., et al.** Self-catalyzed, pure zincblende GaAs nanowires grown on Si(111) by molecular beam epitaxy// Physical Review B. 2010. Vol. 82. No. 3. P. 035302.

4. **De La Mata M., Magйn C., Caroff P., Arbiol J.** Atomic scale strain relaxation in axial semiconductor III-V nanowire heterostructures // Nano Letters. 2014. Vol. 14. No.11. Pp. 6614–6620.

5. **Leandro L., Gunnarsson C. P., Reznik R., Jцns K. D., Shtrom I., Khrebtov A., Kasama T., Zwiller V., Cirlin G., Akopian N.** Nanowire quantum dots tuned to atomic resonances // Nano Letters. 2018. Vol. 18. No. 11. Pp. 7217–7221.

6. **Dvoretckaia L., Mozharov A., Pavlov A., Polozkov R., Mukhin I.** Numerical study of detectivity for near-IR photodetectors based on InAsP NWs // Scripta Materialia. 2023. Vol. 226. 15 March. P. 115246.

7. **Dalal V. L., Hicinbothem W. A., Kressel H.** Carrier lifetimes in epitaxial InAs // Applied Physics Letters. 1974. Vol. 24. No. 4. Pp.184–185.

8. **Adachi S.** Physical properties of III-V semiconductor compounds: InP,InAs, GaAs, GaP, InGaAs, and InGaAsP. New York, Chichester: John Wiley & Sons, 1992.

9. **Adachi S.** Properties of semiconductor alloys: group-IV, III-V and II-VI semiconductors. New York, Chichester: John Wiley and Sons Ltd., 2009. 400 p.

10. **Shugurov K. Y., Mozharov A. M., Bolshakov A. D., et al.** Hydrogen passivation of the *n*-GaN nanowire/*p*-Si heterointerface // Nanotechnology. 2020. Vol. 31. No. 24. P. 244003.

11. **Mozharov A. M., Fedorov V. V., Shugurov K. Y., Vorobyev A. A., Kudryashov D. A.** Study of the electrical properties of InAs nanowires/Si substrate for IR photodetector // Proceedings of The 20th International Conference Laser Optics (ICLO-2022). 20.06.2022–24.06.2022. Saint Petersburg, Russia. Institute of Electrical and Electronics Engineers Inc. 2022. P. 18.

12. **Бонч-Бруевич В. Л., Калашников С. Г.** Физика полупроводников. М.: Наука, 1977. 671 с.

13. **Shockley W.** The theory of *p–n* junctions in semiconductors and *p–n* junction transistors // Bell System Technical Journal. 1949. Vol. 28. No. 3. Pp. 435–489.

THE AUTHORS

DVORETCKAIA Liliya N.
Alferov University,
Peter the Great St. Petersburg Polytechnic University
8-3 Khlopin St., St. Petersburg, 194021, Russia
liliyabutler@gmail.com
ORCID:0000-0002-4172-940X

MOZHAROV Alexey M.
Alferov University,
Peter the Great St. Petersburg Polytechnic University
8-3 Khlopin St., St. Petersburg, 194021, Russia
alex000090@gmail.com
ORCID:0000-0002-8661-4083

GOLTAEV Aleksandr S.
Alferov University,
8-3 Khlopin St., St. Petersburg, 194021, Russia
goltaev@goltaev.ru
ORCID:0000-0001-8179-3169

FEDOROV Vladimir V.
Alferov University,
Peter the Great St. Petersburg Polytechnic University
8-3 Khlopin St., St. Petersburg, 194021, Russia
burunduk.uk@gmail.com
ORCID:0000-0001-5547-9387

MUKHIN Ivan S.
Alferov University,
Peter the Great St. Petersburg Polytechnic University
8-3 Khlopin St., St. Petersburg, 194021, Russia
imukhin@yandex.ru
ORCID:0000-0001-9792-045X

СВЕДЕНИЯ ОБ АВТОРАХ

ДВОРЕЦКАЯ Лилия Николаевна – *кандидат физико-математических наук, научный сотрудник Академического университета имени Ж. И. Алфёрова Российской академии наук, младший научный сотрудник Высшей инженерно-физической школы Санкт-Петербургского политехнического университета Петра Великого.*
194021, Россия, Санкт-Петербург, ул. Хлопина, 8, к. 3
liliyabutler@gmail.com
ORCID:0000-0002-4172-940X

МОЖАРОВ Алексей Михайлович – *кандидат физико-математических наук, старший научный сотрудник Академического университета имени Ж. И. Алфёрова Российской академии наук, старший научный сотрудник Национального центра качества и экспертизы Санкт-Петербургского политехнического университета Петра Великого.*
194021, Россия, Санкт-Петербург, ул. Хлопина, 8, к. 3
alex000090@gmail.com
ORCID:0000-0002-8661-4083

ГОЛТАЕВ Александр Сергеевич – *лаборант Академического университета имени Ж. И. Алфёрова Российской академии наук.*
194021, Россия, Санкт-Петербург, ул. Хлопина, 8, к. 3
goltaev@goltaev.ru
ORCID:0000-0001-8179-3169

ФЁДОРОВ Владимир Викторович – *кандидат физико-математических наук, старший научный сотрудник Академического университета имени Ж. И. Алфёрова Российской академии наук, старший научный сотрудник Высшей инженерно-физической школы Санкт-Петербургского политехнического университета Петра Великого.*
194021, Россия, Санкт-Петербург, ул. Хлопина, 8, к. 3
burunduk.uk@gmail.com
ORCID:0000-0001-5547-9387

МУХИН Иван Сергеевич – *кандидат физико-математических наук, заведующий лабораторией Академического университета имени Ж. И. Алфёрова Российской академии наук, профессор Высшей инженерно-физической школы Санкт-Петербургского политехнического университета Петра Великого.*

194021, Россия, Санкт-Петербург, ул. Хлопина, 8, к. 3

imukhin@yandex.ru

ORCID:0000-0001-9792-045X

Received 30.10.2023. Approved after reviewing 27.11.2023. Accepted 27.11.2023.

Статья поступила в редакцию 30.10.2023. Одобрена после рецензирования 27.11.2023. Принята 27.11.2023.

Original article
DOI: https://doi.org/10.18721/JPM.17105

OSCILLATIONS UNDER A NONLINEAR PARAMETRIC ACTION AND COMBINATIONS OF DELAYS

A. A. Alifov ✉

Mechanical Engineering Research Institute of the RAS, Moscow, Russia

✉ alishir@mail.ru

Abstract. The paper considers oscillations under nonlinear parametric action and combinations of delays in elasticity and damping. The model for the study is a rod with a spring, which is driven by an energy source of limited power. To solve nonlinear differential equations of motion of the system, the method of direct linearization of nonlinearity has been used. Equations were obtained for determining the nonstationary and stationary values of the amplitude and phase of oscillations, the speed of the energy source. Based on the Routh–Hurwitz criteria, the conditions for the stability of stationary motion modes were derived. To obtain information about the combined effect of delays on the dynamics of oscillations, the calculations were carried out for their various values, linear and nonlinear elastic forces. The graphs constructed based on the calculation results clearly show the combined effect of various delay values on the amplitude-frequency curves. The delays measure the amplitude curve, shift it to the right-left, up-down, and affect the stability of the oscillations.

Keywords: oscillation, model, nonlinearity, method, parametric excitation, delay, elasticity, damping

Citation: Alifov A. A., Oscillations under a nonlinear parametric action and combinations of delays, St. Petersburg State Polytechnical University Journal. Physics and Mathematics. 17 (1) (2024) 47–55. DOI: https://doi.org/10.18721/JPM.17105

Научная статья
УДК 534.16
DOI: https://doi.org/10.18721/JPM.17105

КОЛЕБАНИЯ ПРИ НЕЛИНЕЙНОМ ПАРАМЕТРИЧЕСКОМ ВОЗДЕЙСТВИИ И КОМБИНАЦИИ ЗАПАЗДЫВАНИЙ

А. А. Алифов ✉

Институт машиноведения им. А. А. Благонравова РАН, Москва, Россия

✉ alishir@mail.ru

Аннотация. В работе рассмотрены колебания при нелинейном параметрическом воздействии и комбинации запаздываний в упругости и демпфировании. Моделью является стержень с пружиной, приводимый в движение источником энергии ограниченной мощности. Для решения нелинейных дифференциальных уравнений движения системы использован метод прямой линеаризации нелинейности. Получены уравнения для определения нестационарных и стационарных значений амплитуды и фазы колебаний, скорости источника энергии. На основе критериев Рауса – Гурвица выведены условия устойчивости стационарных режимов движения. Проведены расчеты амплитудно-частотных характеристик при различных значениях параметров, линейной и нелинейной силах упругости. Соответствующие графики наглядно представляют совместное влияние различных значений запаздываний на амплитудно-частотные кривые. Показано, что запаздывания изменяют амплитудные кривые, существенно влияя на устойчивость колебаний.

Ключевые слова: колебания, модель, нелинейность, метод, параметрическое воздействие, запаздывание, упругость, демпфирование

Ссылка для цитирования: Алифов А. А. Колебания при нелинейном параметрическом воздействии и комбинации запаздываний // Научно-технические ведомости СПбГПУ. Физико-математические науки. 2024. Т. 17. № 1. С. 47–55. DOI: https://doi.org/10.18721/JPM.17105

Introduction

All phenomena in nature (the Universe) are cyclical, oscillatory motion occurs in all types of systems (physical, biological, technical, etc.) [1]. Excitation of oscillations can be caused by various reasons, including the presence of a delay in many systems [2, 3, etc.]. The appearance of delays in mechanical systems can be caused by the elasticity of materials and internal friction in them. Many studies considered time-delay systems [3–17, etc.], however, they did not take into account the properties of the source supplying energy to the system. Real physical systems function using some kind of energy source with limited power. This is scarcely addressed in the literature. Energy consumption issues, as well as related environmental and climate change issues, have now become particularly important.

In most cases, time-delay systems are analyzed based on nonlinear differential equations with a deviating argument. These equations are solved by various methods of nonlinear mechanics [18–20, etc.], characterized by high labor and time costs. The direct linearization method (DLM), described in [21–23] and other works, does not have these costs, which provides an advantage over known methods of nonlinear mechanics. Its essential properties are also simplicity and the possibility of obtaining finite ratios regardless of the degree of nonlinearity, which makes it easy to use it in practical calculations.

Many systems (pendulum with a vibrating pivot, shaft, driveshaft, gear train, railway bridge, etc.) experience parametric oscillations, which can be caused by both linear and nonlinear excitations. Parametric oscillations under linear and nonlinear (quadratic) excitations were considered in monograph [24].

The goal of this study is to analyze parametric oscillations taking into account the properties of the energy source, nonlinear parametric action (cubic) and the presence of delays in elasticity and friction.

Equations of the system and solutions

Let us take as a basis the model and equations (formulated assuming that oscillations of the rod taking the form of the first eigenmode of free bending oscillations), where the dynamics of the system is supported by a limited-power motor (Fig. 1) [25]. Taking into account the nonlinearity of parametric excitation as well as delays in elasticity and friction, we obtain the following equations of motion:

$$\begin{aligned} &\ddot{y}+\beta_1\dot{y}+\omega^2 y+by^3\sin\varphi=-m^{-1}f(y)-k_\eta\dot{y}_\eta-c_\tau y_\tau,\\ &J\ddot{\varphi}=M(\dot{\varphi})-0.5c_2y^2\cos\varphi-0.5c_3\sin 2\varphi-c_4\cos\varphi, \end{aligned} \tag{1}$$

where $\omega^2=\dfrac{c}{m}$, $c=\dfrac{\pi^4 EI_x}{2l^3}\left(1-\dfrac{P_0}{P_1}\right)$, $b=\dfrac{c_2}{m}$, $c_2=-\dfrac{\pi^2 r_1 c_1}{2l}$, $m=\dfrac{\rho l}{2}$, $\beta_1=\dfrac{\beta}{m}$, $P_0=f_0c_1$,

$P_1=\dfrac{\pi^2 EI_x}{l^2}$, $c_3=c_1r_1^2$, $c_4=f_0r_1c_1$.

The quantities ω, c, m, β, b, c_2, c_3, c_4, P_0, P_1 in Eqs. (1) are constant; c_1, β are the spring constant and the resistance coefficient; ρ is the mass per unit length of the rod; EI_x is the bending stiffness of the rod along the y axis; f_0 is the precompression on the spring; $f(y)$ is the nonlinear component of elasticity; $c_\tau = const$, $k_\eta = const$, $\dot{y}_\tau = y(t-\tau)$, $\dot{y}_\eta = y(t-\eta)$, $\tau = const$ and $\eta = const$ – are the delays; J is the moment of inertia of the motor rotor rotating the crank of radius r_1 connected to the spring; $M(\dot{\varphi})$ is the driving torque of the motor (taking into account the resistance forces); $\dot{\varphi}$ is the rotational speed of the motor.

In practice, representation of nonlinearity by means of a polynomial function has become widespread. Let us adopt it as the nonlinear component of the elastic force $f(y)$ in the form

$$f(y) = \sum_s \gamma_s y^s,$$

where $\gamma_s = const$, $s = 2, 3 \ldots$.

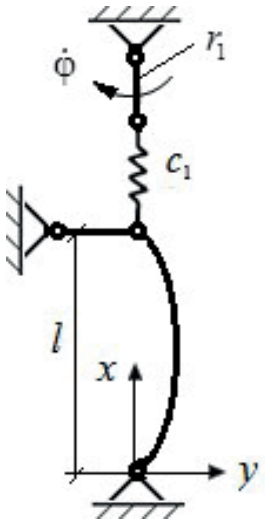

Fig. 1. Model of oscillatory system:
r_1 is the crank radius; l is the geometric size; c_1 is the spring constant; φ is the rotational speed of the motor

$$f_*(y) = B_f + c_f y.$$

Here B_f, c_f are the linearization coefficients defined by the expressions

$$\begin{aligned} B_f &= \sum_s N_s \gamma_s a^s, \ s = 2,4,6, \ \ldots \ (s \text{ is even}), \\ c_f &= \sum_s \bar{N}_s \gamma_s a^{s-1}, \ s = 3,5,7, \ \ldots \ (s \text{ is odd}), \end{aligned} \tag{2}$$

where $a = \max|y|$; $N_s = (2r + 1)/(2r + 1 + s)$, r is the linearization accuracy parameter, whose selection interval is unlimited but sufficient within 0–2.

Taking into account expressions (2), Eqs. (1) take the form

$$\begin{aligned} \ddot{y} + \beta_1 \dot{y} + \omega^2 y + b y^3 \sin\varphi &= -m^{-1}(B_f + c_f y) - k_\eta \dot{y}_\eta - c_\tau y_\tau, \\ J\ddot{\varphi} &= M(\dot{\varphi}) - 0.5 c_2 y^2 \cos\varphi - 0.5 c_3 \sin 2\varphi - c_4 \cos\varphi. \end{aligned} \tag{3}$$

To solve Eqs. (3), we apply the DLM and the procedure presented in [23] and other studies.

Using the functions

$$y = a\cos\psi,\ \ y_\tau = a\cos(\psi - p\tau),\ \ \dot{y}_\eta = -ap\sin(\psi - p\eta),\ \ \dot{\varphi} = \Omega,\ \ \psi = pt + \xi,\ \ p = \Omega/2,$$

we obtain the following equations for nonstationary motion:

$$\begin{gathered}\frac{da}{dt} = -\frac{a}{2}\left(\beta_1 + k_\eta\cos p\eta - 2c_\tau\Omega^{-1}\sin p\tau\right) + \frac{ba^3}{4\Omega}\cos 2\xi,\\ \frac{d\xi}{dt} = \frac{4\omega^2 - \Omega^2}{4\Omega} + \frac{c_f}{m\Omega} + \frac{1}{2}k_\eta\sin p\eta + \frac{c_\tau}{\Omega}\cos p\tau - \frac{ba^2}{2\Omega}\sin 2\xi,\\ \frac{d\Omega}{dt} = \frac{1}{J}\left[M(\Omega) - \frac{c_2a^2}{8}\right].\end{gathered} \tag{4}$$

The conditions $\dot{a} = 0,\ \dot{\xi} = 0,\ \dot{\Omega} = 0$, provide the following relations for stationary motion

$$\begin{gathered}4m^2A^2 + D^2 = 4m^2b^2a^4,\\ tg2\xi = -D/2mA,\\ M(\Omega) - S(a) = 0,\end{gathered} \tag{5}$$

where $A = 2\Omega(\beta_1 + k_\eta\cos p\eta) - 4c_\tau\sin p\tau,$

$D = m(4\omega^2 - \Omega^2) + 4c_f + 2m\Omega k_\eta\sin p\eta + 4mc_\tau\cos p\tau,\ \ S(a) = c_2a^2/8.$

The expression $S(a)$ represents the load on the energy source from the oscillatory system. The intersection points of the curves $M(\Omega)$ and $S(a)$ determine the speeds Ω.

Stability conditions

Stationary motions need to be analyzed for stability. Composing the equations in variations for Eqs. (4) and using the Routh–Hurwitz criteria, we obtain the conditions for the stability of στατιουαρψ oscillations:

$$D_1 > 0,\ D_3 > 0,\ D_1D_2 - D_3 > 0, \tag{6}$$

where $D_1 = -(b_{11} + b_{22} + b_{33}),\ D_2 = b_{11}b_{33} + b_{11}b_{22} + b_{22}b_{33} - b_{23}b_{32} - b_{12}b_{21} - b_{13}b_{31},$

$D_3 = b_{11}b_{23}b_{32} + b_{12}b_{21}b_{33} - b_{11}b_{22}b_{33} - b_{12}b_{23}b_{31} - b_{13}b_{21}b_{32},$

$b_{11} = \frac{1}{J}Q,\ b_{12} = -\frac{c_2a}{4J},\ b_{13} = 0,\ b_{21} = -\frac{a}{\Omega^2}c_\tau\sin p\tau - \frac{ba^3}{4\Omega^2}\cos 2\xi,$

$b_{22} = -\frac{1}{2}\left(\beta_1 + k_\eta\cos p\eta - 2c_\tau\Omega^{-1}\sin p\tau\right) + \frac{3ba^2}{4\Omega}\cos 2\xi,\ b_{23} = -\frac{ba^3}{2\Omega}\sin 2\xi,$

$b_{31} = -0{,}25 - \frac{\omega^2}{\Omega^2} - \frac{c_f}{m\Omega^2} - \frac{c_\tau}{\Omega^2}\cos p\tau + \frac{ba^2}{2\Omega^2}\sin 2\xi,\ b_{32} = \frac{1}{m\Omega}\frac{\partial c_f}{\partial a} - \frac{ba}{\Omega}\sin 2\xi,$

$b_{33} = -\frac{ba^2}{\Omega}\cos 2\xi,\ Q = \frac{d}{d\Omega}M(\Omega).$

The slope of the energy source characteristic $Q = dM/d\Omega$ makes it possible to determine the regions where the oscillations are stable or unstable.

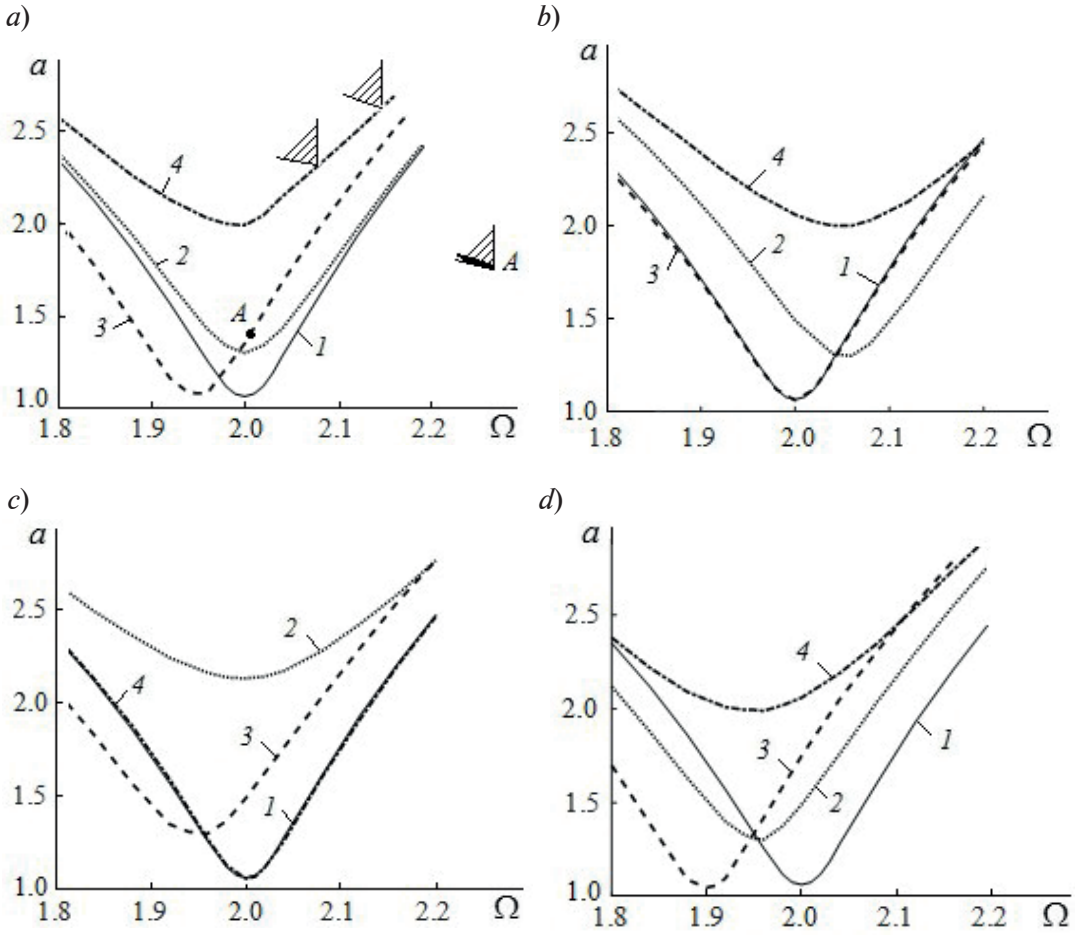

Fig. 2. Amplitude–frequency curves for the case of linear elastic force; $\gamma_3 = 0$; the values of the parameters $p\eta$ and $p\tau$ are varied. For comparison, the case with the absence of delays is given in all graphs ($k_\eta = 0$, $c_\tau = 0$, curves *1*).
The shaded sectors for the slope Q of the energy source characteristic (at point A and others) correspond to stable oscillations. Parameter values: $p\eta = 0$ (*a*), $\pi/2$ (*b*), π (*c*), $3\pi/2$ (*d*); $p_\tau = \pi/2$ (curves *2*), π (curves *3*), $3\pi/2$ (curves *4*)

Calculations performed and main results

Calculations were carried out to obtain information on the effect of nonlinear parametric effects and delays on the dynamics of oscillations. The nonlinear component of the elastic force was taken as

$$f(y) = \gamma_3 y^3,\ \gamma_3 = \pm 0.2\ \text{kgf} \cdot \text{cm}^{-3},$$

and the other parameters had the following values:

$$\omega = 1\ s^{-1},\ m = 1\ \text{kgf} \cdot \text{s}^2 \cdot \text{cm}^{-1},\ c_2 = 0.07\ \text{kgf} \cdot \text{cm}^{-1},$$

$$\beta = 0.02\ \text{kgf} \cdot \text{s} \cdot \text{cm}^{-1},\ k_\eta = 0.05\ \text{kgf} \cdot \text{s} \cdot \text{cm}^{-1},\ c_\tau = 0.05\ \text{kgf} \cdot \text{cm}^{-1}.$$

The following values were accepted for delays:

$$p\eta = 0,\ \pi/2,\ \pi,\ ;\ \ p\tau = 0,\ \pi/2,\ \pi, 3\pi/2.$$

The linearization coefficient $\bar{N}_3 = 3/4$, which corresponds to the linearization accuracy parameter $r = 1.5$.

All results calculated by the DLM completely coincide with those calculated by the widely used Bogolyubov–Mitropolsky asymptotic averaging method [18], as the number 3/4 is obtained using both methods.

Figs. 2–4 shows the amplitude–frequency curves $a(\Omega)$ for linear and nonlinear elastic forces (the quantities in the graphs are normalized). All graphs show different parameter values, and the solid curve *1*, which is given for comparison, corresponds to the absence of delays ($k_\eta = 0$, $c_\tau = 0$). Criteria (6) are satisfied within the shaded sectors (see Fig. 2) for the slope Q of the energy source characteristic, and stable fluctuations occur only in fairly narrow frequency ranges at

$$\gamma_3 = 0,\ k_\eta = 0,\ p\tau = \pi \text{ and } p\tau = 3\pi/2.$$

These sectors should be shown on the load curve $S(a)$ but for brevity they are shown instead on the amplitude–frequency curves. There is no stability in the cases when $\gamma_3 = \pm 0.2$ in the entire range of resonant frequencies for all delays considered.

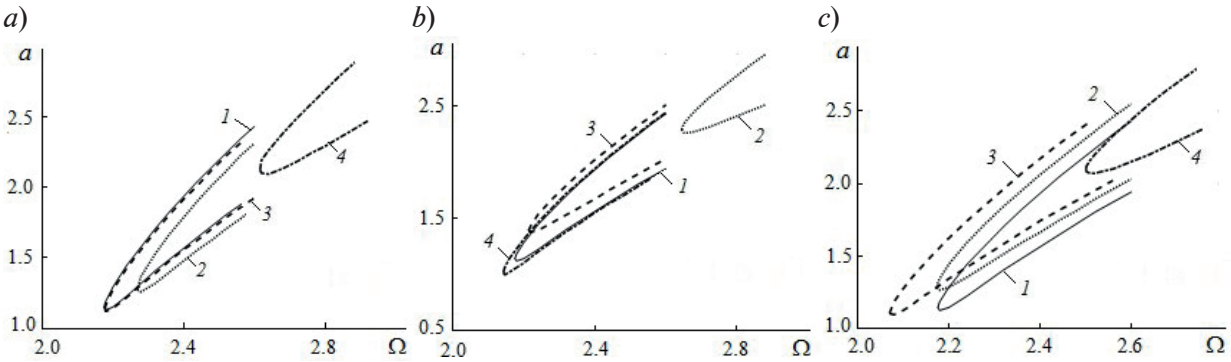

Fig. 3. Amplitude–frequency curves similar to those shown in Fig. 2 but with a nonlinear elastic force; $\gamma_3 = 0.2$. The numbering of the curves also corresponds to that in Fig. 2. Values of parameters $p\eta$: $\pi/2$ (*a*), π (*b*), $3\pi/2$ (*c*)

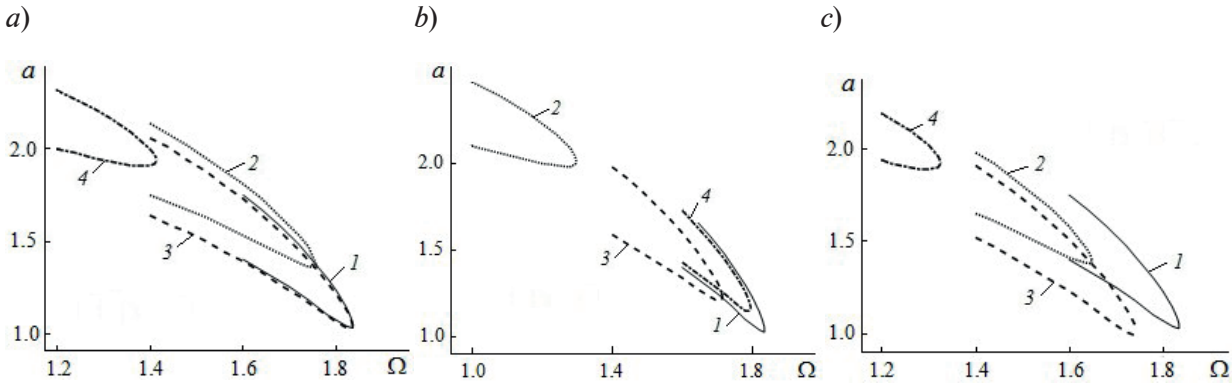

Fig. 4. Amplitude–frequency curves similar to those shown in Fig. 3, but $\gamma_3 = -0.2$. The numbering of the curves corresponds to that in Figs. 2 and 3. Values of parameters $p\eta$: $\pi/2$ (*a*), π (*b*), $3\pi/2$ (*c*)

Conclusion

The paper considers the dynamics of a rod with an energy source of limited power under nonlinear parametric action and a combination of delays in elasticity and damping. To obtain information about the effect of delays on the dynamics of the system, calculations were performed for stationary oscillations. The obtained results clearly illustrate the combined effect of various delays on the amplitude–frequency curves. Analysis of the obtained results allows to conclude that the delays have a significant impact on the picture of interactions:

they change the amplitude curve in the amplitude–frequency plane, shifting it right-left and up-down;

they affect the stability of oscillations.

The results of the analysis of the interaction of oscillatory systems with energy sources and the phenomena that arise in this case are described in detail in monographs [25, 26] and many other works on this area of oscillation theory. For this reason, we will not dwell on them and only note that similar effects are observed in the presence of delays.

REFERENCES

1. **Alifov A. A.,** The fundamental principle which operates the Universe, "Regular & Chaoitic Dynamics" Publishing, Moscow-Izhevsk, 2012 (in Russian).

2. **Tretyakova T. V., Wildemann V. E.,** Prostranstvenno-vremennaya neodnorodnost protsessov neuprugogo deformirovaniya metallov [Spatial-temporal inhomogeneity of the processes of inelastic deformation of metals], Fizmatlit Publishing, Moscow, 2017 (in Russian).

3. **Rubanik V. P.,** Kolebaniya kvazilineynykh sistem s zapazdyvaniyem [Oscillations of quasilinear systems having delay], Nauka Publishing, Moscow, 1969 (in Russian).

4. **Than V. Z., Dement'ev Ju. N., Goncharov V. I.,** Improving the accuracy calculation of time delay automatic control, Software & Systems. (3(31)) (2018) 521–526 (in Russian).

5. **Petrov N. N.,** Simple group pursuit subject to phase constraints and data delay, J. Comput. Syst. Sci. 57 (1) (2018) 37–42.

6. **Kornet M. E., Shishkina A. V.,** About non-parametric identification of infinitely fast systems with delay, Modern technologies. System analysis. Modeling. (3(59)) (2018) 16–23 (in Russian).

7. **Garkina I. A., Danilov A. M., Nashivochnikov V. V.,** Imitatsionnoye modelirovaniye dinamicheskikh sistem s zapazdyvaniyem [Imitative modeling of dynamic systems with delay], Modern Problems of Science and Education. (1-1) (2015) URL: https://science-education.ru/ru/article/view?id=18849 (date of application: 25.01.2024) (in Russian).

8. **Kashchenko S. A.,** Dynamics of a delay logistic equation with diffusion and coefficients rapidly oscillating in a space variable, Doklady Mathematics. 98 (2) (2018) 522–525.

9. **Mulyukov M. V.,** Asymptotic stability of a linear model of an oscillator with delayed feedback, Bulletin of Perm University. Mathematics. Mechanics. Computer Science. (4 (27)) (2014) 62–67 (in Russian).

10. **Gupta S. K., Wang J., Barry O. R.,** Nonlinear vibration analysis in precision motion stage with PID and time-delayed feedback controls, Nonlinear Dyn. 101 (2) (2020) 439–464.

11. **Santos T. L. M., Araujo J. M., Franklin T. S.,** Receptance-based stability criterion for second-order linear systems with time-varying delay, Mech. Syst. Signal Process. 110 (15 Sept) (2018) 428–441.

12. **Otto A., Just W., Radons G.,** Nonlinear dynamics of delay systems: an overview, Phil. Trans. R. Soc. A. 377 (2153) (2019) 20180389.

13. **Coccolo M., Zhu B., Sanjuán M. A. F., Sanz-Serna J. M.,** Bogdanov – Takens resonance in time-delayed systems, Nonlinear Dyn. 2018. 91 (3) (2018) 1939–1947.

14. **Sykora H.T., Sadeghpour M., Ge J.I., et al.,** On the moment dynamics of stochastically delayed linear control systems, Int. J. Robust Nonlinear Control. 30 (18) (2020) 8074–8097.

15. **Araujo J. M., Bettega J., Dantas N. J. B., et al.,** Vibration control of a two-link flexible robot arm with time delay through the robust receptance method, Appl. Sci. 11 (21) (2021) 9907.

16. **Liu C., Han M., Gong Z., Teo K. L,** Robust parameter estimation for constrained time-delay systems with inexact measurements, J. Ind. Manag. Optim. 17 (1) (2021) 317–337.

17. **Keller A. A.,** Time-delay systems with application to mechanical engineering process dynamics and control, Int. J. Math. Comput. Simul. 12 (June) (2018) 64–73.

18. **Bogoliubov N. N., Mitropolsky Y. A.,** Asymptotic methods in the theory of non-linear oscillations, CRC Press, Florida, USA, 1961.

19. **Butenin N. V., Neymark Yu. I., Fufayev N. A.,** Vvedeniye v teoriyu nelineynykh kolebaniy [Introduction to the theory of nonlinear oscillations], Nauka, Moscow, 1976 (in Russian).

20. **Chelomey V. N. (Chairman),** Vibratsii v technike: spravochnik [Vibrations in machinery: Handbook], in 6 Vols., Vol. 2; Edited by Blekhman I. I., Publishing House of Mechanical Engineering, Moscow, 1979 (in Russian).

21. **Alifov A. A.,** Metody pryamoy linearizatsii dlya rascheta nelineynykh system [Methods of direct linearization for calculation of nonlinear systems], Research Center "Regular and Chaotic Dynamics", Moscow, 2015 (in Russian).

22. **Alifov A. A.,** About calculation of oscillatory systems with limited excitement by methods of direct linearization, Engineering and Automation Problems. (4) (2017) 92–97 (in Russian).

23. **Alifov A. A.,** The interaction of mixed forced, parametric and self-excited oscillations at limited excitation and delays, St. Petersburg State Polytechnical University Journal. Physics and Mathematics. 16 (3) (2023) 39–48 (in Russian).

24. **Schmidt G., Schulz R.,** Parametererregte Schwingungen, Deutscher Verlag d. Wiss., VEB, Berlin, 1975.

25. **Kononenko V. O.,** Vibrating systems with limited power-supply, Iliffe, London, 1969.

26. **Alifov A. A., Frolov K. V.,** Interaction of nonlinear oscillatory systems with energy sources, Hemisphere Pub. Corp. Taylor & Francis Group, New York, 1990.

СПИСОК ЛИТЕРАТУРЫ

1. **Алифов А. А.** Фундаментальный принцип, управляющий Вселенной. Москва-Ижевск: НИЦ «Регулярная и хаотическая динамика», 2012. 408 с.

2. **Третьякова Т. В., Вильдеман В. Э.** Пространственно-временная неоднородность процессов неупругого деформирования металлов. М.: Физматлит, 2017. 120 с.

3. **Рубаник В. П.** Колебания квазилинейных систем с запаздыванием. М.: Наука, 1969. 288 с.

4. **Тхан В. З., Дементьев Ю. Н., Гончаров В. И.** Повышение точности расчета систем автоматического управления с запаздыванием // Программные продукты и системы. 2018. Т. 31. № 3. С. 521–526.

5. **Петров Н. Н.** Простое групповое преследование с фазовыми ограничениями и запаздыванием информации // Известия Российской академии наук. Теория и системы управления. 2018. № 1. С. 39–44.

6. **Корнет М. Е., Шишкина А. В.** О непараметрической идентификации безынерционных систем с запаздыванием // Современные технологии. Системный анализ. Моделирование. 2018. № 3 (59). С. 16–23.

7. **Гарькина И. А., Данилов А. М., Нашивочников В. В.** Имитационное моделирование динамических систем с запаздыванием // Современные проблемы науки и образования. 2015. № 1 (часть 1); URL: https://science-education.ru/ru/article/view?id=18849 (дата обращения: 25.01.2024).

8. **Кащенко С. А.** Динамика логистического уравнения с запаздыванием и диффузией и с быстро осциллирующими по пространственной переменной коэффициентами // Доклады Академии наук. 2018. Т. 482. № 5. С. 508–512.

9. **Мулюков М. В.** Устойчивость одной линейной модели осциллятора с запаздывающей обратной связью // Вестник Пермского университета. Математика. Механика. Информатика. 2014. № 4 (27). С. 62–67.

10. **Gupta S. K., Wang J., Barry O. R.** Nonlinear vibration analysis in precision motion stage with PID and time-delayed feedback controls // Nonlinear Dynamics. 2020. Vol. 101. No. 2. Pp. 439–464.

11. **Santos T. L. M., Araujo J. M., Franklin T. S.** Receptance-based stability criterion for second-order linear systems with time-varying delay // Mechanical Systems and Signal Processing. 2018. Vol. 110. 15 September. Pp. 428–441.

12. **Otto A., Just W., Radons G.** Nonlinear dynamics of delay systems: an overview // Philosophical Transactions of the Royal Society A. 2019. Vol. 377. No. 2153. Article ID: 20180389.

13. **Coccolo M., Zhu B., Sanjuбn M. A. F., Sanz-Serna J. M.** Bogdanov – Takens resonance in time-delayed systems // Nonlinear Dynamics. 2018. Vol. 91. No. 3. Pp. 1939–1947.

14. **Sykora H.T., Sadeghpour M., Ge J.I., et al.,** On the moment dynamics of stochastically delayed linear control systems, Int. J. Robust Nonlinear Control. 30 (18) (2020) 8074–8097.

15. **Araujo J. M., Bettega J., Dantas N. J. B., Dyrea C. E. T., Richiedei D., Tamellin I.** Vibration control of a two-link flexible robot arm with time delay through the robust receptance method // Applied Sciences. 2021. Vol. 11. No. 21. P. 9907.

16. **Liu C., Han M., Gong Z., Teo K. L.** Robust parameter estimation for constrained time-delay systems with inexact measurements // Journal of Industrial and Management Optimization. 2021. Vol. 17. No. 1. Pp. 317–337.

17. **Keller A. A.** Time-delay systems with application to mechanical engineering process dynamics and control // International Journal of Mathematics and Computers in Simulation. 2018. Vol. 12. June. Pp. 64–73.

18. **Боголюбов Н. Н., Митропольский Ю. А.** Асимптотические методы в теории нелинейных колебаний. М.: Наука, 1974. 504 с.

19. **Бутенин Н. В., Неймарк Ю. И., Фуфаев Н. А.** Введение в теорию нелинейных колебаний. М.: Наука, 1976. 384 с.

20. **Челомей В. Н.** (предс.). Вибрации в технике: Справочник. В 6 тт. Т. 2. Колебания нелинейных механических систем. Под ред. И. И. Блехмана. М.: Машиностроение, 1979. 351 с.

21. **Алифов А. А.** Методы прямой линеаризации для расчета нелинейных систем. Москва-Ижевск: НИЦ «Регулярная и хаотическая динамика», 2015. 74 с.

22. **Алифов А. А.** О расчете колебательных систем с ограниченным возбуждением методами прямой линеаризации // Проблемы машиностроения и автоматизации. 2017. № 4. С. 92–97.

23. **Алифов А. А.** Взаимодействие вынужденных, параметрических и автоколебаний при ограниченном возбуждении и запаздываниях // Научно-технические ведомости СПбГПУ. Физико-математические науки. 2023. Т. 16. № 3. С. 39–48.

24. **Шмидт Г.** Параметрические колебания. Пер. с нем. М.: Мир, 1978. 336 с.

25. **Кононенко В. О.** Колебательные системы с ограниченным возбуждением. М.: Наука, 1964. 236 с.

26. **Alifov A. A., Frolov K. V.** Interaction of nonlinear oscillatory systems with energy sources. New York: Taylor & Francis Group, 1990. 352 p.

THE AUTHORS

ALIFOV Alishir Ali
Mechanical Engineering Research Institute of the RAS
4 Malij Haritonjevskij lane, Moscow, 101000, Russia
alishir@mail.ru
ORCID: 0000-0003-2327-068X

СВЕДЕНИЯ ОБ АВТОРАХ

АЛИФОВ Алишир Али оглы – *доктор технических наук, главный научный сотрудник лаборатории динамических процессов Института машиноведения имени А. А. Благонравова Российской академии наук.*
101000, Россия, г. Москва, Малый Харитоньевский пер., 4
alishir@mail.ru
ORCID: 0000-0003-2327-068X

Received 08.11.2023. Approved after reviewing 24.11.2023. Accepted 24.11.2023.
Статья поступила в редакцию 08.11.2023. Одобрена после рецензирования 24.11.2023. Принята 24.11.2023.

EXPERIMENTAL TECHNIQUE AND DEVICES

Original article
DOI: https://doi.org/10.18721/JPM.17106

EFFECT OF SHIELD MAGNETIZATION ON VARIATIONS IN THE FREQUENCY OF ONBOARD RUBIDIUM ATOMIC CLOCKS

S. V. Ermak ✉, *V. V. Semenov, A. A. Baranov,*
M. A. Rogatin, M. V. Sergeeva
Peter the Great St. Petersburg Polytechnic University, St. Petersburg, Russia
✉ serge_ermak@mail.ru

Abstract. In the paper, the results of a study of the influence of the magnetic shield magnetization on the relative frequency instability of small-sized rubidium atomic clocks have been presented. The atomic clock was placed in a rotating magnetic field, simulating the magnetic situation in the orbit of a navigation satellite, moving in orbit and rotating around its own axis. The magnetization of the magnetic shield of the atomic clock was shown to increase its shielding factor. This result makes it possible to significantly reduce the influence of geomagnetic field variations on the frequency stability of onboard atomic clocks.

Keywords: atomic clock, magnetic field, magnetic shield, Allan deviation, navigation satellite

Funding: The reported study was funded by Russian Science Foundation (Grant No. 20-19-00146, https://rscf.ru/en/project/20-19-00146/).

Citation: Ermak S. V., Semenov V. V., Baranov A. A., Rogatin M. A., Sergeeva M. V., Effect of shield magnetization on variations in the frequency of onboard rubidium atomic clocks, St. Petersburg State Polytechnical University Journal. Physics and Mathematics. 17 (1) (2024) 56–63. DOI: https://doi.org/10.18721/JPM.17106

Научная статья
УДК 53.098
DOI: https://doi.org/10.18721/JPM.17106

ВЛИЯНИЕ НАМАГНИЧИВАНИЯ ЭКРАНА НА ВАРИАЦИИ ЧАСТОТЫ БОРТОВЫХ АТОМНЫХ ЧАСОВ

С. В. Ермак ✉, *В. В. Семенов, А. А. Баранов,*
М. А. Рогатин, М. В. Сергеева
Санкт-Петербургский политехнический университет Петра Великого,
Санкт-Петербург, Россия
✉ serge_ermak@mail.ru

Аннотация. В работе представлены результаты исследования влияния намагничивания магнитного экрана малогабаритных рубидиевых атомных часов на относительную нестабильность их частоты. Атомные часы размещались во вращающемся магнитном поле, имитирующем магнитную обстановку на орбите навигационного спутника, возникающую как при его орбитальном движении, так и в результате вращения спутника вокруг собственной оси. Показано, что намагничивание магнитного экрана атомных

часов увеличивает его коэффициент экранирования, что позволяет существенно снизить влияние вариаций геомагнитного поля на стабильность частоты атомных часов бортового базирования.

Ключевые слова: атомные часы, магнитное поле, магнитный экран, девиация Аллана, навигационный спутник

Финансирование: Работа выполнена при финансовой поддержке Российского научного фонда (РНФ), грант № 20-19-00146, https://rscf.ru/project/20-19-00146/

Ссылка для цитирования: Ермак С. В., Семенов В. В., Баранов А. А., Рогатин М. А., Сергеева М. В. Влияние намагничивания экрана на вариации частоты бортовых атомных часов // Научно-технические ведомости СПбГПУ. Физико-математические науки. 2024. Т. 17. № 1. С. 56–63. DOI: https://doi.org/10.18721/JPM.17106

Introduction

As a mobile charge carrier moves in a geomagnetic field (for example, a navigation satellite in near-Earth orbit), the geomagnetic field vector changes its direction relative to the optical axis of the onboard rubidium atomic clock (AC), which generates their orientation error due to the difference in the longitudinal and transverse shielding factors of the magnetic shield [1]. The magnitude of this error is determined by the quadratic term in the dependence expressing the relationship between the resonant frequency of the atoms of the working substance ν and the strength of the working magnetic field H inside the shield. This relationship is expressed as [2]:

$$\nu = \nu_0 + \beta H^2, \quad (1)$$

where ν_0 is the frequency of the atomic transition, $\nu_0 = 6.835 \cdot 10^6$ Hz; β is the scale factor, $\beta = 0.0905$ Hz·m^2/A^2 for rubidium-87 atoms.

It follows from expression (1) that relative instability of the AC frequency at the level of 10^{-12} for $H = 8$ A/m and operation in a geomagnetic field on the Earth's surface ($H_E = 40$ A/m) can be achieved for a rubidium-87 AC with the shielding factor of the magnetic shield exceeding 10^4. However, as the direct experiment described in [3] shows, the longitudinal (directed along the optical axis of the AC) shielding factor of the magnetic shield in rubidium AC is orders of magnitude less than this value (due to the presence of seams and holes in the shields). For example, according to [1], the ratio of the longitudinal to transverse shielding factors for miniature AC with a volume of less than 3 cm^3 reaches 10^4. The absolute values of these coefficients are determined not only by the size and shape of the magnetic shield, but also by its magnetic permeability. The value of this parameter, in turn, significantly depends on the external magnetic field, which determines the change in the shielding properties of the magnetic shield during its magnetization.

The goal of this paper was to experimentally study the effect of magnetization of a magnetic shield by an external magnetic field on the relative short-term frequency instability of small-sized rubidium atomic clocks under an alternating magnetic field simulating the geomagnetic situation in the orbit of navigation satellites.

Experimental procedure and results

The experimental evaluation of AC frequency shifts under optical pumping of rubidium vapor was carried out in a rotating magnetic field with a setup similar to the one whose block diagram and measurement technique were described in detail in [3, 4].

The setup contained a magnetic system comprising three pairs of Helmholtz rings, with small-sized rubidium AC placed in the center (their linear dimensions were 75 × 75 × 35 mm), connected to a frequency detector. A working magnetic field with a strength of about 8 A/m was generated inside the magnetic shield. A rotating magnetic field H_r was generated in the plane of

the optical axis of the AC; its amplitude was selected in the range of geomagnetic field strengths (in A/m) in the orbit of satellite navigation systems. Relative variations in the frequency of the AC were measured using a frequency comparator; a stationary configuration of the rubidium AC whose relative instability was 10^{-13} per 100 s was used as a reference. In addition to the relative variations in the frequency of the AC, the dependence of the Allan deviation on the measurement time was recorded.

At the preliminary stage, we obtained an experimental estimate of the longitudinal shielding factor of the AC magnetic shield. For this purpose, compensation of the vertical component of the Earth's magnetic field, amounting to approximately 36 A/m, was performed using a magnetic system. The longitudinal factor of AC shielding was estimated in the presence of a residual horizontal component of the Earth's magnetic field by measuring relative frequency shifts of the AC at the strengths of the magnetic field of 40 and 56 A/m along the optical axis as well as with a sequential change of its polarity. Fig. 1 shows the relative frequency shifts of the AC (the difference $\Delta\nu$ between the frequency standard and the AC considered) measured in the presence of an external magnetic field H.

The obtained values of the relative frequency shift of the AC (see Fig. 1) allowed to estimate the weighted average longitudinal shielding factor, amounting to about 600. The small-sized rubidium AC selected for the study, which, as measurements showed, had a low longitudinal shielding factor, made it possible to better illustrate the influence of the external magnetizing field H_{ex} on the shielding properties of the magnetic shield.

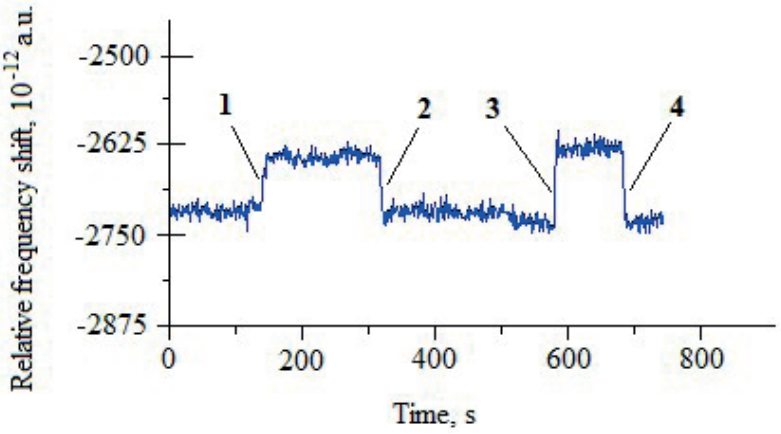

Fig. 1. Relative frequency shifts $\Delta\nu$ of the atomic clock under an external magnetic field H, A/m: −40 (*1*), +40 (*2*), −56 (*3*), +56 (*4*). Corresponding shifts $\Delta\nu$, 10^{-11}: +8 (*1*), −8 (*2*), +10 (*3*), −10 (*4*)

As noted above, the influence of the external magnetic field strength on the shielding properties of magnetic shields is due to a change in the magnetic permeability of their material [5]. For this reason, the choice of material for layers of multilayer magnetic shields (especially the material of the outer layer) of the AC should take into account the magnetic environment where it is planned to use the AC. For example, the magnetic field strength in the orbit of navigation satellites (altitude is about 20,000 km) turns out to be an order of magnitude less than the magnetic field strength on the Earth's surface [6].

As satellite navigation systems travel in orbit, a change in the orientation of the geomagnetic field vector relative to the optical axis of the onboard AC occurs automatically every half-period of the satellite's rotation in orbit, i.e., in the time instants when the orientation error of the AC is manifested to the greatest extent. The half-life of the satellite's rotation lies in the range of values from 5 to 7 hours for different satellite navigation systems, which does not exclude the inversion of the geomagnetic field vector with respect to the optical axis of the AC in shorter time intervals. A similar situation arises under rotation of the satellite relative to its own axis, which causes the corresponding orientation error of the onboard AC.

This particular rotation case was investigated in experiments with AC under conditions simulating the magnetic environment in the satellite orbit at a fixed angular rotation frequency

f_m = 0.01 Hz. The variation in the field generated by the magnetic system was carried out by a sinusoidal law with an amplitude H_r = 2.5 A/m in the plane of the optical axis of the AC. The degree of influence of the rotating magnetic field on the frequency of the AC was determined due to the Allan deviation property, which reaches a maximum value during the measurement time equal to the half-period of the rotating magnetic field [1].

In the absence of an external rotating magnetic field (H_r = 0), the Allan deviation decreased in direct proportion to the square root of the measurement time (by the law $\tau^{1/2}$), which is characteristic for rubidium AC with stationary position.

Fig. 2 shows the dependences of Allan deviations of the atomic clock frequency on the measurement time in the range of 1–100 s. This time range was chosen to reduce the influence of flicker processes on the measurement results. In this case, the Allan deviation was $1.6 \cdot 10^{-12}$ at a measurement time of 50 s.

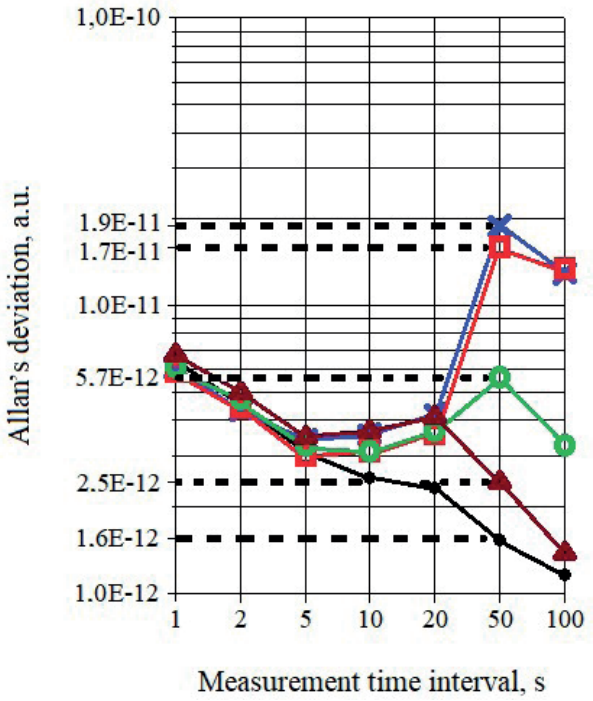

Fig. 2. Experimental dependences of Allan deviations (symbols) on the measurement time, with varying values of the external rotating (H_r) and constant magnetizing (H_{ex}) fields (in A/m): $H_r = H_{ex} = 0$ (black curve); H_r = 2.5 (all other curves); H_{ex} = 0 (black and blue curves), 4.2 (red curve), 8.5 (green), 12.8 (brown). (see Table)

The introduction of an external rotating magnetic field led to a significant change in the nature of the dependence of the Allan deviation on the measurement time: the deviation increased to the level of $1.9 \cdot 10^{-11}$ at τ = 50 s. All three components of the Earth's magnetic field were pre-compensated to preserve experimental validity. A rotating field H_r was applied in the first experiment, and there was no constant magnetizing field H_{ex} oriented along the optical axis of the AC (see Fig. 2, crosses and blue lines).

Fig. 2 also shows the results of subsequent experiments: the dependence of the Allan deviation of the AC frequency on the measurement time in the presence of two magnetic fields: H_r and H_{ex}, with the latter amounting to 4.2, 8.5 and 12.8 A/m, marked with different symbols and lines of different colors. The Allan deviation for the averaging time of 50 seconds was (10^{-12}): 17.0, 5.7 and 2.5, respectively. A certain increase in the value of the Allan deviation for a measurement time of 20 s is due to the peculiarities of the operation of the AC thermostat.

Table

Dependences of Allan deviation on range of measurement time τ at fixed amplitude of external rotating magnetic field and different values of constant magnetizing field Hex (see Fig. 2)

τ, s	Allan deviation, 10^{-12}, for H_{ex} (in A/m)			
	0.0	4.2	8.5	12.8
1	6.0	5.9	6.1	6.8
2	4.3	4.5	4.8	5.0
5	3.4	3.0	3.3	3.5
10	3.5	3.2	3.2	3.7
20	4.2	3.6	3.7	4.1
50	19.0	17.0	5.7	2.5
100	13.0	14.0	3.3	1.4

Note. The amplitude of the rotating external magnetic field H_r = 2.5 A/m.

Table compares the obtained values of the Allan deviation for the dependences shown in Fig. 2.

As follows from the above experimental data, magnetization of the magnetic shield can significantly increase the shielding factor of the AC, while the suppression of magnetic variations is manifested to a greater extent with a decrease in the intensity of the alternating magnetic field H_r, simulating the magnetic situation in the orbit of a navigation satellite. According to the data given in Table, the variations in the external magnetic field were suppressed by about 8 times in the magnetized shield of small-sized rubidium AC at an averaging time of 50 s and at H_r = 2.5 A/m.

If the magnetization field is oriented perpendicular to the optical axis of the AC, the order of Allan deviations and the dynamics of their variations with increasing averaging time are similar to the case of longitudinal orientation of the magnetizing field.

The dependence of the Allan deviation on the strength of the magnetizing field H_{ex} is notable in that it is similar to the initial segment of the curve expressing the dependence of magnetic permeability of the ferromagnetic material (permalloy) used in the magnetic shield on H_{ex} [5]. Interestingly, the magnetic field strength H_{ex} = 12.8 A/m, at which the stability of the AC can be increased by about 8 times, corresponds to a region where the magnetic permeability μ is significantly (by orders of magnitude) higher than its initial value corresponding to zero magnetic field H_{ex}.

Conclusion

Analysis of the results obtained in the experimental study allows to draw the following conclusions:

1. The shielding factor of the magnetic shield significantly depends on the magnitude of the external magnetic field where the small-sized rubidium AC is located. The obtained value of the longitudinal shielding factor increased by about 8 times for the magnetizing field strength of 12.8 A/m and the amplitude of the external rotating magnetic field of 2.5 A/m, corresponding to the geomagnetic field in the orbit of the navigation satellite.

2. The effect of increasing the shielding factor of the magnetic shield is practically independent of the direction of the applied constant magnetizing field Hex (relative to the optical axis of the AC), suggesting an isotropic nature of the influence of this field on the stability of the measured frequency.

3. Exceeding the threshold value of the external magnetic field strength (several to tens of A /m) corresponding to the maximum value of the magnetic permeability of the magnetic shield material may lead to a decrease in its shielding factor, and, consequently, to a deterioration in the stability of the AC frequency.

The experience accumulated in experiments with industrial small-sized rubidium AC can be valuable for developing rubidium AC for small satellites [7] as well as for a wide class of AC using magnetic shielding from an external magnetic field. Such devices include small-sized hydrogen masers [8], miniature AC based on the effect of coherent population trapping [9] as well as atomic-beam quantum frequency standards [10].

Predicting the optimal value of the magnetizing field strength in these devices is a rather complex problem, sing a number of factors have to be taken into account (type of AC, working magnetic field, material, shape and size of the shield).

Therefore, it is preferable to select the strength of the constant magnetizing field Hex empirically for each specific case, which was accomplished in this paper.

REFERENCES

1. **Donley E. A., Hodby E., Hollberg L., Kitching J.,** Demonstration of high-performance compact magnetic shields for chip-scale atomic devices, Rev. Sci. Instrum. 78 (8) (2007) 083102.

2. **Riehle F.,** Frequency standards: Basics and applications, Wiley-VCH, Weinheim, 2005.

3. **Lozov R. K., Ermak S. V., Semenov V. V., Ermak O. V.,** Modeling the geomagnetic field influence on the atomic clock accuracy of the satellite navigation systems on-board equipment, Journal Radioengineering. 83 (12 (20)) (2019) 32–37 (in Russian).

4. **Ermak S., Semenov V.,** The influence of the operation magnetic field modulation on the short-term frequency stability of rubidium atomic clock at magnetic gradient, Proc. 2022 Int. Conf. on Electrical Engineering and Photonics (EExPolytech), 20–21 Oct., St. Petersburg (2022) 347–350.

5. **Chikazumi S.,** Physics of ferromagnetism, Oxford University Press, Inc., Int. Series of monographs in Physics, Vol. 94. New York, 1997.

6. World magnetic model 2020 calculator, URL: http://www.geomag.bgs.ac.uk/data_service/models_compass/wmm_calc.html (Access data: 16.05.2023).

7. **Dinkelaker A. N., Kaparthy A., Reher S. E., Krutzik M.,** Optical quantum technologies for compact rubidium vapor-cell frequency standards in space using small satellites, J. Br. Interplanet. Soc. 72 (3) (2019) 74–82.

8. **Sysoyev V. P., Samokhvalov Yu. S., Vasiliev V. I., et al.,** Compact active hydrogen frequency standard, Al'manac of Modern Metrology. 4 (32) (2022) 8–17 (in Russian).

9. **Palchikov V. G.,** Sverkh-miniatyurnyy kvantovyy standart chastoty na KPN effekte [Subminiature quantum frequency standard based on the CPT effect], Abstracts of the Tenth All-Russian Conference with International Participation: "Fundamental and Applied Coordinate-Time and Navigation Support" (CTNS-2023), Apr. 17–21, 2023, St. Petersburg (2023) 141–142 (in Russian).

10. **Xie W., Wang Q., He X., et al.,** Frequency instability of a miniature optically pumped cesium-beam atomic frequency standard, Rev. Sci. Instrum. 91 (7) (2020) 074705.

СПИСОК ЛИТЕРАТУРЫ

1. **Donley E. A., Hodby E., Hollberg L., Kitching J.** Demonstration of high-performance compact magnetic shields for chip-scale atomic devices // Review of Scientific Instruments. 2007. Vol. 78. No. 8. P. 083102.

2. **Рилe Ф.** Стандарты частоты. Принципы и приложения. Пер. с англ. М.: Физматлит, 2009. 512 с.

3. **Лозов Р. К, Ермак С. В., Семенов В. В., Ермак О. В.** Моделирование влияния геомагнитного поля на точность атомных часов бортовой аппаратуры систем спутниковой навигации // Радиотехника. 2019. Т. 83. № 12 (20). С. 32–37.

4. **Ermak S., Semenov V.** The influence of the operation magnetic field modulation on the short-term frequency stability of rubidium atomic clock at magnetic gradient // Proceedings of 2022 International Conference on Electrical Engineering and Photonics (EExPolytech), 20–21 October, 2022. St. Petersburg. Pp. 347–350.

5. **Тикадзуми С.** Физика ферромагнетизма. Магнитные характеристики и практические применения. М.: Мир, 1987. 420 с.

6. World magnetic model 2020 calculator. Режим доступа: http://www.geomag.bgs.ac.uk/data_service/models_compass/wmm_calc.html (Дата обращения: 16.05.2023).

7. **Dinkelaker A. N., Kaparthy A., Reher S. E., Krutzik M.** Optical quantum technologies for compact rubidium vapor-cell frequency standards in space using small satellites // Journal of the British Interplanetary Society. 2019. Vol. 72. No. 3. Pp. 74–82.

8. **Сысоев В. П., Самохвалов Ю. С., Васильев В. И., Нагирный В. П., Нестеров Н. И., Парехин Д. А., Овчинников С. Н.** Малогабаритный активный водородный стандарт частоты // Альманах современной метрологии. 2022. № 4 (32). С. 8–17.

9. **Пальчиков В. Г.** Сверхминиатюрный квантовый стандарт частоты на КПН-эффекте // Тезисы докладов Десятой всероссийской конференции с международным участием: «Фундаментальное и прикладное координатно-временное и навигационное обеспечение» (КВНО-2023), 17–21 апреля 2023 г., Санкт-Петербург. С. 141–142.

10. **Xie W., Wang Q., He X., Chen N., Xiong Z., Fang S., Qi X., Chen X.** Frequency instability of a miniature optically pumped cesium-beam atomic frequency standard // Review of Scientific Instruments. 2020. Vol. 91. No. 7. P. 074705.

THE AUTHORS

ERMAK Sergey V.
Peter the Great St. Petersburg Polytechnic University
29 Politechnicheskaya St., St. Petersburg, 195251, Russia
ermak_sv@spbstu.ru
ORCID: 0000-0002-6210-4003

SEMENOV Vladimir V.
Peter the Great St. Petersburg Polytechnic University
29 Politechnicheskaya St., St. Petersburg, 195251, Russia
vladimir_semenov@mail.ru
ORCID: 0000-0003-0346-8349

BARANOV Alexey A.
Peter the Great St. Petersburg Polytechnic University
29 Politechnicheskaya St., St. Petersburg, 195251, Russia
79111700994@ya.ru
ORCID: 0000-0001-7095-7981

ROGATIN Maxim A.
Peter the Great St. Petersburg Polytechnic University
29 Politechnicheskaya St., St. Petersburg, 195251, Russia
maxim228rog@mail.ru
ORCID: 0009-0009-6180-6538

SERGEEVA Maria V.
Peter the Great St. Petersburg Polytechnic University
29 Politechnicheskaya St., St. Petersburg, 195251, Russia
mamarvel2001@mail.ru
ORCID: 0009-0005-8838-6845

СВЕДЕНИЯ ОБ АВТОРАХ

ЕРМАК Сергей Викторович – *доктор физико-математических наук, профессор Высшей школы прикладной физики и космических технологий Санкт-Петербургского политехнического университета Петра Великого, Санкт-Петербург, Россия.*
195251, Россия, г. Санкт-Петербург, Политехническая ул., 29
ermak_sv@spbstu.ru
ORCID: 0000-0002-6210-4003

СЕМЕНОВ Владимир Васильевич – *доктор физико-математических наук, ведущий научный сотрудник Высшей школы прикладной физики и космических технологий Санкт-Петербургского политехнического университета Петра Великого, Санкт-Петербург, Россия.*
195251, Россия, г. Санкт-Петербург, Политехническая ул., 29
vladimir_semenov@mail.ru
ORCID: 0000-0003-0346-8349

БАРАНОВ Алексей Анатольевич – *кандидат физико-математических наук, научный сотрудник Высшей школы прикладной физики и космических технологий Санкт-Петербургского политехнического университета Петра Великого, Санкт-Петербург, Россия.*
195251, Россия, г. Санкт-Петербург, Политехническая ул., 29
79111700994@ya.ru
ORCID: 0000-0001-7095-7981

РОГАТИН Максим Александрович – *инженер Высшей школы прикладной физики и космических технологий Санкт-Петербургского политехнического университета Петра Великого, Санкт-Петербург, Россия.*
195251, Россия, г. Санкт-Петербург, Политехническая ул., 29
maxim228rog@mail.ru
ORCID: 0009-0009-6180-6538

СЕРГЕЕВА Мария Вячеславовна – *инженер Высшей школы прикладной физики и космических технологий Санкт-Петербургского политехнического университета Петра Великого, Санкт-Петербург, Россия.*
195251, Россия, г. Санкт-Петербург, Политехническая ул., 29
mamarvel2001@mail.ru
ORCID: 0009-0005-8838-6845

Статья поступила в редакцию 07.12.2023. Одобрена после рецензирования 12.12.2023. Принята 12.12.2023.
Received 07.12.2023. Approved after reviewing 12.12.2023. Accepted 12.12.2023.

PHYSICAL ELECTRONICS

Original article
DOI: https://doi.org/10.18721/JPM.17107

CURRENT AND SPEED CHARACTERISTICS OF ELECTRON FLOWS FORMED BY THE ELECTRON-OPTICAL SYSTEM WITH A MULTI-TIP FIELD EMITTER

E. P. Taradaev ✉, *G. G. Sominskii*, *S. P. Taradaev*

Peter the Great St. Petersburg Polytechnic University, St. Petersburg, Russia

✉ evgeny_tar@hotmail.com

Abstract. The article presents the results of studies of the characteristics of electron flows generated by an electron-optical system with a multi-tip field emitter. Information has been obtained on important beam parameters: the beam current, electron velocity spectrum, pitch factor. The spread in transverse velocity did not exceed 50% in the studied modes. The shape of the spectra did not depend on the magnitude of the magnetic field and did only weakly on the current in the beam.

Keywords: field emission, multi-tip field emitter, electron flow, velocity spread

Funding: The reported study was funded by Russian Science Foundation (Grant No. 23-29-00224).

Citation: Taradaev E. P., Sominskii G. G., Taradaev S. P., Current and speed characteristics of electron flows formed by the electron-optical system with a multi-tip field emitter, St. Petersburg State Polytechnical University Journal. Physics and Mathematics. 17 (1) (2024) 64–70. DOI: https://doi.org/10.18721/JPM.17107

Научная статья
УДК 537.533
DOI: https://doi.org/10.18721/JPM.17107

ТОКОВЫЕ И СКОРОСТНЫЕ ХАРАКТЕРИСТИКИ ЭЛЕКТРОННЫХ ПОТОКОВ, ФОРМИРУЕМЫХ ЭЛЕКТРОННО-ОПТИЧЕСКОЙ СИСТЕМОЙ С МНОГООСТРИЙНЫМ ПОЛЕВЫМ ЭМИТТЕРОМ

Е. П. Тарадаев ✉, *Г. Г. Соминский*, *С. П. Тарадаев*

Санкт-Петербургский политехнический университет Петра Великого,
Санкт-Петербург, Россия

✉ evgeny_tar@hotmail.com

Аннотация. В статье представлены результаты исследований характеристик электронных потоков, формируемых электронно-оптической системой с многоострийным полевым эмиттером. Была получена информация о важных параметрах пучка: токе в пучке, спектре скоростей электронов, питч-факторе. Разброс по поперечной скорости не превышал 50% в исследованных режимах. Форма спектров не зависела от величины магнитного поля и проявляла лишь слабую зависимость от тока в пучке.

Ключевые слова: полевая эмиссия, многоострийный полевой эмиттер, электронный поток, скоростной разброс

Финансирование: Работа выполнена при финансовой поддержке гранта Российского научного фонда № 23-29-00224.

Ссылка для цитирования: Тарадаев Е. П., Соминский Г. Г., Тарадаев С. П. Токовые и скоростные характеристики электронных потоков, формируемых электронно-оптической системой с многоострийным полевым эмиттером // Научно-технические ведомости СПбГПУ. Физико-математические науки. 2024. Т. 17. № 1. С. 64–70. DOI: https://doi.org/10.18721/JPM.17107

Introduction

One of the practically important directions in the development of modern microwave electronics is the creation and improvement of subterahertz radiation sources driven by electron beams (see, for example, [1–3]). In this paper, we consider the possibilities of using field emitters to form electron flows with annular cross-section, necessary for miniature but high-voltage devices of this frequency range. The field emitters developed [4–9] have obvious advantages over hot cathodes, since they do not require heating and provide rapid (practically inertialess) on/off switching of the electron source.

However, the development of electron-optical systems (EOS) with field emitters is difficult due to the lack of information about the characteristics of electron flows that they generate. We previously conducted an experimental study of the spatiotemporal and velocity characteristics of electron flows in EOS with field emitters whose electrode configuration is typical for gyrotron-type devices [10]. However, the measurements were performed only at low magnetic fields not exceeding 0.1 T.

In this paper, we investigate the characteristics of electron flows generated in the EOS with multi-tip field emitters in significantly higher magnetic fields (approximately up to 2.5 T), typical for gyrotron devices of the sub-THz range.

Experimental procedure and instrumentation

The cross-sectional view of the EOS used to measure the characteristics of electron flows is shown schematically in Fig. 1.

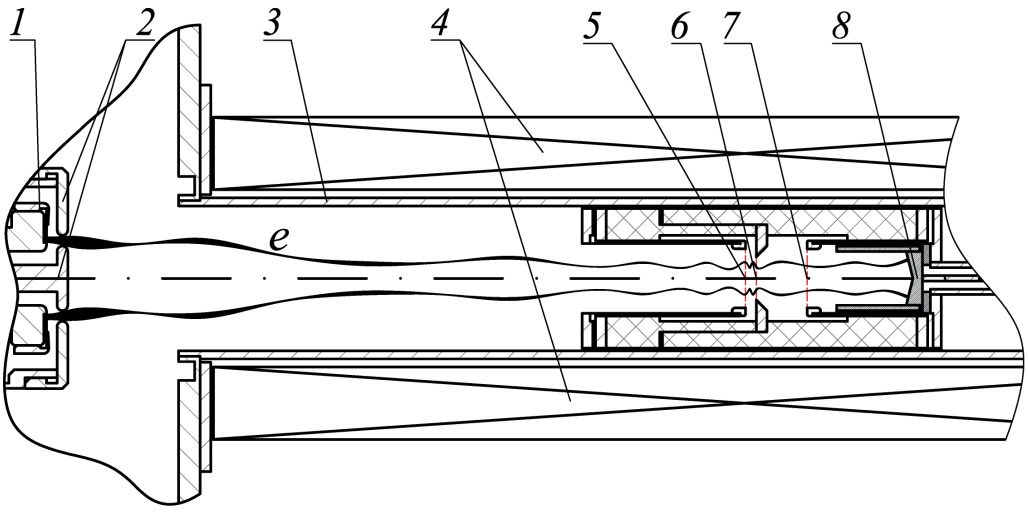

Fig. 1. Schematic of electron-optical system (EOS) with a retarding field analyzer (installed in the center of the solenoid):
cathode system *1*; control electrode with annular aperture *2*; channel *3* for electron beam transport (*e*); solenoid *4*; protective grids *5*, *7*; retarding grid *6*; electron collector *8*

The dimensions of the main parts of the EOS and the analyzer are shown in Table. Magnetic field pulses with a duration of 10 ms were generated using a solenoid to compress and confine the electron flow. To ensure field emission, a pulse of negative (relative to the grounded control electrode) voltage U with an amplitude up to 15 kV was applied to the cathode. The pulse duration was varied from 10 to 100 μs.

Table

Main geometric parameters of electron-optical system (see Fig. 1)

Element	Parameter	Size, mm
Cathode system *1*	Distance between control electrode *2* and cathode *1*	2.00
	Aperture width in control electrode *2*	2.00
	Average diameter of field emitter	14.0
	Width of field emitter	0.65
	Tip height and distance between tips	0.03
Solenoid *4*	Coil diameter:	
	external	42
	internal	30
	Length of solenoid *4*	200
Electron velocity analyzer	Distance between protective (*5*) and retarding (*6*) grids	2

A magnetic field was applied, increasing from a minimum B_c at the cathode to a maximum B_m in the center of the solenoid. The maximum value of the magnetic flux density B_m varied from 0.1 to 2.5 T. The magnetization reversal coefficient $k = B_m/B_c$ could be adjusted by moving the solenoid along the axis. The current I of electrons in the beam and the longitudinal component of the electron velocity $V_{||}$ (directed along the magnetic field lines) were experimentally measured; the transverse component of the velocity $V_{\perp}$ (directed perpendicular to the field lines) was calculated using a previously developed technique [10].

The electron velocities were determined by the retarding field method using the analyzer (see Fig. 1 and Table). The analyzer was placed in the region of magnetic field uniform along the axis, near the central plane of the solenoid section. The delay curves (dependences of the current I of the electrons passing to collector 8 of the analyzer on the magnitude of the retarding negative (relative to the ground) voltage U_r, applied to grid *6*) were measured. Since electrons with the velocity $V_{||} < (2eU_r/m_e)^{1/2}$ do not fall into collector 8, the resulting delay curve $I(U_r)$ was reconstructed in the coordinates $I(V_{||})$.

The spectrum of longitudinal electron velocities $V_{||}$ was obtained by differentiating the curve $I(V_{||})$. The transverse velocity spectrum $V_{\perp}$ was determined taking into account the information about the total energy eU of electrons in the beam and the data obtained on the distribution of electron velocities in the longitudinal direction.

Before taking measurements, the cathode was trained with current sampling up to 20–25 mA for a time of up to ten hours. The operation of the electronic flow generation system was stabilized.

Results and discussion

The electron source operated stably under technical vacuum in the entire studied range of beam currents (the pressure was approximately 10^{-7} Torr). After the training was completed, the variation in the beam current in a single pulse did not exceed 1%.

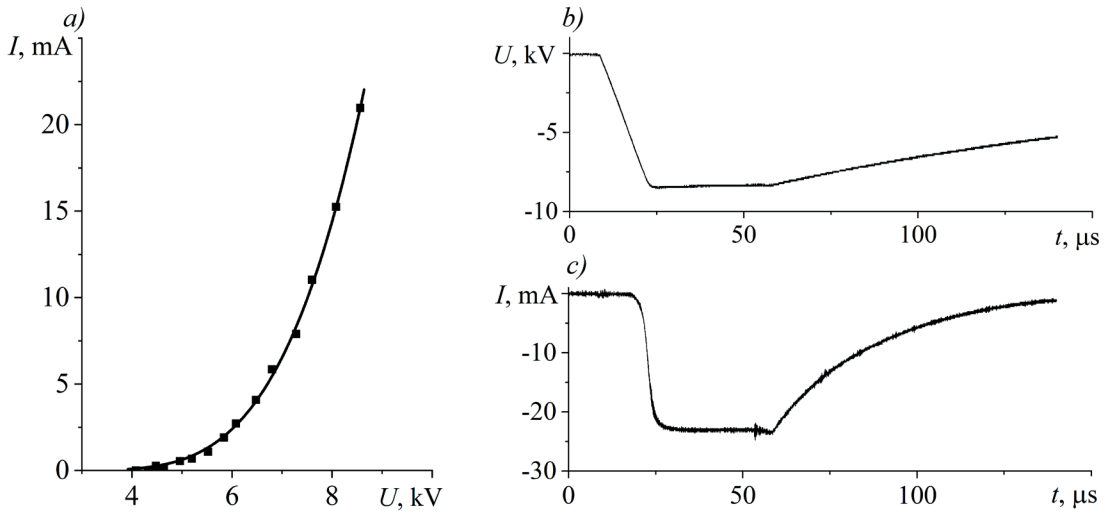

Fig. 2. Measured characteristics of the EOS: voltage characteristic (*a*); waveforms of cathode voltage and the current in the collector, respectively (*b*, *c*)

Fig. 2 shows the current–voltage characteristic of the studied EOS as well as waveforms of voltage pulses and electron current to the analyzer collector. The EOS made it possible to obtain beam currents over 20 mA in the modes considered.

Figs. 3 and 4 illustrate the main results of the analysis of electron velocity spectra in the flow generated by the electron gun with the multi-tip field emitter. Fig. 3 shows experimentally measured spectra of longitudinal and transverse velocities in electron flow at different values of the beam current. Fig. 4 shows the transformation of the spectra with a change in the magnetization reversal coefficient and the maximum magnetic flux density B_m for fixed current in the beam.

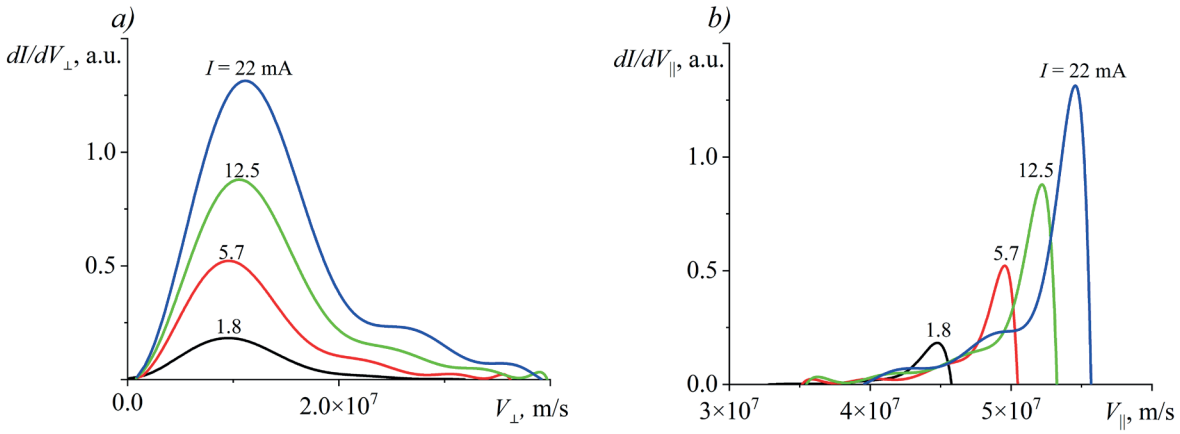

Fig. 3. Spectra of transverse (*a*) and longitudinal (*b*) electron velocities in the electron beam in EOS at different currents; maximum magnetic flux density B_m = 2.5 T, magnetization reversal coefficient k = 13

The RMS spread of electrons over the transverse velocity reached about 50% for the entire electron flow. The data obtained indicate that the shape of the transverse velocity distribution was practically unchanged with the beam current varying over a wide range (from 0.1 to 25 mA). The pitch factor averaged over the entire electron flow increased from 0.26 to 0.30 with an increase in current.

The variation in the magnetic field in the cathode with a fixed magnetization reversal coefficient has practically no effect on the electron velocity spread. An increase in the magnetization reversal coefficient from 13 to 28 at constant voltage U and magnetic flux density B_m leads to a decrease in the beam current. The average pitch factor increases markedly from 0.24 to 0.38.

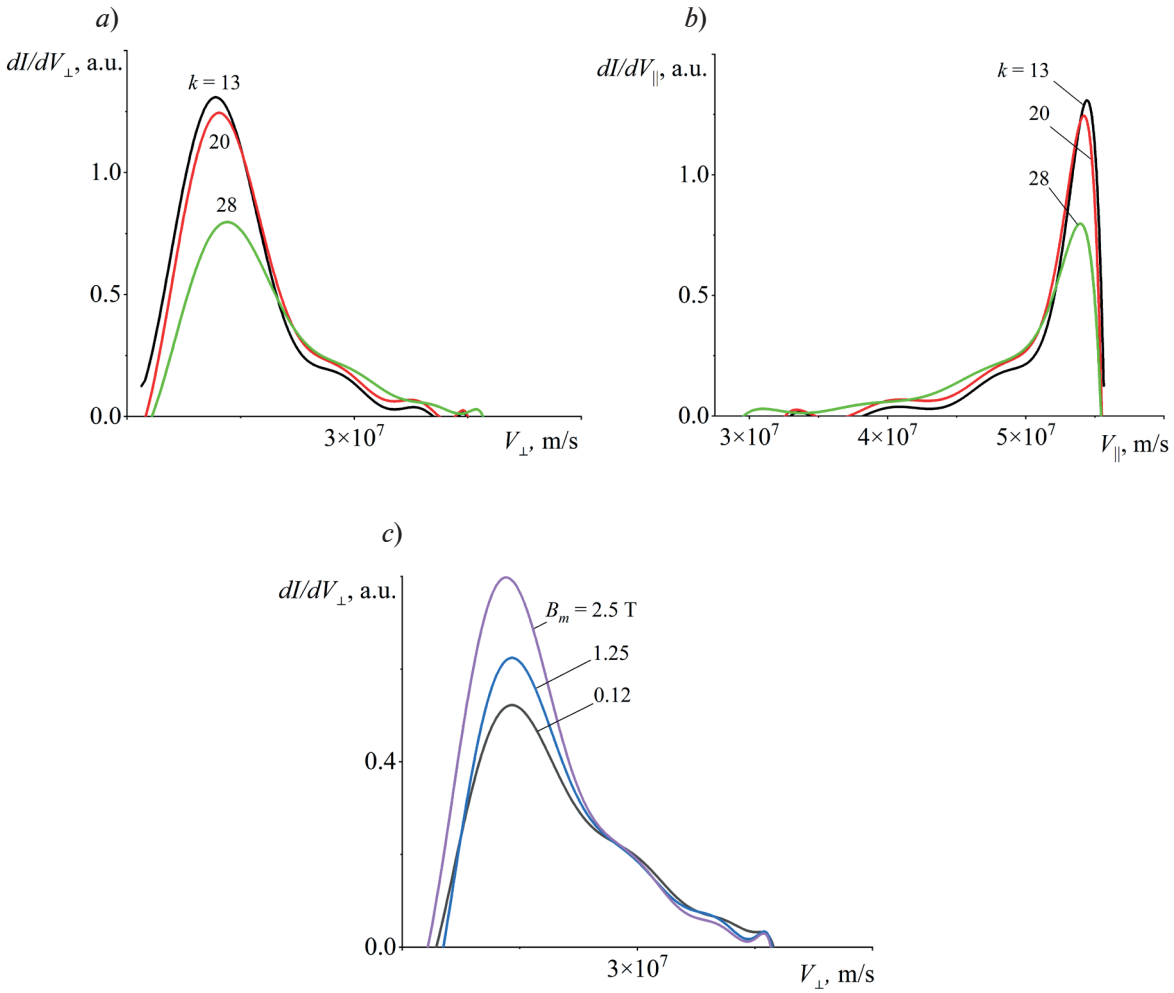

Fig. 4. Spectra of transverse (*a*) and longitudinal (*b*) electron velocities in electron beam in EOS at different magnetization reversal coefficients k and maximum magnetic flux densities B_m (*c*). Current in the electron beam $I = 22$ mA

Conclusion

Let us overview our main findings. We obtained data on the values of currents as well as electron velocity spectra observed in an EOS with a multi-tip field emitter. In our opinion, these results might prove indispensable for developers of subterahertz microwave devices.

In the future, it is planned to study the characteristics of flows in electron-optical systems with multi-tip and multilayer emitters [9].

REFERENCES

1. **Litvak A. G., Denisov G. G., Glyavin M. Y.,** Russian gyrotrons: Achievements and trends, IEEE J. Microw. 1 (1) (2021) 260–268.

2. **Idehara T., Sabchevski S. P., Glyavin M., Mitsudo S.,** The gyrotrons as promising radiation sources for THz sensing and imaging, Appl. Sci. 10 (3) (2020) 980.

3. **Thumm M. K. A., Denisov G. G., Sakamoto K., Tran M. Q.,** High-power gyrotrons for electron cyclotron heating and current drive, Nucl. Fusion. 59 (7) (2019) 073001.

4. **Li J., Zhang Y., Ke Y., et al.,** A cold cathode electron gun using convex carbon nanotube emitter, IEEE Trans. Electron Devices, 69 (3) (2022) 1457–1460.

5. **Chen Q., Yuan X., Xu X., et al.,** Development of a high-beam-transparency gridded electron gun based on a carbon nanotube cold cathode, IEEE Electron Device Lett. 43 (4) (2020) 615–618.

6. **Whaley D. R., Duggal R., Armstrong C. M., et al.,** 100 W operation of a cold cathode TWT, IEEE Trans. Electron Devices. 56 (5) (2009) 896–905.

7. **Yuan X., Zhu W., Zhang Y., et al.,** A fully-sealed carbon-nanotube cold-cathode terahertz gyrotron, Sci. Rep. 6 (09 Sept) (2016) 32936.

8. **Sominskii G. G., Tumareva T. A., Taradaev E. P., et al.,** Annular multi-tip field emitters with metal-fullerene protective coatings, Techn. Phys. 64 (2) (2019) 270–273.

9. **Sominskii G. G., Sezonov V. E., Taradaev S. P., Vdovichev S. N.,** Multilayer field emitters made of contacting hafnium and platinum nanolayers, Techn. Phys. 64 (1) (2019) 116–120.

10. **Taradaev E. P., Sominskii G. G.,** Characteristics of an annular electron flow formed by an electron gun with a field emitter, IEEE Trans. Electron Devices. 69 (5) (2022) 2675–2679.

СПИСОК ЛИТЕРАТУРЫ

1. **Litvak A. G., Denisov G. G., Glyavin M. Y.** Russian gyrotrons: Achievements and trends // IEEE Journal of Microwaves. 2021. Vol. 1. No. 1. Pp. 260–268.

2. **Idehara T., Sabchevski S. P., Glyavin M., Mitsudo S.** The gyrotrons as promising radiation sources for THz sensing and imaging // Applied Sciences. 2020. Vol. 10. No. 3. P. 980.

3. **Thumm M. K. A., Denisov G. G., Sakamoto K., Tran M. Q.** High-power gyrotrons for electron cyclotron heating and current drive // Nuclear Fusion. 2019. Vol. 59. No. 7. P. 073001.

4. **Li J., Zhang Y., Ke Y., Li B., Deng S.** A cold cathode electron gun using convex carbon nanotube emitter // IEEE Transactions on Electron Devices. 2022. Vol. 69. No. 3. Pp. 1457–1460.

5. **Chen Q., Yuan X., Xu X., Zhang Y., Cole M. T., Zu Y., Yan Y.** Development of a high-beam-transparency gridded electron gun based on a carbon nanotube cold cathode // IEEE Electron Device Letters. 2020. Vol. 43. No. 4. Pp. 615–618.

6. **Whaley D. R., Duggal R., Armstrong C. M., Bellew C. L., Holland C. E., Spindt C. A.** 100 W operation of a cold cathode TWT // IEEE Transactions on Electron Devices. 2009. Vol. 56. No. 5. Pp. 896–905.

7. **Yuan X., Zhu W., Zhang Y., Xu N., Yan Y., Wu J., Shen Y., Chen J., She J., Deng S.** A fully-sealed carbon-nanotube cold-cathode terahertz gyrotron // Scientific Reports. 2016. Vol. 6. 09 September. P. 32936.

8. **Соминский Г. Г., Тумарева Т. А., Тарадаев Е. П., Рукавицына А. А., Степанова А. Н.** Многострийные кольцевые полевые эмиттеры с защитными металл-фуллереновыми покрытиями // Журнал технической физики. 2019. Т. 89. № 2. С. 302–305.

9. **Соминский Г. Г., Сезонов В. Е., Тарадаев С. П., Вдовичев С. Н.** Многослойные полевые эмиттеры, изготовленные из приведенных в контакт нанослоев гафния и платины // Журнал технической физики. 2019. Т. 89. № 1. С. 142–146.

10. **Taradaev E. P., Sominskii G. G.** Characteristics of an annular electron flow formed by an electron gun with a field emitter // IEEE Transactions on Electron Devices. 2022. Vol. 69. No. 5. Pp. 2675–2679.

THE AUTHORS

TARADAEV Evgeny P.
Peter the Great St. Petersburg Polytechnic University
29 Politechnicheskaya St., St. Petersburg, 195251, Russia
evgeny_tar@hotmail.com
ORCID: 0000-0001-5219-6744

SOMINSKII Gennadii G.
Peter the Great St. Petersburg Polytechnic University
29 Politechnicheskaya St., St. Petersburg, 195251, Russia
sominski@rphf.spbstu.ru
ORCID: 0000-0001-7945-7238

TARADAEV Sergei P.
Peter the Great St. Petersburg Polytechnic University
29 Politechnicheskaya St., St. Petersburg, 195251, Russia
sergio.rumos@mail.ru
ORCID: 0000-0001-5548-7379

СВЕДЕНИЯ ОБ АВТОРАХ

ТАРАДАЕВ Евгений Петрович – *кандидат физико-математических наук, доцент Высшей инженерно-физической школы Санкт-Петербургского политехнического университета Петра Великого, Санкт-Петербург, Россия.*
195251, Россия, г. Санкт-Петербург, Политехническая ул., 29
evgeny_tar@hotmail.com
ORCID: 0000-0001-5219-6744

СОМИНСКИЙ Геннадий Гиршевич – *доктор физико-математических наук, профессор Высшей инженерно-физической школы Санкт-Петербургского политехнического университета Петра Великого, Санкт-Петербург, Россия.*
195251, Россия, г. Санкт-Петербург, Политехническая ул., 29
sominski@rphf.spbstu.ru
ORCID: 0000-0001-7945-7238

ТАРАДАЕВ Сергей Петрович – *аспирант Высшей инженерно-физической школы Санкт-Петербургского политехнического университета Петра Великого, Санкт-Петербург, Россия.*
195251, Россия, г. Санкт-Петербург, Политехническая ул., 29
sergio.rumos@mail.ru
ORCID: 0000-0001-5548-7379

Статья поступила в редакцию 23.11.2023. Одобрена после рецензирования 08.12.2023. Принята 11.12.2023.
Received 23.11.2023. Approved after reviewing 08.12.2023. Accepted 11.12.2023.

PHYSICAL MATERIALS TECHNOLOGY

Original article
UDC 548.4
DOI: https://doi.org/10.18721/JPM.17108

THE SCALING OF MISORIENTATION ANGLE DISTRIBUTION AT STRAIN-INDUCED BOUNDARIES IN COPPER DEFORMED BY TENSION UNDER VARIOUS CONDITIONS

N. Yu. Zolotorevsky [1] ✉, *V. V. Rybin* [1],
E. A. Ushanova [2], *V. N. Perevezentsev* [3]

[1] Peter the Great St. Petersburg Polytechnic University, St. Petersburg, Russia;
[2] NRC "Kurchatov Institute" – CRISM "Prometey", St. Petersburg, Russia;
[3] Institute of Mechanical Engineering Problems of the RAS –
the branch of the Federal State Budgetary Scientific Institution
"Federal Research Center Institute of Applied Physics of the RAS",
Nizhny Novgorod, Russia

✉ zolotorevsky@phmf.spbstu.ru

Abstract. In the paper, polycrystalline copper deformed by tension under different conditions of loading has been studied using electron backscatter diffraction. The microstructure of areas located on the longitudinal section of the specimens deformed until fracture was examined. The fragmentation of initial grains in case of deformation at room temperature was observed whereas at 400°C, considerable dynamic recovery and recrystallization significantly influenced the microstructure formation. A procedure for computer analysis of the orientation maps has been put forward, which allows separating recrystallized regions from the non-recrystallized ones and further analyzing the misorientation statistics of strain-induced boundaries. A scaling behavior of the strain-induced misorientation distributions was shown to take place. The mechanism of strain-induced boundary evolution was proved to remain unchanged for all studied deformation conditions, in spite of recovery and recrystallization occurring at elevated temperatures.

Keywords: polycrystalline copper, plastic deformation, recrystallization, microstructure, electron backscatter diffraction

Funding: The reported study was funded by Russian Science Foundation (Project No. 21-19-00366).

For citation: Zolotorevsky N. Yu., Rybin V. V., Ushanova E. A., Perevezentsev V. N., The scaling of misorientation angle distribution at strain-induced boundaries in copper deformed by tension under various conditions, St. Petersburg State Polytechnical University Journal. Physics and Mathematics. 17 (1) (2024) 71–80. DOI: https://doi.org/10.18721/JPM.17108

Научная статья
УДК 548.4
DOI: https://doi.org/10.18721/JPM.17108

МАСШТАБНАЯ ИНВАРИАНТНОСТЬ РАСПРЕДЕЛЕНИЯ УГЛОВ РАЗОРИЕНТИРОВКИ НА ГРАНИЦАХ ДЕФОРМАЦИОННОГО ПРОИСХОЖДЕНИЯ В МЕДИ, ДЕФОРМИРОВАННОЙ РАСТЯЖЕНИЕМ В РАЗЛИЧНЫХ УСЛОВИЯХ

Н. Ю. Золоторевский [1] ✉, *В. В. Рыбин* [1],
Э. А. Ушанова [2], *В. Н. Перевезенцев* [3]

[1] Санкт-Петербургский политехнический университет Петра Великого, Санкт-Петербург, Россия;

[2] НИЦ Курчатовский Институт – ФГУП ЦНИИ КМ "Прометей", Санкт-Петербург, Россия;

[3] Институт проблем машиностроения РАН – филиал Федерального государственного бюджетного научного учреждения "Федеральный исследовательский центр «Институт прикладной физики РАН»", г. Нижний Новгород, Россия

✉ zolotorevsky@phmf.spbstu.ru

Аннотация. В работе исследована поликристаллическая медь, деформированная растяжением в различных условиях (использован метод дифракции обратнорассеянных электронов). Проанализирована микроструктура участков, расположенных на продольном сечении образцов, деформированных до разрушения. В случае деформации при комнатной температуре, наблюдали фрагментацию исходных зерен, тогда как при 400 °C на формирование микроструктуры значительное влияние оказывали динамический возврат и рекристаллизация. Нами предложена процедура компьютерного анализа ориентационных карт, позволяющая отделять рекристаллизованные области от нерекристаллизованных и анализировать статистику разориентировок на границах деформационного происхождения. Доказано, что механизм эволюции разориентировок остается неизменным для всех изученных условий деформации, несмотря на динамический возврат и рекристаллизацию при повышенной температуре.

Ключевые слова: поликристаллическая медь, пластическая деформация, рекристаллизация, микроструктура, дифракция обратнорассеянных электронов

Финансирование: Исследование выполнено при финансовой поддержке Российского научного фонда (проект № 21-19-00366).

Ссылка при цитировании: Золоторевский Н. Ю., Рыбин В. В., Ушанова Э. А., Перевезенцев В. Н. Масштабная инвариантность распределения углов разориентировки на границах деформационного происхождения в меди, деформированной растяжением в различных условиях // Научно-технические ведомости СПбГПУ. Физико-математические науки. 2024. Т. 17. № 1. С 71–80. DOI: https://doi.org/10.18721/ JPM.17108

Introduction

During plastic deformation, a significant number of dislocations remain trapped inside original grains, leading in medium to high stacking fault energy metals to the formation of multiple strain-induced boundaries [1, 2]. These boundaries have low misorientation angles at an early stage of the microstructure evolution. The level of misorientation, however, continuously increases with strain so that high-angle boundaries appear at later stages [2, 3]. The distribution of boundary misorientation angles is important for evaluation of strength properties [4 – 7]. Besides, it can provide important evidence concerning the physical mechanism of the grain refinement during deformation [2 – 4].

The exhibition of microstructure evolution depends, in particular, on the deformation temperature. During low-temperature deformation, the phenomenon called fragmentation [2] takes place, namely, the subdivision of original grains into volumes, which mutual misorientations gradually increase in the process of deformation. An increase in temperature promotes dynamic recovery leading to a reduction of dislocation density and formation of lower-energy dislocation substructure [1]. With a further rise in temperature, a dynamic recrystallization (DRX) occurs: both the discontinuous DRX, which involves the formation of new grain nuclei and their subsequent growth at the expense of surrounding substructure, and the continuous DRX, when the new fine grains develop without the nucleation stage by a gradual increase in subgrain misorientations [7 – 9]. At the same time, it remains unclear whether temperature increasing influences the mechanism of grain subdivision [9].

A scaling behavior in the boundary misorientations has been found by D. A. Hughes and co-authors [3]: it turned out that the misorientation angle-distribution determined at various strains was invariant with respect to the average misorientation angle. Such a scaling has a physical significance, since it indicates that a physical mechanism remains unchanged when changing external conditions.

In the present study, this approach has been used in order to clarify to what extent a change in the conditions of deformation influences the mechanism of grain subdivision. In this concern, the misorientation distribution of strain-induced boundaries were examined in polycrystalline copper deformed in tension under various conditions.

Materials and methods

Cylindrical copper specimens were tensile strained until fracture in three ways:

(*i*) at a strain rate of $3 \cdot 10^{-2}$ s^{-1} at room temperature (specimen I),

(*ii*) at the same strain rate but at 400 °C (specimen II),

(*iii*) under a constant stress of 120 MPa at 400 °C (specimen III).

The fracture of specimen III happened after half an hour of deformation. For the following examination, the necked specimen has been cut along the tensile axis direction, and regions for the Electron Backscatter Diffraction (EBSD) analysis were chosen in several places within the neck, on the longitudinal section near the central axis of the specimen. Local strains ε in those places were calculated from the local diameter D of the necked specimen using the equation

$$\varepsilon = 2 \cdot \log(D/D_0),$$

where D_0 is the initial diameter.

For every specimen studied, the boundary misorientations were analyzed in two regions corresponding to strains $\varepsilon \approx 0.7$ and 1.0. The EBSD analysis was carried out on SEM LYRA 3 XMN RL using Oxford HKL AZtec™ software; further processing of orientation maps was performed by means of MTEX software [10]. Orientation maps shown in what follows are the inverse pole figure (IPF) maps plotted with respect to the tensile direction (TD).

In the case of specimen III, a considerable part of material turned out to be recrystallized. Since we were interested in the misorientation distribution of strain-induced boundaries, it was necessary first of all to separate the non-recrystallized material from the recrystallized one. To do this, we used grain average misorientation (GAM) derived by averaging kernel average misorientations over a grain [11]. The latter, in its turn, was calculated as an average of misorientations between a given point and its nearest neighbors. When using GAM for the separation, it was assumed that dynamically recrystallized grains did not have a deformation substructure and hence differ by a

low value of GAM. An example is shown in Fig. 1. One can see that the recrystallized grains, which easily can be distinguished on the orientation map by a uniform orientation and multiple annealing twins (Fig. 1,*a*), are characterized by relatively low GAM values (Fig. 1,*b*). In the given example, one can exclude recrystallized microstructure by eliminating grains with GAM less than 0.3 deg·μm^{-1}. The distributions of boundary misorientation angle (Fig. 1,*c*) obtained for recrystallized and non-recrystallized regions separated in this way confirm correctness of the separation: the first distribution contains the high-angle peaks corresponding to the annealing twins of the first order (60°) and second one (about 39°), whereas the latter contains the low-angle peak corresponding to the strain-induced dislocation boundaries.

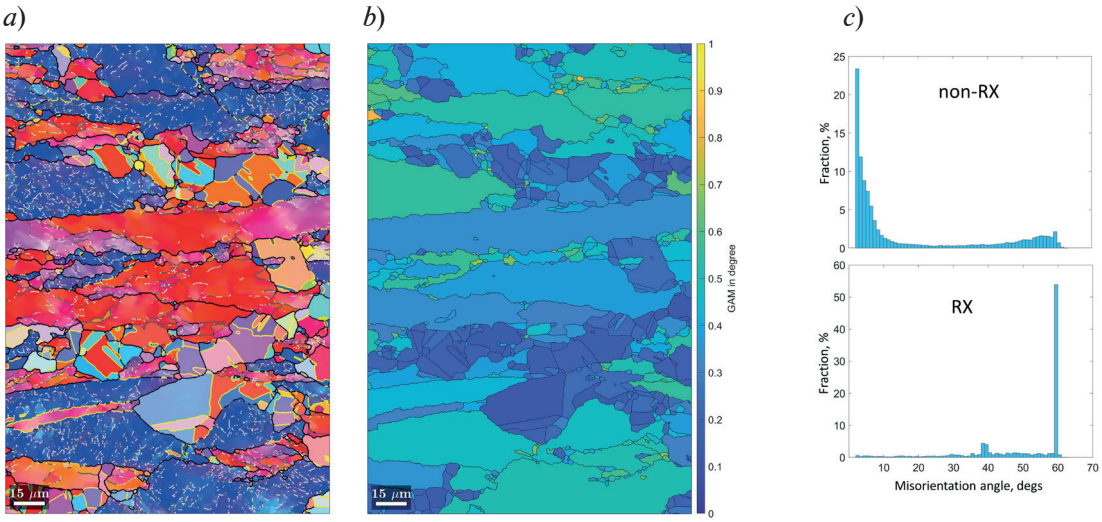

Fig. 1. Inverse pole figure (IPF) (*a*) and grain average misorientation (GAM) (*b*) maps of the same region of specimen III and misorientation angle histograms (*c*) obtained from recrystallized (RX) and non-recrystallized (non-RX) parts of this region.

The boundaries (Bs) on the IPF map are shown: low-angle Bs ($2° < \theta < 5°$) by light grey color; mediate angle Bs ($5° < \theta < 15°$) by dark grey; random high-angle Bs ($\theta > 15°$) by black); Σ3 Bs satisfying Brandon criterion by yellow

Results and discussion

Microstructure evolution. Fig. 2 shows representative examples of the microstructure evolved in the deformed specimens. One can see that a grain-scale orientation heterogeneity and multiple low-angle boundaries develop inside original grains in all specimens. Besides, the orientation dependence of the microstructure, which has been described earlier [12], is observed regardless of deformation conditions. At the same time, apparent differences in the microstructures are observed. In particular, a fraction of [001]-oriented material in the specimens deformed at 400 °C is considerably larger than that in specimen I. The boundaries of [001]-grains in specimen II are serrated (Fig. 2,*e*) suggesting the occurrence of local grain boundary migration, which usually accompanies DRX. Only a small amount of fine recrystallized grains can be found in specimen II, total area occupied by them remains negligible (about 1 %). However, in specimen III, deformation of which proceeds at the same temperature but for a longer period, DRX develops to a much greater extent (Fig. 2,*c*, *f*). The area fractions occupied by recrystallized grains are about 5% at $\varepsilon = 0.70$ and about 20° at $\varepsilon = 1.05$.

In Fig. 3, the misorientation distributions are presented in terms of the boundary length per unit area. This way of presentation allows not only to determine relative frequencies of boundaries as function of their misorientation but also to characterize accumulation of strain-induced boundaries during deformation. One can see that the length of boundaries increases considerably in the course of deformation at room temperature within the range of strains examined (Fig. 3,*a*), both in the low-angle (less than 15°) and high-angle (more than 15°) ranges. With increasing temperature of active deformation, accumulation of strain-induced boundaries slows down (Fig. 3,*b*), supposedly due to dynamic recovery, which promotes more uniform slip and

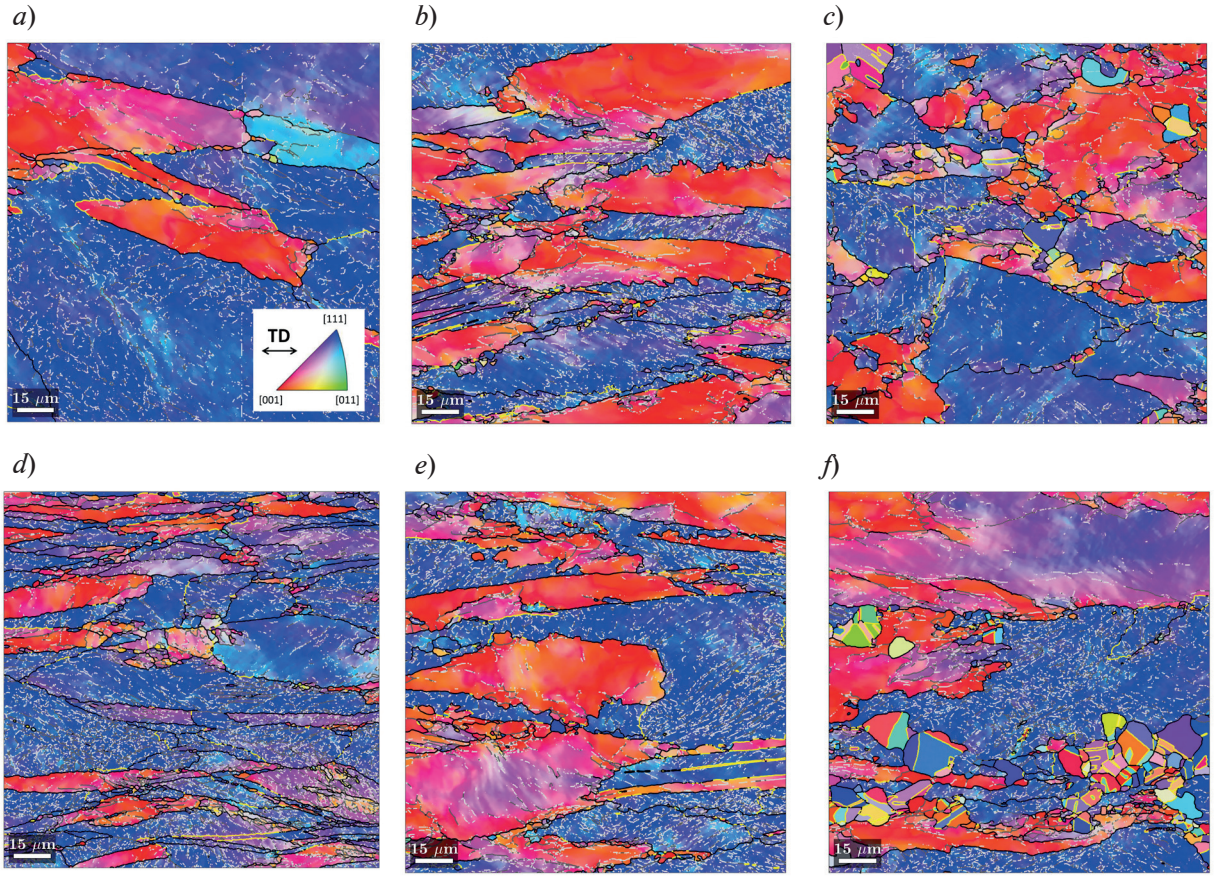

Fig. 2. IPF maps for typical microstructures evolved in the studied specimens I – III: in I, for ε = 0.70 (*a*) and 1.00 (*d*); in II, for ε = 0.65 (*b*) and 1.00 (*e*); in III, for ε = 0.70 (*c*) and 1.05 (*f*).
Standard stereographic triangle, which defines coloring of IPF maps, is inserted in Fig 2,*a*; the tensile direction (TD) is also shown. Color scheme of boundaries on the IPF maps is the same as the one given in Fig. 1

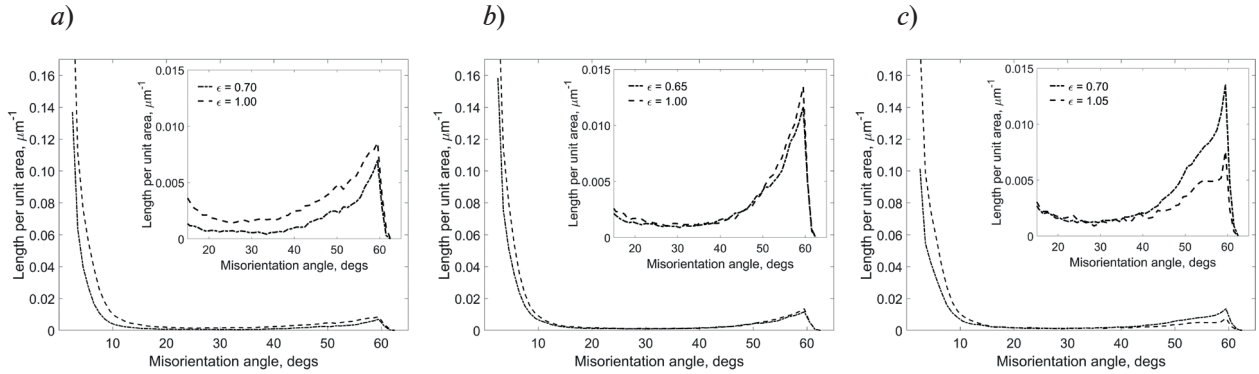

Fig. 3. Distributions of boundary misorientation angles in copper specimens I (*a*), II (*b*), III (*c*), deformed in tension to various strains under different conditions.
In the insets: Enlarged images of the high-angle parts of the graphs

counterbalances strain hardening [1]. In specimen III, the recrystallized part of material was excluded from consideration when calculating the distribution shown in Fig. 3,*c* using the procedure described in the previous section. Nevertheless, a boundary length even decreases with increasing strain for the boundaries corresponding to the high-angle peak. Note that this peak is due to boundaries of original annealing twins distorted as a result of deformation. One can suggest that those twins become hardly fragmented in the course of deformation, and hence, accumulate increased stored strain energy, and, for this reason, new recrystallized grains consume them predominantly.

Application of scaling hypothesis to EBSD data. Two kinds of strain-induced boundaries are distinguished [3]:

geometrically necessary boundaries (GNBs) separating regions with different slip system activity;

incidental dislocation boundaries (IDBs) formed by a statistical trapping of dislocations.

The first kind is also called "fragment boundaries" [2], while the second one is "cell boundaries". The IDBs remain low-angle with strain (the average misorientation is about 2° even after the strains from about 1 to 2), while the average misorientation of GNBs increases significantly [3, 4]. It was shown by the transmission electron microscopy (TEM) [3] that IDBs and GNBs, when considered separately, follow unique distributions f_1 and f_2, respectively. The latter show scaling behavior at small and mediate strains. However, at $\varepsilon \approx 1$ or more, this regularity happens to be violated for GNBs. According to recent study [13], new high-angle boundaries appear at this stage, whose misorientations fall far away beyond the range of scaled distribution f_2, and follow another unique distribution $-f_3$. As a result, a total distribution of strain-induced boundary misorientations consists of three partial distributions: f_1 (IDB), f_2 (GNB) and f_3 (see it in Fig. 4). The boundaries producing distribution f_3 are in essence also geometrically necessary since they separate regions with different combinations of operating slip systems.

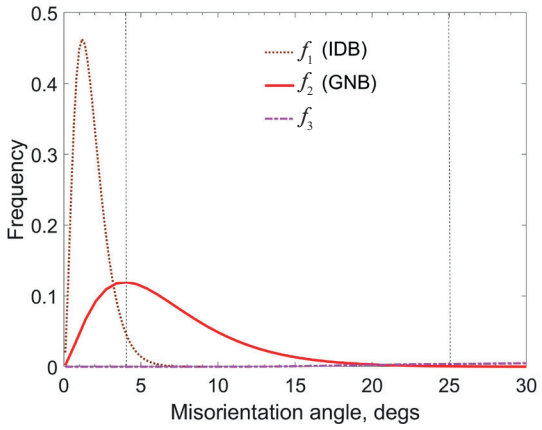

Fig. 4. Partial distributions f_1, f_2 and f_3 constituting total misorientation angle distribution of strain-induced boundaries in copper deformed by compression to strains $\varepsilon \approx 1$ [13].

Vertical lines indicate the bounds of the interval used to test scaling behavior of boundary misorientations

The scaling of GNBs related to distribution f_2 was proved using TEM through their visual separation from IDBs based on different morphological features. The EBSD technique does not allow one to make such a separation. However, one can try finding an approximate solution of this problem from their crystallographic characteristics. To do this, one should isolate an angular range $[\theta_{min}, \theta_{max}]$ where distribution f_2 is presented with minimal overlapping with f_1 on the left and f_3 on the right, and then calculate the probability density $p(\theta/\theta_{av})$ for this range. Here θ_{av} is the average misorientation angle over the given angular interval.

Based on the available data (see Fig. 4), the contribution of IDBs into the overall angle distribution is minor if $\theta_{min} = 4°$ is chosen. On the other hand, the contribution of high-angle strain-induced boundaries (distribution f_3) is negligible for $\theta_{max} = 25°$. A contribution of original grain boundaries is also insignificant within this interval for the large-grained copper investigated in the present study. Obviously, the choice of 25° as an upper bound is rather arbitrary, but its slight variation has no significant effect on the distribution of probability density $p(\theta/\theta_{av})$.

The normalized angle distributions obtained as described above are shown in Fig. 5. It is seen that a scaling of misorientations takes place for three specimens studied, suggesting that physical mechanism of the grain subdivision remains unchanged as the conditions of deformation change.

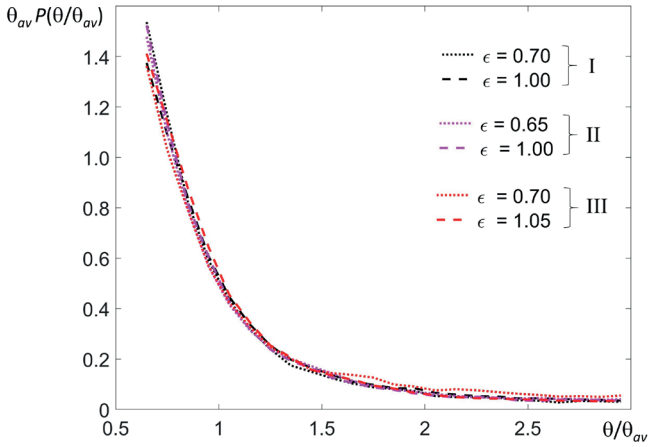

Fig. 5. Scaling behavior of misorientations across GNBs for specimens I, II and III deformed under different conditions

Conclusions

A tensile experiment has been conducted with polycrystalline copper deformed under three different conditions: at a constant strain rate at room temperature (23°C) and at 400°C as well as at a constant stress at 400°C. The evolution of misorientation across strain-induced boundaries were investigated based on EBSD analysis of regions located on the longitudinal section of the specimens. An analysis of the results obtained allows us to make the following main conclusions.

1. The exhibitions of a grain subdivision observed in the examined specimens differ with the deformation conditions. Gradual fragmentation of the original grains occurs at room temperature within the range of strains examined. At the same time, dynamic recovery and recrystallization influence the microstructure and texture evolution in specimens deformed at 400°C considerably.

2. A scaling behavior of strain-induced misorientation takes place. This approves that in spite of recovery and recrystallization effects, the mechanism of strain-induced boundary evolution remains unchanged. Therefore, at 400°C, which is about half the melting point of copper, this evolution is controlled by the micromechanics of polycrystalline material, just like the grain fragmentation at room temperature.

REFERENCES

1. **Gil Sevillano J., van Houtte P., Aernoudt E.,** Large strain work hardening and texture, Progr. Mater. Sci. 25 (2) (1980) 69–134.

2. **Rybin V. V.,** Bolshiye plasticheskiye deformatsii i razrusheniye metallov [Large plastic deformation and destruction of metals], Metallurgy Publishing, Moscow, 1986.

3. **Hughes D. A., Liu Q., Chrzan D. C., Hansen N.,** Scalling of microsructural parameters: Misorientations of deformation induced boundaries, Acta Mater. 45 (1) (1997) 105–112.

4. **Hughes D. A., Hansen N.,** The microstructural origin of work hardening stages, Acta Mater. 148 (15 April) (2018) 374–383.

5. **Wang R., Saleh A., Casillas G., et al.,** An in-situ electron backscattering diffraction and viscoplastic self-consistent study of OFHC copper subjected to uniaxial tension, Mater. Sci. Eng. A. 819 (5 July) (2021) 141184.

6. **Zhang S., Yang M., Yuan F., et al.,** Extraordinary fracture toughness in nickel induced by heterogeneous grain structure, Mater. Sci. Eng. A. 830 (7 Jan) (2022) 142313.

7. **Dolzhenko A., Tikhonova M., Kaibyshev R., Belyakov A.,** Microstructures and mechanical properties of steels and alloys subjected to large-strain cold-to-warm deformation, Metals. 12 (3) (2022) 454.

8. **Tikhonova M., Torganchuk V., Brasche F., et al.,** Effect of warm to hot rolling on microstructure, texture and mechanical properties of an advanced medium-Mn steel, Metall. Mater. Trans. A. 50 (9) (2019) 4245–4256.

9. **Sakai T., Belyakov A., Kaibyshev R., et al.,** Dynamic and post-dynamic recrystallization under hot, cold and severe plastic deformation conditions, Progr. Mater. Sci. 60 (March) (2014) 130–207.

10. **Hielscher R., Silbermann C. B., Schmidl E., Ihlemann J.,** Denoising of crystal orientation maps, J. Appl. Cryst. 52 (5) (2019) 984–996.

11. **Allain-Bonasso N., Wagner F., Berbenni S., Field D. P.,** A study of the heterogeneity of plastic deformation in IF steel by EBSD, Mater. Sci. Eng. A. 548 (30 June) (2012) 56–63.

12. **Zolotorevsky N. Yu., Rybin V. V., Ushanova E. A., Perevezentsev V. N.,** The effect of crystallographic texture formation on the features of microstructure evolution in tensile-strained copper, St. Petersburg State Polytechnical University Journal. Physics and Mathematics. 15 (4) (2022) 147–155 (in Russian).

13. **Zolotorevsky N. Yu., Rybin V. V., Matvienko A. N., et al.,** Misorientation angle distribution of deformation-induced boundaries provided by their EBSD-based separation from original grain boundaries: Case study of copper deformed by compression, Mater. Charact. 147 (Jan) (2019) 184–192.

СПИСОК ЛИТЕРАТУРЫ

1. **Gil Sevillano J., van Houtte P., Aernoudt E.** Large strain work hardening and texture // Progress in Materials Science.1980. Vol. 25. No. 2. Pp. 69–134.

2. **Рыбин В. В.** Большие пластические деформации и разрушение металлов. М.: Металлургия, 1986. 224 с.

3. **Hughes D. A., Liu Q., Chrzan D. C., Hansen N.** Scalling of microsructural parameters: Misorientations of deformation induced boundaries // Acta Materialia. 1997. Vol. 45. No. 1. Pp. 105–112.

4. **Hughes D. A., Hansen N.** The microstructural origin of work hardening stages // Acta Materialia. 2018. Vol. 148. 15 April. Pp. 374–383.

5. **Wang R., Saleh A., Casillas G., Lu C., Gazder A. A.** An in-situ electron backscattering diffraction and viscoplastic self-consistent study of OFHC copper subjected to uniaxial tension // Materials Science and Engineering. A. 2021. Vol. 819. 5 July. P. 141184.

6. **Zhang S., Yang M., Yuan F., Zhou L., Wu X.** Extraordinary fracture toughness in nickel induced by heterogeneous grain structure // Materials Science and Engineering A. 2022. Vol. 830. 7 January. P. 142313.

7. **Dolzhenko A., Tikhonova M., Kaibyshev R., Belyakov A.** Microstructures and mechanical properties of steels and alloys subjected to large-strain cold-to-warm deformation // Metals. 2022. Vol. 12. No. 3. P. 454.

8. **Tikhonova M., Torganchuk V., Brasche F., Molodov D. A., Belyakov A., Kaibyshev R.** Effect of warm to hot rolling on microstructure, texture and mechanical properties of an advanced medium-Mn steel // Metallurgical and Materials Transactions. A. 2019. Vol. 50. No. 9. Pp. 4245–4256.

9. **Sakai T., Belyakov A., Kaibyshev R., Miura H., Jonas J. J.** Dynamic and post-dynamic recrystallization under hot, cold and severe plastic deformation conditions // Progress in Materials Science. 2014. Vol. 60. March. Pp. 130–207.

10. **Hielscher R., Silbermann C. B., Schmidl E., Ihlemann J.** Denoising of crystal orientation maps // Journal of Applied Crystallography. 2019. Vol. 52. Part 5. Pp. 984–996.

11. **Allain-Bonasso N., Wagner F., Berbenni S., Field D. P.** A study of the heterogeneity of plastic deformation in IF steel by EBSD // Materials Science and Engineering A. 2012. Vol. 548. 30 June. Pp. 56–63.

12. **Золоторевский Н. Ю., Рыбин В. В., Ушанова Э. А., Перевезенцев В. Н.** Особенности эволюции микроструктуры меди при растяжении, обусловленные формированием кристаллографической текстуры // Научно-технические ведомости СПбГПУ. Физико-математические науки. 2022. Т. 15. № 4. С. 147–155.

13. **Zolotorevsky N. Yu., Rybin V. V., Matvienko A. N., Ushanova E. A., Philippov S. A.** Misorientation angle distribution of deformation-induced boundaries provided by their EBSD-based separation from original grain boundaries: Case study of copper deformed by compression // Materials Characterization. 2019. Vol. 147. January. Pp. 184–192.

THE AUTHORS

ZOLOTOREVSKY Nikolay Yu.
Peter the Great St. Petersburg Polytechnic University
29 Politechnicheskaya St., St. Petersburg, 195251, Russia
zolotorevsky@phmf.spbstu.ru
ORCID: 0000-0002-0185-5452

RYBIN Valery V.
Peter the Great St. Petersburg Polytechnic University
29 Politechnicheskaya St., St. Petersburg, 195251, Russia
rybin.@gmail.com
ORCID: 0000-0003-1619-309X

USHANOVA Elina A.
NRC "Kurchatov Institute" – CRISM "Prometey",
49 Shpalernaya St., St. Petersburg, 191015, Russia
elinaus@mail.ru
ORCID: 0000-0003-3094-8559

PEREVEZENTSEV Vladimir N.
Institute for Problems in Mechanical Engineering of RAS (the branch of Institute of Applied Physics of RAS)
85 Belinskiy St., Nizhny Novgorod, 603024, Russia
v.n.perevezentsev@gmail.com
ORCID: 0000-0002-0437-8540

СВЕДЕНИЯ ОБ АВТОРАХ

ЗОЛОТОРЕВСКИЙ Николай Юльевич – *доктор физико-математических наук, профессор Высшей школы механики и процессов управления Санкт-Петербургского политехнического университета Петра Великого, Санкт-Петербург, Россия.*
195251, Россия, г. Санкт-Петербург, Политехническая ул., 29
zolotorevsky@phmf.spbstu.ru
ORCID: 0000-0002-0185-5452

РЫБИН Валерий Васильевич – *член-корреспондент РАН, доктор физико-математических наук, профессор Высшей школы механики и процессов управления Санкт-Петербургского политехнического университета Петра Великого, Санкт-Петербург, Россия.*
195251, Россия, г. Санкт-Петербург, Политехническая ул., 29
rybinvv@mail.com
ORCID: 0000-0003-1619-309X

УШАНОВА Элина Артуровна – *кандидат физико-математических наук, старший научный сотрудник Научно-исследовательского центра «Курчатовский институт» – Федерального государственного унитарного предприятия – Центральный научно-исследовательский институт конструкционных материалов «Прометей», Санкт-Петербург, Россия.*
191015, Россия, Санкт-Петербург, Шпалерная ул., 49
elinaus@mail.ru
ORCID: 0000-0003-3094-8559

ПЕРЕВЕЗЕНЦЕВ Владимир Николаевич – *доктор физико-математических наук, ведущий научный сотрудник, руководитель направления Института проблем машиностроения РАН (филиал Федерального государственного бюджетного научного учреждения "Федеральный исследовательский центр «Институт прикладной физики Российской академии наук»"), г. Нижний Новгород, Россия.*

603024, Россия, г. Нижний Новгород, ул. Белинского, 85

v.n.perevezentsev@gmail.com

ORCID: 0000-0002-0437-8540

Received 18.10.2023. Approved after reviewing 28.11.2023. Accepted 28.11.2023.

Статья поступила в редакцию 18.10.2023. Одобрена после рецензирования 28.11.2023. Принята 28.11.2023.

BIOPHYSICS AND MEDICAL PHYSICS

Original article
DOI: https://doi.org/10.18721/JPM.17109

AN ANALYSIS OF THE ASGARDARCHAEA Cas1_3 PROTEIN: EXPERIMENTAL CHARACTERIZATION OF A POTENTIAL INTERMEDIATE IN THE EVOLUTION OF CRISPR-Cas SYSTEMS

M. V. Abramova[1], *A. S. Malykh*[1], *I. M. Gatieva*[1],
M. A. Kazalov[1], *P. A. Selkova*[1], *A. P. Yakimov*[1],
A. A. Vasileva[1, 2], *A. N. Arseniev*[1, 2], *M. A. Khodorkovskii*[1] ✉

[1] Peter the Great St. Petersburg Polytechnic University, St. Petersburg, Russia;
[2] Complex of NBICS Technologies, National Research Center "Kurchatov Institute", Moscow, Russia
✉ khodorkovskii@gmail.com

Abstract. The evolution of CRISPR-Cas systems and their possible origin from mobile genetic elements of transposons are currently being actively studied. Recently, unique systems have been discovered in a new group of Asgardarchaea that presumably function as transposons and contain Cas1-like proteins. In this study, the genetic and biochemical technologies were used, along with electrophoresis, affinity chromatography, and high-resolution mass spectrometry, to obtain and partially characterize a recombinant version of one of these proteins, Cas1_3. In particular, it was shown to have the ATPase activity, the quantitative value of the latter being determined by the spectrophotometric method. The results obtained may be useful in understanding the mechanisms of functioning the potential ancestor of CRISPR-Cas systems.

Keywords: characterization, CRISPR-Cas, evolution intermediate form, Asgardarchaea, transposon, recombinant protein

Funding: The reported study was funded by Russian Science Foundation (Grant No. 21-14-00122), and by the Ministry of Science and Higher Education of the Russian Federation (Agreement No. 075-15-2021-1062).

Citation: Abramova M. V., Malykh A. S., Gatieva I. M., Kazalov M. A., Selkova P. A., Yakimov A. P., Vasileva A. A., Arseniev A. N., Khodorkovskii M. A., An analysis of the Asgardarchaea Cas1_3 protein: Experimental characterization of a potential intermediate in the evolution of CRISPR-Cas systems, St. Petersburg State Polytechnical University Journal. Physics and Mathematics. 17 (2) (2024) 81–92. DOI: https://doi.org/10.18721/JPM.17109

Научная статья
УДК 577.322
DOI: https://doi.org/10.18721/JPM.17109

АНАЛИЗ БЕЛКА Cas1_3 АСГАРДАРХЕЙ: ЭКСПЕРИМЕНТАЛЬНАЯ ХАРАКТЕРИСТИКА ПОТЕНЦИАЛЬНОГО ПРОМЕЖУТОЧНОГО ЗВЕНА В ЭВОЛЮЦИИ СИСТЕМ CRISPR-Cas

М. В. Абрамова[1], *А. С. Малых*[1], *Я. М. Гатиева*[1],
М. А. Казалов[1], *П. А. Селькова*[1], *А. П. Якимов*[1],
А. А. Васильева[1, 2], *А. Н. Арсениев*[1, 2], *М. А. Ходорковский*[1] ✉

[1] Санкт-Петербургский политехнический университет Петра Великого, Санкт-Петербург, Россия;
[2] Комплекс НБИКС-природоподобных технологий, Национальный исследовательский центр «Курчатовский институт», Москва, Россия
✉ khodorkovskii@gmail.com

Аннотация. В настоящее время актуальны исследования эволюции систем CRISPR-Cas и их возможного происхождения от мобильных генетических элементов транспозонов. Недавно у новой группы асгардархей были обнаружены уникальные системы, которые предположительно функционируют как транспозоны и содержат Cas1-подобные белки. В настоящей работе для одного из таких белков, Cas1_3, впервые с использованием генетических и биохимических технологий, а также методов электрофореза, аффинной хроматографии и высокоразрешающей масс-спектрометрии получена и частично охарактеризована его рекомбинантная версия. В частности, показано наличие у него АТФ-азной активности, количественное значение которой было определено с помощью метода спектрофотометрии. Полученные результаты могут быть полезны в понимании механизмов функционирования потенциального предшественника систем CRISPR-Cas.

Ключевые слова: характеризация, CRISPR-Cas, промежуточное звено эволюции, асгардархеи, транспозон, рекомбинантный белок

Финансирование: Исследование выполнено при финансовой поддержке Российского научного фонда (грант № 21-14-00122), а также Министерства науки и высшего образования Российской Федерации (соглашение № 075-15-2021-1062).

Для цитирования: Абрамова М. В., Малых А. С., Гатиева Я. М., Казалов М. А., Селькова П. А., Якимов А. П., Васильева А. А., Арсениев А. Н., Ходорковский М. А. Анализ белка Cas1_3 асгардархей: экспериментальная характеристика потенциального промежуточного звена в эволюции систем CRISPR-Cas // Научно-технические ведомости СПбГПУ. Физико-математические науки. 2024. Т. 17. № 1. С. 81–92. DOI: https://doi.org/10.18721/JPM.17109

Introduction

CRISPR-Cas are specific systems of bacteria and archaea protecting them against the invasion of harmful genetic material (these can be viruses, mobile genetic elements, etc.). Combined with ribonucleic acids (RNA), proteins of such a system are targeted recognize foreign elements and insert spacer sequences into them, leading to subsequent degradation. The CRISPR-Cas system includes a CRISPR cassette and genes encoding Cas proteins [1]. The CRISPR cassette is a locus in the genome transcribed as short palindromic repeats separated by small unique spacer sequences. The latter are fragments of foreign genetic material stored in the genome of the

microorganism from previous infection. Spacers appear due to the adaptation process, i.e., the insertion of foreign genetic material into the CRISPR cassette. The Cas1 and Cas2 proteins are responsible for the adaptation stage in most CRISPR-Cas systems [2].

CRISPR-Cas systems are actively studied from an evolutionary perspective. This not only expands the fundamental understanding of the biology of such systems, but also offers potential for developing new technologies and improveming existing techniques for gene editing. The search for possible evolutionary intermediates can lead to the discovery of proteins useful for subsequent practical applications.

Earlier, bioinformatics methods traced the evolution of different CRISPR-Cas systems. It has been hypothesized that part of the adaptation modules has an evolutionary origin from transposon-encoded integrases, i.e., DNA sequences capable of moving from one location in the genome to another [3, 4]. In 2020, unique systems were discovered in nucleotide sequences of a new group of Asgard archaea (Asgardarchaeota), presumably functioning as transposons. All these systems are united by the presence of large Cas1-like proteins, which are homologues of the Cas1 protein from the CRISPR-Cas system. One of such systems, aCas1_3, can be regarded as a model for one of the ancestors of the CRISPR-Cas system [5].

In this study, we obtained for the first time a recombinant version of the Cas1_3 protein, a giant Cas1-like protein from the presumably transposable aCas1_3 system in Asgard archaea. In addition to obtaining a recombinant version of the protein, we carried out its primary functional characterization.

Materials and methods

Bioinformatic analysis of the Cas1_3 protein sequence. The MOTIF library (https://www.genome.jp/tools/motif/)was used to identify the motifs in the amino acid sequence of the protein. The search was carried out over the PROSITE [6], NCBI-CDD [7] and Pfam libraries [8].

Cloning of the Cas1_3 protein gene for expression in producing cells. DNA sequences of Asgard archaea carrying proteins of the aCas1_3 system exist only as metagenomic data. This paper considered the aCas1_3 protein system, found in the *Candidatus Thorarchaeota archaeon* isolate Yap500.bin9.44 sequence from the GenBank database (ID: JAEOSL000000000.1).

The codon-optimized sequence of the Cas1_3 protein gene was synthesized at Cloning Facility (Moscow, Russia) and cloned into the pEXPR_001 vector. A PCR fragment carrying the Cas1_3 protein sequence was amplified from the resulting pEXPR_001_Cas1_3 plasmid (a small circular DNA molecule) by polymerase chain reaction (PCR). A PCR fragment carrying the sequence of the maltose binding protein (MBP) gene was also amplified from the standard pMJ806 vector (Addgene, USA).

The PCR fragments were amplified using a Q5 High-Fidelity 2X Master Mix (NEB, UK) in accordance with the manufacturer's protocol. The sequences of the primers used are given in Table.

The obtained PCR fragments carrying sequences of Cas1_3 (4986 bp) and MBP (1101 bp) proteins were cloned into the rET21a vector by the Gibson method [9] using Gibson Assembly Master Mix (NEB, UK) (recall that the length of sequenced DNA regions (genes, sites, chromosomes) or the entire genome is measured in base pairs of nucleotides (bp)). NdeI and NotI restriction endonuclease sites were selected for cloning.

Expression of the Cas1_3 protein gene in producing cells. The pET21a_Cas1_3_MBP plasmid was transformed into competent Escherichia coli (*E. coli*) BL21 AI cells using standard methods. The resulting cells were grown in lysogeny broth (LB) with ampicillin (100 mcg/ml) in a volume of 500 ml. Cell cultures were incubated at a temperature of 37 °C and uniform aeration on an orbital rocker until an optical density of 0.6 at a wavelength of 600 nm was reached. Transcription of the target Cas1_3 protein gene was induced by adding arabinose and isopropyl-β-D-1-thiogalactopyranoside (IPTG) to a final concentration of 0.1% and 1 mM, respectively. Cell culture cultivation was continued at a temperature of 18 °C for 16 hours. The cells were collected by centrifugation at a centrifugal acceleration of 3500 g for 30 minutes. The resulting pellet was stored at −20 °C.

The induction of Cas1_3 protein transcription in the obtained pellet was checked by the protocol described earlier [10].

Solubility prediction for Cas1_3 protein. A 1 ml cell culture was selected after incubation with arabinose and IPTG (see the previous section). The cells were collected by centrifugation

Table

Primer sequences used in the study

Sequence, 5′ → 3′ [primer designation]
AACCTGTACTTCCAATCCAATATTGGAATGACACGATCAAGAGGAAGGCCCG [Cas1_3 forward primer]
TGGTGCTCGAGTGCGGCCGCAAGCTTTACAACTGCTGCTCCTCAGACTCCGTCGGTTCGC [Cas1_3 reverse primer]
CTTTAAGAAGGAGATATACATATGCACCACCACCACCACCACATGAAAATCGAAGAAGGTAAAC [MBP forward primer]
ATATTGGATTGGAAGTACAGGTTTTCCTCGATAGTCTGCGCGTCTTTCAGGGCTTC [MBP reverse primer]

Notations: forward and reverse primers are given.

at 12,000 g for 10 minutes. The pellet was resuspended in 700 μl of lysing buffer comprising 50 mM Tris, 5% glycerol, NaCl solution of different concentrations (150, 500 or 1000 mM); the acidity (pH) of the buffer was 6.5 or 8.0. Cell lysis was performed by ultrasonic disruption in an ice bath. Ultrasonic disruption was performed with a LABSONIC device (Sartorius AG, Germany) at 30% amplitude for 0.2 s. The duration of each treatment cycle was 2 minutes, each subsequent cooling cycle lasted 2 minutes; the total treatment time was 10 minutes.

The sample was centrifuged at a centrifugal acceleration of 4000 g and a temperature of 4 °C for 10 minutes, then the supernatant was separated from the pellet. 700 μl of lysing buffer was added to the pellet, resuspended, and then 15 μl were taken from the pellet and from the supernatant for composition analysis. The analysis was performed by electrophoresis in denaturing 10% polyacrylamide gel (PAAG) using the Laemmli method [11].

Preparation of recombinant Cas1_3 protein. The pellet obtained from 500 ml of liquid cell culture containing the induced Cas1_3 protein was resuspended in 15 ml of lysing buffer with lysozyme and incubated on ice for 20 minutes.

The composition of the lysing buffer (pH = 8.0): 50 mM Tris ($C_4H_{11}NO_3$), 5% glycerin, NaCl solution with a concentration of 150 mM, 1 mg/ml lysozyme.

Cell lysis was performed by ultrasonic disruption in an ice bath by the protocol described in the previous section, with an extended treatment time (up to 30 minutes). The soluble part of the lysate and the pellet were separated by centrifugation at 16,000 g and 4 °C for 60 minutes. The supernatant was used for further purification.

Affinity chromatography was performed with MBPTrap HP Columns (GE Healthcare, USA). The samples with protein were concentrated using Amicon Ultra-4 Centrifugal Filter Unit (Merck Millipore, USA) centrifugal concentrators with a 100 kDa filter.

For gel filtration, the resulting sample was applied to a Superose 6 Increase 10/300 GL column (GE Healthcare, USA) in different buffers (see Results and Discussion below). Fractions containing the target protein were collected, combined and concentrated using centrifugal concentrators with a 100 kDa filter.

Glycerin was added to the protein concentrates to a final concentration of 10%. The purified protein was stored at a temperature of −80 °C.

Quantitative analysis of ATPase activity of Cas1_3 protein. The method described in [12] was used to quantify the ATPase activity (recall that ATP is adenosine triphosphate). A buffer consisting of 25 mM Tris (pH = 7.5), 10 mM $MgCl_2$, 2 mM ATP, 2−4 mM phosphoenolpyruvate (PEP), 50 units/ml lactate dehydrogenase, 50 units/ml pyruvate kinase and 4−5 mM reduced nicotinamide adenine dinucleotide (NADH) was used for this purpose.

First, we measured the background characterizing the hydrolytic activity of the buffer, then the activity of the protein in the buffer; at the last stage, the activity of the protein in the buffer was measured in the presence of oligonucleotides consisting of deoxythymines (oligo-dT).

Absorption curves for NADH were obtained at a wavelength of 340 nm using a Cary 5000 spectrophotometer (Varian, USA). To ensure the reliability of the data obtained, the experiment was repeated three times.

Results and discussion

Cas1_3 is a representative of a unique group of Cas1-like proteins of the aCas1_3 Asgard archae systems. This group of proteins has not been studied sufficiently and has not been characterized experimentally before.

Cas1_3, like all other representatives of this group, is a very large protein compared with the well-studied Cas1 proteins that are part of CRISPR-Cas systems. It contains 1,368 amino acid residues, while the Cas1 protein, for example, of the CRISPR-Cas system of the *Streptococcus pyogenes* SF370 (M1 GAS) type II-A bacterium, contains only 289 amino acid residues. Such a difference in size suggests the likely presence of additional domains in the structure of the Cas1_3 protein.

The first step in this study was to analyze which additional domains may be part of the Cas1_3 protein, allowing to draw immediate conclusions about their potential function. Since the spatial model of Cas1_3 has not been solved, such analysis was possible only based on available data on the amino acid sequence of the protein. We searched for the so-called motifs, i.e., the short characteristic sequences of amino acids associated with certain functions.

We were able to detect motifs similar to Walker motifs in the amino acid sequence of the Cas1_3 protein. In particular, the Walker A motif is a characteristic sequence GXXXXGKT/S of amino acid residues, where X is any amino acid residue [13]. The given motif can be represented by amino acid residues in the sequence of the Cas1_3 protein (G143-···-G150-K151-T152). Furthermore, a site similar to the Walker B motif can be found in the amino acid sequence of the Cas1_3 protein (GXXXLhhhD, where X is any amino acid residue and h is a hydrophobic amino acid residue). This site is formed by amino acid residues G167-···-L172-A173-H174-P175-D176.

It is known that the location of the Walker B motif downstream of the Walker A motif is quite characteristic for proteins with ATPase activity. The sequences of these motifs bind to the ATP and are involved in transferring the energy released during hydrolysis of the ATP molecule to the structural changes of the protein. This allows proteins containing Walker motifs to participate in functions involved in active transport, cellular mobility, and other biological processes. This refers to the processes associated with movement and transport within the cell, ensuring efficient use of the energy released during ATP hydrolysis [14]. As noted above, the Cas1_3 protein is part of the system that most likely acts as a transposon (a mobile genetic element). It is reasonable to assume that the additional energy obtained during ATP hydrolysis by the Cas1_3 protein may help the transposon to incorporate into the genome, thus triggering its mobility.

To test the ability of the Cas1_3 protein to hydrolyze ATP, we obtained its recombinant form. For this purpose, its gene was cloned into a construct for expression in producing cells. Additionally, we combined the gene of the target protein with the sequence of the MBP protein gene. The MBP is used to increase the solubility of the target protein in the lysing buffer for its further purification by affinity chromatography [15]. The resulting pET21a_Cas1_3_MBP plasmid is shown in Fig. 1,*a*.

The insertion of target genes into the vector was verified by restriction analysis: the resulting pET21a_Cas1_3_MBP plasmid was digested with restriction endonucleases NdeI, EcoRI, BamHI. Such digestion of the plasmid should produce fragments with a length of approximately 1334 bp, 1841 bp, 2643 bp and 5710 bp (see Fig. 1,*b*). In the case of such treatment of the original pET21a vector without insertion, fragments with the lengths of 5399, 38 and 6 bp should be formed . The sizes of the fragments obtained by restriction correspond to the expected ones (see Fig. 1,*b*), which confirms the insertion of target genes into the pET21a vector. For additional verification, the cloned gene was sequenced (determination of its primary nucleotide sequence) using the Sanger method.

To subsequently isolate the recombinant Cas1_3_MBP protein, we needed to test whether its synthesis is induced in producing cells and whether this protein is soluble.

The verification results for transcription induction of the Cas1_3_MBP protein gene are shown in Fig. 2,*a*. A product corresponding to the expected molecular weight of the target protein (232 kDa) was recorded in the 'after induction' sample, which indicated successful synthesis of Cas1_3_MBP in producing cells.

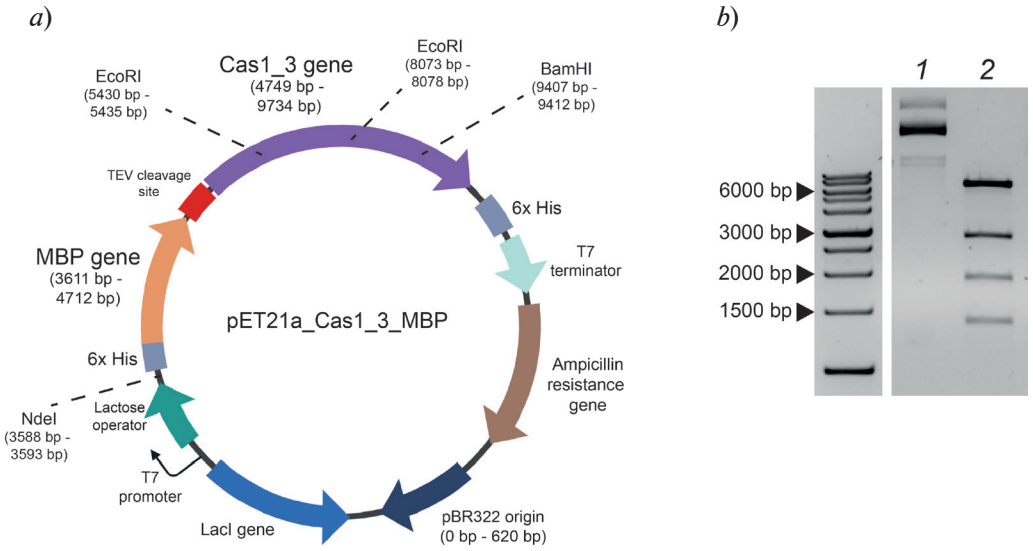

Fig. 1. Result of cloning the genes of Cas1_3 and MBP proteins into the pET21a vector: scheme of the pET21a_Cas1_3_MBP plasmid (carries the genes of the Cas1_3 and MBP proteins) (*a*); results of restriction analysis of this plasmid (*b*).

Fig. 1,*b*: analysis with control without restrictases (*1*) and restricted plasmid with NdeI, EcoRI, BamHI sites (*2*); bp is the base pair

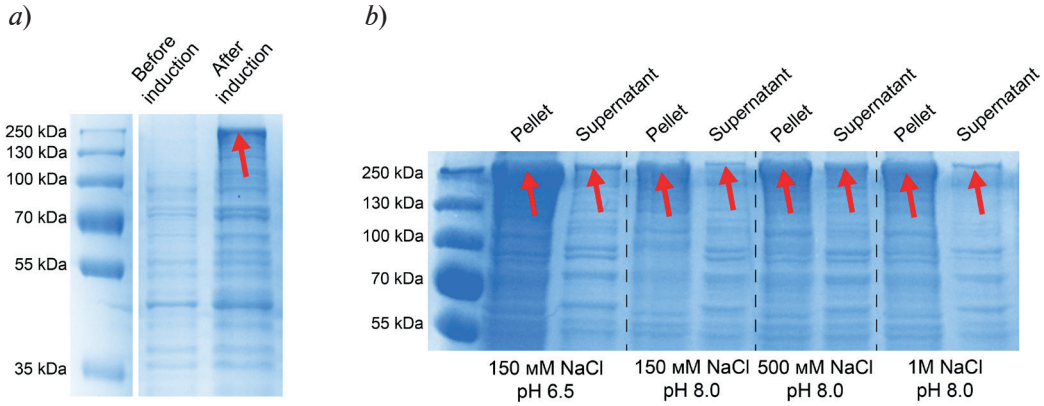

Fig. 2. Results of electrophoretic analyses for samples obtained during two tests: induction of Cas1_3_MBP protein synthesis (a) and solubility (b). The expected molecular weight of the protein was 232 kDa.

Red arrows indicate the positions of the target protein

The solubility of the protein had to be verified chromatographic purification. Therefore, the conditions under which the Cas1_3_MBP protein would have the greatest solubility were selected at the next stage. To select the best conditions, lysing buffers with different concentrations of sodium chloride NaCl (150, 500 and 1000 mM) and pH (6.5 and 8.0) were used. Products corresponding to the molecular weight of the Cas1_3_MBP protein were found in all samples: both in the pellet and in the supernatant (Fig. 2,*b*), which indicated the solubility of the protein in all tested buffer solutions. A buffer with the lowest amount of NaCl (150 mM) and pH = 8.0 was used for further purification of the protein, since higher NaCl concentrations may further interfere with *in vitro* experiments with this protein.

To isolate the functionally active Cas1_3_MBP protein, two-stage purification was performed using affinity chromatography and gel filtration methods.

Gel filtration was carried out in several configurations. Buffers with different NaCl contents were used for this purpose. In addition, we carried out purification in a buffer with 2M NaCl with the protein solution treated with benzonase and TEV protease before gel filtration. Benzonase

treatment was performed to remove nucleic acids from the protein solution, TEV-protease treatment was performed to cleave the MBP peptide from Cas1_3. It turned out that a peak consisting of Cas1_3_MBP appears on the chromatogram in the region of 12–14 ml when the protein is purified in a buffer containing 2M NaCl (Fig. 3). However, as previously noted, buffers with a high NaCl concentration may interfere with further experiments. For this reason, we decided to use protein fractions obtained after the affinity chromatography stage to verify the presence of ATPase activity.

The ability of the recombinant Cas1_3_MBP protein to hydrolyze ATP was tested *in vitro*. The activity of the RecA protein was measured simultaneously as a positive control. Fig. 4 shows the results of the experiment as a dependence of the quantity of hydrolyzed ATP on time. Evidently, the purified Cas1_3_MBP protein has ATPase activity with a constant hydrolysis rate, as does the RecA protein.

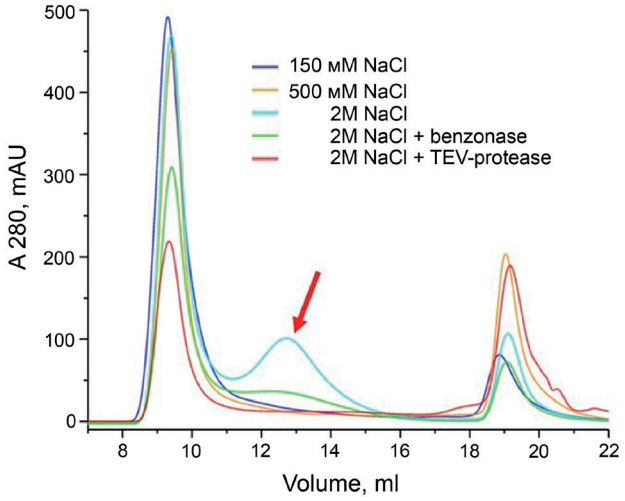

Fig. 3. Chromatographic profiles of gel-filtration purification of Cas1_3_MBP protein using various buffer conditions (see the legend). A peak related to this protein was detected at a volume of 13 ml (marked with a red arrow)upon isolation of this protein in 2M NaCl solution

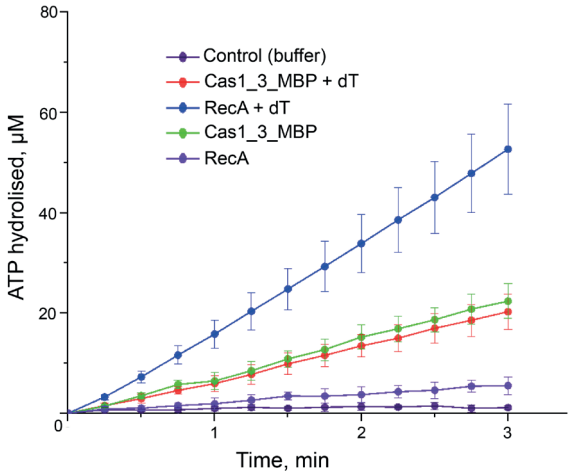

Fig. 4. Time dependences of ATP hydrolyzed by Cas1_3_MBP and RecA proteins in the presence and absence of oligonucleotides consisting of deoxythymines (oligo-dT), in solution

The rate of ATP hydrolysis by RecA protein ranged from 17±3 mmol/min with the addition of oligonucleotides consisting of deoxythymines (oligo-dT), which coincides with the literature data [16]. The hydrolytic activity of RecA depends on oligo-dT, therefore, ATP hydrolysis was not observed in their absence.

The rate of ATP hydrolysis by the Cas1_3_MBP protein was 6.0±1.5 mmol/min both in the presence and in the absence of oligo-dT. The lack of dependence of hydrolytic activity of Cas1_3_MBP on oligo-dT may be due to the fact that we were unable to completely eliminate the DNA from the cell culture during protein purification.

We verified that the observed ATP hydrolysis is due to the action of the Cas1_3_MBP protein by detecting the presence of protein impurities that could in any way affect the result obtained.

For this purpose, the method of high-resolution mass spectrometry was used (see, for example, [17]), which made it possible to verify that proteins released together with Cas1_3_MBP (Fig. 5) cannot make a significant contribution to the measured values of the ATP hydrolysis rate.

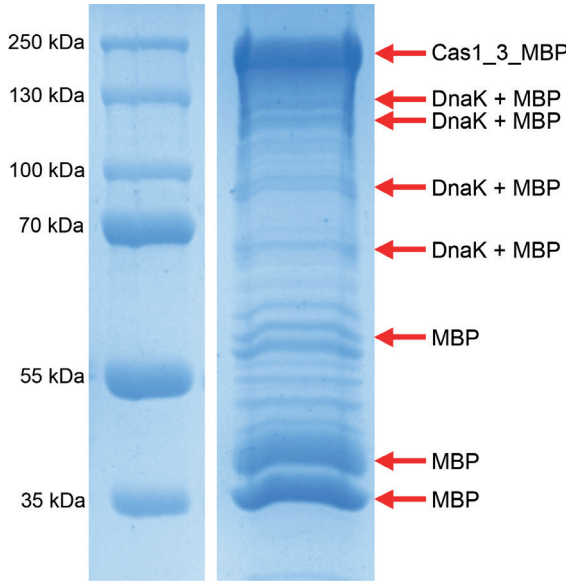

Fig. 5. Result of electrophoretic analysis of the sample obtained by purification of Cas1_3_MBP protein using affinity chromatography.
The red arrows indicate samples of protein impurities analyzed by mass spectrometry

Conclusion

We determined the conditions for obtaining a recombinant version of the Cas1_3 protein of the aCas1_3 Asgard archaea system, not characterized in any previous studies. This system most likely performs the functions of a transposon and is a potential evolutionary ancestor to CRISPR-Cas systems.

Our initial results demonstrate the ability of the Cas1_3 protein to hydrolyze ATP *in vitro*. The detection of ATPase activity allows to assess the possible role of ATP hydrolysis in the life cycle of the transposon as a mobile genetic element and ancestor of CRISPR-Cas systems.

New variants of the Cas1_3 protein should be created to further explain the mechanism of the detected ATPase activity, with mutated motifs potentially responsible for this activity.

REFERENCES

1. **Jansen R., Embden J. D., Gaastra W., Schouls L. M.,** Identification of genes that are associated with DNA repeats in prokaryotes, Mol. Microbiol. 43 (6) (2002) 1565–1575.

2. **Koonin E. V., Makarova K. S.,** Origins and evolution of CRISPR-Cas systems, Philos. Trans. R. Soc. B: Biol. Sci. 374 (1772) (2019) 20180087.

3. **Krupovic M., Shmakov S., Makarova K. S., et al.,** Recent mobility of casposons, self-synthesizing transposons at the origin of the CRISPR-Cas immunity, Genome Biol. Evol. 8 (2) (2016) 375–386.

4. **Faure G., Shmakov S. A., Yan W. X., et al.,** CRISPR-Cas in mobile genetic elements: counter-defence and beyond, Nature Reviews Microbiology. 17 (8) (2019) 513–525.

5. **Makarova K. S., Wolf Y. I., Shmakov S. A., et al.,** Unprecedented diversity of unique CRISPR-Cas-related systems and Cas1 homologs in Asgard archaea, CRISPR J. 3 (3) (2020) 156–163.

6. **Sigrist C. J., de Castro E., Cerutti L., et al.,** New and continuing developments at PROSITE, Nucl. Acids Res. 41 (D1, 1 Jan) (2013) D344–D347.

7. **Marchler-Bauer A., Zheng C., Chitsaz F., et al.,** CDD: conserved domains and protein three-dimensional structure, Nucl. Acids Res. 41 (D1, 1 Jan) (2013) D348–352.

8. **Finn R. D., Bateman A., Clements J., et al.,** Pfam: the protein families database. Nucl. Acids Res. 42 (D1, 1 Jan) (2014) D222–D230.

9. **Gibson D. G., Young L., Chuang R. Y., et al.,** Enzymatic assembly of DNA molecules up to several hundred kilobases, Nat. Methods. 6 (5) (2009) 343–345.

10. **Vasileva A. A., Aliukas S. A., Selkova P. A., et al.,** Type II CRISPR-Cas system nucleases: a pipeline for prediction and in vitro characterization. Molecular Biology (Moscow). 57 (3) (2023) 546–560 (in Russian).

11. **Laemmli U. K.,** Cleavage of structural proteins during the assembly of the head of bacteriophage T4, Nature. 227 (5259) (1970) 680–685.

12. **Kreuzer K. N., Jongeneel C. V.,** *Escherichia coli* phage T4 topoisomerase. Methods Enzymol. 100 (1983) 144–160.

13. **Walker J. E., Saraste M., Runswick M. J., Gay N. J.,** Distantly related sequences in the alpha- and beta-subunits of ATP synthase, myosin, kinases and other ATP-requiring enzymes and a common nucleotide binding fold, EMBO J. 1 (8) (1982) 945–951.

14. **Ramakrishnan C., Dani V. S., Ramasarma T.,** A conformational analysis of Walker motif A [GXXXXGKT (S)] in nucleotide-binding and other proteins, Protein Eng. Des. Sel. 15 (10) (2002) 783–798.

15. **Sun P., Tropea J. E., Waugh D. S.,** Enhancing the solubility of recombinant proteins in *Escherichia coli* by using hexahistidine-tagged maltose-binding protein as a fusion partner, In book: Evans Jr., T., Xu M.Q. (Eds.) Heterologous Gene Expression in *E. coli*, Book series: Methods in Molecular Biology, Vol. 705. Humana Press, Totowa, New Jersey, USA (2011) 259–274.

16. **Kowalczykowski S. C., Clow J., Krupp R. A.,** Properties of the duplex DNA-dependent ATPase activity of *Escherichia coli* RecA protein and its role in branch migration, Proc. Natl. Acad. Sci. 84 (10) (1987) 3127–3131.

17. **Yakunina M., Artamonova T., Borukhov S., et al.,** A non-canonical multisubunit RNA polymerase encoded by a giant bacteriophage, Nucl. Acids Res. 43 (21) (2015) 10411–10420.

СПИСОК ЛИТЕРАТУРЫ

1. **Jansen R., Embden J. D., Gaastra W., Schouls L. M.** Identification of genes that are associated with DNA repeats in prokaryotes // Molecular Microbiology. 2002. Vol. 43. No. 6. Pp. 1565–1575.

2. **Koonin E. V., Makarova K. S.** Origins and evolution of CRISPR-Cas systems // Philosophical Transactions of the Royal Society B: Biological Sciences. 2019. Vol. 374. No. 1772. P. 20180087.

3. **Krupovic M., Shmakov S., Makarova K. S., Forterre P., Koonin E. V.** Recent mobility of casposons, self-synthesizing transposons at the origin of the CRISPR-Cas immunity // Genome Biology and Evolution. 2016. Vol. 8. No. 2. Pp. 375–386.

4. **Faure G., Shmakov S. A., Yan W. X., Cheng D. R., Scott D. A., Peters J. E., Makarova K. S., Koonin E. V.** CRISPR-Cas in mobile genetic elements: Counter-defence and beyond // Nature Reviews Microbiology. 2019. Vol. 17. No. 8. Pp. 513–525.

5. **Makarova K. S., Wolf Y. I., Shmakov S. A., Liu Y., Li M., Koonin E. V.** Unprecedented diversity of unique CRISPR-Cas-related systems and Cas1 homologs in Asgard archaea // The CRISPR Journal. 2020. Vol. 3. No. 3. Pp. 156–163.

6. **Sigrist C. J., de Castro E., Cerutti L., Cuche B. A., Hulo N., Bridge A., Bougueleret L., Xenarios I.** New and continuing developments at PROSITE // Nucleic Acids Research. 2013. Vol. 41. No. D1, 1 January. Pp. D344–D347.

7. **Marchler-Bauer A., Zheng C., Chitsaz F., et al.** CDD: conserved domains and protein three-dimensional structure // Nucleic Acids Research. 2013. Vol. 41. No. D1, 1 January. Pp. D348–D352.

8. **Finn R. D., Bateman A., Clements J., et al.** Pfam: the protein families database // Nucleic Acids Research. 2014. Vol. 42. No. D1, 1 January. Pp. D222–D230.

9. **Gibson D. G., Young L., Chuang R.Y., Venter J. C., Hutchison C. A. 3rd, Smith H. O.** Enzymatic assembly of DNA molecules up to several hundred kilobases // Nature Methods. 2009. Vol. 6. No. 5. Pp. 343–345.

10. **Васильева А. А., Алюкас С. А., Селькова П. А., Арсениев А. Н., Чернова В. Е., Мушарова А. С., Климук Е. И., Ходорковский М. А., Северинов К. В.** Нуклеазы CRISPR-Cas II типа: алгоритм поиска и *in vitro* характеристика // Молекулярная биология. 2023. Т. 57. № 3. С. 546–560.

11. **Laemmli U. K.** Cleavage of structural proteins during the assembly of the head of bacteriophage T4 // Nature. 1970. Vol. 227. No. 5259. Pp. 680–685.

12. **Kreuzer K. N., Jongeneel C. V.** *Escherichia coli* phage T4 topoisomerase // Methods in Enzymology. 1983. Vol. 100. Pp. 144–160.

13. **Walker J. E., Saraste M., Runswick M. J., Gay N. J.** Distantly related sequences in the alpha- and beta-subunits of ATP synthase, myosin, kinases and other ATP-requiring enzymes and a common nucleotide binding fold // The EMBO (European Molecular Biology Organization) Journal. 1982. Vol. 1. No. 8. Pp. 945–951.

14. **Ramakrishnan C., Dani V. S., Ramasarma T.** A conformational analysis of Walker motif A [GXXXXGKT (S)] in nucleotide-binding and other proteins // Protein Engineering, Design, and Selection. 2002. Vol. 15. No. 10. Pp. 783–798.

15. **Sun P., Tropea J. E., Waugh D. S.** Enhancing the solubility of recombinant proteins in *Escherichia coli* by using hexahistidine-tagged maltose-binding protein as a fusion partner // Evans Jr., T., Xu M.Q. (Eds.) Heterologous Gene Expression in *E. coli*. Book series: Methods in Molecular Biology. Vol. 705. Totowa, New Jersey, USA: Humana Press, 2011. Pp. 259–274.

16. **Kowalczykowski S. C., Clow J., Krupp R. A.** Properties of the duplex DNA-dependent ATPase activity of *Escherichia coli* RecA protein and its role in branch migration // Proceedings of the National Academy of Sciences. 1987. Vol. 84. No. 10. Pp. 3127–3131.

17. **Yakunina M., Artamonova T., Borukhov S., Makarova K. S., Severinov K., Minakhin L.** A non-canonical multisubunit RNA polymerase encoded by a giant bacteriophage // Nucleic Acids Research. 2015. Vol. 43. No. 21. Pp. 10411–10420.

THE AUTHORS

ABRAMOVA Marina V.
Peter the Great St. Petersburg Polytechnic University
29 Politechnicheskaya St., St. Petersburg, 195251, Russia
abramova.mv07@gmail.com
ORCID: 0000-0003-4310-1189

MALYKH Anastasia S.
Peter the Great St. Petersburg Polytechnic University
29 Politechnicheskaya St., St. Petersburg, 195251, Russia
anastasiyaa2s3d4f5g6@gmail.com

GATIEVA Iana M.
Peter the Great St. Petersburg Polytechnic University
29 Politechnicheskaya St., St. Petersburg, 195251, Russia
yana.gatieva6@gmail.com

KAZALOV Maksim A.
Peter the Great St. Petersburg Polytechnic University
29 Politechnicheskaya St., St. Petersburg, 195251, Russia
maksim.kazalov@gmail.com
ORCID: 0000-0001-5640-8142

SELKOVA Polina A.
Peter the Great St. Petersburg Polytechnic University
29 Politechnicheskaya St., St. Petersburg, 195251, Russia
polina.nanobio@gmail.com
ORCID: 0000-0002-9562-1998

YAKIMOV Alexander P.
Peter the Great St. Petersburg Polytechnic University
29 Politechnicheskaya St., St. Petersburg, 195251, Russia
yaleks@gmail.com
ORCID: 0000-0003-0462-1157

VASILEVA Aleksandra A.
Peter the Great St. Petersburg Polytechnic University
Complex of NBICS Technologies, National Research Center "Kurchatov Institute"(Moscow)
29 Politechnicheskaya St., St. Petersburg, 195251, Russia
daucussativus7@gmail.com
ORCID: 0000-0002-0070-4898

ARSENIEV Anatolii N.
Peter the Great St. Petersburg Polytechnic University,
Complex of NBICS Technologies, National Research Center "Kurchatov Institute"(Moscow)
29 Politechnicheskaya St., St. Petersburg, 195251, Russia
arsenievanatoly@gmail.com
ORCID: 0000-0003-0901-4188

KHODORKOVSKII Mikhail A.
Peter the Great St. Petersburg Polytechnic University
29 Politechnicheskaya St., St. Petersburg, 195251, Russia
khodorkovskii@gmail.com
ORCID: 0000-0003-0562-0156

СВЕДЕНИЯ ОБ АВТОРАХ

АБРАМОВА Марина Викторовна – *инженер-исследователь лаборатории молекулярной микробиологии Института биомедицинских систем и биотехнологий Санкт-Петербургского политехнического университета Петра Великого, Санкт-Петербург, Россия.*
195251, Россия, г. Санкт-Петербург, Политехническая ул., 29
abramova.mv07@gmail.com
ORCID: 0000-0003-4310-1189

МАЛЫХ Анастасия Сергеевна – *лаборант-исследователь лаборатории молекулярной микробиологии Института биомедицинских систем и биотехнологий Санкт-Петербургского политехнического университета Петра Великого, Санкт-Петербург, Россия.*
195251, Россия, г. Санкт-Петербург, Политехническая ул., 29
malyh.as@edu.spbstu.ru

ГАТИЕВА Яна Маратовна – *лаборант-исследователь лаборатории молекулярной микробиологии Института биомедицинских систем и биотехнологий Санкт-Петербургского политехнического университета Петра Великого, Санкт-Петербург, Россия.*
195251, Россия, г. Санкт-Петербург, Политехническая ул., 29
yana.gatieva6@gmail.com

КАЗАЛОВ Максим Алексеевич – *инженер-исследователь лаборатории молекулярной микробиологии Института биомедицинских систем и биотехнологий Санкт-Петербургского политехнического университета Петра Великого, Санкт-Петербург, Россия.*
195251, Россия, г. Санкт-Петербург, Политехническая ул., 29
maksim.kazalov@gmail.com
ORCID: 0000-0001-5640-8142

СЕЛЬКОВА Полина Анатольевна – *инженер-исследователь лаборатории молекулярной микробиологии Института биомедицинских систем и биотехнологий Санкт-Петербургского политехнического университета Петра Великого, Санкт-Петербург, Россия.*
195251, Россия, г. Санкт-Петербург, Политехническая ул., 29
polina.nanobio@gmail.com
ORCID: 0000-0002-9562-1998

ЯКИМОВ Александр Павлович – *кандидат физико-математических наук, научный сотрудник лаборатории молекулярной микробиологии Института биомедицинских систем и биотехнологий Санкт-Петербургского политехнического университета Петра Великого, Санкт-Петербург, Россия.*
195251, Россия, г. Санкт-Петербург, Политехническая ул., 29
yaleks@gmail.com
ORCID: 0000-0003-0462-1157

ВАСИЛЬЕВА Александра Андреевна – *инженер-исследователь лаборатории молекулярной микробиологии Института биомедицинских систем и биотехнологий Санкт-Петербургского политехнического университета Петра Великого, Санкт-Петербург; инженер комплекса НБИКС-природоподобных технологий Национального исследовательского центра «Курчатовский институт», Москва, Россия.*
195251, Россия, г. Санкт-Петербург, Политехническая ул., 29
daucussativus7@gmail.com
ORCID: 0000-0002-0070-4898

АРСЕНИЕВ Анатолий Николаевич – *научный сотрудник Научно-исследовательского комплекса «Нанобиотехнологии» Института биомедицинских систем и биотехнологий Санкт-Петербургского политехнического университета Петра Великого, Санкт-Петербург; лаборант-исследователь комплекса НБИКС-природоподобных технологий Национального исследовательского центра «Курчатовский институт», Москва, Россия.*
195251, Россия, г. Санкт-Петербург, Политехническая ул., 29
arsenievanatoly@gmail.com
ORCID: 0000-0003-0901-4188

ХОДОРКОВСКИЙ Михаил Алексеевич – *кандидат физико-математических наук, директор Научно-исследовательского комплекса «Нанобиотехнологии» Института биомедицинских систем и биотехнологий Санкт-Петербургского политехнического университета Петра Великого, Санкт-Петербург, Россия.*
195251, Россия, г. Санкт-Петербург, Политехническая ул., 29
khodorkovskii@gmail.com
ORCID: 0000-0003-0562-0156

Received 08.12.2023. Approved after reviewing 26.02.2024. Accepted 26.02.2024.
Статья поступила в редакцию 08.12.2023. Одобрена после рецензирования 26.02.2024. Принята 26.02.2024.

NUCLEAR PHYSICS

Original article
DOI: https://doi.org/10.18721/JPM.17110

A GENERATIVE ADVERSARIAL NETWORK AS THE BASIS FOR A SEMI-INCLUSIVE DEEP INELASTIC LEPTON SCATTERING GENERATOR ON A POLARIZED PROTON

A. A. Lobanov ✉, *Ya. A. Berdnikov, E. V. Muzyaev*

Peter the Great St. Petersburg Polytechnic University, St. Petersburg, Russia

✉ lobanov2.aa@edu.spbstu.ru

Abstract. A neural network, that allows someone to obtain results for semi-inclusive deep inelastic scattering of charged leptons on polarized protons, with the production of pions or strange K mesons, has been developed in this study. The research covered both transverse and longitudinal polarizations of the proton. A range of initial energies of colliding particles was chosen from 20 to 100 GeV in a central mass system. The range is typical for electron-ion colliders currently being designed. It has been shown that it is possible to predict the physical characteristics of the final lepton and hadron with high accuracy as well as different variants of proton polarization using the proposed neural network.

Keywords: semi-inclusive deep inelastic scattering, asymmetries, machine learning, neural network, generative-adversarial network

Citation: Lobanov A. A., Berdnikov Ya. A., Muzyaev E. V., A generative adversarial network as the basis for a semi-inclusive deep inelastic lepton scattering generator on a polarized proton, St. Petersburg State Polytechnical University Journal. Physics and Mathematics. 17 (1) (2024) 93–102. DOI: https://doi.org/10.18721/JPM.17110

Научная статья
УДК 539.12
DOI: https://doi.org/10.18721/JPM.17110

ГЕНЕРАТИВНО-СОСТЯЗАТЕЛЬНАЯ СЕТЬ КАК ОСНОВА ГЕНЕРАТОРА ПОЛУИНКЛЮЗИВНОГО ГЛУБОКОНЕУПРУГОГО РАССЕЯНИЯ ЛЕПТОНА НА ПОЛЯРИЗОВАННОМ ПРОТОНЕ

А. А. Лобанов ✉, *Я. А. Бердников, Е. В. Музяев*

Санкт-Петербургский политехнический университет Петра Великого,
Санкт-Петербург, Россия

✉ lobanov2.aa@edu.spbstu.ru

Аннотация. В статье предложена разработанная нейронная сеть, позволяющая получать результаты полуинклюзивного глубоконеупругого рассеяния заряженных лептонов на поляризованных протонах с рождением пионов или странных K-мезонов. Рассмотрены состояния поляризации протона (поперечная и продольная). Выбран диапазон начальных энергий сталкивающихся частиц 20 − 100 ГэВ в системе центра масс, характерный для электрон-ионных коллайдеров, проектируемых в настоящее время. Показано, что с помощью предложенной разработки можно с высокой точностью предсказывать физические характеристики конечного лептона и адрона, а также различные варианты поляризации протона.

Ключевые слова: полуинклюзивное глубоконеупругое рассеяние, асимметрия, машинное обучение, нейронная сеть, генеративно-состязательная сеть

Ссылка для цитирования: Лобанов А. А., Бердников Я. А., Музяев Е. В. Генеративно-состязательная сеть как основа генератора полуинклюзивного глубоконеупругого рассеяния лептона на поляризованном протоне // Научно-технические ведомости СПбГПУ. Физико-математические науки. 2024. Т. 17. № 1. С. 93–102. DOI: https://doi.org/10.18721/JPM.17110

Introduction

Deep inelastic scattering (DIS) of charged leptons by protons is one of the processes allowing to gain insight into the internal structure of the proton [1].

It is well-known that a large number of different particles are generated in the DIS process.

Experimental research and theoretical approaches to description of such processes are usually complex and require very sophisticated detector systems, involving various phenomenological models for the analysis of experimental results, related, for example, to hadronization [2]. For this reason, exclusive DIS studies have not yet been conducted.

However, as a rule, inclusive (with detection of only the scattered lepton) and semi-inclusive (with detection of the scattered lepton and one of the hadrons produced) DIS is considered.

Study of semi-exclusive DIS of leptons by protons becomes much more complicated if the lepton interacts with a polarized (longitudinally or transversely) proton [3].

At the same time, experiments with polarized particles are significantly more informative and allow to come close to solving problems related to the origins of proton spin.

Taking into account the polarization of the proton in the initial state of semi-inclusive GNR allows to measure various spin asymmetries that arise in the final state (after the process of semi-inclusive DIS) [3].

Transverse single-spin asymmetries occur during transverse polarization of the proton; these can be described within the framework of the Sivers [4] and Collins effects [3]. The Sivers asymmetry A_{Siv} can be used to generate the Sievers parton distribution functions,

describing the correlations between the transverse momenta of quarks and the nucleon spin. The Collins asymmetries A_{Col} help measure the transverse functions of the parton distribution together with the Collins fragmentation functions [3]. All these functions are of great importance for describing the internal structure of the nucleon [3].

In the case of longitudinal polarization of the proton, a longitudinal single-spin asymmetry A_{ul} occurs. Its values allow to generate the T-odd correlation functions (parton distributions and fragmentation functions), which arise due to the exchange between quarks and longitudinally polarized gluons [5]. It was established relatively recently that non-zero T-odd parton distributions are compatible with the invariance of the strong interaction with respect to time reversal [5].

Large amounts of data obtained in each experiment are required to investigate any of the above-mentioned asymmetries and the associated mechanisms of their formation, which are determined by the parton distribution functions and fragmentation functions. In addition, it is necessary to carry out experimental studies with a large set of initial energies (reference points). Analysis of results of such experiments makes it possible to gain information about the parton distribution functions and fragmentation functions [6].

Due to limited experimental capabilities (particularly financial resources), it is impossible to obtain a sufficient number of reference points that can be used to approximate the distribution functions. As a result, it is necessary to develop programs that can interpolate or extrapolate experimental data by the selected parameters. The increase in data volumes (due to interpolation and extrapolation) should have a positive effect on the accuracy of the obtained distribution functions.

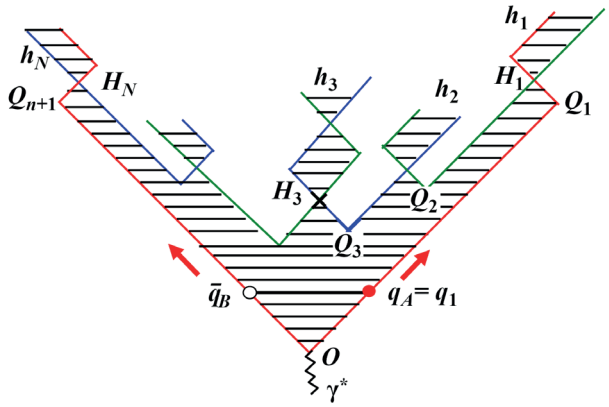

Fig. 1. Simplified scheme of hadronization process:
O is the interaction point; Q_1, Q_2, ..., Q_{n+1} are the string breaking points;
H_1, H_2, ..., H_N are the emission points of hadrons h_1, h_2, ..., h_N; q_A, $\bar{q}_B$ are the interacting quark A and the remnant B, respectively; γ^* is the virtual photon; arrows indicate the directions of motion of q_A and $\bar{q}_B$

Machine learning methods and, in particular, generative adversarial networks (GANs) can be used to solve problems related handling big data [7].

GANs allow to develop algorithms and write computer programs (called event generators) that can quickly obtain the necessary values from the original dataset, without specialized simulation of the interaction of particles and the detector. We should also note that such programs allow to avoid using large amounts of disk space, since they preserve the target distributions as small subsets of parameters [9].

Methodology

As noted in the introduction, the current state of experimental technology, the financial capabilities of the global scientific community and the presence of a large number of competing physical problems do not allow to experimentally obtain a sufficient number of data points that could be used for machine learning.

Due to this circumstance (lack of sufficient experimental data), the reference points were obtained in our study via modeling semi-inclusive deep-inelastic scattering of leptons by a

polarized proton. The simulation was carried out using the PYTHIA8 program based on the Monte Carlo generator [10], expanded by the StringSpinner software package [11]. The latter includes the string+$^3P_0$ model [12], based on the Lund model [2], making it possible to account for the fragmentation of polarized quarks during hadronization.

The Lund model of hadronization can be illustrated by a simplified scheme (Fig. 1) [12].

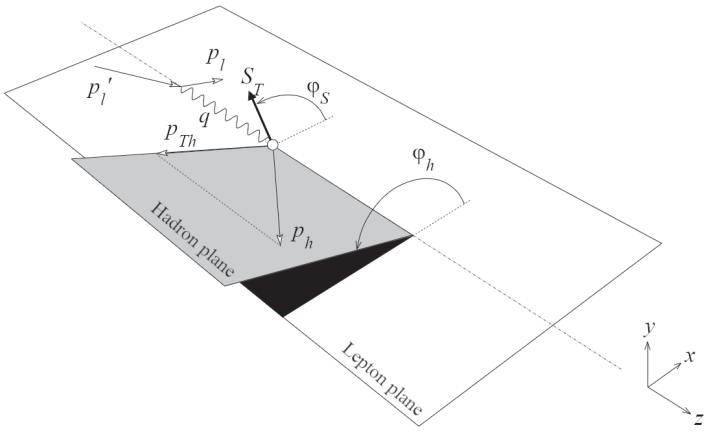

Fig. 2. Kinematics of semi-inclusive deep inelastic scattering [13];
planes of hadrons and leptons are shown
(see the notations used in the text)

We assume that the proton interacting with the charged lepton consists of a quark A and a remnant B (q_A and $\bar{q}_B$, respectively, in Fig. 1) [12].

The virtual photon γ* emitted by the charged lepton is absorbed by one of the quarks of the unpolarized proton (for example, the quark q_A in Fig. 1). The photon γ* transfers its momentum to quark A, so that the separation of quark A and proton remnant B consequently begins. According to the Lund model, a relativistic string is stretched between objects A and B as a result of color interaction whose energy increases throughout the separation. The increase in tension continues until a quark-antiquark pair $q\bar{q}$ can be produced. The string then breaks with the production of a $q\bar{q}$ pair at the breaking points Q_1, Q_2, ..., Q_{n+1} [12]. This process can occur repeatedly, as long as the law of energy-momentum conservation allows it. In some cases, quarks and antiquarks can form a bound state, producing mesons [2]. This leads to semi-exclusive deep-inelastic scattering of charged leptons by unpolarized protons.

As noted above, the PYTHIA8+StringSpinner software package should be used for semi-exclusive deep-elastic scattering of a charged lepton by a polarized proton.

Using PYTHIA8+StringSpinner made it possible to simulate semi−inclusive deep inelastic lepton scattering by a polarized proton in the initial energy range $\sqrt{S_{lN}}$ = 20−100 GeV. The values of 20, 40, 60, 80 and 100 GeV were considered as reference initial energies.

100,000 events were generated for the considered charged leptons (e^+, e^-, μ^+, μ^-) and hadrons (π^0, $\pi+$, π^-, K^+, K^- at reference initial energies and at various polarizations of the proton (longitudinal, transverse, and without polarization). The four-momenta of the finite lepton p_l and hadron p_h were obtained from each event. These are referred to as real data. Using real data allows to obtain the Sivers and Collins asymmetries A_{Siv} and A_{Col} for transversely polarized proton and the asymmetry A_{ul} for longitudinally polarized proton.

The multiplicity distribution N_h for Collins asymmetry A_{Col} is proportional to the binomial in the case of transversely polarized proton [14]:

$$\frac{dN_h}{dx_{\text{Bj}}dzdp_{Th}d\varphi_{\text{Col}}} \propto 1 + D_{NN}S_T A_{\text{Col}} \sin\varphi_{\text{Col}}, \quad (1)$$

where D_{NN} is the depolarization factor, $D_{NN} = 2(1-y)/[1+(1-y)^2]$.

The quantity φ_{Col} in Eq. (1) is defined as

$$\varphi_{\text{Col}} = \varphi_h + \varphi_S + \pi,$$

where φ_S is the azimuthal angle between the transverse component of the spin vector **S** and the lepton scattering plane; φ_h is the azimuthal angle between the hadron emission plane and the lepton scattering plane (Fig. 2).

The hadron multiplicity distribution N_h for the Sivers asymmetry A_{Siv} is defined as [14]:

$$\frac{dN_h}{dx_{\text{Bj}}dzdp_{Th}d\varphi_{\text{Siv}}} \propto 1 + S_T A_{\text{Siv}} \sin\varphi_{\text{Siv}}, \quad (2)$$

where $\varphi_{\text{Siv}} = \varphi_h - \varphi_S$.

$\mathbf{S}_T$ in expressions (1), (2) is the nucleon spin vector perpendicular to both the virtual photon and the emitted hadron.

The values of asymmetry A_{ul} for longitudinallu polarized proton can be obtained from the hadron multiplicity distribution N_h, which is defined as [14]:

$$\frac{dN_h}{dx_{\text{Bj}}dzdp_{Th}d\varphi_h} \propto 1 + (1-y)A_{ul} \sin 2\varphi_h. \quad (3)$$

The following quantities were used in expressions (1)–(3):

$x_{\text{Bj}} = \dfrac{Q^2}{2Pq}$ is the Bjerken variable [13] describing the fraction of the proton momentum carried by the parton (P is the four-momentum of the proton, q is the four-momentum of the virtual photon, $Q^2 = -q^2$);

$z = \dfrac{P \cdot p_h}{P \cdot q}$ is the fraction of the four-momentum of the virtual photon transferred to the emitted hadron [13] (p_h is the four-momentum of the hadron produced);

p_{Th} is the projection of the hadron momentum, perpendicular to the virtual photon;

$y = \dfrac{P \cdot q}{P \cdot p_l'}$ is the fraction of the energy of the incident lepton transferred to the virtual photon [13] (p'_l is the four-momentum of the lepton before interaction).

The described method for calculating asymmetries was successfully tested by comparing it with experimental data obtained in the HERMES and COMPASS experiments [12, 13], yielding good agreement of the predictions with the experimental results. This success gives us reason to select and use a technique for calculating semi-inclusive scattering of leptons by a polarized proton. The range of initial energies typical for future electron-ion colliders is taken [16].

As noted above, specific calculations can be performed using the PYTHIA8+StringSpinner software package.

More details can be found in [17] (see the section “Methodology”), where PYTHIA8 is combined with a generative adversarial network (GAN) to build a generator for semi-exclusive deep-elastic scattering of charged leptons by polarized protons.

In this paper, the type of proton polarization was added as another input parameter of the generator (in addition to those used in [17]). Furthermore, the number of hidden layers of the GAN generator and discriminator was increased to 6

Results of neural network construction and discussion

Fig. 3 shows the values of the Collins asymmetry as a function of the Bjerken variable x_{Bj} for the hadrons π^- and π^+ with the electron e^- and muon μ^- scattered by transversely polarized protons at an initial energy of 40 GeV. Evidently, the asymmetries obtained based on GAN predictions coincide within the uncertainty range with the predictions obtained based on PYTHIA8+StringSpinner data.

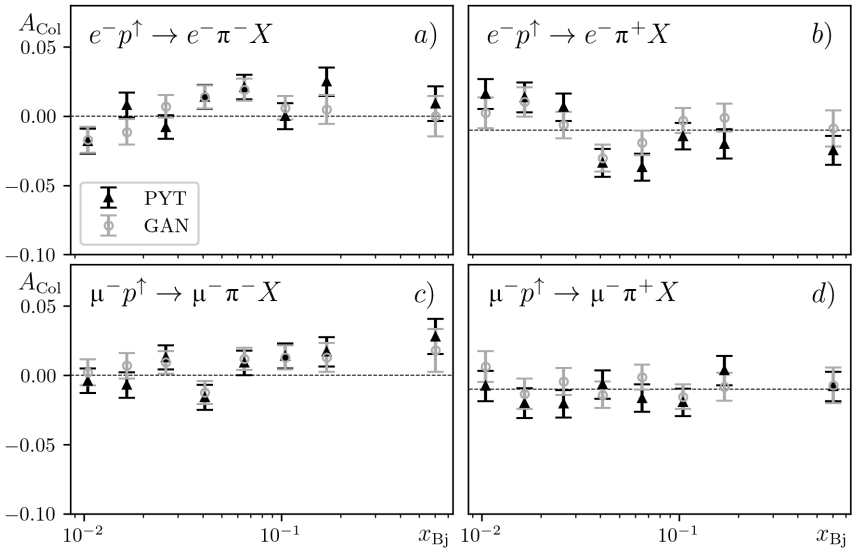

Fig. 3. Dependences of Collins asymmetry ACol on the Bjerken variable x_{Bj} for scattering of electrons e^- (*a*, *b*) and muons μ^- (*c*, *d*) by transversely polarized protons with the production of negative (π^-) (*a*, *c*) and positive (π^+) (*b*, *d*) pions. The initial energy of the particles is 40 GeV.
The data were obtained using GAN (gray dots) and PYTHIA8+StringSpinner (black triangles)

Fig. 4 shows the values of the Sivers asymmetry as a function of the Bjerken variable x_{Bj} for kaons K^- and pions π^0 under scattering of positrons e^+ and antimuon μ^+ by transversely polarized protons at an interpolated initial energy of 70 GeV; the results were obtained based on GAN and PYTHIA8+StringSpinner. It follows from the data presented in Fig. 4 that the GAN-based generator retains the prediction accuracy with a different scattering configuration for Sivers asymmetries, including at energies that were not involved in the learning process.

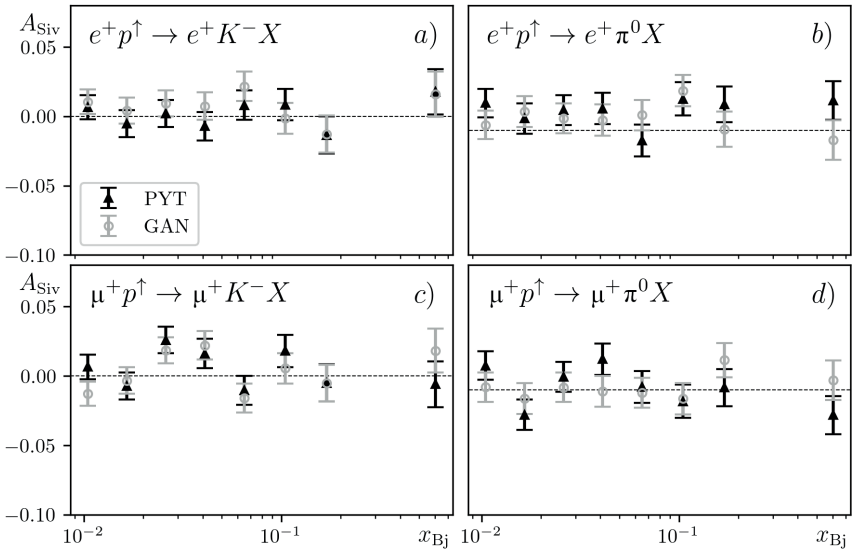

Fig. 4. Dependences of Sivers asymmetry A_{Siv} on the Bjerken variable x_{Bj} for scattering of positrons e^+ (*a*, *b*) and antimuons μ^+ (*c*, *d*) by transversely polarized protons with the production of negative kaons K^- (*a*, *c*) and neutral pions π^0 (*b*, *d*).
The data were obtained using GAN (gray dots) and PYTHIA8+StringSpinner (black triangles)

Fig. 5 shows the values of asymmetries A_{ul} depending on the values of the Bjerken variable x_{Bj} for kaons K^+ and pions π^- under scattering of electrons e^- and antimuons μ^+ by transversely polarized protons at an initial energy of 120 GeV, obtained based on GAN and PYTHIA8+StringSpinner. The analysis of these data shows that the GAN model can work with longitudinally polarized protons as well as at energies exceeding the energy range considered during training (extrapolated values).

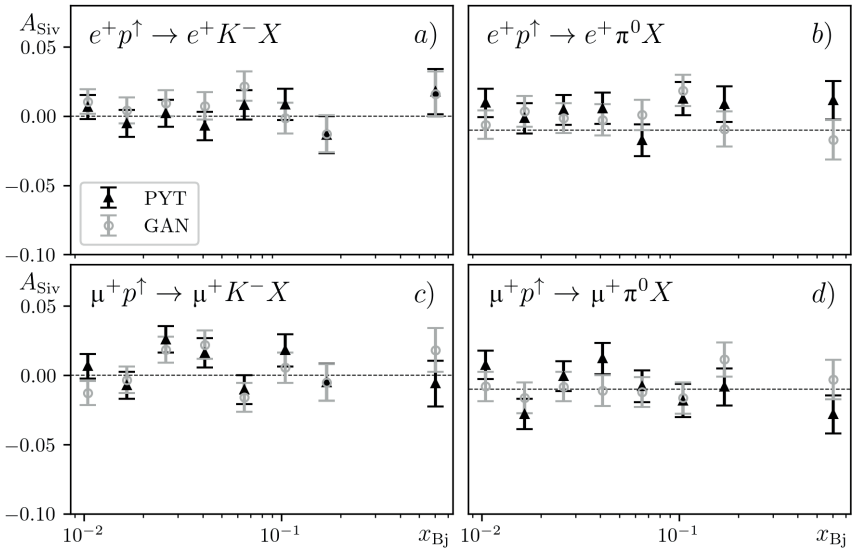

Fig. 5. Dependences of asymmetry A_{ul} on the Bjerken variable x_{Bj} for scattering of electrons e^- (*a*, *b*) and antimuons μ^+ (*c*, *d*) by longitudinally polarized protons with the production of positive kaons K^+ (*a*, *c*) and negative pions π^- (*b*, *d*). The initial energy is 120 GeV.
The data were obtained using GAN (gray dots) and PYTHIA8+StringSpinner (black triangles)

Conclusion

In the presented study, a software package (event generator) was developed based on a generative-adversarial network model in order to predict the characteristics of the final state of a lepton and an additional hadron as a result of semi-exclusive deep-elastic scattering of a lepton on a polarized proton.

It is established that the constructed event generator can work accurately with various scattering configurations: incident leptons (e^+, e^-, μ^+, μ^-), hadrons (π^0, π^+, π^-, K^+, K^-), proton polarization states (longitudinal, transverse, without polarization) and initial energies (we considered the range of 20−100 GeV). Moreover, the generator works with the initial energies on which it was pre-trained (20, 40, 60, 80, 100 GeV), with the interpolated energies (between the reference values) and extrapolated ones (values above the considered range).

Studies indicate that the event generator can accurately (accounting for errors) predict various types of asymmetry (A_{Col}, A_{Siv}, A_{ul}) that occur in the presence of proton polarization. The prediction accuracy is preserved for various scattering configurations.

REFERENCES

1. **Blümlein J.,** The theory of deeply inelastic scattering, Prog. Part. Nucl. Phys. 69 (March) (2013) 28–84.

2. **Ferreres-Solé S., Sjöstrand T.,** The space–time structure of hadronization in the Lund model, Eur. Phys. J. C. 78 (11) (2018) 983.

3. **Airapetian A. Akopov N., Akopov Z., et al.** (Hermes Collaboration), Effects of transversity in deep-inelastic scattering by polarized protons, Phys. Lett. B. 693 (1) (2010) 11–16.

4. **Airapetian A. Akopov N., Akopov Z., et al.** (Hermes Collaboration), Observation of the naive-T-odd Sivers effect in deep-inelastic scattering, Phys. Rev. Lett. 103 (15) (2009) 152002.

5. **Metz A., Schlegel M.,** Twist-3 single-spin asymmetries in semi-inclusive deep-inelastic scattering, Eur. Phys. J. A. 22 (3) (2004) 489–494.

6. **Barone V., Bradamante F., Bressan A., et al.,** Transversity distributions from difference asymmetries in semi-inclusive DIS, Phys. Rev. D. 99 (11) (2019) 114004.

7. **Goodfellow I., Pouget-Abadie J., Mirza M., et al.,** Generative adversarial networks, Commun. ACM. 63 (11) (2020) 139–144.

8. **Clark A., Donahue J., Simonyan K.,** Adversarial video generation on complex datasets; arXiv: 1907.06571v2, 2019. https://doi.org/10.48550/arXiv. 1907.06571.

9. **Hashemi B., Amin N., Datta K., et al.,** LHC analysis-specific datasets with Generative Adversarial Networks. arXiv:1901.05282, 2019. https://doi.org/10.48550/arXiv.1901.05282.

10. **Sjöstrand T., Mrenna S., Skands P.,** A brief introduction to PYTHIA 8.1, Comp. Phys. Commun. 178 (11) (2008) 852–867.

11. **Kerbizi A., Lönnblad L.,** StringSpinner-adding spin to the PYTHIA string fragmentation, Comp. Phys. Commun. 272 (March) (2022) 108234.

12. **Kerbizi A., Artux X., Belghobsi Z., Martin A.,** Simplified recursive $^3P_0$ model for the fragmentation of polarized quarks, Phys. Rev. D. 100 (1) (2019) 014003.

13. **Whitehill R. M., Zhou Y., Sato N., Melnitchouk W.,** Accessing gluon polarization with high-P_T hadrons in SIDIS, Phys. Rev. D. 107 (3) (2023) 034033.

14. **Anselmino M., Boglione M., D'Alesia U., et al.,** General helicity formalism for semi-inclusive deep inelastic scattering, Phys. Rev. D. 83 (11) (2011) 114019.

15. **Mao X., Li Q., Xie H., et al.,** On the effectiveness of least squares generative adversarial networks, IEEE Trans. Pattern Anal. Mach. Intell. 41 (12) (2019) 2947–2960.

16. **Accardi A., Albacete J. L., Anselmino M., et al.,** Electron-ion collider: The next QCD frontier. Understanding the glue that binds us all, Eur. Phys. J. A. 52 (9) (2016) 268.

17. **Lobanov A. A., Berdnikov Ya. A.,** Simulation of semi-inclusive deep inelastic lepton scattering on a proton at energies of 20–100 GeV on the basis of the Generative-Adversarial Neural Network, St. Petersburg State Polytechnical University Journal. Physics and Mathematics. 16 (4) (2023) 189–197 (in Russian).

СПИСОК ЛИТЕРАТУРЫ

1. **Blümlein J.** The theory of deeply inelastic scattering // Progress in Particle and Nuclear Physics. 2013. Vol. 69. March. Pp. 28–84.

2. **Ferreres-Solé S., Sjöstrand T.** The space–time structure of hadronization in the Lund model // The European Physical Journal C. 2018. Vol. 78. No. 11. P. 983.

3. **Airapetian A. Akopov N., Akopov Z., et al.** (Hermes Collaboration). Effects of transversity in deep-inelastic scattering by polarized protons // Physics Letters B. 2010. Vol. 693. No. 1. Pp. 11–16.

4. **Airapetian A. Akopov N., Akopov Z., et al.** (Hermes Collaboration). Observation of the naive-T-odd Sivers effect in deep-inelastic scattering // Physical Review Letters. 2009. Vol. 103. No. 15. P. 152002.

5. **Metz A., Schlegel M.** Twist-3 single-spin asymmetries in semi-inclusive deep-inelastic scattering // The European Physical Journal A. 2004. Vol. 22. No. 3. Pp. 489–494.

6. **Barone V., Bradamante F., Bressan A., Kerbizi A., Martin A., Moretti A., Matousek J., Sbrizzai G.** Transversity distributions from difference asymmetries in semi-inclusive DIS // Physical Review D. 2019. Vol. 99. No. 11. P. 114004.

7. **Goodfellow I., Pouget-Abadie J., Mirza M., Xu B., Warde-Farley D., Ozair S., Courville A., Bengio Y.** Generative adversarial networks // Communications of the ACM. 2020. Vol. 63. No. 11. Pp. 139–144.

8. **Clark A., Donahue J., Simonyan K.** Adversarial video generation on complex datasets. arXiv: 1907.06571v2, 2019. https://doi.org/10.48550/arXiv. 1907.06571.

9. **Hashemi B., Amin N., Datta K., Olivito D., Pierini M.** LHC analysis-specific datasets with Generative Adversarial Networks. arXiv:1901.05282, 2019. https://doi.org/10.48550/arXiv.1901.05282.

10. **Sjöstrand T., Mrenna S., Skands P.** A brief introduction to PYTHIA 8.1 // Computer Physics Communications. 2008. Vol. 178. No. 11. Pp. 852–867.

11. **Kerbizi A., Lönnblad L.** StringSpinner-adding spin to the PYTHIA string fragmentation // Computer Physics Communications. 2022. Vol. 272. March. P. 108234.

12. **Kerbizi A., Artux X., Belghobsi Z., Martin A.** Simplified recursive $^3P_0$ model for the fragmentation of polarized quarks // Physical Review D. 2019. Vol. 100. No. 1. P. 014003.

13. **Whitehill R. M., Zhou Y., Sato N., Melnitchouk W.** Accessing gluon polarization with high-P_T hadrons in SIDIS // Physical Review D. 2023. Vol. 107. No. 3. P. 034033.

14. **Anselmino M., Boglione M., D'Alesia U., Melis S., Nocera ER., Prokudin A.** General helicity formalism for semi-inclusive deep inelastic scattering // Physical Review D. 2011. Vol. 83. No. 11. P. 114019.

15. **Mao X., Li Q., Xie H., Lau R. Y. K., Wang Zh., Smolley S. P.** On the effectiveness of least squares generative adversarial networks // IEEE Transactions on Pattern Analysis and Machine Intelligence. 2019. Vol. 41. No. 12. Pp. 2947–2960.

16. **Accardi A., Albacete J. L., Anselmino M., et al.** Electron-ion collider: The next QCD frontier. Understanding the glue that binds us all // The European Physical Journal A. 2016. Vol. 52. No. 9. P. 268.

17. **Лобанов А. А., Бердников Я. А.** Моделирование полуинклюзивного, глубоконеупругого рассеяния лептона на протоне при энергиях 20–100 ГэВ на основе генеративно-состязательной нейронной сети // Научно-технические ведомости СПбГПУ. Физико-математические науки. 2023. Т. 16. № 4. С. 189–197.

THE AUTHORS

LOBANOV Andrey A.
Peter the Great St. Petersburg Polytechnic University
29 Politechnicheskaya St., St. Petersburg, 195251, Russia
lobanov2.aa@edu.spbstu.ru
ORCID: 0000-0002-8910-4775

BERDNIKOV Yaroslav A.
Peter the Great St. Petersburg Polytechnic University
29 Politechnicheskaya St., St. Petersburg, 195251, Russia
berdnikov@spbstu.ru
ORCID: 0000-0003-0309-5917

MUZYAEV Evgeniy V.
Peter the Great St. Petersburg Polytechnic University
29 Politechnicheskaya St., St. Petersburg, 195251, Russia
muzyaev.ev@edu.spbstu.ru
ORCID: 0009-0005-7144-4746

СВЕДЕНИЯ ОБ АВТОРАХ

ЛОБАНОВ Андрей Александрович — *студент Физико-механического института Санкт-Петербургского политехнического университета Петра Великого, Санкт-Петербург, Россия.*
195251, Россия, г. Санкт-Петербург, Политехническая ул., 29
lobanov2.aa@edu.spbstu.ru
ORCID: 0000-0002-8910-4775

БЕРДНИКОВ Ярослав Александрович — *доктор физико-математических наук, профессор Высшей школы фундаментальных физических исследований Санкт-Петербургского политехнического университета Петра Великого, Санкт-Петербург, Россия.*
195251, Россия, г. Санкт-Петербург, Политехническая ул., 29
berdnikov@spbstu.ru
ORCID: 0000-0003-0309-5917

МУЗЯЕВ Евгений Валерьевич — *студент Физико-механического института Санкт-Петербургского политехнического университета Петра Великого, Санкт-Петербург, Россия.*
195251, Россия, г. Санкт-Петербург, Политехническая ул., 29
muzyaev.ev@edu.spbstu.ru
ORCID: 0009-0005-7144-4746

Received 28.11.2023. Approved after reviewing 19.12.2023. Accepted 19.12.2023.
Статья поступила в редакцию 28.11.2023. Одобрена после рецензирования 19.12.2023. Принята 19.12.2023.

RADIOPHYSICS

Original article
DOI: https://doi.org/10.18721/JPM.17111

A PICOSECOND FIBER LASER BASED ON A TAPERED YTTERBIUM FIBER WITH THE LOW BIREFRINGENCE

A. S. Kozlov ✉, *A. V. Medvedev, E. A. Motorin*

E. A. Savelyev, V. S. Temkina, V. N. Filippov

Peter the Great St. Petersburg Polytechnic University, St. Petersburg, Russia

✉ kozlov_as@spbstu.ru

Abstract. This paper presents the results of the experimental study of a fiber laser connected according to the MOPA scheme, where a power amplifier was made of an ytterbium double-clad tapered spun fiber with low intrinsic birefringence. A peak output power of 160 kW with the average power of 160 W has been achieved at 1040 nm wavelength, 50 ps pulse duration and its repetition frequency of 20 MHz; the laser beam quality parameter and the mode-spot diameter being 1.15 and 35 μm, respectively. The values of azimuth, ellipticity and degree of polarization of the output radiation were found; their little sensitivity to the pump power was demonstrated. This research was the next important step in the development of high-power picosecond fiber lasers technology.

Keywords: ytterbium spun tapered fiber, picosecond fiber laser, intrinsic birefringence

Funding: The reported study was funded by Russian Science Foundation (Grant No. 22-19-00513 (https://rscf.ru/project/22-19-00513/)).

Citation: Kozlov A. S., Medvedev A. V., Motorin E. A., Savelyev E. A., Temkina V. S., Filippov V. N., A picosecond fiber laser based on a tapered ytterbium fiber with the low birefringence, St. Petersburg State Polytechnical University Journal. Physics and Mathematics. 17 (1) (2024) 103–113. DOI: https://doi.org/10.18721/JPM.17111

Научная статья
УДК 535.515
DOI: https://doi.org/10.18721/JPM.17111

ПИКОСЕКУНДНЫЙ ИМПУЛЬСНЫЙ ВОЛОКОННЫЙ ЛАЗЕР НА ОСНОВЕ КОНИЧЕСКОГО ИТТЕРБИЕВОГО ВОЛОКНА С НИЗКИМ СОБСТВЕННЫМ ДВУЛУЧЕПРЕЛОМЛЕНИЕМ

А. С. Козлов ✉, *А. В. Медведев, Е. А. Моторин*

Е. А. Савельев, В. С. Темкина, В. Н. Филиппов

Санкт-Петербургский политехнический университет Петра Великого,
Санкт-Петербург, Россия

✉ kozlov_as@spbstu.ru

Аннотация. В работе приведены результаты экспериментального исследования волоконного лазера, построенного по схеме задающего генератора и усилителя мощности, изготовленного из иттербиевого конического spun-волокна с двойной оболочкой и малой величиной собственного двулучепреломления. На длине волны 1040 нм при длительности импульсов 50 пс и частоте повторения 20 МГц достигнута пиковая

выходная мощность 160 кВт при средней мощности 160 Вт. Параметр качества лазерного пучка M^2 = 1,15, диаметр модового пятна – 35 мкм. Определены значения азимута, эллиптичности и степени поляризации выходного излучения и продемонстрирована их слабая зависимость от мощности накачки. Проведенное исследование стало следующим важным шагом в развитии технологии мощных пикосекундных волоконных лазеров.

Ключевые слова: иттербиевое коническое волокно, пикосекундный волоконный лазер, активное spun-волокно, собственное двулучепреломление

Финансирование: Исследование выполнено при финансовой поддержке Российского научного фонда (грант 22-19-00513 (https://rscf.ru/project/22-19-00513/)).

Ссылка для цитирования: Козлов А. С., Медведев А. В., Моторин Е. А., Савельев Е. А., Темкина В. С., Филиппов В. Н. Пикосекундный импульсный волоконный лазер на основе конического иттербиевого волокна с низким собственным двулучепреломлением // Научно-технические ведомости СПбГПУ. Физико-математические науки. 2024. Т. 17. № 1. С. 103–113. DOI: https://doi.org/10.18721/JPM.17111

Introduction

The technology of high-power picosecond fiber lasers has been developing rapidly over the past decade [1]. They are widely used in materials processing, medicine and lithography. Such lasers are typically made by the Master Oscillator Power Amplifier scheme (MOPA). Such a scheme includes a master oscillator generating low-power laser pulses with good spatiotemporal coherence, and a chain of optical power amplifiers increasing the pulse energy to the required level.

The main problem limiting the peak output power of such a system is the occurrence of undesirable nonlinear effects in the active fiber of the last amplifier stage. To overcome the limitations imposed by these effects, active optical fibers of special types are used. These include, for example, fibers with large mode area (LMA), low aperture and large spot size (up to 14 μm [2]), microstructured fibers [3], 3C fibers (chirally-coupled-core) [4], anisotropic tapered fibers with large mode area [5]. A characteristic of a high-power fiber laser, which is important for coherent combination or nonlinear wavelength conversion, is stable output polarization.

The most common technical solution available for overcoming these limitations are fibers with large intrinsic anisotropy [6]. However, while this approach is successful for passive fibers, a number of negative phenomena begin to arise in the case of active fibers. When exciting radiation is pumped into the cladding, part of it is absorbed and heats the fiber (the so-called quantum defect), leading to a change in internal stresses in the fiber and unpredictable distortions of its birefringence [7, 8]. As a result, the polarization state of laser radiation changes.

To solve this problem, it was proposed to use active fiber with small intrinsic birefringence [9], namely, a spun fiber, for which this parameter is usually about 10^{-8} rad/m.

The first picosecond lasers with an average output power of up to 70 W and mode field diameter of 26 μm, built according by the MOPE scheme, were experimentally studied in [9–12], using spun fiber as the last amplifier. Using spun fiber with spin pitch from 7.5 to 30 mm made it possible to obtain the output polarization that was an order of magnitude more stable than in the case of active optical fibers with large intrinsic anisotropy.

Furthermore, it was found in [10, 11] that the state of polarization of light at the output of active tapered fiber with strong anisotropy significantly depends on the power of the pump radiation injected into the cladding. The authors of these papers observed a significant drift in the polarization state of radiation at the output of an amplifier with a PANDA-type tapered fiber (a customized polarization-maintaining fiber). The ellipticity and azimuth of the fiber changed by tens of degrees even at the input pump power of 20 W. At the same time, high stability of output polarization was demonstrated in [11] for an amplifier with spun fiber with low intrinsic birefringence at the same input pump power of 20 W, without any measures to stabilize the temperature of the fiber.

Our study is aimed at further developing the technology of high-power picosecond fiber lasers using active tapered fiber with small intrinsic birefringence as the last amplifier stage. The article is aimed at increasing the peak and average radiation power in this type of laser, also considering its polarization characteristics and their dependence on the power of the injected pump radiation and its operating time.

Spun tapered double-clad fiber (sT-DCF)

We used sT-DCF fibers in the experiments, manufactured at the Fryazino Branch of the Kotelnikov Institute of Radioengineering and Electronics of the Russian Academy of Sciences (Fryazino, Moscow Oblast, Russia) [9]. The optical fibers were drawn from a preform doped with ytterbium ions Yb^{3+}, which had a step-index core, using a technology similar to that used for spun passive [13] and active tapered [9–13] fibers. During the extraction process, the workpiece was fed into a high-temperature furnace at a speed variable in time according to a given law, which was necessary to form an optimal longitudinal profile [14]. The profile of the fiber prepared is shown in Fig. 1. The angular rotation velocity of the preform was also varied during fiber drawing in the range of 200–300 rpm.

The ratio of the diameters of the core, the first and the second claddings was 1.0:12.7:15.9, and the numerical apertures of the shells were 0.13 and 0.27, respectively. The in-core absorption was 850 dB/m at a wavelength of 976 nm. Two segments were cut off from the first cladding, which made it possible to reduce the proportion of helical modes that do not pass through the core of the fiber. A photograph of the wide end of the fiber is also shown in Fig. 1. Note that this is a standard method for increasing pump absorption in active fibers [15].

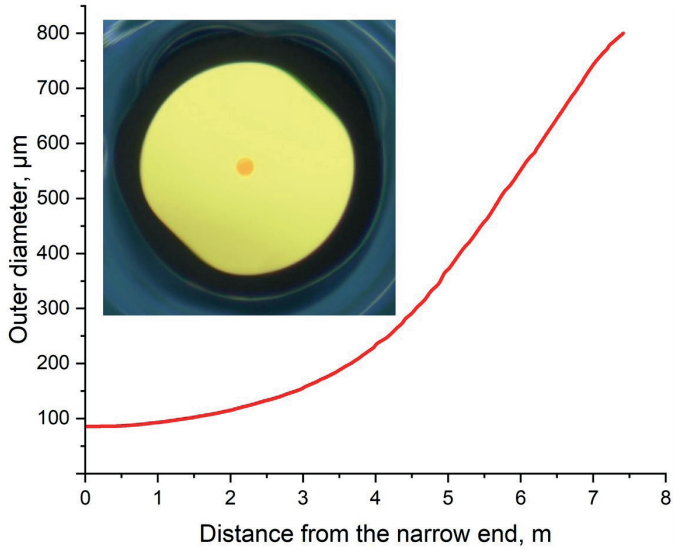

Fig. 1. Profile of fiber considered. Graph of variation in diameter of second cladding along the length of sT-DCF fiber is given.
Inset: photograph of wide end of the fiber

Thus, the diameter of the outer glass cladding changed smoothly from 85 to 800 μm, and the diameter of the core from 5.3 to 50.3 μm, so that only the fundamental mode was excited in the narrow end of the tapered fiber. The total length of the fiber was 7.5 m, the spin pitch was 30 mm. A reflective coating with a low refractive index (numerical aperture of 0.53) was applied to the outer surface of the fiber, with a protective acrylate coating then applied over it.

The value of intrinsic birefringence (the difference in the propagation constants of eigenmodes) for this sT-DCF fiber was

$1.45 \cdot 10^{-8}$ rad/m; the latter was determined experimentally by the Jones method [11, 16–18].

Experimental setup

A prototype of a fiber laser was assembled by the MOPA scheme, using the prepared optical fibers as the gain medium of the last amplifier stage (Fig. 2).

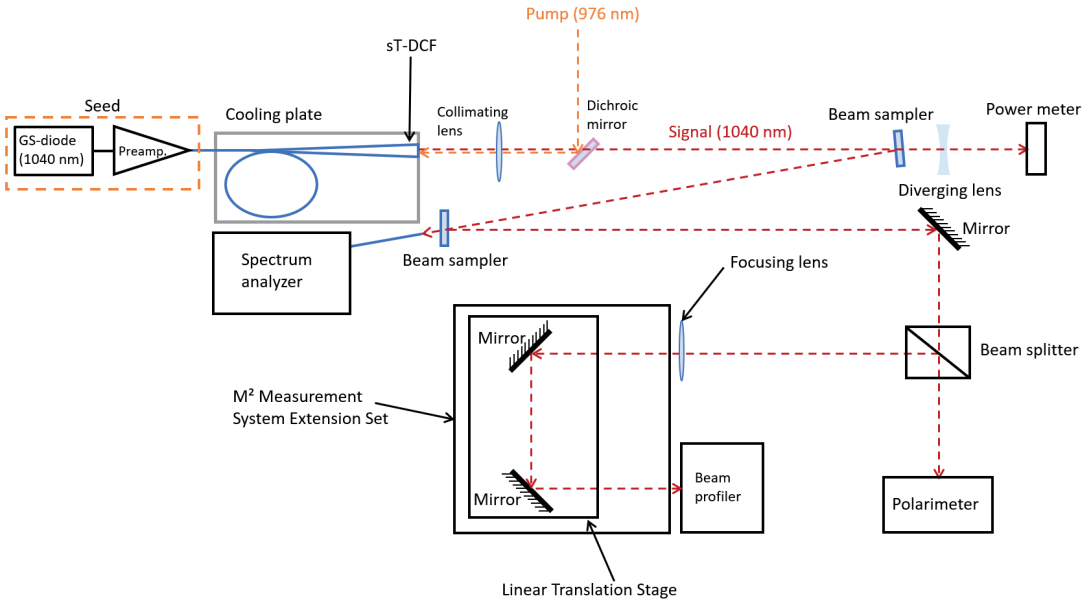

Fig. 2. Layout of fiber laser prototype for studying the parameters of its radiation

A commercially available laser diode with a fiber output (GS-diode) was used as the master source, emitting linearly polarized light with a wavelength of 1040 nm; the repetition rate of 50 ps pulses was equal to 20 MHz. Radiation with a power of about 1 MW was pre-amplified to an average power of about 100 MW while maintaining a spectral linewidth of 50 pm (Fig. 3), after which it was injected into the core of the narrow end of the active sT-DCF.

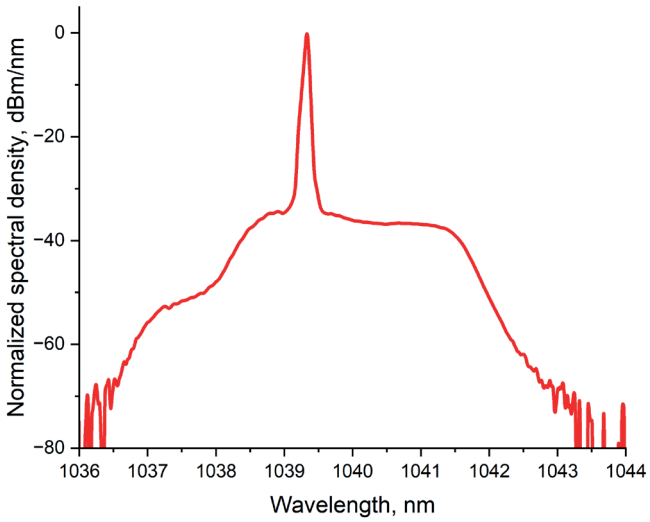

Fig. 3. Spectral density of master laser emission

The active fiber was pumped using a system of two laser diodes emitting at a wavelength of 976 nm and combined by means of a fused fiber-optic coupler. Pump radiation was injected into the cladding of the wide end of the fiber using a dichroic mirror and an aspherical lens. The entire active fiber was located on a special cooled plate so as to reduce the temperature gradient inside the gain medium and avoid thermal damage to the fiber.

The output power, radiation spectrum, beam quality and polarization characteristics of radiation (degree of polarization, ellipticity and azimuth) were constantly monitored during the laser's operation. The Ophir L1500W-SH power meter (Ophir Optronics, Israel), Ando optical spectrum analyzer (AAATesters, USA), Thorlabs M2MS-BC106VIS/M beam analyzer and

Thorlabs PAX1000IR2/M polarimeter (Thorlabs, USA) were used. If it was necessary to measure the divergence of the output beam, the focusing lens in front of the entrance slit of the beam analyzer was removed. The maximum range of displacements of the linear translation stage located inside the analyzer was 100 mm.

Experimental results

The gain parameters of MOPA. Fig. 4 shows the dependence of the output power of the fiber laser on the pump power injected into the wide end of the active spun fiber. The efficiency of the pump radiation conversion of the amplifier we manufactured reached 63%. The average output power in pulse mode (duration of 50 ps, repetition rate of 20 MHz) was 160 W for an input pump power of 270 W, the peak output power was 160 kW.

The average power was limited solely by the available pump power. The conversion efficiency did not decrease with increasing pump power.

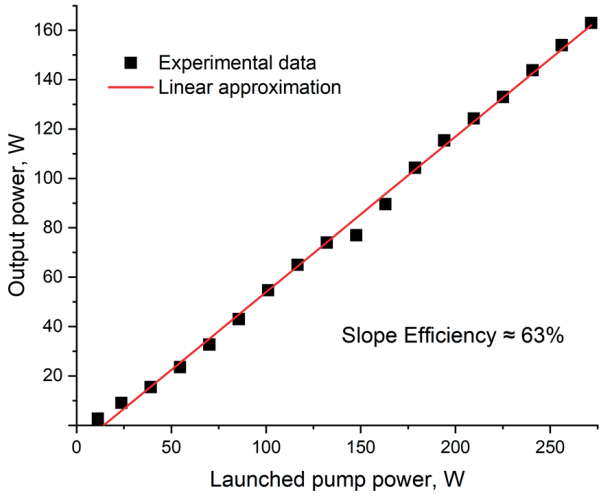

Fig. 4. Experimental dependence of average output power of amplifier (fiber laser) (symbols) on pump power and its linear approximation (solid red line)

The mode field diameter (MFD) was determined by measuring the divergence of the output beam, using the following ratio for the diffraction-limited divergence [19]:

$$\mathrm{MFD} = 4\lambda / \pi\Theta, \qquad (1)$$

where λ is the wavelength, Θ is the divergence of the beam.

The measured MFD for the used tapered spun fiber was 35 μm.

The laser radiation spectra obtained at different amplified signal powers are shown in Fig. 5. As follows from the experimental results, the contribution made by radiation outside the spectral range of the master laser increases with an increase in the output signal power. It is caused by self-phase modulation and four-wave mixing.

We studied the shape of the caustics, as well as its cross sections in the near and far fields (Fig. 6). The above results, as well as the high beam quality ($M^2 < 1.3$) (Fig. 7) indicate the predominance of the fundamental mode inside the active tapered fiber.

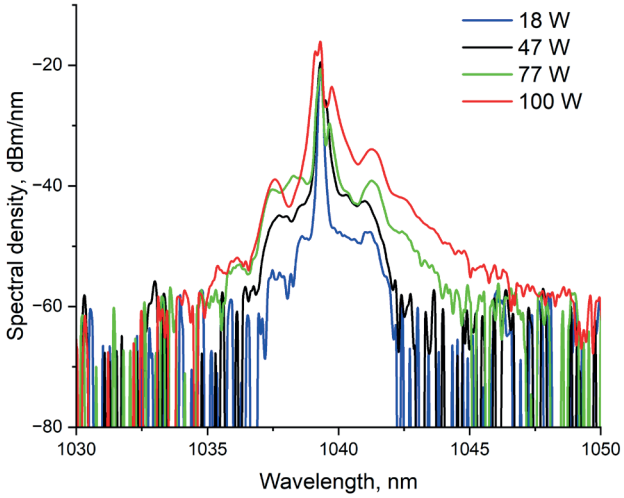

Fig. 5. Laser emission spectra at different values of average output power of amplified signal

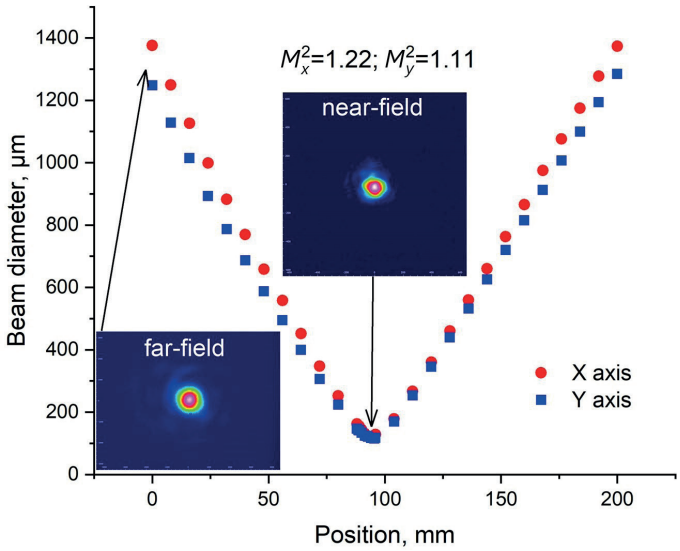

Fig. 6. Dependences of mode field diameter (measured by the 4-sigma method (ISO Standard)) on distances along two axes between the focusing lens and the beam analyzer.
Insets: photographs of the far and near fields

Polarization state of output radiation. The polarization states of laser radiation at different output power levels are shown on the Poincarй sphere (Fig. 8). Similar analysis was carried out in [10, 11] but for small values (25 W) of the pump power injected into cladding shell of active tapered spun fiber. Pump radiation with a power of up to 270 W was injected in this study, causing changes in the polarization state with an increase in output radiation power.

To study the long-term stability of the polarization state at the output of the amplifier with spun fiber, we conducted a two-hour test at constant output power of 125 W (Fig. 9).

The standard deviation for azimuth, ellipticity and degree of polarization was approximately 0.4°, 0.5° and 1.5%, respectively. This result indicates a high temporal stability of the polarization state of the amplifier considered. The smooth change in the dependences, only amounting to a few degrees, is caused by the instability of water temperature cooling the fiber during the experiment.

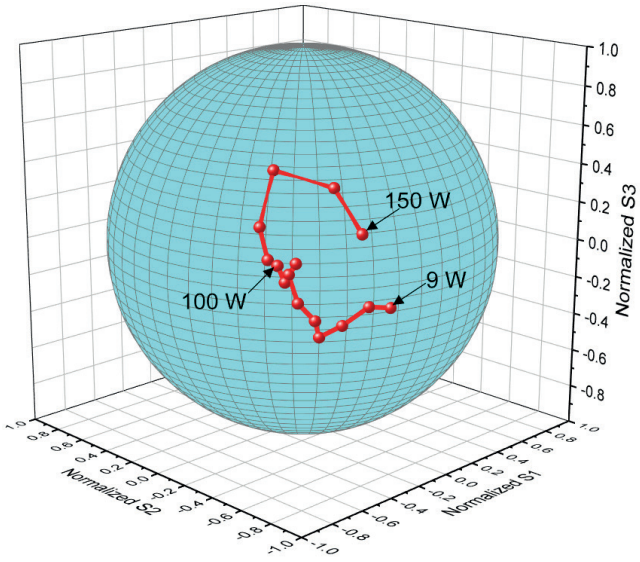

Fig. 8. Representation of polarization states of output radiation at different power levels on the Poincaré sphere

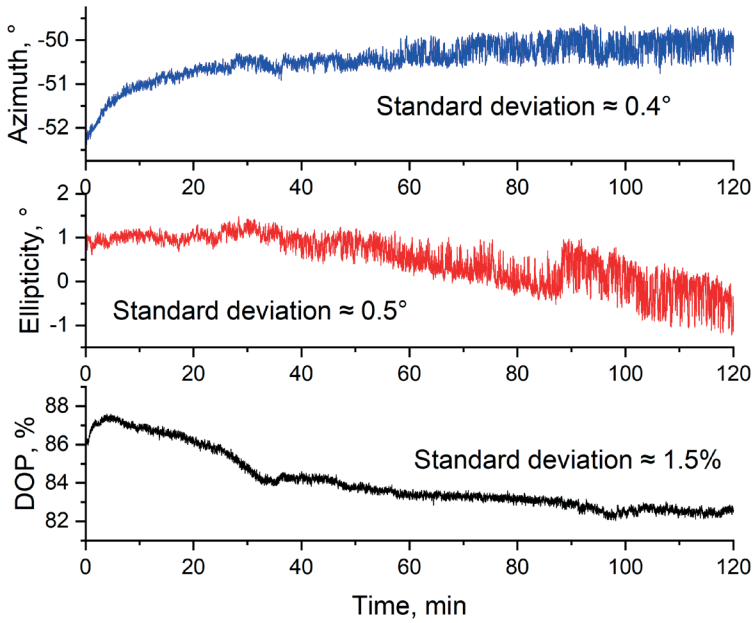

Fig. 9. Results of two-hour test for polarization characteristics of output radiation of amplifier with active tapered spun fiber.
Drifts are shown for azimuth (upper graph), ellipticity (central graph) and degree of polarization (lower graph).
Signal power during the experiment was 125 W

Discussion and conclusions

We considered double-clad active tapered ytterbium-doped spun fiber with low intrinsic birefringence ($1.45 \cdot 10^{-8}$ rad/m) with large mode field diameter (35 μm). The longitudinal change in the core diameter is an effective measure for suppressing stimulated Mandelstam–Brillouin scattering [20]. The large spot size makes it possible to increase the threshold for Raman scattering. Thanks to the appropriately selected geometry of the fiber, namely, the variable diameter along its length and large diameter of the core at the wide end, using an active tapered fiber in a power

amplifier allowed to significantly increase the threshold for the appearance of nonlinear effects and achieve simultaneously high values of both average and peak output power. The low intrinsic birefringence of the tapered spun fiber ensured high stability of the output state of polarization with varying pump power.

As a result of the conducted study, we presented a fiber laser based on active tapered spun fiber, designed by the MOPA scheme, generating radiation with a peak power of 160 kW at a wavelength of 1040 nm, an average output power of 160 W in pulsed mode and an output beam quality of $M^2 \approx 1.15$. The linewidth at the level of −3 dB was about 0.2 nm with an average output power of 100 W with an optical pulse duration of 50 ps and a pulse repetition rate of 20 MHz.

It is important to note that one of the significant results of this study, compared with those published earlier (see, for example, [9−12]), is that stable polarization of output radiation was achieved for a powerful (160 W) amplifier with active fiber. Moreover, the dependence of output polarization state on the injected pump power was obtained at pump power values significantly higher than in [9−12], up to 270 W. In addition, the dependences of fiber parameters such as azimuth and ellipticity on the injected pump power were experimentally recorded.

The conducted study takes the next important step in the development of high-power picosecond fiber laser technology.

Acknowledgment

The authors express their gratitude to the staff of the laboratory of Special Fibers of the Kotelnikov Institute of Radioengineering and Electronics for the samples of optical fibers provided for research.

REFERENCES

1. **Petrov A., Odnoblyudov M., Gumenyuk R., et al.,** Picosecond Yb-doped tapered fiber laser system with 1.26 MW peak power and 200 W average output power, Sci. Rep. 10 (20 Oct) (2020) 17781.

2. **Kliner D. A. V., Koplow J. P., Goldberg L., et al.,** Polarization-maintaining amplifier employing double-clad bow-tie fiber, Opt. Lett. 26 (4) (2001) 184−186.

3. **Schmidt O., Rothhardt J., Eidam T., et al.,** Single-polarization large-mode-area Yb-doped photonic crystal fiber, Proc. Conf. on Lasers and ElectroOptics/Quantum Electronics and Laser Sci. Conf. & Photonic Appl. Syst. Technol, OSA (2008) CMB2.

4. **Ma X., Zhu Ch., Hu I-N., et al.,** Single-mode chirally-coupled-core fibers with larger than 50 μm diameter cores, Opt. Express. 22 (1) (2014) 9206−9219.

5. **Fedotov A., Noronen T., Gumenyuk R., et al.,** Ultra-large core birefringent Yb-doped tapered double clad fiber for high power amplifiers, Opt. Express. 26 (6) (2018) 6581−6592.

6. **Rashleigh S.** Origins and control of polarization effects in single-mode fibers, J. Light. Technol. 1 (2) (1983) 312−331.

7. **Ourmazd A., Varnham M. P., Birch R. D., Payne D. N.,** Thermal properties of highly birefringent optical fibers and preforms, Appl. Opt. 22 (15) (1983) 2374−2379.

8. **Rashleigh S. C., Marrone M. J.,** Temperature dependence of stress birefringence in an elliptically clad fiber, Opt. Lett. 8 (2) (1983) 127−129.

9. **Fedotov A., Ustimchik V., Chamorovskii Y., et al.,** Low-birefringence active tapered fibers for high-power applications, OSA (Optical Society of America) Advanced Photonics Congress, 13−16 July, 2020. Washington, USA (2020) SoTu2H.7.

10. **Fedotov A., Ustimchik V., Rissanen J., et al.,** Large mode area double-clad ytterbium-doped spun tapered fiber, J. Opt. Soc. Am. B. 38 (12) (2021) F161−F169.

11. **Fedotov A., Ustimchik V., Rissanen J., et al.,** Active tapered double-clad fiber with low birefringence, Opt. Express. 29 (11) (2021) 16506−16519.

12. **Fedotov A., Ustimchik V., Rissanen J., et al.,** Large mode area double-clad ytterbium-doped tapered fiber with low birefringence, Proc. SPIE, 11665 (March) (2021) 116651T.

13. **Chamorovskiy Yu., Starostin N., Ryabko M., et al.,** Miniature microstructured fiber coil with high magneto-optical sensitivity, Opt. Commun. 282 (23) (2009) 4618−4621.

14. **Filippov V., Kerttula J., Chamorovskii Yu., et al.,** Highly efficient 750 W tapered double-clad ytterbium fiber laser, Opt. Express. 18 (12) (2010) 12499−12512.

15. **Kouznetsov D., Moloney J. V.,** Efficiency of pump absorption in double-clad fiber amplifiers. II. Broken circular symmetry J. Opt. Soc. Am. B. 19 (6) (2002) 1259–1263.

16. **Jones R. C.,** A new calculus for the treatment of optical systems. VI. Experimental determination of the matrix*, J. Opt. Soc. Am. 37 (2) (1947) 110–112.

17. **Jones R. C.,** A new calculus for the treatment of optical systems. VII. Properties of the *N*-matrices, J. Opt. Soc. Am. 38 (8) (1948) 671–685.

18. **Kozlov A., Medvedev A., Temkina V., et al.,** Investigation of polarization characteristics of active tapered fibers, Proc. 2023 Int. Conf. Electrical Engineering and Photonics (EExPolytech-2023), Oct. 19–20, 2023. Peter the Great St. Petersburg Polytechnic University, St. Petersburg, Russia (2024) 402–405.

19. **Guttman J. L.,** Mode-field diameter and "spot size" measurements of lensed and tapered specialty fibers, Proc. Symp. on Optical Fiber Measurements, Sept. 24–26, 2002. National Institute of Standards and Technology, San-Jose, USA, 2002.

20. **Shiraki K., Ohashi M., Tateda M.,** Suppression of stimulated Brillouin scattering in a fiber by changing the core radius, Electron. Lett. 31 (8) (1995) 668–669.

СПИСОК ЛИТЕРАТУРЫ

1. **Petrov A., Odnoblyudov M., Gumenyuk R., Minyonok L., Chumachenko A., Filippov V.** Picosecond Yb-doped tapered fiber laser system with 1.26 MW peak power and 200 W average output power // Scientific Reports. 2020. Vol. 10. 20 October. P. 17781.

2. **Kliner D. A. V., Koplow J. P., Goldberg L., Carter A. L. G., Digweed J. A.** Polarization-maintaining amplifier employing double-clad bow-tie fiber // Optics Letters. 2001. Vol. 26. No. 4. Pp. 184–186.

3. **Schmidt O., Rothhardt J., Eidam T., Röser F., Limpert J., Tünnermann A., Hansen K., Jakobsen C., Broeng J.** Single-polarization large-mode-area Yb-doped photonic crystal fiber // Conference on Lasers and ElectroOptics/Quantum Electronics and Laser Science Conference and Photonic Applications Systems Technologies. Optical Society of America, (2008) CMB2.

4. **Ma X., Zhu Ch., Hu I-N., Kaplan A., Galvanauskas A.** Single-mode chirally-coupled-core fibers with larger than 50 μm diameter cores // Optics Express. 2014. Vol. 22. No. 1. Pp. 9206–9219.

5. **Fedotov A., Noronen T., Gumenyuk R., Ustimchik V., Chamorovskii Y., Golant K., Odnoblyudov M., Rissanen J., Niemi T., Filippov V.** Ultra-large core birefringent Yb-doped tapered double clad fiber for high power amplifiers // Optics Express. 2018. Vol. 26. No. 6. Pp. 6581–6592.

6. **Rashleigh S.** Origins and control of polarization effects in single-mode fibers // Journal of Lightwave Technology. 1983. Vol. 1. No. 2. Pp. 312–331.

7. **Ourmazd A., Varnham M. P., Birch R. D., Payne D. N.** Thermal properties of highly birefringent optical fibers and preforms // Applied Optics. 1983. Vol. 22. No. 15. Pp. 2374–2379.

8. **Rashleigh S. C., Marrone M. J.** Temperature dependence of stress birefringence in an elliptically clad fiber // Optics Letters. 1983. Vol. 8. No. 2. Pp. 127–129.

9. **Fedotov A., Ustimchik V., Chamorovskii Y., Gumenyuk R., Filippov V.** Low-birefringence active tapered fibers for high-power applications // OSA (Optical Society of America) Advanced Photonics Congress, 13–16 July, 2020. Washington, USA (2020) SoTu2H.7.

10. **Fedotov A., Ustimchik V., Rissanen J., Noronen T., Gumenyuk R., Kolosovskii A., Voloshin V., Vorob'ev I., Yu. Chamorovskii, Filippov V.** Large mode area double-clad ytterbium-doped spun tapered fiber // Journal of the Optical Society of America B. 2021. Vol. 38. No. 12. Pp. F161–F169.

11. **Fedotov A., Ustimchik V., Rissanen J., Kolosovskii A., Voloshin V., Vorob'ev I., Gumenyuk R., Chamorovskiy Yu., Filippov V.** Active tapered double-clad fiber with low birefringence // Optics Express. 2021. Vol. 29. No. 11. Pp.16506–16519.

12. **Fedotov A., Ustimchik V., Rissanen J., Noronen T., Gumenyuk R., Chamorovskiy Yu., Kolosovskii A., Voloshin V., Vorob'ev I., Filippov V.** Large mode area double-clad ytterbium-doped tapered fiber with low birefringence // Proceedings of SPIE. March 2021. Vol. 11665. P. 116651T.

13. **Chamorovskiy Yu., Starostin N., Ryabko M., Sazonov A., Morshnev S., Gubin V., Vorob'ev I., Nikitov S.** Miniature microstructured fiber coil with high magneto-optical sensitivity // Optics Communications. 2009. Vol. 282. No. 23. Pp. 4618–4621.

14. **Filippov V., Kerttula J., Chamorovskii Yu., Golant K., Okhotnikov O. G.** Highly efficient 750 W tapered double-clad ytterbium fiber laser // Optics Express. 2010. Vol. 18. No. 12. Pp. 12499–12512.

15. **Kouznetsov D., Moloney J. V.** Efficiency of pump absorption in double-clad fiber amplifiers. II. Broken circular symmetry // Journal of the Optical Society of America B. 2002. Vol. 19. No. 6. Pp. 1259–1263.

16. **Jones R. C.** A new calculus for the treatment of optical systems. VI. Experimental determination of the matrix* // Journal of the Optical Society of America. 1947. Vol. 37. No. 2. Pp. 110–112.

17. **Jones R. C.** A new calculus for the treatment of optical systems. VII. Properties of the *N*-matrices // Journal of the Optical Society of America. 1948. Vol. 38. No. 8. Pp. 671–685.

18. **Kozlov A., Medvedev A., Temkina V., Fillipov V., Chamorovskiy Y.** Investigation of polarization characteristics of active tapered fibers // Proceedings of the 2023 International Conference on Electrical Engineering and Photonics (EExPolytech-2023). October 19–20, 2023. Peter the Great St. Petersburg Polytechnic University, Saint Petersburg, Russia, 2024. Pp. 402–405.

19. **Guttman J. L.** Mode-field diameter and "spot size" measurements of lensed and tapered specialty fibers // Proceedings of Symposium on Optical Fiber Measurements. September 24–26, 2002. National Institute of Standards and Technology, San-Jose, USA, 2002. 34 p.

20. **Shiraki K., Ohashi M., Tateda M.** Suppression of stimulated Brillouin scattering in a fiber by changing the core radius // Electronics Letters. 1995. Vol. 31. No. 8. Pp. 668–669.

THE AUTHORS

KOZLOV Artemy S.
Peter the Great St. Petersburg Polytechnic University
29 Politechnicheskaya St., St. Petersburg, 195251, Russia
kozlov_as@spbstu.ru
ORCID: 0000-0002-1722-1964

MEDVEDEV Andrey V.
Peter the Great St. Petersburg Polytechnic University
29 Politechnicheskaya St., St. Petersburg, 195251, Russia
medvedev@spbstu.ru
ORCID: 0000-0001-7083-9184

MOTORIN Evgenii A.
Peter the Great St. Petersburg Polytechnic University
29 Politechnicheskaya St., St. Petersburg, 195251, Russia
eug.motorin@yandex.ru
ORCID: 0000-0002-7901-3933

SAVELYEV Evgeny A.
Peter the Great St. Petersburg Polytechnic University
29 Politechnicheskaya St., St. Petersburg, 195251, Russia
swoopermsu@yandex.ru
ORCID: 0000-0003-0213-5833

TEMKINA Valentina S.
Peter the Great St. Petersburg Polytechnic University
29 Politechnicheskaya St., St. Petersburg, 195251, Russia
temkina_vs@spbstu.ru
ORCID: 0000-0003-2083-8989

FILIPPOV Valery N.
Peter the Great St. Petersburg Polytechnic University
29 Politechnicheskaya St., St. Petersburg, 195251, Russia
filippov_vn@spbstu.ru
ORCID: 0000-0002-0354-8616

СВЕДЕНИЯ ОБ АВТОРАХ

КОЗЛОВ Артемий Сергеевич – *инженер Высшей школы прикладной физики и космических технологий Санкт-Петербургского политехнического университета Петра Великого, Санкт-Петербург, Россия.*
195251, Россия, Санкт-Петербург, Политехническая ул., 29
kozlov_as@spbstu.ru
ORCID: 0000-0002-1722-1964

МЕДВЕДЕВ Андрей Викторович – *кандидат физико-математических наук, доцент Высшей школы прикладной физики и космических технологий Санкт-Петербургского политехнического университета Петра Великого, Санкт-Петербург, Россия.*
195251, Россия, Санкт-Петербург, Политехническая ул., 29
medvedev@spbstu.ru
ORCID: 0000-0001-7083-9184

МОТОРИН Евгений Анатольевич – *инженер Высшей школы прикладной физики и космических технологий Санкт-Петербургского политехнического университета Петра Великого, Санкт-Петербург, Россия.*
195251, Россия, Санкт-Петербург, Политехническая ул., 29
eug.motorin@yandex.ru
ORCID: 0000-0002-7901-3933

САВЕЛЬЕВ Евгений Александрович – *инженер Высшей школы прикладной физики и космических технологий Санкт-Петербургского политехнического университета Петра Великого, Санкт-Петербург, Россия.*
195251, Россия, Санкт-Петербург, Политехническая ул., 29
swoopermsu@yandex.ru
ORCID: 0000-0003-0213-5833

ТЕМКИНА Валентина Сергеевна – *ассистентка Высшей школы прикладной физики и космических технологий Санкт-Петербургского политехнического университета Петра Великого, Санкт-Петербург, Россия.*

195251, Россия, Санкт-Петербург, Политехническая ул., 29
temkina_vs@spbstu.ru
ORCID: 0000-0003-2083-8989

ФИЛИППОВ Валерий Николавевич – *кандидат физико-математических наук, ведущий научный сотрудник Высшей школы прикладной физики и космических технологий Санкт-Петербургского политехнического университета Петра Великого, Санкт-Петербург, Россия.*
195251, Россия, Санкт-Петербург, Политехническая ул., 29
filippov_vn@spbstu.ru
ORCID: 0000-0002-0354-8616

Received 30.09.2023. Approved after reviewing 24.11.2023. Accepted 24.11.2023.
Статья поступила в редакцию 30.09.2023. Одобрена после рецензирования 24.11.2023. Принята 24.11.2023.

MECHANICS

Original article
DOI: https://doi.org/10.18721/JPM.17112

A COMPARISON OF APPROACHES TO SPECIFYING THE MODAL MATRICES IN THE MODAL CONTROL OF ELASTIC SYSTEMS WITH AND WITHOUT OBSERVERS

A. V. Fedotov ✉

Institute for Problems of Mechanical Engineering RAS, St. Petersburg, Russia

✉ alvafed@yandex.ru

Abstract. The implementation of modal control of distributed elastic objects involves the use of modal matrices: a mode analyzer and a mode synthesizer specifying the linear transformation of vectors of measured and control signals in order to separate the eigenmodes of the object in the control system. The standard method for calculating the modal matrices is the inversion of the influence matrices. The article proposes an alternative method: transposing the influence matrices with normalization of the action on different modes. As an example, the problem of suppression of forced vibrations of a thin metal beam using piezoelectric sensors and actuators has been solved numerically, and different combinations of the above methods and different variants of normalization have been tested. Two types of control systems were considered, the former being based on modal and frequency filters and the latter being based on modal observers. The best control result was shown to be achieved with the combined use of the above methods for both types of control systems considered.

Keywords: modal control, modal matrices, mode analyzer, mode synthesizer, observer

Citation: Fedotov A. V., A comparison of approaches to specifying the modal matrices in the modal control of elastic systems with and without observers, St. Petersburg State Polytechnical University Journal. Physics and Mathematics. 17 (1) (2024) 114–129. DOI: https://doi.org/10.18721/JPM.17112

Научная статья
УДК 531.391+681.5
DOI: https://doi.org/10.18721/JPM.17112

СРАВНЕНИЕ ПОДХОДОВ К ЗАДАНИЮ МОДАЛЬНЫХ МАТРИЦ ПРИ МОДАЛЬНОМ УПРАВЛЕНИИ УПРУГИМИ СИСТЕМАМИ С НАБЛЮДАТЕЛЯМИ И БЕЗ НИХ

А. В. Федотов ✉

Институт проблем машиноведения РАН, Санкт-Петербург, Россия

✉ alvafed@yandex.ru

Аннотация. Реализация модального управления распределенными упругими объектами предполагает использование модальных матриц – анализатора и синтезатора форм, задающих линейные преобразования векторов измеренных и управляющих сигналов с целью разделения собственных форм объекта в системе управления. Стандартный способ задания модальных матриц заключается в обращении матриц влияния. В статье предлагается альтернативный способ: транспонирование данных матриц с нормированием воздействия на разные формы. На примере численного решения задачи гашения вынужденных колебаний тонкой металлической балки

с помощью пьезоэлектрических сенсоров и актуаторов тестируются разные комбинации названных методов и разные варианты нормирования. Рассмотрено управление как с наблюдателями, так и без них – на основе модальных и частотных фильтров. Показано, что наилучший результат управления достигается при комбинированном использовании рассмотренных методов в системах как с наблюдателями, так и без них.

Ключевые слова: модальное управление, модальные матрицы, анализатор форм, синтезатор форм, наблюдатель

Ссылка для цитирования: Федотов А. В. Сравнение подходов к заданию модальных матриц при модальном управлении упругими системами с наблюдателями и без них // Научно-технические ведомости СПбГПУ. Физико-математические науки. 2024. Т. 17. № 1. С. 114–129. DOI: https://doi.org/10.18721/JPM.17112

Introduction

In recent decades, modal control has become a widespread approach to active control of distributed systems, including elastic ones [1–3]. Its basic principle is separate control of different vibration modes of an object, assumed to be independent from each other. The efficiency of this method depends on how accurately it is possible to separate different modes of the object in the control system (CS). In control with feedback, this problem involves both accurate measurement of activation of individual modes that are controlled, and specific control actions applied to these modes.

Arrays of discrete sensors and actuators are commonly used in modal control of elastic objects. Each actuator commonly affects several modes at once, and, similarly, each sensor also reacts to several vibrational modes of the object. In this case, information about different modes in the control system is separated using modal matrices (or modal filters), setting the linear transformations of vectors of measured and control signals.

The modal approach to control can be implemented both based on modal and frequency filters [4–7], and based on observers [8–11]. In the second case, the control system turns out to be more complex, since it uses a known object model to determine the state vector of an elastic object, allowing to determine the required values more accurately.

The efficiency of these two modal approaches to damping forced vibrations in a thin metal beam was compared in our earlier paper [12]. It was established that control with observers is more efficient than control based on modal and frequency filters. Both approaches considered rely on modal matrices to separate the vibrational modes of the object in the control system.

The standard technique for calculating modal matrices consists in calculating the inverse influence matrices [5, 13] (or pseudo-inverse in the more general case [14, 15]). These matrices show the proportions in which each sensor and actuator measures or excites various modes of the object.

Thus, ideally, inversion of the influence matrices allows to obtain a system where each control loop works only with its specific eigenmode and the loops do not interfere with each other's operation. This method for calculating modal matrices was also invariably used in our earlier studies [12, 13, 16–18].

However, the given method cannot be considered a universal solution to the problem of modal separations.

Firstly, higher forms are always present, inevitably excited by the control system, since the number of modes of a distributed elastic object is infinite, while the number of controlled modes is finite. The phenomenon where energy flows to higher modes is called the spillover effect. It limits the efficiency of modal control and can lead to instability of a closed system.

Secondly, the number of sensors and actuators in the control system is also limited. If control is intended to be exercised over the number of modes exceeding the number of sensors and actuators, it is usually impossible to completely separate these modes in the control system.

In any case, ideal selection of the necessary modes during control is possible only in the rather rare situation when distributed modal sensors and actuators are used [6] (so there is no need for modal matrices); in the more common case when discrete control arrays are used, there is no universal solution to this problem, so alternative approaches should be found.

One such alternative technique for calculating modal matrices was proposed by us in [12]. It consists in transposing these matrices instead of inverting the weight coefficient matrices. They are also multiplied by additional diagonal matrices that normalize the degree of excitation and measurements of individual modes.

Instead of separating different modes to be controlled, the algorithm is primarily intended for achieving the most efficient actuation on each mode, approximating it in accordance with the influence coefficients for this particular mode.

Firstly, the proposed method is computationally simpler than the standard one, since it does not require inversion of matrices but only their transposition and multiplication by a diagonal matrix. Secondly, if the number of controlled modes changes, modal matrices do not need to be completely recalculated: it is sufficient to either add necessary columns to them or remove rows from them.

The goal of this study is to analyze the efficiency of various methods for calculating modal matrices in modal control of elastic systems.

A problem similar to the ones we discussed earlier in [12, 13, 16–18] is solved numerically for this purpose: damping of forced bending vibrations in a thin metal beam using piezoelectric sensors and actuators. Optimal control laws are synthesized for each calculation method, and the results of vibration damping for all obtained matrices are compared with each other.

Theoretical foundations of the considered control methods

Modal control is widely used to control the vibrations of elastic systems in various spheres of technology. In this paper, two of the most common approaches to modal control are investigated: a simpler one based on modal and frequency filters, and a more complex one based on observers.

This section provides a brief theoretical description of the methods under consideration (they are described in more detail in [12]), additionally substantiating various techniques for calculating modal matrices: both standard and alternative (proposed by the author of this paper).

Method of modal and frequency filters. Consider the problem of damping forced bending vibrations in a Bernoulli–Euler beam using piezoelectric sensors and actuators. Let us write the vibration equation for an elastic object in matrix form as an eigenmode expansion, assuming that vibrations in different modes occur independently:

$$\ddot{q} + 2\xi\Omega\dot{q} + \Omega^2 q = Q^c + Q^d, \tag{1}$$

where $q_{n\times 1}(t)$ is the vector of generalized coordinates, its length n corresponds to the number of the object's modes taken into account in the model; $\Omega_{n\times n}$ is the diagonal matrix of natural frequencies of the vibrating beam; ξ is the scalar damping coefficient (for simplicity, we assume it to be the same for all modes); $Q^c_{n\times 1}(t)$, $Q^d_{n\times 1}(t)$ are the vectors of generalized forces corresponding to control and external perturbation, respectively.

Let the number of sensors and actuators be the same and equal to m ($m \le n$). Their operation is described by the following equations:

$$y_{m\times 1} = \Theta^s_{m\times n} q_{n\times 1}, \; Q^c_{n\times 1} = \Theta^a_{n\times m} u_{m\times 1}, \tag{2}$$

where $y_{m\times 1}(t)$ is the vector of sensor signals; $u_{m\times 1}(t)$ is the vector of control signals applied to the actuators; $\Theta^s_{m\times n}$, $\Theta^a_{n\times m}$ are the influence matrices for sensors and for actuators, respectively.

If distributed modal sensors and actuators are used [6], the modes of the object are already separated in the control system: each sensor reacts, and each actuator affects only one specific mode. However, such sensors and actuators are used in exceptional cases; they are often inconvenient and too expensive, especially if several modes of the object are to be controlled simultaneously. For this reason, below we consider the case of discrete sensors and actuators.

We assume that control is carried out for k lower modes ($k \le n$), therefore, the control system includes k loops. Modal matrices T and F (mode analyzer and synthesizer) carry out linear

transformations of measured and control signals in the CS. These transformations ensure that each control loop corresponds to a specific mode of the object:

$$\hat{q}_{k\times 1} = T_{k\times m} y_{m\times 1}, u_{m\times 1} = F_{m\times k}\hat{Q}_{k\times 1}, \tag{3}$$

where $\hat{q}_{k\times 1}(t)$ is the estimate vector of k lower generalized coordinates, $\hat{Q}_{k\times 1}(t)$ is the vector of required control actions on k lower eigenmodes.

The required action on the mode in each loop of the modal system depends on the estimate of the respective generalized coordinate:

$$\hat{Q}_i = -R_i(s)\hat{q}_i, \tag{4}$$

where $R_i(s)$ is the control law in the ith circuit, written as a function of the complex variable s.

The control laws in the loops are also called frequency filters, set in such a way that the control system exerts the action on the object required with respect to amplitude and phase, precisely near the resonant frequency of the object corresponding to this loop.

Evidently, in the simplest case, when $k = m = n$, modal matrices should be calculated as follows:

$$T = \left(\Theta^s\right)^{-1}, F = \left(\Theta^a\right)^{-1}. \tag{5}$$

In this case, system of equations (1) is expanded into n independent equations for each of its eigenmodes:

$$\ddot{q}_i + 2\xi\Omega_i\dot{q}_i + \Omega_i^2 q_i = -R_i(s)q_i + Q_i^d, \tag{6}$$

and efficient separate control of each eigenmode of the object can be carried out by selecting the control laws $R_i(s)$.

However, the number of modes n to be taken into account in control of distributed systems generally exceeds the number of sensors and actuators m as well as the number of modes k controlled; the numbers m and k are also not necessarily the same. In this case, the influence matrices can be represented as follows:

$$\Theta^s_{m\times n} = \left[\overline{\Theta}^s_{m\times k} \quad \tilde{\Theta}^s_{m\times(n-k)}\right], \Theta^a_{n\times m} = \begin{bmatrix} \overline{\Theta}^a_{k\times m} \\ \tilde{\Theta}^a_{(n-k)\times m} \end{bmatrix}, \tag{7}$$

while the modal filters are defined as pseudo-inverse to the corresponding components of these matrices:

$$T_{k\times m} = \left(\overline{\Theta}^s_{m\times k}\right)^+, F_{m\times k} = \left(\overline{\Theta}^a_{k\times m}\right)^+. \tag{8}$$

The above method for calculating modal matrices can be considered the standard approach [14, 15, 19]. Below we discuss an alternative we proposed in [12].

Observer method. To describe this method, we represent system (1), (2) in the state space:

$$\dot{q}^n = Aq^n + Bu + Dd, \tag{9}$$

$$y = Cq^n, \tag{10}$$

where d is the vector of external influences; y, u are the vectors of the measured signals and control actions; q^n is the vector of the state of the system related as follows to the vector of generalized coordinates from Eq. (1):

$$q^n = \left(q_1 \quad \ldots \quad q_n \quad \dot{q}_1 \quad \ldots \quad \dot{q}_n\right)^T; \tag{11}$$

matrices A, B and C can be expressed in terms of matrices describing the dynamics of the object and the operation of sensors and actuators:

$$A = \begin{bmatrix} 0_{n\times n} & I_{n\times n} \\ -\Omega^2_{n\times n} & -2\xi\Omega_{n\times n} \end{bmatrix}, B = \begin{bmatrix} 0_{n\times m} \\ \Theta^a_{n\times m} \end{bmatrix}, C = \begin{bmatrix} \Theta^s_{m\times n} & 0_{m\times n} \end{bmatrix}. \quad (12)$$

Here $0_{n\times n}$, $0_{n\times m}$ and $0_{m\times n}$ are matrices consisting of zeros; $I_{n\times n}$ is the unit matrix.

We assume that observation and control are carried out for k lower modes of the object ($k \le n$). The observer's task is to estimate the state vector q^k corresponding to these modes:

$$q^k = \begin{pmatrix} q_1 & \dots & q_k & \dot{q}_1 & \dots & \dot{q}_k \end{pmatrix}^T. \quad (13)$$

The observer generates an estimate $\hat{q}_{2k\times 1}$ of this vector using known matrices $A^{(1)}_{2k\times 2k}$, $B^{(1)}_{2k\times m}$ and $C^{(1)}_{m\times 2k}$ describing the dynamics of k lower modes of the object (they can be obtained from matrices A, B and C by removing unnecessary columns and rows):

$$\dot{\hat{q}} = A^{(1)}\hat{q} + B^{(1)}u + L\left(y - C^{(1)}\hat{q}\right), \quad (14)$$

where $L_{2k\times m}$ is the observation matrix to be calculated.

The control action depends on the estimates of the state vector:

$$u = -R\hat{q}, \quad (15)$$

where $R_{m\times 2k}$ is the control matrix that also is to be calculated.

The principle of separate control of the object's different modes dictates the following structure for the observation matrix L and control matrix R:

$$L_{2k\times k} = \begin{bmatrix} K^L_{k\times k} \\ K^{Ld}_{k\times k} \end{bmatrix} T_{k\times m}, R_{m\times 2k} = F_{m\times k}\begin{bmatrix} K^R_{k\times k} & K^{Rd}_{k\times k} \end{bmatrix}, \quad (16)$$

where K^L, K^{Ld}, K^R, K^{Rd} are diagonal matrices of size $k \times k$; T, F are modal matrices that are already known (mode analyzer and synthesizer).

Modal matrices can be calculated by the same technique as in the case of control without observers.

Alternative technique for calculating modal matrices. The idea of the method presented below was first proposed by the author of this study earlier in [12], however, theoretical substantiation as well as the first results and study of the efficiency of the proposed method are presented for the first time in this paper.

Thus, the central idea of the proposed method is to calculate modal matrices not by inversion, but rather by transposition of influence matrices. An additional mathematical operation is also performed, consisting of multiplying the resulting matrices by the diagonal matrices giving the degree of excitation and response of the control system to the object's individual modes. The proposed method is described by the following equations:

$$T_{k\times m} = M^s_{k\times k}\left(\overline{\Theta}^s_{m\times k}\right)^T, F_{m\times k} = \left(\overline{\Theta}^a_{k\times m}\right)^T M^a_{k\times k}, \quad (17)$$

where $M^s_{k\times k}$, $M^a_{k\times k}$ are the diagonal matrices to be determined.

Next, we consider different approaches to calculating these matrices.

The proposed method can be substantiated theoretically by expanding on the theory of modal filters, described in one of the fundamental studies on this subject [19]. Let us apply this theory to the problem of controlling the bending vibrations in a Bernoulli–Euler beam using piezoelectric sensors and actuators.

Consider a beam of length l located along the x axis, making bending vibrations in the XZ plane. Let us represent the transverse displacement of the points of the beam $w(x,t)$ as an expansion in terms of eigenmodes:

$$w(x,t)=\sum_{i=1}^{n}X_i(x)q_i(t), \tag{18}$$

where all the notations introduced in the previous sections are preserved, and $X_i(x)$ are the eigenmodes of the beam's bending vibrations.

We assume that the eigenmodes are normalized as follows:

$$\int_0^l \rho_l(x)X_i(x)X_j(x)dx=\delta_{ij}, \tag{19}$$

where $\rho_l(x)$ is the linear density of the beam material, δ_{ij} is the Kronecker symbol.

The normalization condition for the second derivative modes also holds true:

$$\int_0^l EI(x)X_i''(x)X_j''(x)dx=\Omega_i^2\delta_{ij}, \tag{20}$$

where $EI(x)$ is the bending stiffness of the beam's cross sections.

The operation of sensors and actuators is described by Eq. (2). We consider them as rectangular piezoelectric plates glued on both sides of the beam in sensor-actuator pairs.

In this case, the following relations hold true for the influence coefficients:

$$\Theta_{ij}^s=k^s\Theta_{ij},\ \Theta_{ji}^a=k^a\Theta_{ij}, \tag{21}$$

$$\Theta_{ij}=X_j'\left(x_i^{(2)}\right)-X_j'\left(x_i^{(1)}\right)=\int_{x_i^{(1)}}^{x_i^{(2)}}X_j''(x)dx\approx X_j''(x_i)l_p, \tag{22}$$

where k^s, k^a are the coefficients for sensors and actuators, respectively, depending on their geometric parameters and material properties; $x_i^{(1)}$, $x_i^{(2)}$, x_i are the coordinates the left and right ends as well as the center of the ith sensor–actuator pair, respectively; is the length of each piezoelectric element.

These quantities are related as follows:

$$x_i=\frac{x_i^{(1)}+x_i^{(2)}}{2},\ l_p=x_i^{(2)}-x_i^{(1)}. \tag{23}$$

Eq. (22) uses the assumption that the length of the sensors and actuators is small, allowing to approximately replace the integral of the second derivative of the beam's eigenmodes along the length of the piezoelectric element with the value of this function in the midsection. The influence coefficients essentially turn out to be proportional to the curvature of individual eigenmodes in the given cross sections. The reason for this is that longitudinal deformation of sensors and actuators is associated precisely with bending deformation (i.e., curvature) of the corresponding sections of the beam.

It is proposed in [19] to calculate the approximation of the transverse displacement function $\hat{w}(x,t)$ of beam points in terms of estimates of this function in separate cross sections corresponding to the location of sensors, $\hat{w}(x_j,t)$:

$$\hat{w}(x,t)=\sum_{j=1}^{m}G(x,x_j)\hat{w}(x_j,t), \tag{24}$$

where $G(x,x_j)$ are the interpolation functions given for each sensor.

The alternative technique for calculated the matrices, presented in this paper, assumes a slightly modified definition for the function $\hat{w}(x,t)$:

$$\hat{w}(x,t)=\sum_{j=1}^{m}\overline{G}(x,x_j)y_j(t). \tag{25}$$

A modification introduced here is that the actual signals $\hat{w}\left(x_j,t\right)$ of the sensors are used instead of the displacement estimate $y_j\left(t\right)$ in the points where the sensors are mounted. This substitution is made because the sensors in the given problem measure not the transverse displacement of the beam's cross sections, as is the case in [19], but the curvature of the beam in these cross sections, therefore it is impossible to obtain an estimate of the displacement $\hat{w}\left(x_j,t\right)$ from their signals. Therefore, the function $\bar{G}\left(x,x_j\right)$ takes on a slightly different meaning than the function $G\left(x,x_j\right)$ in the original formula.

The formula for determining the interpolation functions $\bar{G}\left(x,x_j\right)$ plays the central role in developing the proposed method.

We propose the following definition:

$$\bar{G}\left(x,x_j\right)=\sum\nolimits_{i=1}^{k}\bar{M}_i^s X_i\left(x\right)X_i''\left(x_j\right). \tag{26}$$

Thus, the interpolation function for each of the sensors is a combination of the beam's eigenmodes, where the weight of each eigenmode is proportional to the curvature of this eigenmode in the beam cross section corresponding to this sensor (i.e., in fact corresponding to the influence coefficient Θ_{ji}). In addition, the contribution of various modes is regulated by coefficients $\bar{M}_i^s$. Next, let us consider several approaches to determining them.

The following expression for the estimate of the ith generalized coordinate can be obtained from the condition of orthogonality and normalization of eigenmodes (19):

$$\hat{q}_i\left(t\right)=\int_0^l \rho_l\left(x\right)X_i\left(x\right)\hat{w}\left(x,t\right)dx. \tag{27}$$

Substituting expressions (25) and (26) here, and taking into account condition (19) and the definition of the mode analyzer (3), we obtain the following expression for the components of this matrix:

$$T_{ij}=\int_0^l \rho_l\left(x\right)X_i\left(x\right)\bar{G}\left(x,x_j\right)dx=\bar{M}_i^s X_i''\left(x_j\right)=\frac{\bar{M}_i^s}{l_p}\Theta_{ji}=\frac{\bar{M}_i^s}{l_p k^s}\Theta_{ji}^s. \tag{28}$$

Thus, we have obtained an expression for the matrix T, which coincides with Eq. (17). In this case, the coefficients are related as follows:

$$\bar{M}_i^s=l_p k^s M_i^s. \tag{29}$$

Next, let us discuss how these normalizing coefficients are to be determined. To do this, recall the standard definition of the matrix T, that is, Eq. (5). It assumes that the diagonal of the matrix, which is the product of the matrices T and Θ^s, is composed of units, i.e., the following equality holds true:

$$\sum\nolimits_{j=1}^{m}T_{ij}\Theta_{ji}^s=\frac{k^s}{l_p}\bar{M}_i^s\sum\nolimits_{j=1}^{m}\left(\Theta_{ji}\right)^2=1. \tag{30}$$

This leads to the first method for normalization, consisting of fitting:

$$\bar{M}_i^s=\frac{l_p}{k^s}\cdot\frac{1}{\sum\nolimits_{j=1}^{m}\left(\Theta_{ji}\right)^2}=\frac{l_p}{k^s}M_i,\ M_i^s=\frac{\bar{M}_i^s}{l_p k^s}=\frac{1}{\left(k^s\right)^2}M_i, \tag{31}$$

where the components of the diagonal normalizing matrix are introduced:

$$M_i=\frac{1}{\sum\nolimits_{j=1}^{m}\left(\Theta_{ji}\right)^2}. \tag{32}$$

The matrix synthesizing the modes is found by calculating the normalizing matrix M^a from Eq. (17) similarly to expression (31):

$$M_i^a = \frac{1}{\left(k^a\right)^2} M_i. \tag{33}$$

The second approach to calculating the normalizing matrices is asymptotic. It is formulated assuming that there is a sufficiently large number of sensors and actuators, and the sum of the squared second derivatives of the eigenmodes can be replaced by the average value of this function along the length of the beam multiplied by the number of piezoelectric elements:

$$\sum_{j=1}^{m}\left(\Theta_{ji}\right)^2 = l_p^2 \sum_{j=1}^{m}\left(X_i''\left(x_j\right)\right)^2 \approx \frac{l_p^2 m}{l}\int_0^l \left(X_i''(x)\right)^2 dx = \frac{l_p^2 m \Omega_i^2}{lEI}. \tag{34}$$

In this case, the components of the diagonal normalizing matrix take the following form:

$$M_i = \frac{EIl}{\Omega_i^2 l_p^2 m}. \tag{35}$$

Finally, another normalization method is trivial (in fact, the absence of normalization), where the matrix M is assumed to be singular:

$$M = I_{k\times k}. \tag{36}$$

Regardless of the method for determining the normalizing matrix, the proposed method for calculating modal matrices is much simpler than the standard method (8) from the standpoint of calculations. It also has another advantage: if the number of controlled modes is changed (while maintaining the sensor and actuator system) there is no need to completely recalculate the modal matrices, as with the standard method; it is sufficient to either add the corresponding columns to them or remove rows from them.

This raises the natural question whether the standard and alternative approaches to calculating modal matrices are fundamentally different; if the answer is yes, the conundrum is how this is possible since both approaches are aimed at solving the same problem.

This apparent contradiction is explained simply: if the number of sensors and actuators, evenly distributed over the control object, is increased, the results yielded by these approaches converge, since in this case the columns of the matrix Θ become orthogonal to each other, and the results of inverting this matrix and transposing it (provided that the first normalization method (32) is used) become identical.

In view of this remark, the greatest difference between the considered approaches to calculating modal matrices is manifested in the case when the number of sensors and actuators used turns out to be small. This specific case is considered below: the number of pairs of piezoelectric elements in the problem is taken equal to two.

In addition to the formulation of the proposed approach, the novelty of this study is that we consider the case when the number of modes controlled exceeds the number of sensor-actuator pairs ($k > m$), while the opposite situation is traditionally considered in the literature on modal control ($k \le m$) [14, 15]. This means that the modes controlled in the systems discussed below cannot be strictly separated from each other, which further complicates the problem of determining modal matrices and increases the importance of studying the alternative approaches to solving this problem.

Problem statement

The problem solved in this study involves damping of forced bending vibrations in a thin aluminum beam elastically restrained in the midsection by piezoelectric sensors and actuators glued to the beam in certain regions. This problem has already been considered in some of our earlier studies: first in an experimental study [16], then in numerical ones [12, 17, 18], where the goal was to simulate the processes occurring in the experiment as accurately as possible.

The experimental setup is shown schematically in Fig. 1. Beam *1* with a cross section of 3 × 35 mm and a length of 70 cm is arranged vertically and fixed at one point at a distance of 10 cm from the lower end. Piezoelectric stack actuator *2* is included in the fastener connecting the

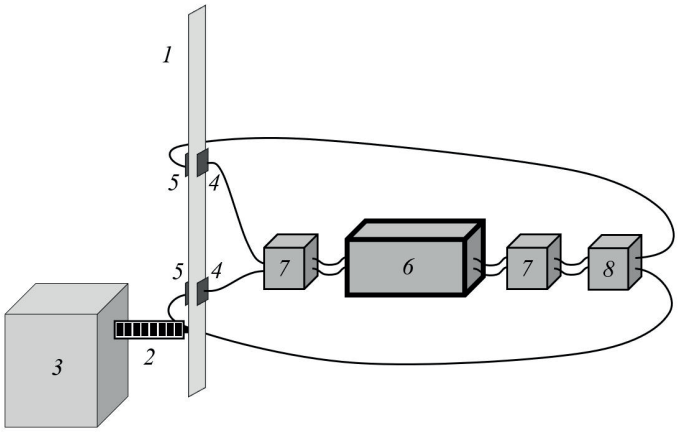

Fig. 1. Schematic of experimental setup:
aluminum beam 1; piezoelectric stack actuator 2;
fixed base 3; sensors 4; actuators 5;
digital controller 6; low-pass filters 7; amplifier 8

beam to fixed base *3*. Longitudinal vibrations of the actuator, occurring when an AC voltage is applied to it with a certain frequency, induce vibrations in the point where the beam is connected. Such vibration acts as external excitation, whose consequences the control system should mitigate.

The control system consists of two sensor-actuator pairs (sensors *4*, actuators *5*), which are thin rectangular piezoelectric plates measuring 50 × 30 mm, covered with electrodes on both sides.

In addition to digital controller *6*, converting the measured signals into control signals, the control circuit includes additional elements: low-pass filters *7* and amplifier *8*. Filters smooth out the high-frequency components of the signal arising from discretization in the controller, and generally increase the stability of the closed system; the amplifier increases the amplitude of the control signal by 25 times before it is fed to the actuators.

The frequency characteristics of the filters and the amplifier are also taken into account in numerical simulation of a closed system [12], which distinguishes this study from most numerical studies on this subject.

Initially, the initial goal of control in the experiment and subsequent numerical studies, where control systems were synthesized without observers, was to dampen the forced bending vibrations of the beam only at the first and second resonances. The arrangement of sensors and actuators on the beam was chosen in accordance with this goal [16]. However, our most recent studies, starting with [12], consider, among other things, more efficient modal systems with observers allowing to increase the number of beam eigenmodes to be controlled, while preserving the number and arrangement of sensors and actuators. Therefore, the goal of control for such systems was formulated as damping forced beam vibrations at three lower resonances.

The efficiency of control in the experiment was monitored with a laser vibrometer measuring the vibration amplitude of a point at the upper end of the beam (since it is this point that experiences the largest displacements during forced vibrations of the beam).

A finite element model of the control object (beams with piezoelectric elements and fastener) was constructed at the first stage of numerical simulation of the closed system; analysis of the model allows to obtain the frequency characteristics of the object [17]. Next, the frequency characteristics of the closed system were calculated for each type of control system tested based on the frequency characteristics of both the object and the CS itself [17]. To determine the efficiency of control, we analyzed the frequency response of displacement of a point at the upper end of the beam.

Synthesis of control systems

This study was aimed at synthesizing optimal control systems within the framework of the approaches considered, i.e., such system that achieve the goal of control posed the most efficiently.

For this purpose, an optimization procedure is used to construct the control systems [17, 18], allowing to vary the parameters of the control system and select their optimal combinations, satisfying the condition for stability of the closed system.

The optimization criterion is either the height of a specific resonant peak on the frequency response of the beam (corresponding to displacement of the point at the upper end), or the sum of the vibration amplitudes (in decibels) at the corresponding resonant peaks in the case when the system must dampen vibrations at several resonances.

The stability of the closed system was analyzed using the Nyquist criterion, modified for the case of several control loops [17].

Modal matrices, a mode analyzer and a mode synthesizer (T and F) are calculated at the first stage of CS synthesis, both with and without observers. They are calculated by different techniques, discussed above. Then, control laws are synthesized for each combination of modal matrices using the optimization procedure: for systems without observers, these are frequency filters $R_1(s)$ and $R_2(s)$ (see Eq. (4)), and for systems with observers, these are diagonal matrices K^L, K^{Ld}, K^R and K^{Rd}, included in the definition of observation and control matrices L and R (see expressions (16)). Various goals of control are set: both the damping of beam vibrations at each resonance separately, and simultaneous damping at several resonances.

Let us focus more closely on different techniques for calculating the modal matrices used in this study. We assume that equalities (21) hold true for the influence matrices. In this case, two approaches to calculating the matrices are globally possible.

The first method is inversion (or pseudo-inversion) (8):

$$T = \left(\Theta^s\right)^+ = k^s \Theta^+, F = \left(\Theta^a\right)^+ = k^a \left(\Theta^T\right)^+. \tag{37}$$

The second method is transposition with multiplication by the matrix M (see expressions (31, 33)):

$$T = \frac{1}{\left(k^s\right)^2} M \left(\Theta^s\right)^T = \frac{1}{k^s} M \Theta^T, F = \frac{1}{\left(k^a\right)^2} \left(\Theta^a\right)^T M = \frac{1}{k^a} \Theta M. \tag{38}$$

The following influence matrices were obtained from the object model for cases of control over two or three modes:

$$\Theta_{2\times 2} = \begin{bmatrix} 3.659 & -17.07 \\ 1.187 & 17.76 \end{bmatrix}, \Theta_{2\times 3} = \begin{bmatrix} 3.659 & -17.07 & 21.48 \\ 1.187 & 17.76 & 10.09 \end{bmatrix}. \tag{39}$$

The normalizing matrix M was determined by one of the three techniques (see Eqs. (32), (35), (36)) (the last row and column are removed for control over two modes):

$$\begin{cases} M^{triv} = I_{3\times 3}, M^{asimp} = diag\{0.574 \quad 0.0159 \quad 0.00223\}, \\ M^{fit} = diag\{0.0676 \quad 0.00165 \quad 0.00178\}. \end{cases} \tag{40}$$

In this case, the product of multiplying the modal matrices by the corresponding influence matrices is of greater interest for analysis than the matrices themselves; let us denote it as $\tilde{\Theta}$. The matrix $\tilde{\Theta}$ should have as much similarity as possible to the unit matrix for the best separation of modes.

This requirement is satisfied for the case of control over two modes ($k = 2$) and inversion of the influence matrices:

$$\tilde{\Theta}^{inv}_{2\times 2} = T\Theta^s = \left(\Theta^a F\right)^T = I_{2\times 2}. \tag{41}$$

Below we present the matrices corresponding to pseudo-inversion and different normalization methods for transposition with $k = 3$: trivial, asymptotic and fitting (matrices for $k = 2$ can be obtained by removing the last row and column from these matrices):

$$\begin{cases} \tilde{\Theta}^{inv} = \begin{bmatrix} 0.0236 & -0.0201 & 0.150 \\ -0.0201 & 1.00 & 0.00310 \\ 0.150 & 0.00310 & 0.977 \end{bmatrix}, \ \tilde{\Theta}^{triv} = \begin{bmatrix} 14.8 & -41.4 & 90.6 \\ -41.4 & -607 & -187 \\ 90.6 & -187 & 563 \end{bmatrix}, \\ \tilde{\Theta}^{asimp} = \begin{bmatrix} 8.49 & -23.8 & 52.0 \\ -0.658 & 9.65 & -2.98 \\ 0.202 & -0.417 & 1.25 \end{bmatrix}, \ \tilde{\Theta}^{fit} = \begin{bmatrix} 1.00 & -2.80 & 6.12 \\ -0.0682 & 1.00 & -0.309 \\ 0.161 & -0.333 & 1.00 \end{bmatrix}. \end{cases} \quad (42)$$

As evident from the formulas obtained, different techniques for calculating the modal matrices produce significantly different results for separation of the beam's eigenmodes in the control system. Next, we can compare the efficiency of the considered approaches.

Comparison of results obtained from different control systems

This section presents the results from the synthesized control systems. Examples of control laws for the CS based on the method of modal and frequency filters are given in [18], and examples for the CS with observers are given [12].

Results of damping of forced beam vibrations at the first (I) and second (II) resonances for systems without observers are given in Table 1. If the modal matrices are calculated by the transposition method in such CS, it does not matter which normalization method is used, since different methods produce the same result with the appropriate choice of gain coefficients in the control laws in each of the loops. The CS synthesized for each technique for calculating modal matrices (inversion or transposition) were efficient only at the first or second resonances separately or at both resonances together.

As evident from the data presented, the most efficient damping of vibrations at both resonances is achieved when one of the modal matrices is determined by inversion, and the other by transposition (cases 3 and 4), the latter case is slightly more efficient.

Table 1

Decrease in resonant amplitudes of beam vibrations for various control systems (without observers)

Calculation technique			Damping	Amplitude decrease, dB, at resonance	
Case	*T*	*F*		I (Δy_1)	II (Δy_2)
1	Tr	Inv	separately	32.04	30.84
			together	32.00	31.05
2	Tr	Tr	separately	32.31	31.41
			together	32.32	29.9
3	Inv	Tr	separately	32.72	31.48
			together	32.72	31.48
4	Tr	Inv	separately	32.77	31.45
			together	32.77	31.50

Notations: *T*, *F* are the mode analyzer and synthesizer, respectively; Tr, Inv are transposition and inversion of influence matrices, respectively.

Table 2 gives the results obtained from different CS with observers at the first three resonances. Two cases are considered for each combination of modal matrices: control over only two ($k = 2$) or over all three modes ($k = 3$). In each of these cases, various normalization methods were considered: all three methods for $k = 3$, only trivial and asymptotic for $k = 2$, since in this case there is practically no difference between the asymptotic and fitting cases. The best results of vibration damping at each of the resonances for each combination of modal matrices are highlighted in bold in Table 2.

Table 2

Decrease in resonant amplitudes of beam vibrations for various control systems (with observers)

Calculation technique			k	Normalization	Amplitude decrease, dB, at resonance		
Case	T	F			I (Δy_1)	II (Δy_2)	III (Δy_3)
1	Inv	Inv	2	–	34.75	35.66	-
			3	–	**36.50**	**36.52**	**22.85**
2	Tr	Tr	2	*triv*	36.44	36.55	–
				asymp	**36.68**	36.53	–
			3	*triv*	35.48	**37.02**	**23.91**
				asymp	36.33	36.95	23.88
				fit	36.18	36.99	22.75
3	Inv	Tr	2	*triv*	35.97	31.76	–
				asymp	36.06	31.86	–
			3	*triv*	36.18	37.09	**21.99**
				asymp	**36.78**	38.23	21.69
				fit	36.73	**38.33**	21.83
4	Tr	Inv	2	*triv*	36.93	36.98	–
				asymp	36.94	37.18	–
			3	*triv*	37.68	**37.65**	24.28
				asymp	37.86	37.62	24.35
				fit	**37.93**	37.64	**24.46**

Notations: k is the number of modes; *triv*, *asimp*, *fit* are trivial, asymptotic and fitting normalization methods used for transposition.

Fig. 2 shows the frequency response of the closed system, where the vibration amplitude of the point at the upper end of the beam, near each of the three lower resonances, acts as the observable. The efficiency of four CS corresponding to each of the combinations of modal matrices in the case of fitting normalization with simultaneous damping of vibrations at three resonances is compared.

Notably, the difference between all the considered calculation techniques is small: it is within a few decibels for control with observers, and about a decibel for control without observers. Thus, robustness is observed in this aspect of the approaches to control considered. The most efficient combinations of matrices for systems with observers are also 3 and 4, and the latter is again preferable: it allows to damp the first and third resonances, while combination 3 allows to damp the second resonance.

On average, the results for cases of asymptotic and fitting normalization are better than for trivial the trivial normalization: asymptotic normalization is better for combination 2, and fitting normalization is better for combinations 3 and 4. In general however, the normalization method

is less important than the technique for calculating the matrices (inversion or transposition). It is also worth noting that, on average, the first two resonances are damped better with control over three modes ($k = 3$) than over two modes ($k = 2$).

In addition, the study confirms the conclusion drawn in [12]: control with observers remains significantly more efficient than that based on modal and frequency filters for any techniques for calculating modal matrices, besides it allows to damp vibrations at a larger number of resonances exceeding the number of sensors and actuators.

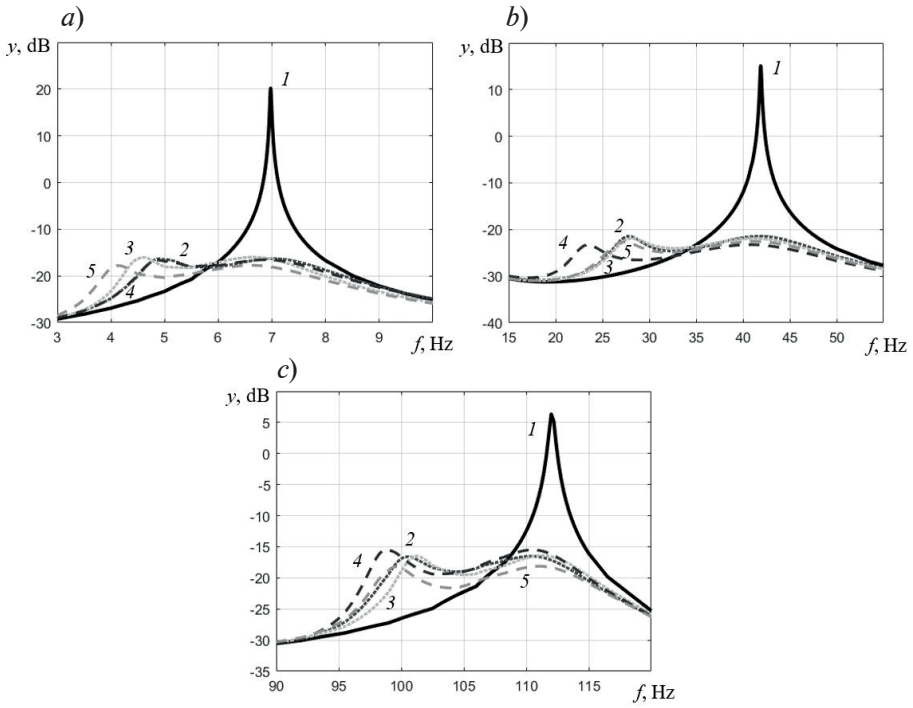

Fig. 2. Frequency response of the beam for different control systems (with observers) near resonances I (*a*), II (*b*) and III (*c*): without control (curves *1*) and for different techniques 1–4 used to calculate modal matrices (curves *2–5*) (see Table 2 for calculation techniques 1–4)

Conclusion

The paper considers various techniques for calculating modal matrices within the modal approach to control of distributed systems. Along with the traditional method involving inversion of influence matrices, an alternative method was considered and substantiated, consisting in transposition of these matrices with subsequent normalization. The example of the numerical solution to the problem of damping of forced bending vibrations in a thin metal beam was used to prove that the best result of control was achieved by combining the given methods, when the mode analyzer matrix was calculated by transposition, and the mode synthesizer matrix was calculated by inversion. This conclusion is valid for systems both with observers and based on modal and frequency filters. In addition, it is established that the results of control can be improved through normalization of modal matrices calculated by transposition.

REFERENCES

1. **Pusch M., Ossmann D., Luspay T.,** Structured control design for a highly flexible flutter demonstrator, Aerospace. 6 (3) (2019) 27–46.

2. **Carvalhal R., Silva S., Lopes V.,** Modal control applications in intelligent truss structures, ABCM Symp. Ser. Mechatron. 1 (Jan) (2004) 304–310.

3. **Chomette B., Chesne S., Remond D., Gaudiller L.,** Damage reduction of on-board structures using piezoelectric components and active modal control – application to a printed circuit board, Mech. Syst. Signal Proc. 24 (2) (2010) 352–364.

4. **Zenz G., Berger W., Gerstmayr J., et al.,** Design of piezoelectric transducer arrays for passive and active modal control of thin plates, Smart Struct. Syst. 12 (5) (2013) 547–577.

5. **Peukert C., Pöhlmann P., Merx M., et al.,** Investigation of local and modal based active vibration control strategies on the example of an elastic system, J. Mach. Eng. 19 (2) (2019) 32–45.

6. **Lee C.-K., Moon F. C.,** Modal sensors/actuators, J. Appl. Mech. 57 (2) (1990) 434–441.

7. **Donoso A., Bellido J. C.,** Systematic design of distributed piezoelectric modal sensors/actuators for rectangular plates by optimizing the polarization profile, Struct. Multidisc. Optim. 38 (4) (2009) 347–356.

8. **Guo X., Jiang J.,** Optimization of actuator placement in a truss-cored sandwich plate with independent modal space control, Smart Mater. Struct. 20 (11) (2011) 115011.

9. **Sharma M., Singh S. P., Sachdeva B. L.,** Modal control of a plate using a fuzzy logic controller, Smart Mater. Struct. 16 (4) (2007) 1331–1341.

10. **Lu J., Wang P., Zhan Z.,** Active vibration control of thin-plate structures with partial SCLD treatment, Mech. Syst. Signal Process. 84 (A) (2017) 531–550.

11. **Katz R., Fridman E.,** Delayed finite-dimensional observer-based control of 1D parabolic PDEs via reduced-order LMIs, Autom. 142 (August) (2022) 110341.

12. **Fedotov A. V., Belyaev A. K., Polyanskiy V. A.,** Numerical study of the efficiency of modal filter method and observer method for implementation of modal control of vibrations of elastic systems, St. Petersburg State Polytechnical University Journal. Physics and Mathematics. 16 (3) (2023) 160–176 (in Russian).

13. **Belyaev A. K., Polyanskiy V. A., Smirnova N. A., Fedotov A. V.,** Identification procedure in the modal control of a distributed elastic system, St. Petersburg State Polytechnical University Journal. Physics and Mathematics. 10 (2) (2017) 69–81.

14. **Gawronski W.,** Modal actuators and sensors, J. Sound Vib. 229 (4) (2000) 1013–1022.

15. **Friswell M. I.,** On the design of modal actuators and sensors, J. Sound Vib. 241 (3) (2001) 361–372.

16. **Belyaev A. K., Fedotov A. V., Irschik H., et al.,** Experimental study of local and modal approaches to active vibration control of elastic systems, Struct. Control Health Monit. 25 (8) (2018) e2105.

17. **Fedotov A. V.,** The damping of the distributed system vibrations using piezoelectric transducers: simulation, St. Petersburg State Polytechnical University Journal. Physics and Mathematics. 12 (1) (2019) 142–155 (in Russian).

18. **Fedotov A. V., Belyaev A. K., Polyanskiy V. A., Smirnova N. A.,** Local, modal and shape control strategies for active vibration suppression of elastic systems: experiment and numerical simulation, In book: V. A. Polyanskiy, A. K. Belyaev (Eds.). Mechanics and Control of Solids and Structures (Book Series: Advanced Structured Materials. Vol. 164). Springer, Cham, Switzerland (2022) 151–169.

19. **Meirovitch L., Baruh H.,** The implementation of modal filters for control of structures, J. Guid. Control. Dynam. 8 (6) (1985) 707–716.

СПИСОК ЛИТЕРАТУРЫ

1. **Pusch M., Ossmann D., Luspay T.** Structured control design for a highly flexible flutter demonstrator // Aerospace. 2019. Vol. 6. No. 3. Pp. 27–46.

2. **Carvalhal R., Silva S., Lopes V.** Modal control applications in intelligent truss structures // ABCM Symposium Series in Mechatronics. 2004. Vol. 1. January. Pp. 304–310.

3. **Chomette B., Chesne S., Remond D., Gaudiller L.** Damage reduction of on-board structures using piezoelectric components and active modal control – application to a printed circuit board // Mechanical Systems and Signal Processing. 2010. Vol. 24. No. 2. Pp. 352–364.

4. **Zenz G., Berger W., Gerstmayr J., Nader M., Krommer M.** Design of piezoelectric transducer arrays for passive and active modal control of thin plates // Smart Structures and Systems. 2013. Vol. 12. No. 5. Pp. 547–577.

5. **Peukert C., Pöhlmann P., Merx M., Müller J., Ihlenfeldt S.** Investigation of local and modal based active vibration control strategies on the example of an elastic system // Journal of Machine Engineering. 2019. Vol. 19. No. 2. Pp. 32–45.

6. **Lee C.-K., Moon F. C.** Modal sensors/actuators // Journal of Applied Mechanics. 1990. Vol. 57. No. 2. Pp. 434–441.

7. **Donoso A., Bellido J. C.** Systematic design of distributed piezoelectric modal sensors/actuators for rectangular plates by optimizing the polarization profile // Structural and Multidisciplinary Optimization. 2009. Vol. 38. No. 4. Pp. 347–356.

8. **Guo X., Jiang J.** Optimization of actuator placement in a truss-cored sandwich plate with independent modal space control // Smart Materials and Structures. 2011. Vol. 20. No. 11. 115011.

9. **Sharma M., Singh S. P., Sachdeva B. L.** Modal control of a plate using a fuzzy logic controller // Smart Materials and Structures. 2007. Vol. 16. No. 4. Pp. 1331–1341.

10. **Lu J., Wang P., Zhan Z.** Active vibration control of thin-plate structures with partial SCLD treatment // Mechanical Systems and Signal Processing. 2017. Vol. 84. Part A. Pp. 531–550.

11. **Katz R., Fridman E.** Delayed finite-dimensional observer-based control of 1D parabolic PDEs via reduced-order LMIs // Automatica. 2022. Vol. 142. August. P. 110341.

12. **Федотов А. В., Беляев А. К., Полянский В. А.** Численное исследование эффективности метода модальных фильтров и метода наблюдателей при реализации модального управления колебаниями упругих систем // Научно-технические ведомости СПбГПУ. Физико-математические науки. 2023. Т. 16. № 3. С. 160–176.

13. **Беляев А. К., Полянский В. А., Смирнова Н. А., Федотов А. В.** Процедура идентификации при модальном управлении распределенным упругим объектом // Научно-технические ведомости СПБГПУ. Физико-математические науки. 2017. Т. 10. № 2. С. 69–81.

14. **Gawronski W.** Modal actuators and sensors // Journal of Sound and Vibration. 2000. Vol. 229. No. 4. Pp. 1013–1022.

15. **Friswell M. I.** On the design of modal actuators and sensors // Journal of Sound and Vibration. 2001. Vol. 241. No. 3. Pp. 361–372.

16. **Belyaev A. K., Fedotov A. V., Irschik H., Nader M., Polyanskiy V. A., Smirnova N. A.** Experimental study of local and modal approaches to active vibration control of elastic systems // Structural Control and Health Monitoring. 2018. Vol. 25. No. 8. P. e2105.

17. **Федотов А. В.** Численное моделирование гашения колебаний распределенной системы с помощью пьезоэлементов // Научно-технические ведомости СПбГПУ. Физико-математические науки. 2019. Т. 12. № 1. С. 142–155.

18. **Fedotov A. V., Belyaev A. K., Polyanskiy V. A., Smirnova N. A.** Local, modal and shape control strategies for active vibration suppression of elastic systems: Experiment and numerical simulation // V. A. Polyanskiy, A. K. Belyaev (Eds.). Mechanics and Control of Solids and Structures (Book Series: Advanced Structured Materials. Vol. 164). Cham, Switzerland: Springer, 2022. Pp. 151–169.

19. **Meirovitch L., Baruh H.** The implementation of modal filters for control of structures // Journal of Guidance, Control, and Dynamics. 1985. Vol. 8. No. 6. Pp. 707–716.

THE AUTHORS

FEDOTOV Aleksandr V.
Institute for Problems of Mechanical Engineering of RAS
61, Bolshoi Ave. V. Isl., St. Petersburg, 199178, Russia
alvafed@yandex.ru
ORCID: 0000-0001-6028-7566

СВЕДЕНИЯ ОБ АВТОРАХ

ФЕДОТОВ Александр Васильевич – *кандидат технических наук, старший научный сотрудник лаборатории мехатроники Института проблем машиноведения РАН, Санкт-Петербург, Россия.*
199178, Россия, г. Санкт-Петербург, Большой проспект В. О., 61.
alvafed@yandex.ru
ORCID: 0000-0001-6028-7566

Received 29.09.2023. Approved after reviewing 24.11.2023. Accepted 24.11.2023.
Статья поступила в редакцию 29.09.2023. Одобрена после рецензирования 24.11.2023. Принята 24.11.2023.

Journal

ST. PETERSBURG STATE POLYTECHNICAL UNIVERSITY JOURNAL: PHYSICS AND MATHEMATICS

Vol. 17, No. 1, 2024

Founder and publisher: Peter the Great St. Petersburg Polytechnic University

The journal is registered with the Federal Service for Supervision of Communications, Information Technology and Mass Media (Roskomnadzor).
Certificate ПИ ФС77-51457 issued 19.10.2012.

Phone 8 (812) 294-22-85

Website https://physmath.spbstu.ru/

E-mail: physics@spbstu.ru

Typesetting by A.S. Kolgatina

Published 30.03.2024. Format 60x84/8. Digital print.
Printer's sheets Print circulation 1000. Order ID